# Photon Beam Asymmetry Measurement from the $\gamma n \to K^{+} \Sigma^{-}$ Reaction

by Edwin Munévar Espitia

B.Sc in Physics, April 2001, Universidad Distrital, Bogotá, Colombia
M.Sc in Physics, May 2005, Universidad de los Andes, Bogotá, Colombia
M.Phil. Physics, January 2008, The George Washington University

A Dissertation submitted to

The Faculty of
The Columbian College of Arts and Sciences
of The George Washington University
in partial fulfillment of the requirements
for the degree of *Doctor of Philosophy*

January 31, 2014

Dissertation directed by

Barry L. Berman
Professor of Physics

Pawel Nadel-Turoński
Nathan Isgur Fellow, Jefferson Laboratory

Gerald Feldman
Professor of Physics

The Columbian College of Arts and Sciences of The George Washington University certifies that Edwin Munévar Espitia has passed the Final Examination for the degree of Doctor of Philosophy as of October 17, 2013. This is the final and approved form of the dissertation.

# Photon Beam Asymmetry Measurement from the $\gamma n \to K^{+} \Sigma^{-}$ Reaction

Edwin Munévar Espitia

Dissertation Research Committee:

Barry L. Berman, Professor of Physics, Dissertation Director

Pawel Nadel-Turoński, Nathan Isgur Fellow, Jefferson Laboratory, Dissertation Co-Director

Gerald Feldman, Professor of Physics, Dissertation Co-Director

Andrei Alexandru, Assistant Professor of Physics, Committee Member

Allena Opper, Professor of Physics, Committee Member

# Dedication

This dissertation is dedicated to the memory of Professor Barry L. Berman

## Acknowledgments

I would like to express my greatest appreciation to all those who provided me the possibility to complete this work. This project would not have been possible without their help and support.

At the outset, I would like to express my deepest gratitude to my late advisor Barry Berman. I was always impressed by his clear knowledge on nuclear physics as well as by his astonishing ability to do math calculations very quickly and draw interesting conclusions from them. His ability to face any situation in physics, even the toughest ones, is something I hope to match some day. The trust and autonomy he gave me during most of my Ph.D is something I consider was very important to succeed in my research project. I will always be very thankful with him for the flexibility, kindness, and understanding he always had with me.

I would truly like to thank Pawel Nadel-Turoński and Gerald Feldman for volunteering to take over the supervision of my research. Their advice and support throughout the research project, as well as their pain-staking effort in proof reading the drafts, are greatly appreciated. I would like to thank Pawel for all the useful comments and remarks through the learning process of my Ph.D. The discussions we had periodically were always very helpful giving me a strong insight about the research topic not only at the experimental level but also at the theoretical level. His commitment with this project is invaluable. Without his guidance, it would have been very difficult to me to put the topic together. I would like to thank Jerry for all the support and cooperation I received from him throughout the time I have spent on this dissertation. He was always willing to help me solve the various school administrative issues that came up along the way. Without his assistance and support, this work would not have finalized successfully.

I am also grateful to the other members of my dissertation committee, Dr. Alexandru, Dr. Opper, Dr. Park, and Dr. Strauch for their valuable comments and suggestions. A special thanks goes to Dr. Strauch from the University of South Carolina for taking time out from his schedule to serve as my external reader.

I want to thank the Faculty of the Department of Physics at GWU for the knowledge and tools I was given during my course-work period; these have been proved to be very useful and important for my career in both aspects research and teaching. I would also like to thank administrative and technical staff members of GWU who have been kind enough to advise and help in their respective roles. I gratefully acknowledge the George Washington University for providing the financial support to pursue my doctoral studies.

I would like to express my gratitude to The CLAS Collaboration. I am particularly grateful with the g13 fellows. Their comments and support were very important for the analysis performed in this work, specially in those times when the neutrons were reluctant to show up in the data.

I owe my deepest gratitude to Rakhsha and her family Rob and Bardia for the kindness and hospitality they always had with me. My best wishes to them.

I am deeply grateful to my relatives in the United States: my aunt María Helena, my cousins Elkin, Sandra, Natalia and their corresponding families. They have a special gift for being obliging with people and I was not the exception. My stay in the United States was notably less painful thanks to their warmth and love. They treated me like a son and a brother and were always there for me. My infinite gratitude to them.

I would like to thank my brother Jaime, his wife Bibiana, and my beloved nephews Valeria, Tomas, and Mariana for their love. They represented to me a true reason to come back home. I also wish to thank the rest of my family: uncles, aunts, cousins, and grandmas for their trust, love, and encouragement to pursue my studies. I will always have my grandpa in my heart; he passed away while I was in the United States.

Finally, I would like to give my special thanks to my parents, Maria and Jaime, for all the love and continued support they have had to me throughout my life. I thank God for having them. Their humility, effort, and life lessons have been an inspiration to me to get where I am now. Without their prayers, I would not have lasted for long far away from my beloved country Colombia. I will be forever indebted to them.

# Abstract of Dissertation

## Photon Beam Asymmetry Measurement from the $\gamma n \rightarrow K^+ \Sigma^-$ Reaction

Strangeness channels are important in the experimental search for missing baryon resonances. Phenomenological reaction models for the extraction of resonance parameters, such as coupled-channels analyses, require data for many observables, in different channels, and on different targets. The analysis presented in this thesis is the first measurement of the beam asymmetry over a wide range in the kaon azimuthal center-of-mass angle (which is essential for accessing the s-channel contribution) for the exclusive $\gamma n \rightarrow K^+ \Sigma^-$ reaction, using the deuteron as a quasi-free neutron target. The data used were from the CLAS g13b run period (experiment E06-103) at Jefferson Lab, which used linearly polarized tagged real photons with energies between 1.1 and 2.3 GeV. Results are shown for two photon-energy bins: 1.9-2.1 and 2.1-2.3 GeV. They agree well (within uncertainties) with the beam asymmetries obtained at LEPS for forward angles, but show a clear disagreement with the predictions from the current Kaon-MAID over wide range of kaon c.m. angles.

# Table of Contents

# List of Figures

# List of Tables

# Chapter 1: Introduction

Since the discovery of the atomic nucleus, physicists have sought to understand its constituents and the strong interactions between them. Experimental and theoretical efforts during the second half of the 20th century led to a gradually improved qualitative understanding of the nucleon. Significant developments included, among many, Deep Inelastic Scattering experiments and symmetry-based classification schemes. Such developments contributed greatly to our understanding of hadrons (mesons and baryons) through their interpretation as composite systems rather than fundamental particles and, in particular, through the introduction of a new quantum number, the *color charge*, which led to the development of Quantum Chromodynamics (QCD), the now accepted theory of strong interactions.

Among the various properties of QCD, the phenomena of asymptotic freedom and quark confinement are of great interest for both theorists and experimentalists. At high energies the interaction is weak (asymptotically), but at lower energies the strength of the interaction increases significantly. As a consequence, the low-energy behavior of QCD is manifestly non-perturbative, which restricts the possibilities to perform calculations in this regime. The confinement of quarks in hadrons is a key part of QCD phenomenology, but understanding it requires experimental input. Quark confinement as well as intra-hadron dynamics are manifest in the structure of hadrons. Experiments that test fundamental aspects of the nucleon structure include Spectroscopy, Deep Inelastic Scattering (DIS), and Deep Exclusive Scattering (DES) such as Deep Virtual Compton Scattering (DVCS). Spectroscopy is the topic of this thesis. Contrary to DIS and DES, spectroscopy experiments probe the nucleon as a whole by means of hadronic (pion) or electromagnetic (photon) probes. In the latter case, the photon virtuality, or four-momentum transfer ($-q^2$) from the electron, is usually low. As a result of the ($s$-channel) process, the nucleon is left in an excited state. To be considered a true resonant state, the lifetime has to be sufficiently long to allow the constituents to reach an equilibrium (thermalization) well before the de-excitation process occurs.[1] When the excitation energies become very high, the lifetimes are too short to form

[1]In this sense, the decay of the resonance depends only on its energy, angular momentum, and parity,

proper states, and the spectrum transitions into a continuum. To determine its properties, the decay products of the resonant state are measured and analyzed. As in atomic physics, the analysis of the spectrum of excited states can reveal important information about the structure and properties of nucleons. The investigation of this spectrum therefore plays a vital role in the achievement of a comprehensive picture of strong interaction physics.

## 1.1 The Strong Interaction

Over the years there have been many attempts to try to explain the properties of physical systems in terms of their symmetries. Such attempts gave birth to the symmetry-based quark model, which in turn led to the development of QCD−the theory of the strong interaction.

### 1.1.1 The Symmetry-based Quark Model

The generalization of simple rotation symmetries (isospin) to include new properties (strangeness), forming larger symmetry groups, led to the formulation of schemes aimed at categorizing the rapidly expanding list of new particles discovered by the middle of the 20th century. The best known, and most successful of these schemes was the classification developed by Murray Gell-Mann [1], given the popular name "the Eightfold Way". Within this scheme, hadrons fit into patterns forming octets, nonets, and decuplets. Gell-Mann recognized that these geometrical patterns could be described mathematically in terms of representations of a symmetry group. Based on this symmetry and the observed mass differences between particles with different values of strangeness ($S$), Gell-Mann was able to predict the existence of a new particle with charge $Q$=$-1$ and strangeness $S$=$-3$. He was further able to calculate its mass and lifetime, and tell the experimentalists exactly how to produce it. The correctness of the scheme was confirmed when in 1964 the $\Omega^-$ was discovered at the Brookhaven National Laboratory [2].

An understanding of the Eightfold Way came when Gell-Mann and Zweig [3] independently proposed a model in which all hadrons correspond to bound states of more elementary

but not on the specific way in which it was produced.

constituents–with spin 1/2 and positive parity–which Gell-Mann called quarks. In this model, referred to as "the quark model", all the Eightfold Way patterns emerge naturally from the combination of different type of quarks.

There are currently six known types or "flavors" of quarks (along with six corresponding anti-quarks): three light quarks, up ($u$), down ($d$), and strange ($s$), and three heavy quarks, charm ($c$), bottom ($b$), and top ($t$), with the lifetime of the last being, however, too short to form hadrons.[2] Light quarks and anti-quarks form themselves the fundamental representation (Figure 1.1) of an approximate symmetry, known as flavor SU(3), from which the flavor contents of light hadrons can be obtained.[3]

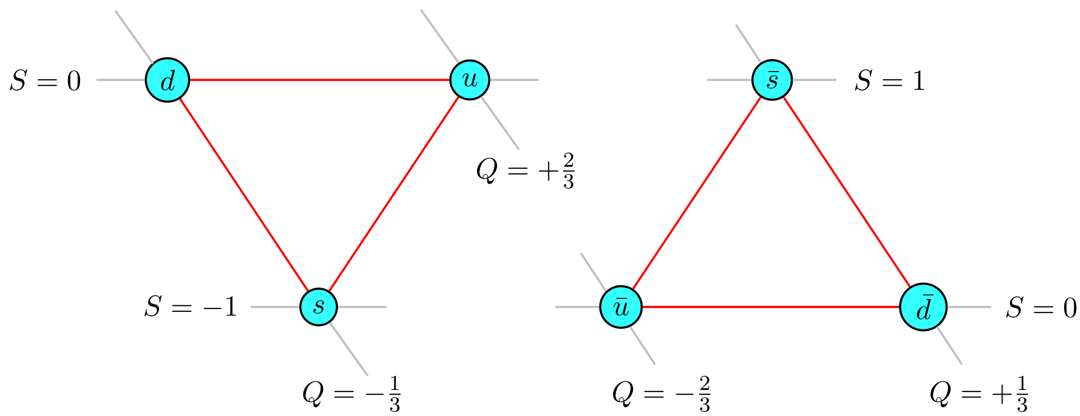


Figure 1.1: Light quarks (left) and light anti-quarks (right) as fundamental representation of flavor SU(3). The horizontal axis in SU(3) representations is called isospin, while the vertical one is called hypercharge (here associated with strangeness).

Within the quark model, the hadron spectrum is classified in the following way:

- Mesons correspond to bound states of quark-antiquark pairs ($q\bar{q}$). For the light quarks there is a total of nine ($3 \otimes \bar{3}$) possible $q\bar{q}$ flavor combinations with a total spin $J$ and angular momentum $L$. These can be decomposed into a sum of two irreducible SU(3) representations, an octet and a singlet: $3 \otimes \bar{3} = 8 \oplus 1$. For ground-state pseudoscalar mesons ($J^P = 0^+$) these correspond to an octet formed by $\pi^\pm$, $\pi^0$, $\eta$, $K^\pm$, $K^0$, $\bar{K}^0$ and

[2] With a very short lifetime ($\sim 5{\times}10^{-25}$ s) the top quark decays through the weak interaction before it hadronizes.

[3] In group theory, the SU(n) group describes rotations in complex space, and can be represented by a set of $n \times n$ Special Unitary matrices with a determinant that is equal to +1. The number of generators in the group is given by $n^2 - 1$. Based on the generators, each group with a certain value of n can have representations with dimensions $(n, n{+}1, n{+}2, n{+}3, ...)$, with $n$ being called the fundamental representation of the corresponding SU(n) group.

the $\eta'$ as a singlet. If flavor SU(3) were an exact symmetry, all nine mesons would have the same mass.

- Baryons (antibaryons) correspond to bound states of three quarks $qqq$ (antiquarks $\bar{q}\bar{q}\bar{q}$). In contrast to mesons, which are bosons, baryons are fermions, and their wave functions must be antisymmetric under exchange of any two quarks. The number of possible light flavor ($qqq$) combinations rises to 27 ($3\otimes3\otimes3$). These can be decomposed into a decuplet, two octets, and a singlet: $3 \otimes 3 \otimes 3 = 10 \oplus 8 \oplus 8 \oplus 1$. The lowest-mass baryons ($L$=0) form a spin-$\frac{1}{2}$ octet ($n$, $p$, $\Lambda^0$, $\Sigma^0$, $\Sigma^\pm$, $\Xi^-$, $\Xi^0$) and a spin-$\frac{3}{2}$ decuplet ($\Delta^0$, $\Delta^\pm$, $\Delta^{++}$, $\Sigma^{*0}$, $\Sigma^{*\pm}$, $\Xi^{*0}$, $\Xi^{*-}$, $\Omega^-$).

The quark model (at this level of simplicity) is, in essence, a symmetry-based classification scheme for hadrons.[4] However, despite its success, an apparent problem was revealed with the $\Delta^{++}$ and $\Delta^-$ baryons, as well as with the predicted $\Omega^-$. These baryons are composed of three identical quarks: $uuu, ddd$, and $sss$, respectively. For these baryons, the exchange of any two quarks leads to a symmetric total wave function, which contradicts the antisymmetric behavior expected for a fermionic system. The problem was solved by introducing an additional quantum number called "*color*", which can take three possible values: r, g, and b. The color wave function for a baryon is:

$$(qqq)_{color} = \sqrt{\frac{1}{6}}\,(rgb - rbg + brg - bgr + gbr - grb)$$

which is antisymmetric and shows that the probability of finding a quark in any of the three color states is 1/3. Thus, by assuming each quark to be in a different color state, they are no longer identical, and the required antisymmetric character of the total wave function is recovered. The introduction of the color charge as a new quantum number led to the development of Quantum ChromoDynamics (QCD).

[4] Further developments of the flavor-symmetric quark model provide a more quantitative description of the different states of hadrons through calculations including asymptotic freedom and quark confinement in the form of phenomenological potentials.

### 1.1.2 Quantum Chromodynamics

The formulation of the quantum field theory of the strong interaction (QCD) was inspired by Quantum ElectroDynamics (QED). However, although both theories share some similarities in their structure, they have fundamental differences that make non-abelian QCD much more complicated. This is related to the fact that in QCD there are three different types of "positive" and "negative" charge, which comes in three colors: red ($r$), green ($g$), and blue ($b$) and for anti-quarks, in three anti-colors: anti-red ($\bar{r}$), anti-green ($\bar{g}$), and anti-blue ($\bar{b}$).[5] As with the flavor SU(3) symmetry for the light quarks encountered in the quark model, the 3 colors and 3 anti-colors form the fundamental representations of a new symmetry in QCD called color SU(3). In contrast to flavor SU(3), this is a symmetry expected to be exact since the color charge seems to be a conserved quantity.

As in QED, the strong interaction is mediated via the exchange of massless spin-1 bosons called gluons (from *glue*). Unlike the QED photon, which does not carry any charge, a gluon does carry color charge. Therefore, gluons play a dual role: they act as generators of the SU(3) color group transforming one color state into another, and they also act as "particles" that can couple directly not only to quarks but also to other gluons. This characteristic of QCD creates the possibility of having bound states of only interacting gluons, called *glueballs*, and states formed of the combination of a gluonic excitation with either three quarks or a quark-antiquark pair, called *hybrid baryons* and *hybrid mesons*, respectively. The gluon-gluon interaction also results in a complex behavior of the strong "coupling constant" $\alpha_s$. In the surroundings of a quark, the quantum vacuum creates virtual clouds of both quark-antiquark pairs and gluons that appear from nothing and immediately disappear. Such clouds, in terms of expansions of the QCD vertex in Feynman diagrams, are included as fermionic and bosonic loops, respectively. The effect of the quark-antiquark loops coming out of the vacuum is to screen the color charge, reducing its value for increasing distance. This effect is known as charge screening and, as a consequence, shows that the magnitude of the measured charge depends on the distance (or the energy) at which one is probing the charge. The action of the gluon loops dominates and goes in the opposite direction,

[5] More generally, the various color charges and anti-charges can be interpreted as eigenstates of color isospin and color hypercharge.

producing charge antiscreening. Thus, the net effect concerning QCD (in contrast to QED) is that the color charge increases with the increasing probe distances [4]. A comparison of the screening characteristic of the electric and color charge is shown in Figure 1.2.

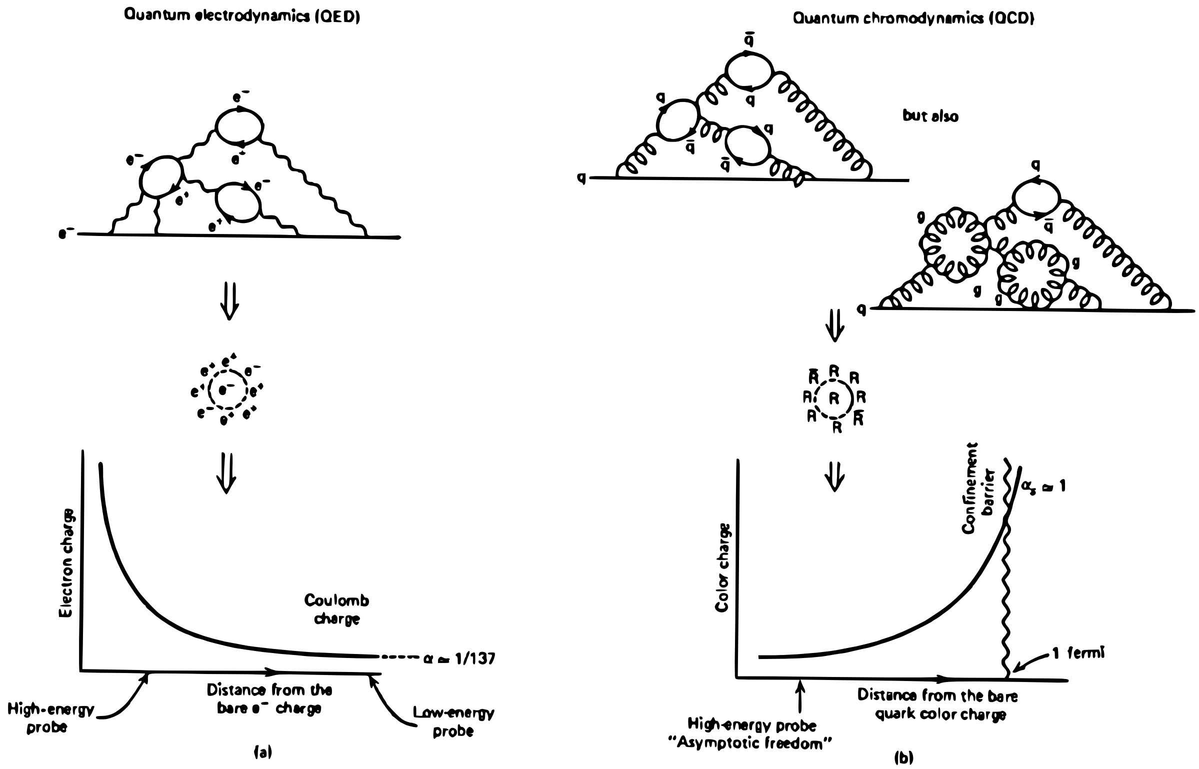


Figure 1.2: Screening of the (a) electric and (b) color charge. Only one of all the possible diagrams for the electron and quark charge clouds is shown. Figure taken from [5].

The screening of the color charge is reflected in the behavior of the strong "coupling constant" $\alpha_s$. At high energies, two quarks interact through color fields of reduced strength (small $\alpha_s$) and asymptotically approach a state where they behave as essentially free, non-interacting particles. Hence, a perturbative treatment of QCD at these energies is justified. In contrast, at low energies, the strength of the color field increases asymptotically (large $\alpha_s$), creating strongly bound states of quarks and antiquarks (hadrons). This makes a perturbative treatment of the physical quantities analytically unfeasible. This property of QCD manifested by the behavior of the coupling constant (better called the running of the coupling constant) is known as "*asymptotic freedom*" and was found theoretically by Politzer, Gross, and Wilczek [6, 7].[6] Experimentally, the value of $\alpha_s$ has been determined

[6]This theoretical discovery saved QCD from being thrown out as it acquired the status of a QED-like

from the analysis of various processes, for instance, through scaling violations in deep inelastic scattering, the probability of observing a third jet in $e^+e^-$ hadronic processes, and excessive hadronic production in $e^+e^-$ interactions. Figure 1.3 presents the results obtained for $\alpha_s$ from such analyses along with corresponding theoretical predictions [6, 7]. The effect of the non-perturbative QCD behavior is evident from the results for $\alpha_s$ observed at low energies.

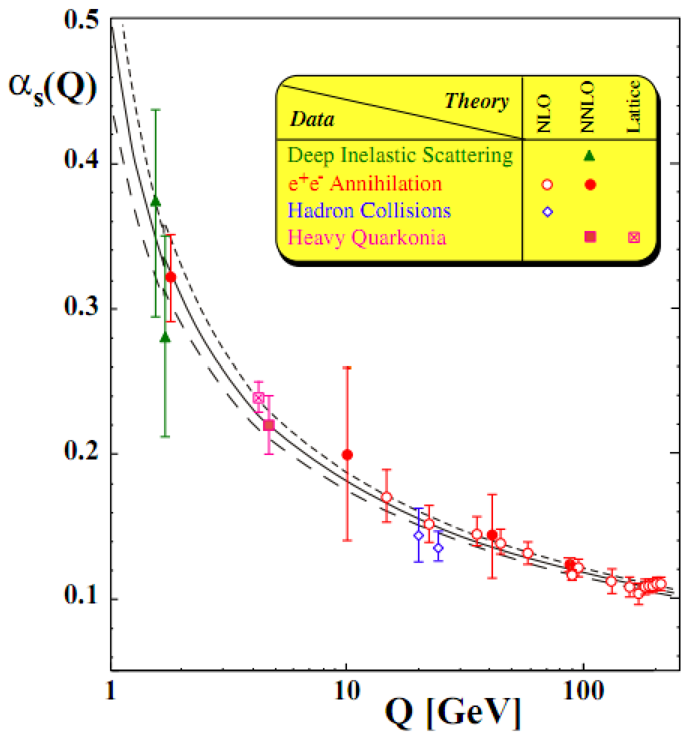


Figure 1.3: Energy dependence of the strong running coupling constant $\alpha_s$. World data points from different experiments are shown as well as some QCD calculations (solid and dashed lines) [6, 7]. Figure taken from reference [8].

While many particles carry electric charge, no observed particles have ever been found to carry color. Experimentally, quarks seem to be confined in colorless packages of two and three quarks, that is to say, confined within mesons and baryons. The particles measured in the laboratory (hadrons) are therefore indirect and complicated manifestations of Chromodynamics rather than elements of the theory itself. Hadrons are not present in QCD directly as particles, but as bound states of quarks and antiquarks. The unsuccessful attempts to

theory useful to calculate interquark potentials (in the asymptotic limit).

observe free quarks formed the basis for the confinement hypothesis. Confinement is the mechanism that is believed to keep quarks and antiquarks permanently inside the hadrons. Figure 1.4 represents an interpretation of quark confinement. At distances of about one fermi (where $\alpha_s$ approaches one), the color field can be seen as concentrated in a narrow flux tube (the shaded region). As the quark-antiquark separation distance increases, the length of the tube increases, but its diameter remains approximately constant. Therefore, the energy density of the field remains constant, and the potential energy of the quark system has to increase proportionally to its separation length. When the potential energy in the tube is large enough, it becomes energetically more convenient to break the tube producing a new quark-antiquark pair rather than further separate the original quarks, causing the system to be left with two mesons instead of one. Since an infinite amount of energy is needed to separate two quarks [4], the model prevents the possibility of breaking the hadron to produce free quarks.

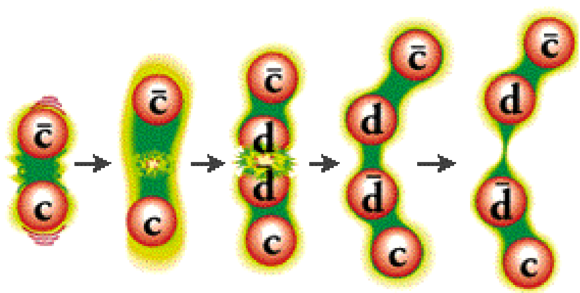


Figure 1.4: Sketch of the confinement between a quark ($c$) and an antiquark ($\bar{c}$). The color field is represented by the shaded region. Figure taken from reference [9].

It is therefore at low energies—where perturbation theory cannot be applied to QCD—that most of the puzzling features of the strong interaction reveal themselves most clearly. Since many of the nucleon resonant states dominate at low energies, the nucleon constitutes a promising testing ground for understanding some of the features of QCD. One of the avenues is to explore the nucleon through its excited states. The discussion of some of the techniques, approaches, and models applicable in the low-energy regime will be the focus of the next subsections.

## 1.2 Experimental Studies of the Nucleon

There are basically two complementary ways of approaching the experimental study of nucleon structure: either through a direct or an indirect process. Directly probing the constituents of the nucleon in its ground state requires sufficiently good resolution. This means that the wavelength of the probe particle has to be small compared to the nucleon radius, $\lambda << R$, or the four-momentum transfer from the photon $Q^2 >> \hbar^2/R^2$. To achieve large four-momentum transfers in scattering experiments, high energies are required [10]. The use of high-energy elementary particles (electrons, muons, and neutrinos) as probes allows one to go deep inside the nucleon and directly explore its composition at the quark-gluon level. Direct processes are divided into inclusive and exclusive reactions. In the first case, only the scattered electron is detected while all the final states are summed over; in the second case, the complete final state is measured. Direct inclusive experiments include Deep Inelastic scattering (DIS). For direct exclusive experiments, form-factor measurements and Deep Virtual Compton Scattering (DVCS) are good examples.

In the indirect process, the nucleon is explored as a whole (a compound system) rather than through its components. Information about nucleon structure is obtained by studying the characteristics of the nucleon and its excited states. This indirect approach is used in spectroscopy experiments where the nucleon is excited by an intermediate-energy probe. The nucleon then decays into a measurable final state. The analysis of such decays of the excited nucleon can, for instance, provide insight into quark correlations.

Worthy of mention is the fact that both direct and indirect methods share similarities in their procedures. Their main goal is to learn about different aspects of nucleon structure that are not observables. Direct methods provide structure functions from which parton distributions have to be extracted while indirect methods give global information on the nucleons excited states from which one can understand the behavior of its constituents through model calculations.

### 1.2.1 Direct Inclusive Processes

In Deep Inelastic Scattering (DIS), the structure of the nucleon is explored through scattering of high-energy leptons (electrons, muons, and neutrinos) off the nucleon. In this process, one of the partons (quarks) in the nucleon is struck, but neither the hadrons from the struck quark nor the nucleon remnant are detected directly. By measuring only the scattered electron one thus sums over all possible final states. This allows application of the optical theorem, which together with factorization gives access to the Parton Distribution Functions (PDFs). Diagrams of the inelastic process and the DIS "handbag" are shown in Figure 1.5.

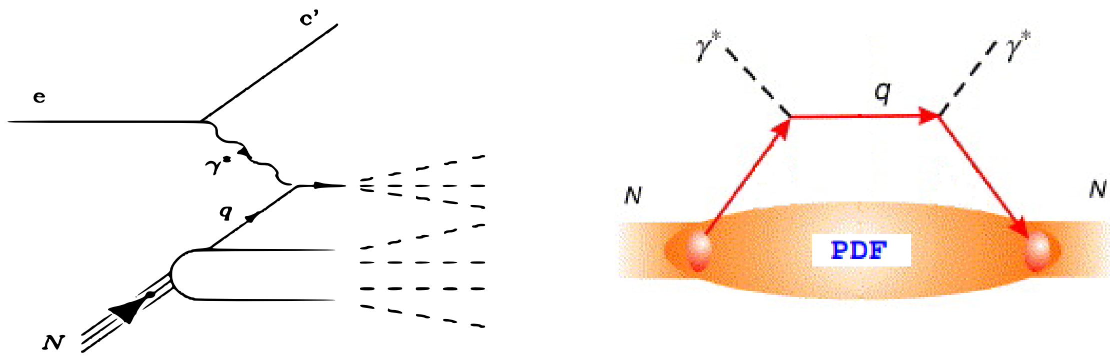


Figure 1.5: (left) Schematic diagram of the lowest-order electron-nucleon "inelastic" scattering. The virtual photon $\gamma^*$ interacts with a single quark of the nucleon. The hit quark hadronizes and escapes the nucleon leaving the final hadronic state undetermined. The only particle measured in DIS is the scattered electron $e'$. (right) The optical theorem: the cross section of the DIS process is equivalent to the imaginary part of the forward amplitude of the double virtual Compton scattering on a quark.

The PDFs, as functions of $-q^2$ and $x$ (the momentum fraction carried by the struck quark in a fast-moving nucleon), reveal the longitudinal momentum distributions of quarks and gluons inside the nucleon. PDFs are obtained indirectly through global fits of cross section data. The DIS cross section is expressed in terms of structure functions. Unpolarized structure functions are called $f$, and polarized ones are called $g$.[7] Figure 1.6 shows the longitudinal momentum fraction carried by quarks and gluons as a function of the momentum fraction $x$. At high values of $x$, the nucleon is dominated by valence quarks ($u$ and $d$

[7] The structure function $h$, which is related to the target polarization, cannot be measured in DIS.

for the case of protons) and gluons. In contrast, at lower $x$, quark-antiquark pairs (known as the "sea quarks") and gluons become more prominent.

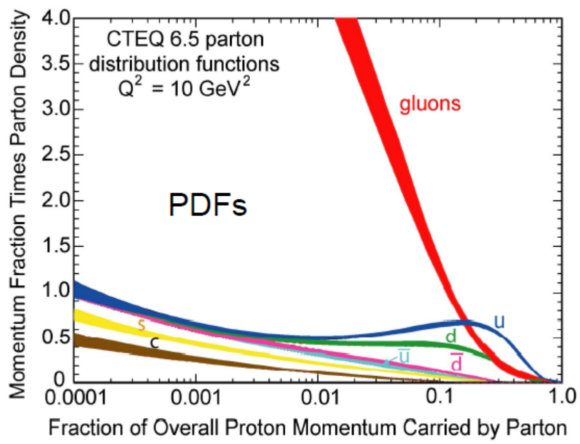


Figure 1.6: Parton Function Distributions (PDFs) in DIS. At high $x$, valence quarks and gluons govern the nucleon while at low $x$, virtual quarks and gluons are more noticeable.

Deep inelastic scattering experiments also allow for the possibility of exploring the longitudinal spin of the proton. Using polarized electron beams, it has been demonstrated that no more than ∼30% of the spin of the nucleon comes from the spin of the quarks [11]. There is a variation of DIS called semi-inclusive DIS (or SIDIS), in which the hadron coming from the struck quark is also detected. By tagging the active quark, semi-inclusive DIS offers the opportunity for determining spin-flavor decomposition of nucleon PDFs. If in addition, the kinematics of that specific hadron are measured, one can learn about the transverse momentum distribution of quarks and gluons inside the nucleons (known as TMDs). Using polarized beams and targets, TMDs may offer a way of understanding the orbital angular momentum of quarks, a fact that seems important for a complete decomposition of the proton spin.

### 1.2.2 Direct Exclusive Processes

#### 1.2.2.1 Form Factors (Elastic Scattering)

Nucleon form factors describe the spatial distribution of charge and magnetization inside the nucleon. The form factors are measured through the elastic scattering of leptons (electrons or muons) off protons or neutrons: $eN \to eN'$. In elastic scattering no additional particles are produced and the target remains intact after the interaction (see Figure 1.7). As a consequence, the four-momentum transfer to the nucleon, $t$, is identical to the four-momentum transfer from the electron, $-q^2$.

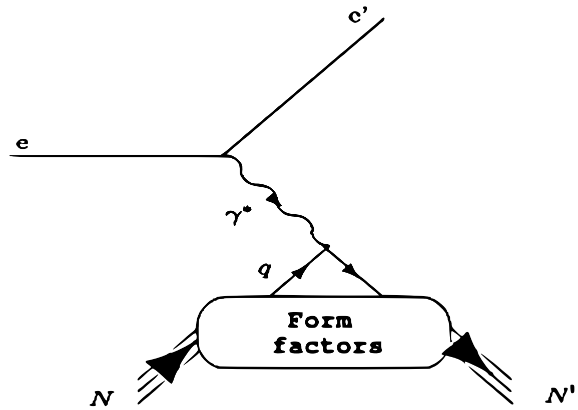


Figure 1.7: Schematic diagram of the lowest-order electron-nucleon "elastic" scattering. The virtual photon $\gamma^*$ interacts with a single quark which remains in the nucleon. The nucleon changes its momentum in the process but it remains a nucleon, unlike the DIS process where it is "smashed into pieces".

In non-relativistic theory, the charge distribution is simply given by the Fourier transform of the form factors. The nucleons require a description with two form factors, $F_1$ and $F_2$, which generalize the "effective" charge and magnetic moment. $F_1$ is associated with the deviation from a point charge Dirac particle and $F_2$ with the deviation from a point anomalous magnetic moment. The linear combination of $F_1$ and $F_2$ leads to a more convenient set of form factors, one electric $G_E(t)$ and one magnetic $G_M(t)$. For the case of electron scattering off a nucleon, $G_E$ and $G_M$ can be accessed experimentally through the measurement of the $eN$ scattering differential cross section for a given value of $t$ at various scattering angles $\theta$, corresponding to different beam energies. This is known as the Rosenbluth method [10, 5]. Another alternative, newer method to determine $G_E/G_M$ is to measure polarization observables in $eN$ scattering rather than cross sections. This leads to a more accurate determination of the form factors since radiative corrections are greatly reduced. Some of the most recent and accurate measurements of nucleon form factors following this polarization method have been taken in Hall A [12, 13] and Hall C [14] at JLab. However, the Rosenbluth and Polarization methods differ significantly in their results, and there is not yet a clear explanation of the disagreement, although two-photon exchange is now being investigated as a possible cause [15]. Nonetheless, the measurement of the $t$-dependence of the electromagnetic form factors $G_E$ and $G_M$ is important to obtain information about the radial charge distributions and the magnetic moments which is very valuable to understand the transverse spatial distribution of quarks inside the nucleon.[8]

#### 1.2.2.2 Generalized Parton Distributions (GPDs)

Extensive information about the structure of the nucleon can be obtained from the correlation between spatial and momentum coordinates of partons, *i.e.,* simultaneous knowledge of the transverse position and the longitudinal momentum of quarks and gluons in the nucleon. Such a generalization of the phase space allows one to to create an image of the nucleon in longitudinal momentum ($x$) and impact parameter ($b$) space within a single framework. Generalized Parton Distributions (GPDs) carry the information needed to generate such phase-space images of the quarks and gluons in hadrons.

GPDs are probed through the study of hard processes.[9] A key point here is QCD factorization, the separation of a "hard" scattering on a single quark, which is exactly calculable in pQCD and a "soft" non-perturbative part encoding the nucleon-structure part amplitude parametrized in terms of a set of generic structure functions, GPDs. While moments of GPDs are also possible to calculate in Lattice QCD [16], in terms of measurements, the simplest processes accessing GPDs are deep-inelastic exclusive production of mesons and photons. These include Deep Virtual Meson Production (DVMP), where both vector ($\rho^{0,\pm}, \omega, \phi$) and pseudoscalar ($\pi, \eta$) mesons are produced off the nucleon, and Deep Virtual Compton Scattering (DVCS), where a real photon is produced in the final state. DVMP involves gluon-exchange processes that make testing against GPD models technically much more difficult (especially at low $Q^2$) compared to DVCS. As a consequence, Compton scattering (DVCS) is the theoretically cleanest and most easily understood reaction to infer

[8]The interpretation of the Fourier transform of the form factors as the charge and magnetic distributions of the nucleon only has meaning in the Breit frame, a frame in which the scattered electron transfers momentum but no energy to the proton.

[9]Hard processes are defined as reactions in which the large transfer of momentum to quarks and gluons allows for the application of perturbative QCD.

information at low energies about GPDs. Figure 1.8 shows the leading-twist "handbag" diagram for DVCS and DVMP where the complex structure of the nucleon is parametrized in terms of GPDs. A point to notice is that DVCS can probe the nucleon at values of $x$ that can be different before and after the reaction. The difference in $x$, represented by $\xi$, is called "skewness".

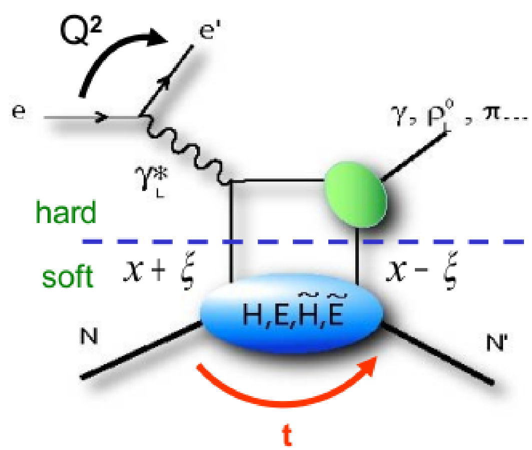


Figure 1.8: Exclusive electron-nucleon scattering $eN \to e'N'(\gamma, M)$ for Deep Virtual Compton Scattering (DVCS) and Deep Virtual Meson Production (DVMP). $\gamma$ stands for a real photon produced off the nucleon and $M = \{\rho^0, \pi, \dots\}$ for a meson. The lower blob represents the unknown structure of the nucleon which is parametrized in terms of four independent generalized structure functions: H, E, $\widetilde{\mathrm{H}}$, and $\widetilde{\mathrm{E}}$.

The GPD framework unifies PDFs (DIS) and elastic form factors. The DIS diagram is an asymptotic case of DVCS when $\xi = 0$ and $t = 0$. Therefore, in that limit, Compton scattering should give access to PDFs. On the other hand, in the limit of small skewness ($\xi \to 0$), the $t$-distribution at each ($Q^2$, $x$) point can be related to a transverse spatial distribution through a Fourier transform, providing similar information to that extracted from elastic form factors, if integrated over $x$. In addition, at large skewness, GPDs can also reflect the correlations between partons (e.g. $q\bar{q}$ pairs) inside the nucleon. This can be seen as being directly complementary to the studies of correlations between constituents (essentially valence) quarks that we can carry out through $N^*$ spectroscopy.

### 1.2.3 Nucleon Spectroscopy

The nucleon can be explored as a whole through its interaction with low-energy beams. As a result, it is left in an excited state (resonance). Since much of the work in nucleon spectroscopy has been done with the pion + nucleon ($\pi$N) system, an excited state is conventionally written as $L(\sqrt{s})_{2I,2J}$ where $L$, being defined as the relative orbital angular momentum between the pion and nucleon, is labeled as $S$, $P$, $D$, $F$, $G$ according to its value $L$=0, 1, 2, 3, 4. $\sqrt{s}$ is the center-of-mass energy at which the resonance is observed, and $I$ and $J$ are the isospin and total angular momentum, respectively. Nucleon resonances with $I = \frac{1}{2}$ are called $N^*$ while resonances with $I = \frac{3}{2}$ are known as $\Delta^*$.

The study of the properties of the nucleon resonance spectrum, known as nucleon spectroscopy, offers the opportunity to learn about the dynamics of constituent quarks, and in particular, about their collective behavior and correlations between them, shedding light on the comportment of QCD in the non-perturbative energy regime. The study of nucleon resonances is, however, not a matter of just extracting resonance parameters from experimental data. It is the interpretation of such extracted resonances through either predictions from phenomenological models of the nucleon or numerical solutions from QCD-based calculations that allows one to learn the underlying physics. Predictions from phenomenological models, represented by constituent quark models (CQM), are connected with the understanding of correlations between quarks inside the nucleon. On the other hand, reproducing the measured spectrum of nucleons from QCD-based calculations, like lattice QCD (LQCD), would validate QCD as the correct theory of strong interactions.

Extracting nucleon resonances from data is thus fundamental for corroborating models and QCD calculations. Particularly, it is important for two reasons: to characterize the resonance spectrum, firmly establishing the resonance properties (mass, spin, decay widths, etc), and to search for nucleon resonances predicted by phenomenological models of the nucleon (e.g. CQM) but not found experimentally yet. These unobserved nucleon excited states, known as the “missing resonances”, call into question whether the quark correlations implicit in CQM are correct or not. There are two possible solutions to this problem. One solution points to reduce the dynamical degrees of freedom used in CQM since three symmetrical constituent quarks might not be physically realized. A model having fewer degrees of freedom in the system would lead to a spectrum with fewer missing states. Such an alternative model, consisting of a quark and a strongly correlated pair of quarks, is called the di-quark model. The other solution deals with the fact of possibly not looking for the missing resonances in the correct place. Most of the experimentally known resonances come from channels that include pions in the final state of the reaction. Capstick and Roberts [17] have shown that some missing nucleon resonances could couple weakly to pion final states but may have significant couplings to different final states, like strangeness production, vector-meson production, etc. In fact, recent theoretical analyses [18, 19] of the same CLAS polarization data for strangeness photoproduction on the proton [20] result in claims of evidence either for a $D_{13}$ or a $P_{13}$ missing resonance at about 1900 MeV. Data for strangeness photoproduction on the neutron is needed to tell which theoretical analysis, if either, is correct. Therefore, investigation of nucleon resonances from formation channels other than pion-production might lead to the discovery of some of the missing states. However, finding some of the missing states would not necessarily imply a confirmation of the validity of the constituent quark models. In addition to the usual three valence quark states, QCD predicts the existence of baryons with "excited glue", the so-called hybrid baryons. As a consequence, the discovery of a new resonant state can be interpreted either as one of the missing resonances predicted by the constituent quark models, or as one of the undiscovered hybrid states predicted by QCD, or even as a mixture of both of them.

The nucleon resonances cannot be extracted directly from the experimental observables. Instead, the observables are linked to the nucleon excited states through the use of reaction models. This is connected with the existence of interfering resonances in the nucleon resonance spectrum. At intermediate energies (see Figure 1.9), the spectrum (the nucleon photoproduction cross section) shows three prominent peaks referred to as "first", "second", and "third" resonance regions (the low-lying states). The first region is well understood as it is composed mainly of a single resonant state, the $\Delta(1232)$. In contrast, the other two resonance regions−where most of the missing resonances are located−are composed of a set of broad overlapping resonant states with significant background contributions. Isolating these resonant states from each other and from the background is a non-trivial task to solve. Reaction models are an attempt to carry out such a task. These fit-based reaction models—with no predictive power at all, and performed on a partial-wave basis—make assumptions about both the input resonances and the functional form of the background that, when combined, might satisfactorily describe a certain partial wave. The best fit to experimental observables dictates the reasonableness of the assumptions. However, since this involves many fitting parameters, the process typically yields a large number of solutions; often several random searches are made, each giving a different best fit. The fit ambiguity in the reaction models can be reduced by having several independent observables per channel determined with small uncertainties and spread over an ample angular range. Access to a fair number of independent observables can be achieved by using polarized beams (e.g. photon beams). Hence, high-quality measurements concerning photoproduction data off the nucleon play a key role as input for reaction models which, at the end, are the way to go to improve the current picture of the nucleon and as such, of non-perturbative QCD.

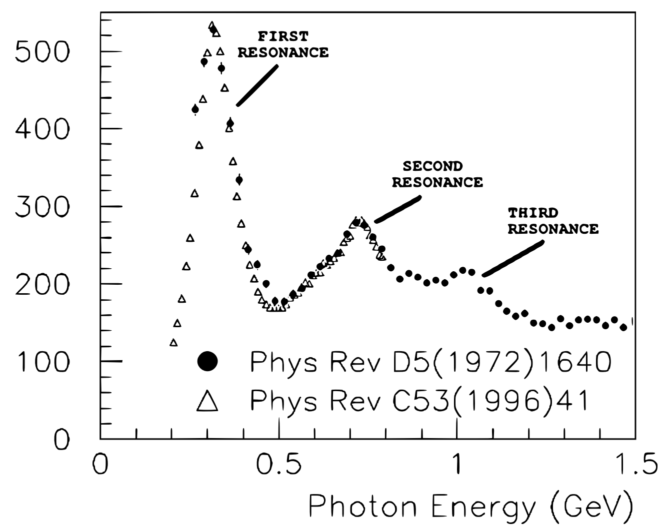


Figure 1.9: Total cross section for the reaction $\gamma p \to$ “anything”. The bumps observed at photon energies below 2.0 GeV are interpreted as nucleon resonances.

## 1.3 Outline of the Thesis

Chapter 2 gives a more comprehensive description of the main tools involved in a complete study of nucleon spectroscopy. The first part of the chapter is focused on the interpretation of resonance parameters via quark models and lattice QCD calculations. The second part discusses some of the models used to extract resonance parameters from partial-wave amplitudes.

Chapter 3 deals with the state of the art at the experimental level for the reaction of interest $\gamma n \to K^+ \Sigma^-$. Here, the experimental data on both cross section and beam asymmetry acquired at different experimental facilities are reviewed. This chapter demonstrates the importance of the measurements performed in this thesis to extend the kinematic coverage of the current beam asymmetry measurement found in the literature.

Chapter 4 describes the experimental setup involved in the experiment. The chapter starts with a brief description of the CEBAF accelerator which delivers the electron beam required to run the experiment. Then, the techniques used to produce a polarized photon beam based on the electron beam are described. Subsequently, the main components of experimental Hall B where the data were taken are delineated, starting with the tagging spectrometer used to tag bremsstrahlung photons, continuing with a description of the CLAS detector system, and ending with some general comments about the target type, the data acquisition and trigger characteristics.

Chapter 5 reports on the methods carried out to reconstruct the particle energy and momentum from the measured energy, path lengths and time values. All the analysis steps needed to reconstruct the invariant mass of the $\Sigma^-$ are explained in detail in this chapter. The conditions required to select the quasi-free events as well as the background studies also form part of this chapter.

Chapter 6 concentrates on the determination of the photon beam asymmetry. The procedure adopted to extract the photon beam asymmetry is explained in detail. This involves the use of two different extraction methods: the $\phi$-bin and the moments methods. Employing two different methods is useful to evaluate the systematic uncertainty associated with the extraction procedure.

Chapter 7 is devoted to the study of the sources of systematic errors associated with the determination of the photon beam asymmetry. Different sources are investigated: methods followed to extract the asymmetry, kinematical cuts used to extract the yields for the $K^+\Sigma^-$ final state, and the effect of varying the parameters involved in the photon beam asymmetry determination.

In the final Chapter, the results obtained in this work are compared with those obtained by H. Kohri for the LEPS collaboration [21]. The results are also compared with the predictions of the kaon-MAID [22] model.

# Chapter 2: Nucleon Excited States

As mentioned in the Introduction (Section 1.2), the study of nucleon excited states plays a vital role in the understanding of intra-nucleon dynamics as well as of QCD as a valid theory for strong interactions in the medium-energy range. Given the non-perturbative behavior of QCD at these energies, such an understanding has to be investigated through approximate solutions of QCD: QCD-inspired models and QCD-based calculations. Within the QCD-inspired models, constituent quark models solve, in an exact way, an "approximate" QCD Lagrangian where the valence quarks are replaced by effective quarks which interact through potentials that mimic QCD asymptotic freedom and quark confinement. Conversely, in QCD-based calculations, lattice QCD tries to solve the "exact" QCD Lagrangian with a minimum set of approximations by discretizing space-time. Solving the QCD Lagrangian provides an avenue for accessing the hadronic spectrum. The underlying physics emerges then from the comparison between the "approximate" spectra obtained from the QCD approaches and the spectrum extracted from experimental data.

The extraction of resonances from data brings in some difficulties due to the need for reaction models to isolate interfering resonant states and non-resonant states. The use of reaction models leads to model dependency in the extraction procedure. Therefore, the extracted nucleon spectrum can vary from group to group depending on the specific characteristics of the reaction model used. As a consequence, there is not a general consensus about the correct "experimental" nucleon resonance spectrum, and the comparison with "approximate" spectra turns out not to be very fruitful. Having high-precision measurements off the nucleon of independent experimental observables on as many channels as possible is thought to be the solution to minimize the model dependency in the extraction of resonance parameters.

Figure 2.1 summarizes the scheme followed in the analysis of reactions produced off the nucleon (nucleon spectroscopy): (1) extraction of nucleon resonance parameters from experimental data, and (2) interpretation of such parameters by means of QCD-based approaches. Resonances are extracted from experimental data by initially decomposing the observables in terms of partial-wave amplitudes which subsequently are analyzed through reaction models. On the other hand, resonances can be predicted from quark models or calculated from lattice QCD. The interpretation of the experimental resonances is only viable when compared either with the predicted or calculated resonance states.

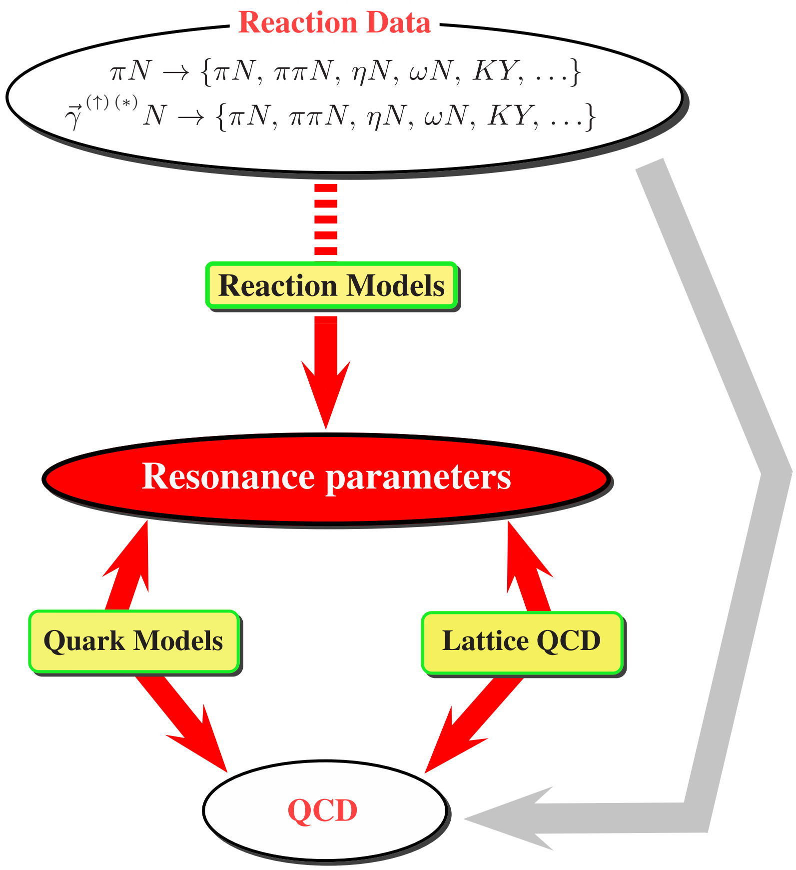


Figure 2.1: The study of nucleon structure from nucleon spectroscopy data. Nucleon resonance parameters (resonances) are extracted from experimental data by means of reaction models. The understanding of the extracted parameters depends on comparisons with the results from phenomenological QCD-inspired models of the nucleon and QCD-based numerical calculations.

This chapter will focus on giving an overview of the approaches used for interpretation of experimental resonance parameters (constituent quark models and lattice QCD) as well as of the main reaction models aimed at extracting resonance parameters from data.

## 2.1 Quark model

In addition to the three quarks determining the quantum numbers of the baryons (called *valence quarks*), the QCD Lagrangian gives rise to a large number of virtual quark-antiquark pairs and gluon combinations inside the nucleon (*the quark sea*). The QCD picture of the nucleon is therefore a rather complicated system to study as shown in panel (a) of Figure 2.2. Given that complexity, the properties of the nucleon can be alternatively studied in terms of bound quarks through an approach known as the constituent quark model (CQM). In this model, the nucleon is no longer formed of current quarks (or QCD quarks) but instead, it is assumed to be composed of three "effective" weakly-correlated quarks, called constituent quarks. Qualitatively, a constituent quark may be viewed as an object in which a "bare" valence quark is dressed by clouds of quark-antiquark pairs and gluons. The quark sea is therefore accounted for by assuming the constituent quarks to have a spatial extent, large masses, and the same quantum numbers as those of the valence quarks.[1] Panel (b) of Figure 2.2 shows the CQM nucleon picture.

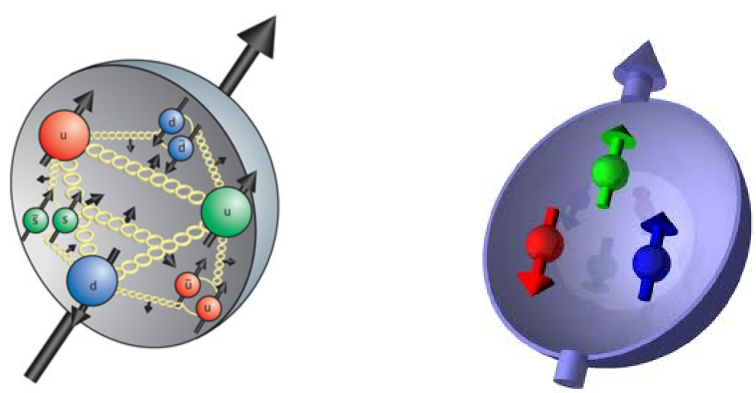

(a) (b)

Figure 2.2: (a) The QCD picture of the nucleon: three valence quarks embedded within the quark sea. (b) The quark model picture of the nucleon: three constituent quarks.

The simplest form of the CQM model is the static quark model in which no interactions between quarks are included. The predictions from this model arise solely from symmetry

[1]The point to keep in mind is that QCD quarks and constituent quarks are quite different objects, with the former being much lighter than the latter.

rather than from detailed dynamics, which makes it useful to determine only properties like masses of ground states or magnetic moments. However, despite the simplicity of the model, the general agreement of its predictions with experimental data is quite impressive [23]. The inability of the static quark model to explain the observed values for the mass splitting of hadrons ($\Delta - N$, $\Sigma - \Lambda$) led to the development of non-relativistic[2] dynamical quark models that introduced aspects of QCD into the description of constituent quark interactions. The two key pieces that any formulation of a dynamical quark model must include are a model for the strong interaction and a confinement potential.[3] The Hamiltonian of a conventional dynamical quark model is then written as

$$H = \sum_{i=1}^{3} \left( m_i + \frac{|\vec{p}_i|^2}{2m_i} \right) + \sum_{i<j}^{3} V_{ij} + V_{\text{conf}} \tag{2.1}$$

where the first term represents the kinetic energy of the three quarks with mass $m_i$ and momentum $|\vec{p}_i|$. $V_{ij}$ is the interaction potential and $V_{\text{conf}}$ is the effective confinement potential.

The pioneering version of the dynamical quark models is that by De Rujula, Georgi, and Glashow (RGG) [24]. In this model, it is assumed that the hadron-mass splitting is caused only by the short-range term (spin-spin term) of an interaction connected with the exchange of one gluon between quarks. Many studies of excited baryon states and electromagnetic transition amplitudes connecting the nucleon and its excited states were made based on the observations of the RGG model; the most detailed, representative and phenomenologically successful of these is the model of Isgur and Karl [25, 26] which describes the interaction $V_{ij}$ between quarks not only by a short-range term but also by a long-range term and omits any contribution of the spin-orbit force term.[4] This interaction is expressed as

$$V_{ij} = -\alpha_s \frac{\boldsymbol{\lambda}_i^c \cdot \boldsymbol{\lambda}_j^c}{16 m_i m_j} \left( \frac{8\pi}{3} \delta(\mathbf{r}_{ij}) \boldsymbol{\sigma}_i \cdot \boldsymbol{\sigma}_j + \frac{1}{r_{ij}^3} S_{ij} \right) \tag{2.2}$$

[2] A system is considered non-relativistic when its binding energy is small compared to the rest energies of its constituents. Otherwise, the system is relativistic. For nucleons, quark-quark binding energies are on the order of a few hundred MeV, which is about the same as the effective rest energy of $u$, $d$, or $s$ quarks. Therefore, the nucleon is a relativistic system. Paradoxically, most of the conventional quark models approximate the nucleon as a non-relativistic system!

[3] Different versions of the dynamical quark model correspond to different assumptions for the interaction model approach and/or the confinement potential.

[4] Except for a factor (related to gluon color), this interaction coincides with the spin-dependent part of the perturbative Fermi-Breit interaction of QED, which describes the interaction of two fermions by means of the exchange of one photon.

where $\alpha_s$ is the strong coupling constant, $r_i$, $m_i$, $\sigma_i$ and $\lambda_i^c$ are the coordinate, mass, spin, and color of the $i$th quark, respectively, $\mathbf{r}_{ij} = \mathbf{r}_i - \mathbf{r}_j$, and $S_{ij}$ is the tensor operator defined by $S_{ij} = 3\boldsymbol{\sigma}_i \cdot \hat{\mathbf{r}}_{ij} \boldsymbol{\sigma}_j \cdot \hat{\mathbf{r}}_{ij} - \boldsymbol{\sigma}_i \cdot \boldsymbol{\sigma}_j$ with $\hat{\mathbf{r}} = \mathbf{r}/|\mathbf{r}|$. For the confinement potential $V_{\text{conf}}$ of Equation (2.1), the Isgur-Karl model uses a quadratic form (harmonic oscillator) combined with an anharmonic potential. The quadratic potential is especially suited for some $S_{11}$ resonances ($N(1535)$ and $N(1650)$) which have similar internal structures that are not sensitive to the details of the confinement potential. The anharmonic potential is introduced in the model as a perturbation.

The Isgur-Karl model describes adequately the systematics of the baryon spectrum, being especially successful in the description of higher baryon resonances like P-wave baryons. Although the Isgur-Karl model (and in general, any dynamical constituent quark model) predicts more states than those actually observed (as mentioned in Section 1.2.3), its ability to perform calculations of the couplings of resonance states to the $\pi N$ channel revealed that most of the unobserved states are weakly coupled to the $\pi N$ channel. This observation opened the study of strange channels as a means to search for the extra resonances. On the other hand, whereas the phenomenology of the Isgur-Karl model indicates that spin-orbit forces between constituent quarks are not important in the baryon mass spectrum, the QCD Breit interaction certainly yields such forces. This raises a conceptual problem about the detailed properties of the residual interactions beyond one-gluon exchange. The issues are relativistic corrections, $\vec{L} \cdot \vec{S}$ forces from a Lorentz scalar confining potential via Thomas precession, and genuine three-body interactions between quarks. Relativistic extensions of the Isgur-Karl model by Godfrey and Isgur [27] and others [28] have been addressed to discuss some of those unanswered questions about the deeper foundations of the non-relativistic quark models. Nevertheless, in spite of their conceptual problems and its lack of a field theoretical basis, the non-relativistic models have a major virtue, namely their phenomenological simplicity. From this perspective, the Isgur-Karl model presents a prototype hamiltonian which successfully combines the group theoretical framework of $SU(6) \times O(3)$ symmetry with minimal dynamical input and gives a surprisingly good description of a large amount of baryon data [23].

Besides the quark model, it is important to mention that there exist other phenomenological approaches used to analyze and interpret the vast amount of experimental data dealing with nucleon structure. Among them, one can find the bag model and soliton models. Bag models start from a picture of hadrons as color singlet cavities, or bags, of perturbative vacuum occupied by relativistic quarks and gluons. The bag is embedded in a condensed medium which represents the QCD ground state. Soliton models view the nucleon as a localized lump of energy density formed out of mesons and quarks. All these models, including the quark model, are constructed to mimic certain selected aspects of QCD but none of them is QCD. Each one has its specific merits and limitations. Non-relativistic quark models emphasize the role of massive constituent quarks as quasi-particles and have some features reminiscent of phenomenological shell models in nuclear physics. Soliton models are typically representative of collective models: they operate with the low-mass mesons as collective degrees of freedom. Bag models are an attempt to unify quark and meson descriptions [23].

## 2.2 Lattice QCD

Nowadays, numerical calculations of QCD offer the only possibility to understand the dynamics of strong interactions in the non-perturbative regime (intermediate energies). Lattice QCD (LQCD) represents the best known non-perturbative tool for addressing issues like the confinement mechanism and chiral symmetry breaking, the role of topology, and the equilibrium properties of QCD at finite temperature, and, in particular, for calculating−within statistical errors−the hadronic spectrum from first principles.

Lattice QCD is the formulation of QCD on a discrete space-time grid. Since no new parameters or field variables are introduced in this discretization, LQCD retains the fundamental character of QCD. Lattice calculations are performed computationally using methods analogous to those used for Statistical Mechanics systems. This strategy allows one to calculate observables and correlation functions of hadronic operators in terms of the fundamental quark and gluon degrees of freedom. The starting point of a lattice calculation is the exact QCD Lagrangian:

$$\mathcal{L}_{QCD} = \sum_j \bar{\psi}_j (i\not{D} - m_j)\psi_j + \mathcal{L}_{YM}[A_\mu] \tag{2.3}$$

where $\psi_j$ is the quark field of flavor $j$, $m_j$ is the quark mass for flavor $j$, $\not{D} = \gamma^\mu(\partial_\mu - iA_\mu^a \lambda^a)$ is the covariant derivative for the quarks that includes the quark-gluon interaction term, with $\gamma^\mu$ and $\lambda^a$ corresponding to the standard Dirac and Gell-Mann matrices, respectively. The term $\mathcal{L}_{YM}$ is the Yang-Mills Lagrangian for the gluon gauge boson field $A_\mu$.

In order to perform the calculation of an observable using QCD, the Lagrangian $\mathcal{L}_{QCD}$ is turned in the context of a path integral according to:

$$Z_{QCD} = \int [DA_\mu D\bar{\psi} D\psi] \exp(iS) \tag{2.4}$$

where $S = \left(i \int d^4x \mathcal{L}_{QCD}\right)$ is the QCD action. The expectation value of an observable $\hat{O}$ is then defined as

$$< \hat{O} >= Z^{-1} \int [DA_\mu] O(A_\mu) \det(i\not{D} - M) \exp(iS) \tag{2.5}$$

with $M$ arising from the dynamics of the virtual quarks. The integral in Equation (2.5) is performed over the fields $A_\mu$, $\psi$, and $\bar{\psi}$ which accounts for each possible field configuration (an example of a field configuration is shown above in Figure 2.2 (a)). Given that the number of configurations is infinite and each configuration contributes with a weight given by the imaginary exponential $\exp(iS)$, numerical calculations require limiting the number of field configurations to a finite representative subset comprised only of those configurations with large contributions to the integral (importance sampling). The imaginary exponential, however, gives rise to large oscillations from configuration to configuration, making it hard to probabilistically sample those configurations that will contribute the most to the observable in question. A convenient numerical formulation of QCD thus implies the use of a Euclidean formulation (Wick rotation). This formulation consists in the rotation from Minkowski time to Euclidean time by means of the substitution $t \to i\tau$. Equation (2.5) then turns into:

$$< \hat{O} >= Z^{-1} \int [DA_\mu] O(A_\mu, \psi, \bar{\psi}) \det(\not{D} + M) \exp(-S) \tag{2.6}$$

where the exponential and the determinant factor can now be interpreted as a probabilistic weight function.

The numerical evaluation of Equation (2.6) is to be performed on a lattice, with the Euclidean space-time discretized into a finite four-dimensional volume of grid points with spacing $a$, spatial extent $L = N_x a$, and temporal extent $T = N_t a$. In this volume, consisting of a collection of $N_x^3 \times N_t$ grid points, the quark fields $\psi$ reside on the grid points while the gluon fields are defined on each link between the points (see Figure 2.3). A few key elements of this discretized scheme are:

- The gauge symmetry can be fully preserved, and no additional unphysical degrees of freedom are thus introduced.
- The details of the discretization become (in general) irrelevant in the continuum limit. Any reasonable lattice formulation will give the same continuum theory up to finite renormalizations of the gauge coupling and the quark masses.
- Lattice QCD admits an expansion in terms of Feynman diagrams that coincides with the usual expansion up to terms proportional to the lattice spacing. The consistency of the lattice theory with the standard perturbative approach to QCD is thus guaranteed.
- The discrete space-time lattice acts as a nonperturbative regularization scheme. Finite values of the lattice spacing $a$ as well as of the lattice sizes $L$ and $T$ provide natural ultraviolet (at $\pi/a$) and infrared cutoffs which result in renormalized physical quantities free of any divergence, that is, with a finite well-behaved limit as $a \to 0$.

The above-mentioned discretized schemes leads however to the challenge of developing and implementing efficient simulation methods for LQCD that work well under conditions of large lattices and small quark masses. The efficiency of such methods is related to the computational cost of the calculations, defining cost as the number of arithmetic operations required to generate a field configuration [29]. An approximate formula for the computational cost is given in reference [30] according to

$$\text{cost} \approx 3.3 \left(\frac{140\,\text{MeV}}{m_\pi}\right)^6 \left(\frac{L}{3\,\text{fm}}\right)^5 \left(\frac{0.1\,\text{fm}}{a}\right)^7 \ \text{Tflops year} \tag{2.7}$$

which shows clearly the dependence of the cost on the lattice parameters $a$ and $L$, and on the value $m_\pi$ determined for the pion mass (which depends on the specified values of the quark masses). The units of Tflops year means $10^{12}$ floating-point operations per second performed in a computer in one year of running time.

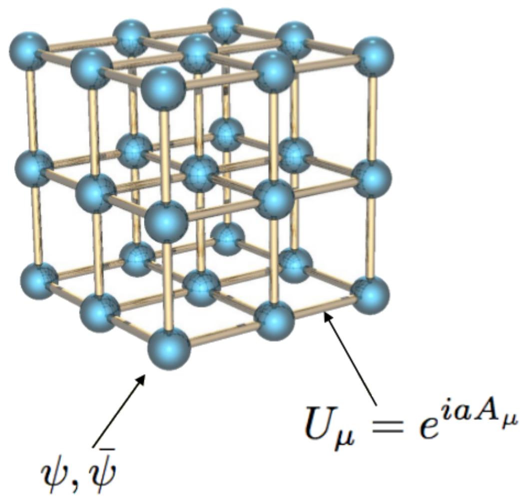


Figure 2.3: Scheme of a cubic lattice with the quark fields $\psi$ on the grid points and the color field (gluons) retained along the links of the lattice. Typical lattice QCD calculations are performed with a spatial lattice size $L$ of at least 2 fm in order to minimize finite-volume effects.

In general, lattice QCD is used to test QCD by computing a wide range of hadron properties like masses, decay constants, form factors and weak transition matrix elements. In addition to this, given that the only tunable input parameters in the calculations are the strong coupling constant and the bare masses of the quarks, LQCD allows one to make detailed predictions of the dependence of quantities on such adjustable parameters. Despite the important advances and successes of LQCD calculations over the last years, there are still some challenges or issues present in LQCD. Among them, one can mention the difficulties in exploring hadronic decays given that the lattice, using Euclidean time, has no concept of asymptotic states, and the significant high errors associated with the quantities calculated from LQCD when compared to those in the corresponding experimental measurements [31]. These issues are expected to be improved in the next few years.

## 2.3 Reaction Models

The extraction of resonance parameters requires an amplitude analysis of reaction processes. Such an analysis involves the extraction of scattering amplitudes from data (experimental observables), and the extraction of resonance parameters from the extracted amplitudes [32].

The determination of the scattering amplitudes forms the basis for the parametrization of any observable. For the case of scattering of a spinless particle from a central potential, the complex scattering amplitude $f_k(\theta)$ is a function of the outgoing momentum $k$ and the scattered angle $\theta$. The connection between data + amplitude is given by the relation

$$\frac{d\sigma}{d\Omega} \sim |f_k(\theta)|^2 = f_k(\theta) f_k^*(\theta) \tag{2.8}$$

where the differential cross section $d\sigma/d\Omega$ is the only available observable in the spinless case. Since any function of $\theta$ can be written in terms of Legendre polynomials $P_l(\cos\theta)$, the scattering amplitude can be expanded in these polynomials with $k$-dependent coefficients:

$$f_k(\theta) = \frac{1}{k} \sum_{l=0}^{\infty} (2l+1) a_l(k) P_l(\cos\theta) \tag{2.9}$$

where $l$ is the relative orbital angular momentum between the target and the scattered particle, and $a_l(k)$ is called the $lth$ partial wave amplitude [33]. The interpretation of Equation (2.9) is as follows: because the angular momentum is conserved in a reaction involving central potentials, the scattering amplitude $f_k$ can be decomposed into several amplitude terms $a_l$ each one related to scattering in a specific angular momentum $l$ sector.

For the case of $\gamma N$ reactions, experimental observables are described in terms of scattering amplitudes based on a spin formalism. Helicity is the standard formalism applicable to most spectroscopy experiments.[5] It offers a uniform description for both massive and massless particles (being especially suitable for photons) and allows one to take advantage of the symmetry properties of the interaction. Figure 2.4 shows the coordinate system used in the helicity representation.

A correct description of $\gamma N$ scattering requires expression (2.9) to be generalized in order to include spin and isospin for photons and nucleons. The combination of the projection of the nucleon isospin ($\mu = \pm\frac{1}{2}$) and the total isospin of the $\gamma$-$N$ system ($\lambda = \frac{1}{2}$ and $\lambda = \frac{3}{2}$) yields a total of four complex scattering amplitudes instead of one, as in the case of a spinless particle. These scattering amplitudes correspond to the four complex helicity amplitudes:

[5]Helicity is defined as the projection of the spin of the particle along the direction of its momentum $\vec{p}$.

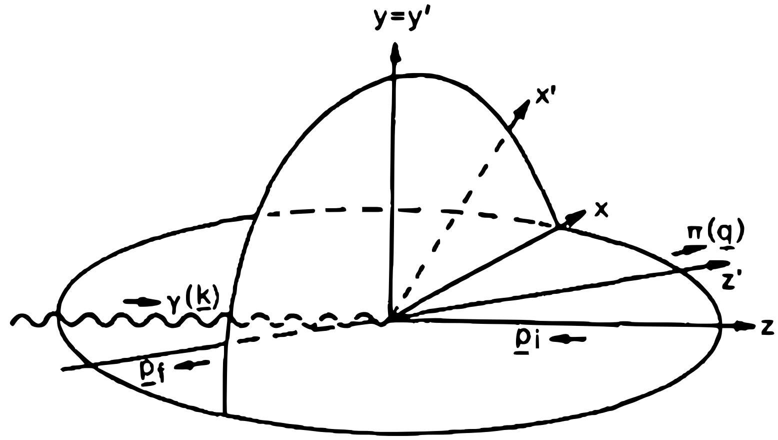


Figure 2.4: Coordinate system definition in the helicity representation. $\vec{k}$ represents the incoming photon momentum, $\vec{q}$ the outgoing meson momentum, and $\vec{r}$ the cross product $\vec{k} \times \vec{q}$. The axes are defined by $x = y \times z$, $y = \vec{r}/|\vec{r}|$, $x' = y \times z'$, and $y' = y$. The $z$ and $z'$ axes point along the direction of $\vec{k}$ and $\vec{q}$, respectively. Figure taken from [34].

$H_1, H_2, H_3$, and $H_4$.[6] Following the work developed in [36], $\gamma N$ scattering is written as:

$$H_n = \sum_J A^J_{\mu,\lambda}(2J+1)d^J_{\mu,\lambda}(\theta)e^{i(\lambda-\mu)\phi} \qquad n = 1, 2, 3, 4 \tag{2.10}$$

which emerges from the fact that helicity amplitudes can be decomposed into partial-wave-amplitude terms derived by requiring conservation of angular momentum, isospin, and parity. $J$, a positive half-integer number, is the spin of the intermediate state, $d^J_{\mu,\lambda}$ is proportional to the so-called $d$-functions, and $A^J_{\mu,\lambda}$ represents a partial-wave amplitude in a specific $J, \mu, \lambda$ sector. In order to fully exploit the symmetry properties of the interaction (rotational invariance, parity and four-momentum conservation) inherent in the helicity formalism, the helicity amplitudes are usually parametrized in terms of electric $E$ and magnetic $M$ multipoles. These multipoles are the amplitudes conventionally used in a partial-wave analysis of experimental data [37]. The connection between data and amplitudes for all the observables available in pseudo-scalar meson photoproduction reactions is shown in Table 2.1.

Since all observables are bi-linear combinations of the helicity amplitudes, the extrac-

[6] $H_1$ means spin-flip with photon and initial nucleon having parallel spins; $H_2$, nonspin-flip; $H_3$, double-spin-flip, and $H_4$, spin-flip with photon and initial nucleon having anti-parallel spins [35].

Table 2.1: Polarization observables in terms of helicity amplitudes for pseudo-scalar meson photoproduction reactions [34].

| Spin observable | Helicity representation |
|---|---|
| $d\sigma_0/d\Omega$ | $\frac{1}{2}\{H_1H_1^\star + H_2H_2^\star + H_3H_3^\star + H_4H_4^\star\}$ |
| $\hat{\Sigma}$ | $+Re\{H_1H_4^\star - H_2H_3^\star\}$ |
| $\hat{T}$ | $+Im\{H_1H_2^\star + H_3H_4^\star\}$ |
| $\hat{P}$ | $-Im\{H_1H_3^\star + H_2H_4^\star\}$ |
| $\hat{G}$ | $-Im\{H_1H_4^\star + H_2H_3^\star\}$ |
| $\hat{H}$ | $-Im\{H_1H_3^\star - H_2H_4^\star\}$ |
| $\hat{F}$ | $+Re\{H_1H_2^\star + H_3H_4^\star\}$ |
| $\hat{E}$ | $\frac{1}{2}\{-H_1H_1^\star + H_2H_2^\star - H_3H_3^\star + H_4H_4^\star\}$ |
| $\hat{O}_{x'}$ | $-Im\{H_1H_2^\star - H_3H_4^\star\}$ |
| $\hat{O}_{z'}$ | $-Im\{H_1H_4^\star - H_2H_3^\star\}$ |
| $\hat{C}_{x'}$ | $-Re\{H_1H_3^\star + H_2H_4^\star\}$ |
| $\hat{C}_{z'}$ | $\frac{1}{2}\{-H_1H_1^\star - H_2H_2^\star + H_3H_3^\star + H_4H_4^\star\}$ |
| $\hat{T}_{x'}$ | $+Re\{H_1H_4^\star + H_2H_3^\star\}$ |
| $\hat{T}_{z'}$ | $+Re\{H_1H_2^\star - H_3H_4^\star\}$ |
| $\hat{L}_{x'}$ | $-Re\{H_1H_3^\star - H_2H_4^\star\}$ |
| $\hat{L}_{z'}$ | $\frac{1}{2}\{H_1H_1^\star - H_2H_2^\star - H_3H_3^\star + H_4H_4^\star\}$ |

tion of such amplitudes, as opposed to the spinless-particle case, is a non-trivial problem to solve. In principle, a solution would imply having high-precision measurements covering a wide range of kinematics for all of the observables available in meson photoproduction. Early studies from [34] and later on from [38] showed, however, that not all of them have to be measured in order to extract the amplitudes to an overall phase and discrete ambiguities. In such an ideal scenario, known as the "complete measurement", an unambiguous determination of the helicity amplitudes in meson photoproduction requires the determination of only eight observables: four single polarization observables ($\sigma_0, \Sigma, T$, and $P$) and four suitably chosen double polarization observables [34, 38].[7]

A complete measurement is technically difficult to achieve as the measurement of some observables is extremely challenging in most of the channels opened in the nucleon resonance region. In other cases, the available measurements for some channels provide a limited kinematic coverage and low statistics. Measurements then concern a very few observables in

[7] This can be thought as solving a system consisting of eight equations (eight observables) and eight unknowns (the real and imaginary parts of the four complex amplitudes $H_1, H_2, H_3$, and $H_4$).

narrow energy and angular regions so that, in general, what can be inferred from the data available is information about the combination of helicity amplitudes (product of amplitudes) rather than the amplitudes themselves [39]. Therefore, the extraction of amplitudes from data and, consequently, the extraction of the corresponding resonances requires the availability of good-quality data as well as the use of theoretical models.

The starting point of most of the theoretical models aimed at extracting amplitudes and resonance parameters from data is the parametrization of the transition $T$-matrix in terms of resonant $T^R$ and non-resonant $T^{NR}$ background contributions. The resonant part refers to the $s$ channel (nucleon) resonances like $S_{11}(1650)$, $P_{11}(1710)$, $P_{13}(1720)$, and $D_{13}(1895)$. The Born terms, the $t$ channel resonances and the $u$ channel hyperon resonances all contribute to what is called the background. Resonances in the $t$ and $u$ channels however do not "resonate" since their poles are beyond the physical plane of the reaction. The $T$-matrix of the interaction associated with the transition from the initial state $a$ to the initial state $b$ can be written as:

$$T_{ab} = T_{ab}^{R} + T_{ab}^{NR} \tag{2.11}$$

allowing one to study both contributions in a separate way, with the details varying from model to model. Currently, there exist several different models for analyzing pion- and photon-induced reactions on the nucleon in the resonance region. In general, these models can be divided into three groups: phase-shift analysis, isobar models, and coupled-channels models. The first one attempts to make a resonance parameter extraction from a fit-based determination of multipoles. The other two make assumptions about the set of input resonances that best describe each partial wave.

### 2.3.1 Phase-shift analyses

Phase-shift analysis is the attempt to extract the scattering amplitude from fitting procedures on the experimental cross section and other experimental observables in a model-independent fashion. It is an example of sort of a "pure" partial-wave analysis because one does not really include any model in it. The drawback of this method is that it only works under very limited conditions, essentially when there is only one channel involved in the analysis (e.g. single-pion production).

In practice, the scattering amplitude is usually calculated in terms of the phase shifts and elasticities in each partial wave up to a certain cut-off imposed on the angular momentum. These two parameters are varied until the resultant calculated cross sections and polarization observables describe a best fit to the data at a particular energy bin. This process typically yields a large number of solutions; often several hundred random searches are made, each giving a different best fit. A complementary method is to expand the cross section according to Equations (2.9) or (2.10) and fit the coefficients ($a_l$ or $A^J_{\mu\lambda}$) to those obtained from the calculated amplitudes. An energy-smoothing criterion is then used to select the solution which fits smoothly to lower energies.

### 2.3.2 Isobar model

The basis of the calculations within the isobar-model framework is an effective Lagrangian defined on the basis of a selected set of Feynman diagrams concerning the process of interest. Such diagrams are grouped into resonant and background diagrams. Resonant diagrams are related to $s$-channel diagrams while background is represented, in general, by tree diagrams known as Born terms.[8] At high energies, the contribution of such Born terms can increase dramatically compared to the corresponding measured data for which is necessary the introduction of form factors in order to reduce the strength of the background contribution. Gauge invariance is then respected through the inclusion of contact diagrams. In addition to $s$-channel diagrams and Born terms, more refined versions of the isobar model incorporate a particular selection of extra $t$- and $u$-channel diagrams in both resonant and background parts. The inclusion of those additional diagrams constitutes the model dependency of the model.

The most relevant isobar models for the analysis of pion production and photoproduction data are SAID and MAID. SAID is a multi-channel model developed by the Center for Nuclear Studies (CNS) at the George Washington University [35, 40]. Rather than assuming certain resonances for the description of partial waves, it extracts resonance couplings from a fit-based determination of multipoles using both an energy-dependent and an energy-independent parametrization. MAID is a unitary isobar model for partial wave analysis in

[8] In a typical calculation, a particular reaction is modeled based on the selection of a certain number of $s$-diagrams (resonant states) that presumably describe correctly the reaction.

the resonance region developed by the Mainz group [41]. Based on the effective Lagrangian approach, the model attempts to link photoproduction observables directly to the degrees of freedom from various quark models, reducing, in this way, the number of required adjustable parameters [42].

Although the isobar model has been extensively used because of its simplicity and dominance of resonance excitation in the energy domain under 2 GeV, its main drawback is the large number of adjustable parameters required in the calculations. Coupling constants as well as form factors and cut-off masses are adjusted according to fits to experimental data. Consequently, the results of the isobar model, in general, depend not only on the quality of the data used to adjust the model parameters but also on the input terms for resonant and non-resonant contributions.

### 2.3.3 Coupled-channels analyses

For the case of the isobar model, different sets of resonances used as input can describe equally well the data. The question is which set of resonances is the correct one? The answer is provided by a simultaneous analysis over several observables (instead of an independent analysis of just one observable) measured on further final states ($\pi N$, $\eta N$, $K\Lambda$, $K\Sigma$, or $\omega N$) for as large an energy range as possible that also consistently uses the same Lagrangian to describe the reaction mechanism of both the pion- and photon-induced reactions, thereby generating all non-resonant contributions (background) dynamically from Born, $u$-, and $t$-channel contributions without new parameters. As a consequence, more constraints are added to the reaction, increasing the probability of selecting the best set of resonance parameters. This formalism, known as coupled-channels analysis, constitutes a theoretical approach aimed at improving in a systematic way the decision about which resonances have to be put in and which resonances have to be ignored in the models, improving in this way the reliability of the extracted resonance parameters.

# Chapter 3: Previous Measurements

## 3.1 Previous measurements

Prior to the CLAS g13 run period there have been only a few experiments that measured the strangeness channels on the neutron in the resonance region, and in particular, the $\gamma n \to K^+\Sigma^-$ channel. One can find an experiment conducted at Cornell in the late 1950's, the CLAS g2 and g10 run periods, and one carried out at SPring-8/LEPS. Among them, however, the one from SPring-8/LEPS is the only one that used linearly polarized photons, which are needed to determine the photon beam asymmetry for $\gamma n \to K^+\Sigma^-$.

### 3.1.1 Cornell

The experiment at Cornell [43], performed by Anderson *et al.* in 1961, detected charged kaons with a magnetic spectrometer, using a 1.170 GeV bremsstrahlung photon beam, and both liquid hydrogen and liquid deuterium targets. The differential cross section for the $\gamma n \to K^+\Sigma^-$ reaction was determined in an inclusive way by comparing the $K^+$ yields from hydrogen and deuterium at $K^+$ momenta of 0.405 and 0.455 GeV/c. Only two data points were extracted from this analysis, with error bars of the order of 50-60%.

### 3.1.2 CLAS g2

One of the initial goals of the CLAS g2 run period [44] from 1999 was to study the $\gamma n \to K^+\Sigma^-$ channel. The experiment used a 10-cm-long liquid-deuterium target and a photon beam with some degree of circular polarization covering photon energies from 0.50 to 2.95 GeV. The data-acquisition system was triggered by a single charged particle in CLAS, in coincidence with the photon tagging system, resulting in a data recording rate of $\sim$1 kHz. Although this experiment was an important beginning, its results showed insufficient statistics, allowing only restricted studies of the $\gamma n \to K^+\Sigma^-$ reaction. Both inclusive and exclusive analyses were performed on this channel, aimed at determining the differential cross section. As better data came along, however, none of these results were published.

### 3.1.3 CLAS g10

The other CLAS data set important for strangeness photoproduction on the neutron is g10 [45], which ran in 2004. Although originally focused on searching for the $\Theta^+$ pentaquark, the data from g10 are suitable for studying the regular strangeness-production channels as well. The experiment used a 24-cm-long liquid-deuterium target with an unpolarized photon beam. A trigger requiring two charged particles in coincidence with the tagger was used, giving a rate of ∼2 kHz. This made it possible for g10 to increase the statistics by a factor of 20 compared with the g2 experiment. An exclusive analysis of $\gamma n \to K^+\Sigma^-$ using the g10 data has been published [46] where the differential cross section was measured with tagged photons in the energy range 1.0-3.6 GeV and at $K^+$ center-of-mass polar angles between 10° and 140°. As expected, for photon energies above the resonance region, a dominance of $t$-channel production was observed, but the differential cross section suggested a significant $s$-channel contribution in the resonance region. The combined statistical and systematic uncertainty is below 5% in the central CLAS region, and increases up to ∼13.5% at forward and backward angles.

### 3.1.4 LEPS

A series of experiments aimed at studying strangeness photoproduction has also been carried out in the last decade at the SPring-8/LEPS facility in Japan. LEPS is a forward detector designed to study $\phi$-meson photoproduction by using linearly polarized photons from an ultraviolet Ar laser Compton backscattered from 8-GeV electrons, reaching a high degree of linear photon polarization (∼92% at the maximum photon energy).[1] As part of an inclusive analysis [21], both the differential cross section and the beam asymmetry were measured for the reaction $\gamma n \to K^+\Sigma^-$.[2] The data were taken using liquid hydrogen ($LH_2$) and liquid deuterium ($LD_2$) targets, each with an effective length of 16 cm, and photon energies ranging

[1] In contrast with the CLAS, the LEPS acceptance is limited to very forward angles ($\theta < 30°$), which is not well suited for exclusive measurements and cannot provide the kinematic coverage needed for $N^\star$ physics. The CLAS, however, has limited acceptance at very forward angles (∼20°). In this sense, the data from LEPS are complementary to those from CLAS.

[2] This is currently the only determination existing in the literature of the beam asymmetry for $\gamma n \to K^+\Sigma^-$, representing the only available data to which the results obtained in this thesis can be compared.

from 1.5 to 2.4 GeV. The missing-mass spectra for hydrogen and deuterium, integrated over all photon energies and all polar angles, are shown in Figure 3.1. The $\Sigma^-$ yield was obtained by subtracting the total $\Sigma$ yield ($\Sigma^0$ and $\Sigma^-$) in $LD_2$ from the $\Sigma^0$ yield in $LH_2$. This assumes that: (i) for the $LD_2$ data, the target mass was $M_{LD_2} \approx (M_p + M_n)/2$ with $M_p$ and $M_n$ being the mass of the proton and neutron, respectively, and (ii) the ratio $N(\Sigma^0)/N(\Lambda)$ for $LD_2$ was the same as for $LH_2$, leaving the nuclear effects to be evaluated as systematic errors.

The photon beam asymmetries for $\gamma n \rightarrow K^+\Sigma^-$ extracted in [21] are displayed in panel (a) of Figure 3.2. They correspond to the four $\cos\theta_{cm}$ bins that could be measured for $E_\gamma$ between 1.5 and 2.4 GeV. As can be seen, the asymmetries are positive, and the fact that their values are close to +1 for $\cos\theta_{cm} < 0.9$ might indicate the dominance of $K^\star$ exchange in the $t$-channel. Conversely, phenomenological models like Kaon-MAID [22] assume the dominance of $K$ instead of $K^\star$ exchange in the $t$-channel, predicting therefore negative asymmetries for the $K^+\Sigma^-$ channel (see panel (b) of Figure 3.2).

In summary, all the previous experiments and analyses discussed above show the need for a large and high-quality data set that allow to extend kinematically the current measurements of the photon beam asymmetry for $\gamma n \rightarrow K^+\Sigma^-$ providing in that way better constraints in the search for missing $N^\star$ states and contributing to the refinement of some of the current phenomenological models. The analysis presented in this work will provide data for the photon beam asymmetry associated with the $\gamma n \rightarrow K^+\Sigma^-$ reaction in a photon energy range between 1.9 and 2.3 GeV and spanning the $K^+$ azimuthal center-of-mass angle from 55° to 155°.

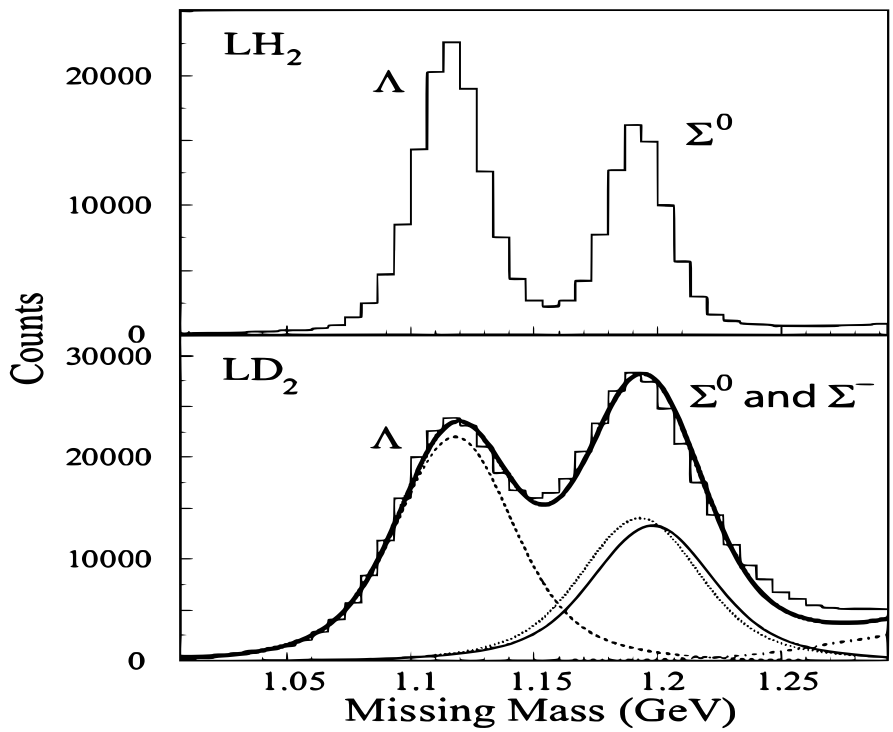


Figure 3.1: Inclusive missing-mass distribution for $K^+$off $LH_2$ and $LD_2$ targets from LEPS/SPring-8. The dashed, dotted, and solid thin curves correspond to $\Lambda$, $\Sigma^0$, and $\Sigma^-$production, respectively, and the dot-dashed curve corresponds to the estimated background. The thick solid curve is the sum of all contributions [21].

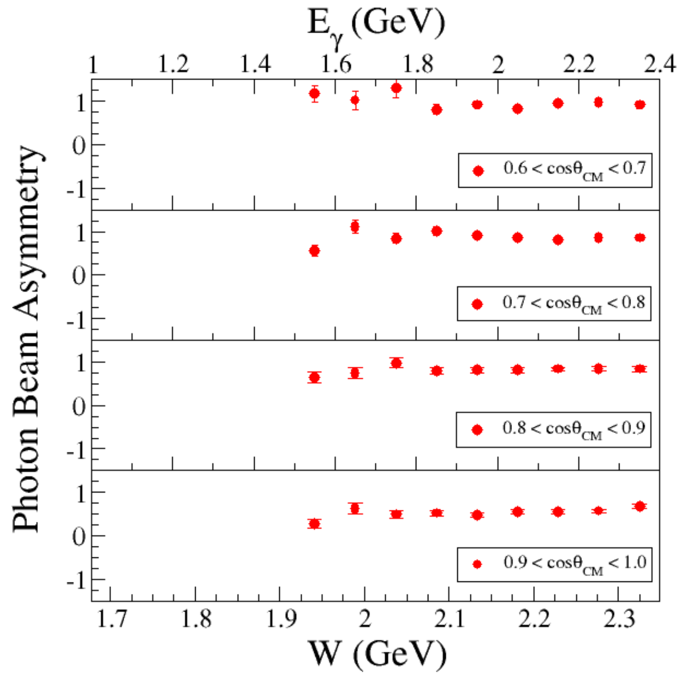


(a)

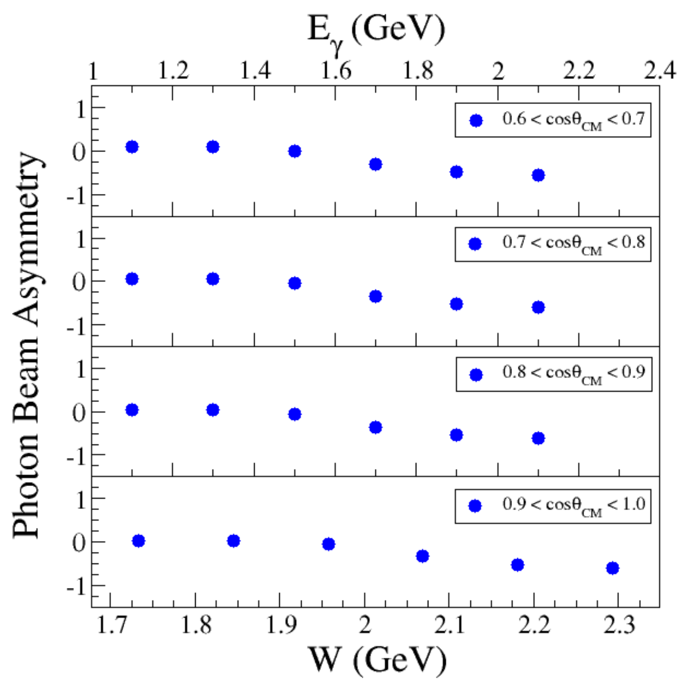


(b)

Figure 3.2: (a) The only published data for the photon beam asymmetry of the $\gamma n \rightarrow K^+\Sigma^-$ reaction. The data, limited to very forward angles, come from the LEPS collaboration [21] and were published in 2006. The data were taken from reference [47]. (b) Predictions from Kaon-MAID [22] of the beam asymmetry for the $\gamma n \rightarrow K^+\Sigma^-$ reaction.

# Chapter 4: Experimental Setup

The data used for this analysis were taken as part of the g13 run period in 2007 in Hall B at the Thomas Jefferson National Accelerator Facility located in Newport News, Virginia. The g13 period corresponds to experiment E-06-103, "Kaon Photoproduction on the Deuteron Using Polarized Photons" [48]. This experiment was the only one to run during the g13 period and collected a significant number of events aimed at searching for *missing resonances* that couple weakly to pion channels.

General running conditions in g13 included a photon-tagging system, a 40-cm long liquid-deuterium target, the CEBAF Large Acceptance Spectrometer (CLAS) detector, and both circularly and linearly polarized photon beams. The photon energy in the circular polarization part (g13a) ranged from 0.4 GeV to 2.5 GeV, while in the linear polarization part (g13b), it varied between 1.1 and 2.3 GeV.

This chapter describes the main features of the experimental setup utilized during the g13 CLAS run period.

## 4.1 CEBAF Accelerator

At the heart of the Thomas Jefferson National Accelerator Laboratory is the Continuous Electron Beam Accelerator Facility or CEBAF [49], a five-pass recirculating linac that operates with superconducting cavities to accelerate high currents of electrons into the few-GeV range. CEBAF consists of a 56 MeV injector, two superconducting linacs of 0.6 GeV energy gain, and nine recirculation arcs. To keep the cavities superconducting, CEBAF has the world's largest liquid-helium refrigeration plant, which produces temperatures down to 1.8 K. The accelerator is able to deliver beam bunches of electrons to three different experimental end stations simultaneously. The currents delivered to Halls A and C ($1 - 200$ $\mu$A) make it possible to reach luminosities of about $10^{38}$ cm$^{-2}$ s$^{-1}$. For Hall B, the luminosity is limited by drift chamber occupancies in CLAS to about $10^{34}$ cm$^{-2}$ s$^{-1}$, restricting the beam current to $1 - 100$ nA. These currents result in beam bunches composed of between 12,500 and 2,500,000 electrons for Halls A and C, and between 12 and 1,250 electrons for Hall B.

Worthy of mention is the fact that the beam bunches delivered to each Hall are accelerated together (despite differing significantly in magnitude) along the linacs and the recirculation paths. Therefore, there can be three different currents coexisting at the same pass. This is an underlying feature of the accelerator. The schematic of the CEBAF accelerator is shown in Figure 4.1.

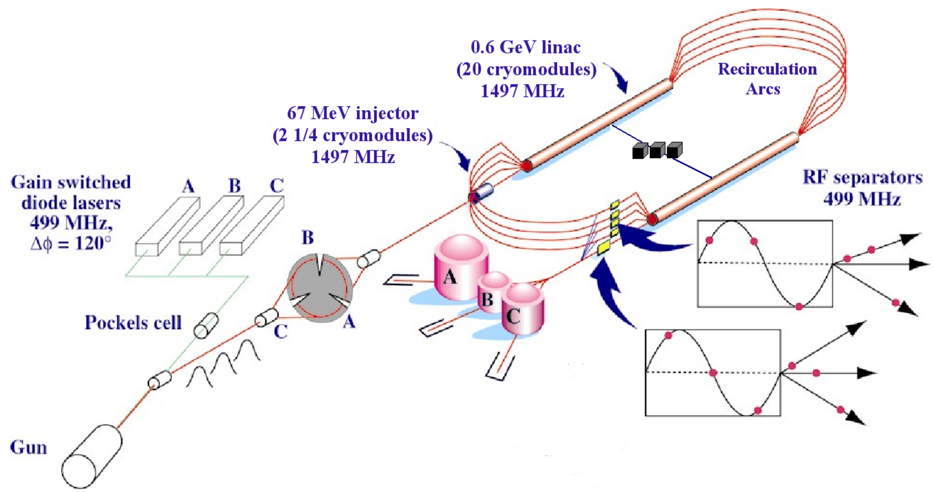


Figure 4.1: The Continuous Electron Beam Accelerator Facility (CEBAF) at Jefferson Lab. The explanation of the main components of the accelerator is given in the text.

The CEBAF beam originates (at 100 keV) in an electron gun through photoemission of electrons from a GaAs photocathode [50, 51]. The photoemission takes place by illuminating the cathode with three RF gain-switched lasers independently pulsed at 499 MHz and 120° out of phase.[1] As a result, three independent electron beams, one for each Hall, are produced. The beams are combined through a rotating disk with three variable-size slits, into a 1497 MHz pulse train of electrons. The combined electron beam is accelerated to 67 MeV by two cryomodules and then injected into the accelerator. Passing through each linear accelerator (linac) increases the energy of the electrons by up to 0.6 GeV. Therefore, a complete loop around the track boosts the electron beam energy up to 1.2 GeV. With the two linacs connected to each other by nine recirculation arcs, the electron beam is allowed to make a total of five passes through both linacs for a maximum energy of 6 GeV (a 12-GeV upgrade is in progress).

[1]This laser arrangement allows each Hall to have independent control of its beam current.

The beam for each experimental Hall is extracted using warm sub-harmonic RF separator cavities (five in total) operating at 499 MHz[2] [52, 53]. The phasing of these separators provides the required extraction: the four separators that are placed on the lower-energy recirculating arcs are phased in a manner that allows a portion of the beam to be steered to only one of the experimental Halls, while the remainder is recirculated back into the linacs. The phasing of the fifth separator on the high-energy leg (the final recirculation pass) permits splitting the beam into three directions to be driven to the experimental Halls for simultaneous data taking by three different experiments. Currently, the electron beam is delivered to Halls A, B, and C. Halls A and C have two-arm spectrometers which provide high-resolution measurements but limited acceptance. Conversely, Hall B has a large-acceptance detector for multi-particle detection, but lower resolution compared to that of the other two Halls. Because our experiment (g13) took place in Hall B, some of the main Hall B components will be described in the following sections.

## 4.2 Hall B

Hall B, which is 100 feet across, is the smallest of the three experimental end-stations at Jefferson Lab. An overview of Hall B is shown in Figure 4.2. It houses the CLAS detector and its associated electronics as well as some beam-related systems. Although CLAS was designed for operation with both electron and photon beams, the g13 run period is concerned only with photoproduction. Therefore, the next sections will provide an overview of the essential systems used for photoproduction experiments in Hall B. They include the photon beam, the photon-tagging system, and the CLAS detector.

## 4.3 Photon Beam Production

In general, high-energy beams of real photons can be produced mainly via two techniques: Compton back-scattering and bremsstrahlung radiation. In the Compton back-scattering technique, a high-energy electron beam collides with a polarized photon beam produced by a laser (few keV). The energy and polarization of the scattered photons depend mainly on the angle between the incident-electron and the scattered-photon momenta; backward-

[2]Each Hall receives bunches of electrons once every 2.004 ns.

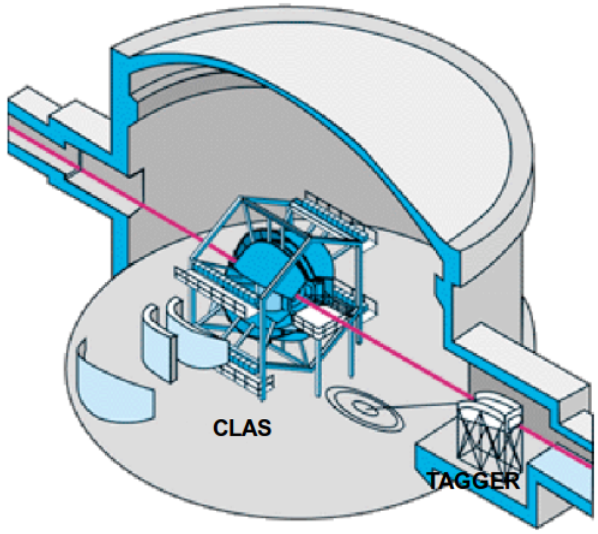


Figure 4.2: Schematic layout of Hall B showing the locations of the tagger and the CLAS detector. In the picture, the photon beam (red line) travels from right to left.

scattered photons, in particular, carry a significant amount of the incident electron-beam energy with a high degree of linear polarization [54, 55]. By collimation of the scattered photons along the electron-beam axis, one can produce a photon beam of high energy (from a high-energy electron beam) and high polarization (from a low-energy laser beam). The Compton back-scattering technique is usually used at synchrotron light sources.

The bremsstrahlung radiation technique, employed in Hall B, involves a beam of electrons interacting with the electromagnetic field of an atomic nucleus with charge $Z$ (radiator). As a consequence of the interaction, an incoming electron, initially with energy $E_o$, is accelerated and emerges with lower energy $E_e$, hence emitting a photon of energy $k$. This process is kinematically possible only if a small amount of momentum $\vec{q}$ is transferred to the nucleus (recoil momentum). In the relativistic limit, bremsstrahlung is the dominant mode of energy loss for electrons in a material, and the nucleus recoil energy can usually be neglected. Energy and momentum conservation then give $(E_0, \vec{P}_o) = (E_e + k, \vec{P}_e + \vec{k} + \vec{q})$, with $\vec{P}_o$, $\vec{P}_e$, and $\vec{k}$, being the momenta of the incident electron, emerging electron, and emitted bremsstrahlung photon, respectively. The spectrum of bremsstrahlung photons is not monoenergetic, however. A beam of incident electrons with a fixed energy $E_o$ produces a beam of photons spread over a range of energies. The energy $k$ of each photon in the beam is determined based on $E_o$, which is provided by the accelerator, and $E_e$, which is measured by means of a tagging spectrometer.

The production of polarized bremsstrahlung photons depends mainly on the polarization state of the electron beam and on the nature of the radiator used (amorphous or crystal radiator). Circular polarization is induced by a longitudinally polarized electron beam incident on an amorphous radiator, while linear polarization depends on the crystalline structure of the radiator. The following subsections describe the production of circularly and linearly polarized bremsstrahlung photons in more detail.

### 4.3.1 Circular Polarization

Production of circularly polarized photons requires the incident electron beam to be longitudinally polarized[3]. Thin foils of high-$Z$ materials are usually used as a radiator. This choice has a double purpose: to maximize the probability of the electron-nucleus interaction given that the bremsstrahlung cross section is proportional to $Z^2$ [56], and to minimize the number of interaction centers such that each electron interacts once, producing only one photon. The circular polarization production process is quantum mechanical in origin. From QED calculations, the degree of circular polarization transfer to the photon, $P_c$, is seen to depend on the relative photon energy to the bremsstrahlung photon, $x$:

$$P_c = \left( \frac{4x - x^2}{4 - 4x + 3x^2} \right) P_e \tag{4.1}$$

where $x = k/E_o$ with $k$ and $E_o$ corresponding to the photon and incident electron energies, respectively, and $P_e$ is the longitudinal polarization of the incident electron beam. As shown in Figure 4.3, the transfer of circular polarization is maximum at the higher end of the energy spectrum ($k/E_o$) and decreases towards the lower end of the spectrum. The circular polarization of the photon is transferred directly from the polarization of the electron, with the atomic nucleus or radiator playing no role. Such a transfer is favored when the radiated photons take up large fractions of the incident electron energy. Coulomb and screening corrections (due to the atomic electrons) do not significantly affect the polarization of the emitted photons [56].

[3] A transversely polarized electron beam does not contribute significantly to the photon polarization [56].

In g13a, a $10^{-4}$ r.l.[4] gold foil radiator (placed upstream of the tagger) and two different electron beam energies were used: a three-pass electron beam (2.0 GeV) and a four-pass electron beam (2.6 GeV) with polarizations of 84% and 78%, respectively [57].

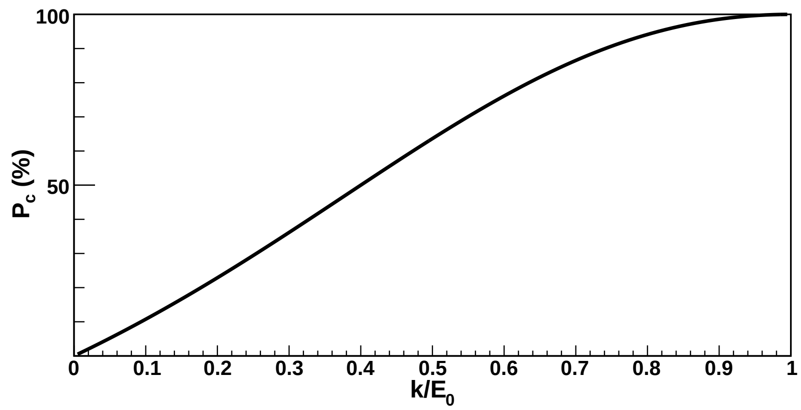


Figure 4.3: QED calculation for the degree of circular polarization of 50-MeV electrons in lead. The curve is a Born-approximation calculation neglecting screening corrections. An exact calculation involving Coulomb and screening corrections (not shown) yields similar results. The similarity of both curves is evidence for the independence of the circular polarization with such corrections [56].

### 4.3.2 Linear Polarization

Linear polarization can be treated both quantum-mechanically and classically. In Hall B, linearly polarized photons are obtained through the coherent bremsstrahlung technique [58, 59] where an unpolarized electron beam $(E_o, \vec{P}_o)$ illuminates a crystal radiator. In this case, the total bremsstrahlung photon spectrum consists of both coherent (linearly polarized) and incoherent (unpolarized) radiation. The mechanism of coherent bremsstrahlung is governed by two conditions imposed on the momentum $\vec{q} = \vec{P}_o - \vec{P}_e - \vec{k}$ transferred to the crystal [60]. As a first condition, the longitudinal $q_l$ and transversal $q_t$ components of $\vec{q}$ with respect to $\vec{P}_o$ are constrained to values which depend on the relative photon energy $x = k/E_o$:

$$q_l^{min} \simeq m_e^2 c^3 \delta(x) \leq q_l \leq \frac{m_e^2 c^3 \delta(x)}{x} \quad \text{and} \quad 0 \leq q_t \lesssim m_e c \tag{4.2}$$

where $m_e$ is the electron mass and $\delta(x) = \dfrac{x}{2E_o(1-x)}$. The lower limits are of kinematical

[4] r.l. stands for radiation length. This parameter, given either in g·cm$^{-2}$ or in cm, is defined as the distance over which the electron energy is reduced by a factor $1/e$ due to radiation loss only.

origin while the upper limits are due to the rapid decrease of the bremsstrahlung cross section with increasing $q$. In momentum space, this allowed momentum transfer region is known as the "pancake", a shallow volume which is normal to, and centered on, the $\vec{P}_o$ direction [61]. The crystal imposes the second condition[5]. The regular structure of the crystal, described by the reciprocal lattice basis vectors $\vec{b}_k$, requires $\vec{q}$ to take only values that coincide with a reciprocal lattice vector $\vec{g}$ (Laue condition). Thus, in order to have coherent bremsstrahlung production, the momentum transfer $\vec{q}$ has to lie within the "pancake" and, at the same time, must match with any of the preferential directions $\vec{g}$ of the lattice.

When any or both of the momentum-transfer conditions fail, the recoil is absorbed in such a way that the bremsstrahlung process takes place separately on each atom. Therefore, bremsstrahlung photons are isotropically distributed along the electron beam axis, leading to an unpolarized beam. Incoherent bremsstrahlung is consequently the sum of contributions of atoms acting individually in the lattice. The incoherent spectrum obtained with a crystal radiator can be reproduced using a non-crystalline radiator. In this way, the total bremsstrahlung spectrum is normalized to the incoherent spectrum such that the coherent contribution of the crystal can be clearly observed. Panel (a) of Figure 4.4 shows a typical incoherent spectrum produced by an amorphous radiator.

When both conditions on $\vec{q}$ are fulfilled, the recoil momentum is taken up by several atoms (a large region within the lattice) acting collectively. In a simplified picture, the contributions of these atoms add "coherently" in the bremsstrahlung process such that most of the photons emitted have the same polarization and both electrons and photons emerge from the crystal at fixed angles. In addition, the fact that $\vec{q}$ remains constant fixes the polarization plane. As a result, a linearly polarized photon beam is produced for a specific orientation of the crystal and a specific incident electron beam energy. Figure 4.4 shows the total bremsstrahlung spectrum (panel (b)), the enhancement, obtained as the ratio between total and incoherent spectra (panel (c)), and the linear polarization spectrum (panel (d)) as a function of the photon energy for a fixed incident electron beam energy. The peaks observed at certain energies represent linearly polarized photons, with the most

[5]Contrary to circular polarization, the crystal structure of the radiator does play a vital role in the linear polarization production.

prominent peak ("the primary" coherent peak) corresponding to the highest degree of linear polarization[6]. For a fixed electron energy, the position of the coherent peak can be changed by carefully adjusting the alignment (orientation) of the crystal with respect to the electron beam.

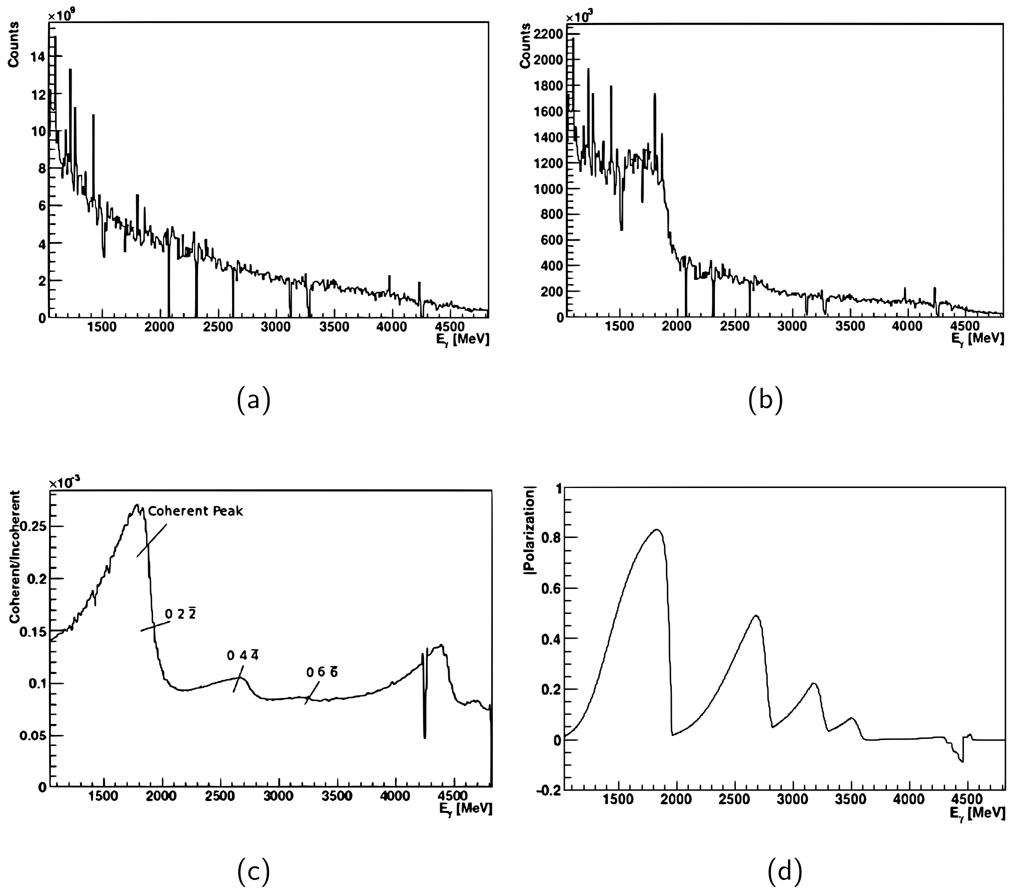


Figure 4.4: Data from the CLAS g13b run period: (a) Incoherent bremsstrahlung spectrum with a carbon radiator. (b) Total bremsstrahlung spectrum: coherent + incoherent, (c) Enhancement ratio of total coherent/incoherent spectra. The relevant reciprocal lattice vectors are labeled. (d) Linear polarization spectrum calculated using a 5052 MeV electron beam on a 50 $\mu$m diamond radiator. The coherent peak is observed at about 1900 MeV. The figure was taken from reference [62].

In g13b, linearly polarized photons were produced in a 50 $\mu$m ($3\times10^{-4}$ r.l.) diamond radiator mounted on a goniometer [63] located 22 m upstream of the tagger. The goniometer performs the proper alignment of the diamond by allowing five degrees of freedom: hori-

[6]Each peak in the energy spectrum is related with a different reciprocal lattice vector $\vec{g}$.

zontal and vertical motion of the diamond as well as rotation with high accuracy (between 25-180 $\mu$m and 0.7-1.3 $\mu$rad) about all three independent axes. Electron beam energies varying from 3.3 to 5.2 GeV were used in g13b, with six coherent peak positions, each about 200 MeV wide, covering photon energies between 1.1 and 2.3 GeV with the maximum linear polarization reaching up to 90% [57].

### 4.3.3 Photon Beam Collimation

The collimation of the photon beam upstream of the CLAS target plays an important role in photoproduction experiments. For example, collimators can be used to enhance the level of linear beam polarization. The choice of a specific collimator reflects the type of observables that can be determined in the experiment. The photon beam collimator is placed downstream of the tagger and its width depends on the type of photon polarization used.

Unpolarized and circularly polarized photons are emitted isotropically in $\phi$, describing a cone-like shape around the incident-beam axis such that when reaching the target, the photon beam can become sizable relative to the target width. The number of photons interacting with the target will then be large, but there can be background related to interactions with the target walls. Therefore, the selection of the collimator for unpolarized or circularly polarized photons is a trade-off between maximizing the photon flux and minimizing the potential electromagnetic background. Typically, the collimator width in this case is selected based on a photon beam profile taken in the proximity of the collimator. Photons in the beam are distributed according to a gaussian function centered on the beam axis. A collimator with at least a $3\sigma$ width represents a good choice as it cuts sufficient unwanted events in the tails of the photon distribution but, at the same time, keeps a conservative number for the photon transmission. This choice of collimator is appropriate for high-quality cross-section measurements.

Linearly polarized photons from coherent bremsstrahlung are characterized by having an emission angle with respect to the incident beam smaller than that for incoherent bremsstrahlung. Given that the latter is a background for the former, the level of linear polarization can be enhanced by employing small-width collimators to reduce the incoherent contribution at all photon energies. However, although this enhances the linear polarization, the photon transmission is significantly reduced. Narrow collimators are therefore convenient for determination of observables like the photon-beam asymmetry, but not cross sections.

The produced photons in g13a passed a 6.4 mm collimator, which provided about 90% transmission on the way to the deuterium target. In g13b, a 2 mm collimator was used, and polarizations varying between 70% and 90% were obtained.

## 4.4 Photon Tagging Spectrometer

The polychromatic nature of the bremsstrahlung photons produced by an electron beam of energy $E_o$ requires the use of a photon-tagging system [64] to find the energy of the photons interacting in the target. The photon energy $k$ is calculated by energy conservation (neglecting the recoil energy) from $k = E_o - E_e$, where $E_e$ is the outgoing electron energy.

After the bremsstrahlung process, the electron and photon beams come out from the radiator nearly parallel with respect to the incident electron beam direction. The outgoing beams are separated when passing through the tagger magnet; the electrons are bent downwards by the dipole magnet while the photons continue through a hole in the magnet yoke towards the CLAS target (see Figure 4.5). The tagger magnetic field is properly matched to the incident electron beam energy ($E_o$) such that electrons which do not radiate (full-energy electrons) are directed into a beam dump below the floor of Hall B. Electrons which do generate a bremsstrahlung photon are deflected more by the tagger magnet, with a radius of curvature depending on the fraction of incident energy transferred to the photon ($k/E_o$). This setting allows the photon-tagging system to tag photons with energies between 20% and 95% of the incident electron energy [64].

The detection of the electrons is performed in a plastic scintillator hodoscope, a system composed of two separate arrays of scintillators, similar in construction but differing in purpose: the "$E$-counters" and the "$T$-counters." The former are used to determine the energy of the electrons, while the latter record the umbral time, used to match the electron with the corresponding nuclear interaction in CLAS triggered by the photon (see Figure 4.5).

The $E$-counter array contains 384 partially overlapping plastic scintillators, each 20 cm long and 4 mm thick. The scintillator width varies between 6 and 18 mm in order to have each cover nearly the same energy fraction of the incident electron beam ($0.003E_o$). The $E$-counters overlap each other by one-third of their respective widths (Figure 4.5), thus creating 767 $E$-channels that provide an energy resolution of $0.001E_o$ per bin.

The $T$-counter array contains 61 scintillators, each 2 cm thick. To equalize the rate on each counter, their widths are varied according to the $1/k$ distribution of incoherent bremsstrahlung. The $T$-counters overlap by about 10% of their widths (Figure 4.5), forming 121 $T$-channels with a timing resolution of 110 ps. The overlap helps eliminate potential gaps between the counters [64].

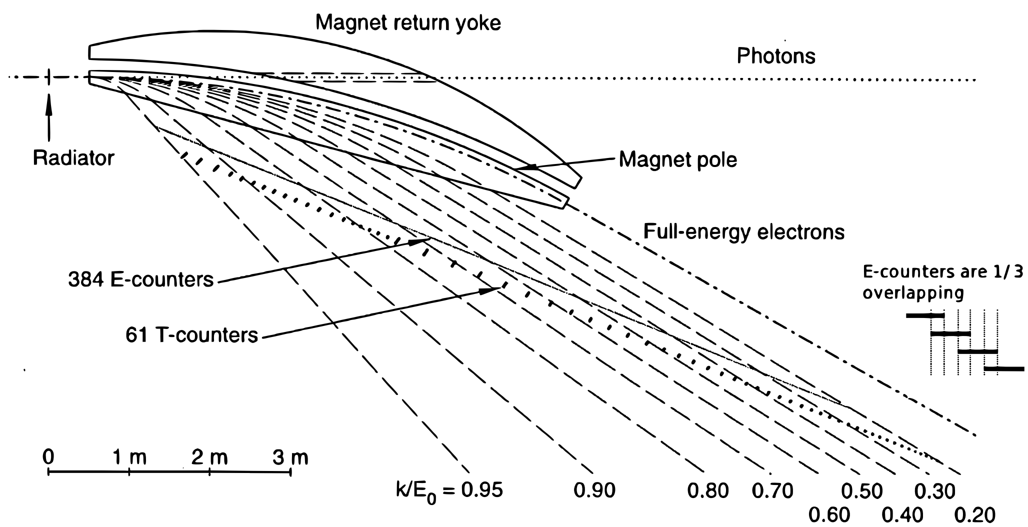


Figure 4.5: Layout of the photon tagging system [64].

## 4.5 The CLAS Detector

The CLAS detector was designed to study photo- and electro-induced nuclear and hadronic reactions by providing efficient detection of neutral and charged particles over a large fraction of the full solid angle. A picture and a 3-D representation of CLAS are shown in Figure 4.6. The CLAS design is based on a toroidal magnetic field generated by six coils centered on the beamline. The coils divide the CLAS into six azimuthal sectors forming six independent spectrometers (each with a corresponding coordinate system) that share the same target, trigger, and data-acquisition (DAQ) system. Each spectrometer is comprised of three regions of drift chambers (DC) which are used to determine the trajectories and momenta of the charged particles produced in the target. In addition, CLAS contains scintillation counters for time-of-flight measurements (TOF), electromagnetic calorimeters (EC) and large angle calorimeters (LAC) for detection of electrons, photons, and neutrons. Together with the EC, Gas Cherenkov counters (CC) are used for electron identification. In photoproduction experiments, a start-counter scintillator (ST) is placed surrounding the target to provide with a correct start-time for TOF measurements. The next subsections will provide an overview of the CLAS subsystems.

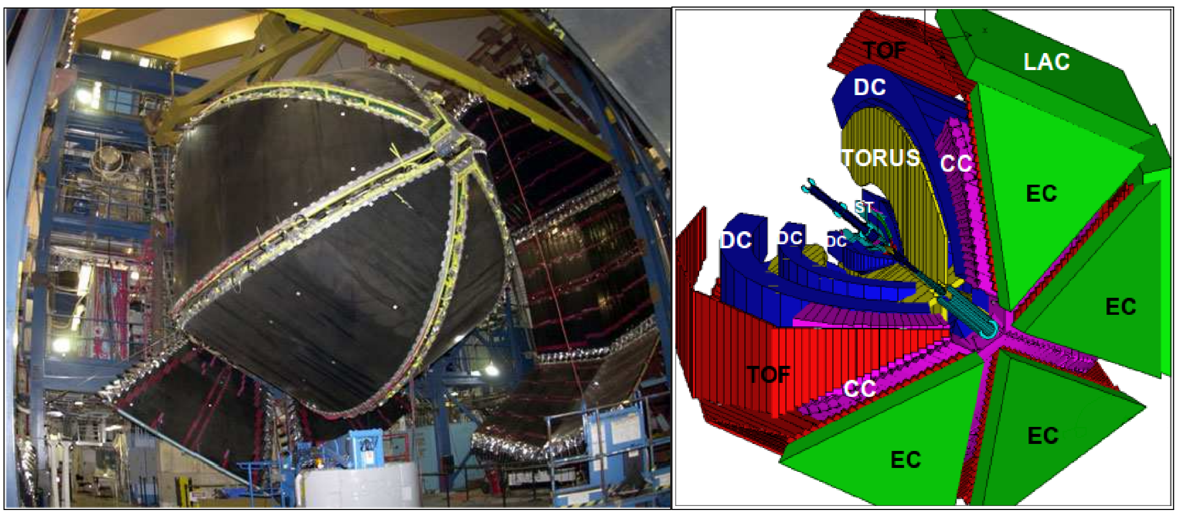


(a) (b)

Figure 4.6: CLAS: (a) photograph of CLAS opened up showing the region 3 of the drift chambers (DC) and some of the time-of-flight (TOF) components. (b) 3-D visualization illustrating all the subsystems comprising CLAS.

### 4.5.1 Torus Magnet

The torus magnet consists of six iron-free[7] superconducting coils symmetrically arranged in a toroidal-like shape[8] centered on the beamline (see Figure 4.7). Each coil, 5 m long, has

[7]The lack of iron allows calculating the magnetic field directly from the current in the coils.

[8]The toroidal shape was chosen in order to maximize the integral field $\int \vec{B} \cdot d\vec{l}$ at forward angles.

a kidney shape with 216 turns of aluminum-stabilized NbTi/Cu wire. The coils are placed in between regions 1 and 3 of the drift chambers, as shown in panel (a) of Figure 4.8, and generate a magnetic field that extends radially up to approximately 2.5 m with respect to the beamline.

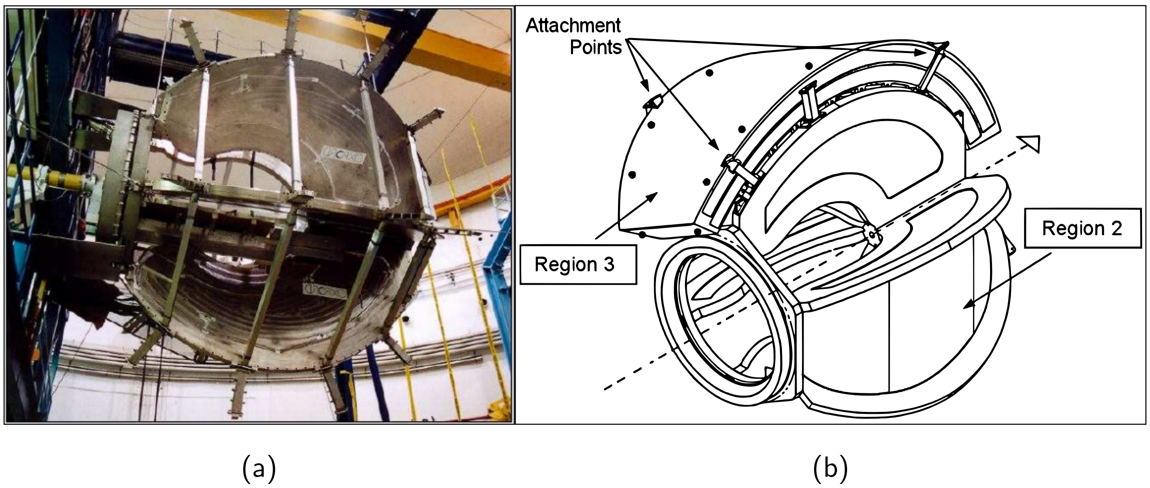


Figure 4.7: Torus magnet: (a) bare coils. None of the other subsystem detectors have been assembled in this picture. (b) Schematic view of the torus magnet.

As a consequence of the kidney shape and the location of the coils, the integral magnetic field generated is high at forward angles (2.5 T·m at maximum current) and low at backward angles (0.6 T·m at $\theta = 90°$), and concentrated mostly in region 2 of the drift chambers. The other two regions are virtually field-free. These features of the CLAS magnetic field optimize the detection of high-momentum particles (which usually are forward-going) and at the same time, permit the use of polarized targets. Panel (b) of Figure 4.8 shows the magnetic field distribution in a plane perpendicular to the beamline. Except for the regions close to the coils, the magnetic field is nearly a pure azimuthal field. As a result, the trajectory of a charged particle in CLAS is confined to a single sector. Deflections along the $\phi$-direction are negligible.

The magnetic field in g13 was set with a negative polarity by passing a current of -1500 A through the coils. Consequently, positively charged particles bent toward the beamline and negatively charged particles bent away from the beamline. This setting was chosen in order to increase the acceptance of low-momentum negative pions coming from the decay of hyperons like $\Lambda$ and $\Sigma^-$.

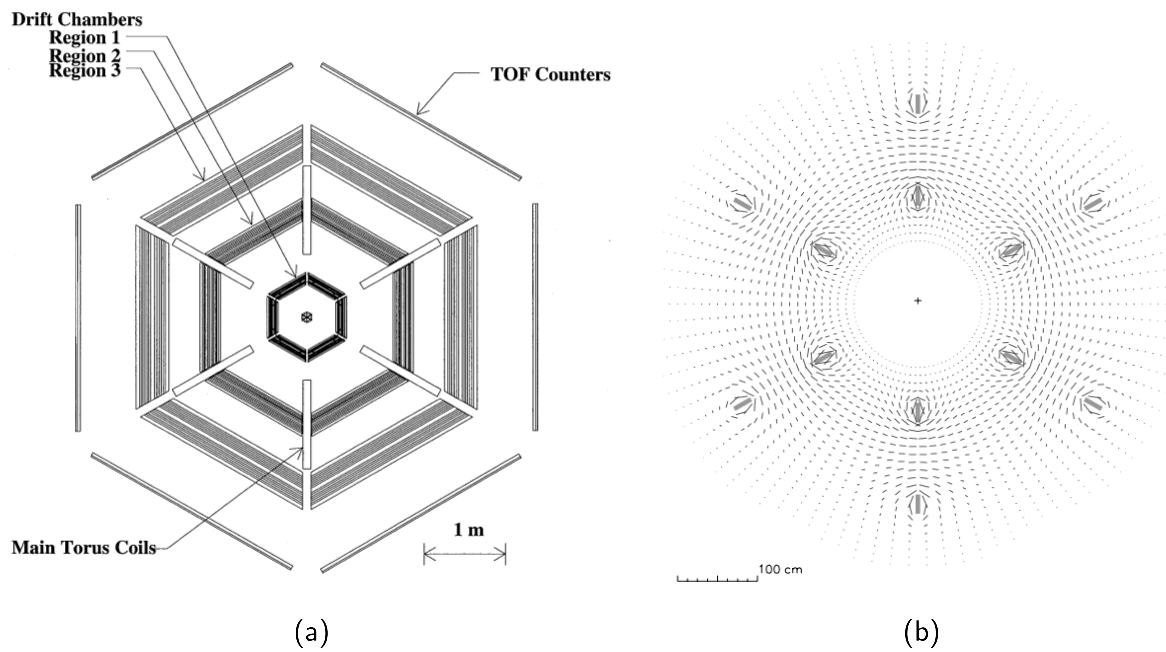


Figure 4.8: (a) Schematic cross-sectional view of the CLAS detector, perpendicular to the beam line. The torus coils are located within DC region 2. (b) Magnetic field distribution corresponding to the view in (a). The field is purely azimuthal. The six torus coils are shown in grey.

### 4.5.2 Drift Chambers

The CLAS Drift Chamber system (DC) is responsible for the tracking of charged particles. Effective track reconstruction depends on the accuracy with which the drift chambers determine a particle's position along its trajectory from the target to the outer detector systems (TOF, EC, LAC). For the typical momenta of the particles that CLAS is capable of measuring, the drift chambers allow for position measurements with a precision of a few microns, resulting in a resolution of 0.5% for the reconstructed momentum at forward angles and 2 mrad for the reconstructed scattering angles.

#### 4.5.2.1 Design

The drift-chamber system (DC) in each of the six sectors of CLAS consists of three regions of wires (Region 1, Region 2, and Region 3) radially separated by helium-filled gas bags. The relative positioning of these regions is shown in Figure 4.9. Region 1 is located closest to the target and the beamline in a low magnetic field. This region is used to determine the initial trajectory of charged particles before entering the $\vec{B}$ field. Region 2 is located between the torus coils, in the area of high magnetic field, and is used to obtain a second set of measurements of the particle track in the region of maximum curvature, to achieve good momentum resolution. Region 3 is outside the torus coils in a low-magnetic field and serves to further determine the trajectory (in this region, a straight line) of charged particles headed towards the outer detectors.

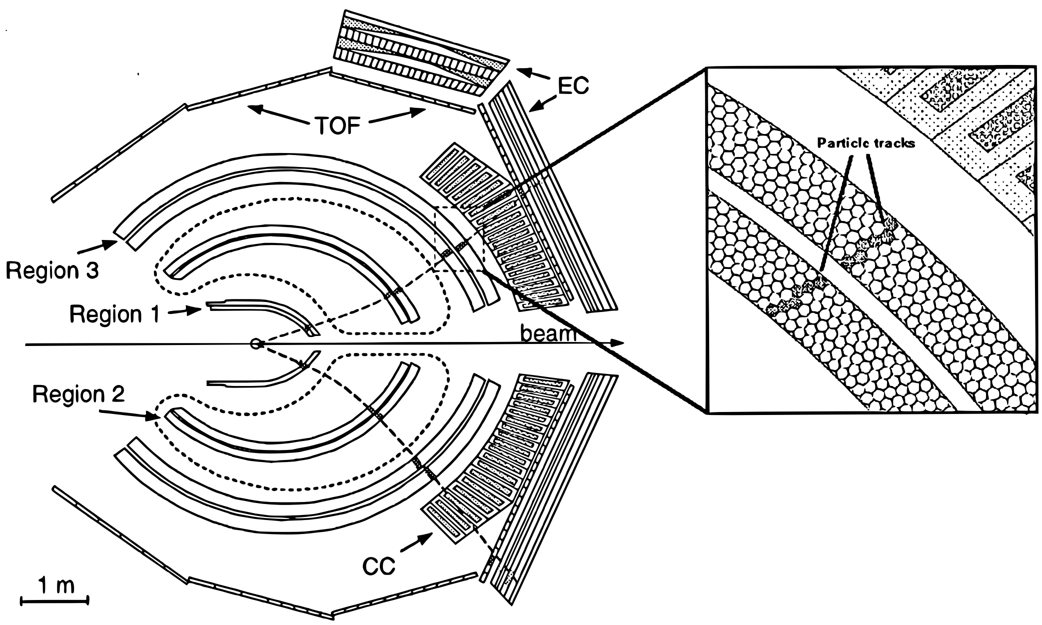


Figure 4.9: Schematic view of the CLAS detector showing the relative position of the three drift chamber regions. Tracking reconstruction of both negative and positive charged particles is observed along with a representation (inset) of a portion of a region 3 chamber showing the layout of its two superlayers.

Each region is a separate chamber filled with a 90% Argon and 10% $CO_2$ mixture and composed of two superlayers of six wire layers each[9]. There are two types of layers in each region: one axial to the magnetic field, and the other tilted at a 6° stereo angle that provides azimuthal information. Likewise, there are two types of wires: sense wires and field wires. The former are maintained at a high positive voltage while the latter are maintained at a high negative voltage. The voltage on the wires creates an electric field whose direction causes the negative charged particles to accelerate towards the sense wires. Sense and field

[9]Because of space constraints, there are only four layers in the second superlayer of Region 1.

wires are arranged in such a way that each of the sense wires is surrounded by six field wires forming an hexagonal pattern called "cell" whose size increases uniformly with increasing radial distance from the target. This hexagonal pattern, besides minimizing the effects of multiple scattering[10], significantly decreases the electric forces on the wires. Figure 4.9 shows a representation of the tracking in a Region 3 chamber clearly showing the layout of the two superlayers and the corresponding cell-layer structure. In addition to the field wires that form the cell, there is an extra layer of field wires known as "guard" wires placed at the edges of each superlayer and kept at a low voltage. These wires correct for the finite number of cells, making the electric field in each cell roughly independent of the cell's position within the chamber.

#### 4.5.2.2 Track reconstruction

When a charged particle goes through the drift chambers, each of the 34 layers is traversed. Particles passing through the drift chambers ionize the gas and create free electrons along their path. Due to the electric field present inside the chambers, these free electrons drift toward the sense wires at a low and roughly constant velocity (due to collisions with molecules in the gas). As each electron is accelerated very near the sense wire, it ionizes additional gas molecules, creating an avalanche of electrons moving toward the sense wires which produces a strong signal and therefore much easier to detect than would have been the case if only one electron reached the sense wire. The time it takes for ions created by the particle to drift to the sense wire is known as the drift time $T_{drift}$ [65].

Each hit detected in the drift chamber is used to determine the particle's track by means of a least squares fit performed in the CLAS reconstruction software program. The reconstruction of charged-particle tracks in CLAS is performed in two stages. In the first stage, individual tracks are fit only to hit-wire positions in a procedure known as "hit-based" tracking. In this procedure, data are combined into track segments within individual superlayers; these segments are then grouped together using a "link table" to form tracks (within one sector) across the three DC regions. Due to the small size of the drift cells and

[10] A cylindrical symmetry pattern between field and sense wires produces a cylindrical electric field. Such a field configuration leads to a one-to-one relationship between the distance field-sense wire and the drift time.

the large number of wire layers, the track momenta can be reconstructed with a resolution of 3% to 5%. In the second stage of the reconstruction, the measured drift times are corrected by using flight-time information of the particles from the target to the outer scintillators [65]. An example of a particle's track in the drift chambers is shown in Figure 4.13.

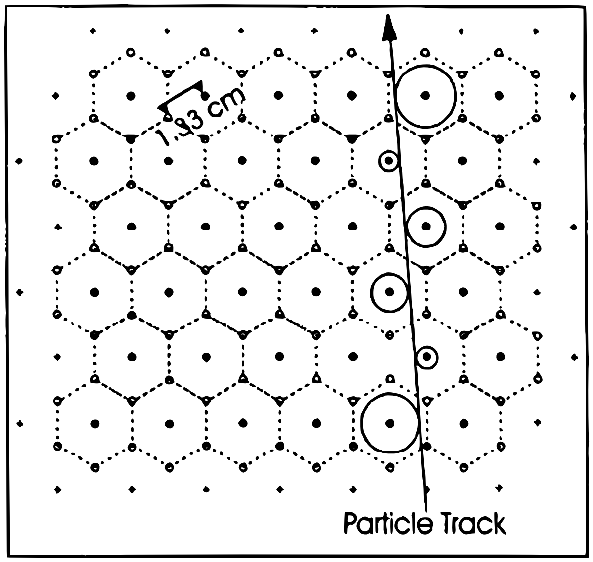


Figure 4.10: An example of a particle's track reconstructed in the drift chambers.

A look-up table is used to convert the corrected drift time in the calculated distance of closest approach (CALCDOCA). Within a given superlayer, a second method to determine the distance of closest approach consists of fitting a track to all hits except those in a specific layer. This produces the fitted distance of closest approach (FITDOCA). The difference between CALDOCA and FITDOCA, known as the residual, is the primary method for calibrating and measuring the resolution of the drift chambers.

#### 4.5.2.3 Calibration

As part of my work in g13, I was in charge of the calibration of the DC system for both the g13a and g13b run periods. The calibration of the drift chambers in CLAS starts by setting the minimum and maximum values of the drift time distribution (See Figure 4.11). The minimum value $T_0$ (primarily related by cable delays) of the drift time is found by fitting the leading edge of the time distribution. The maximum value $T_{max}$ represents physically the maximum time it would take ions created at the edge of a cell in the drift chambers to drift to the sense wire in the center of the cell. $T_{max}$ is determined by looking for the point where the fraction of the total integral of the drift time distribution is equal to some value (typically 99% for region 1 and 97% for regions 2 and 3). Once these limits are fixed, the procedure follows with an initial selection of the calibration parameters based on the fitting of the drift-velocity function [11] for every superlayer in every sector. The functional form of the fitting function depends on the DC region: polynomials forms are used for regions 1 and 2 while for region 3 a power form works better. The corresponding parameters of the fitting functions are determined by fits to the FITDOCA vs drift time plots. An example of the FITDOCA vs drift time relationship is illustrated in Figure 4.12.

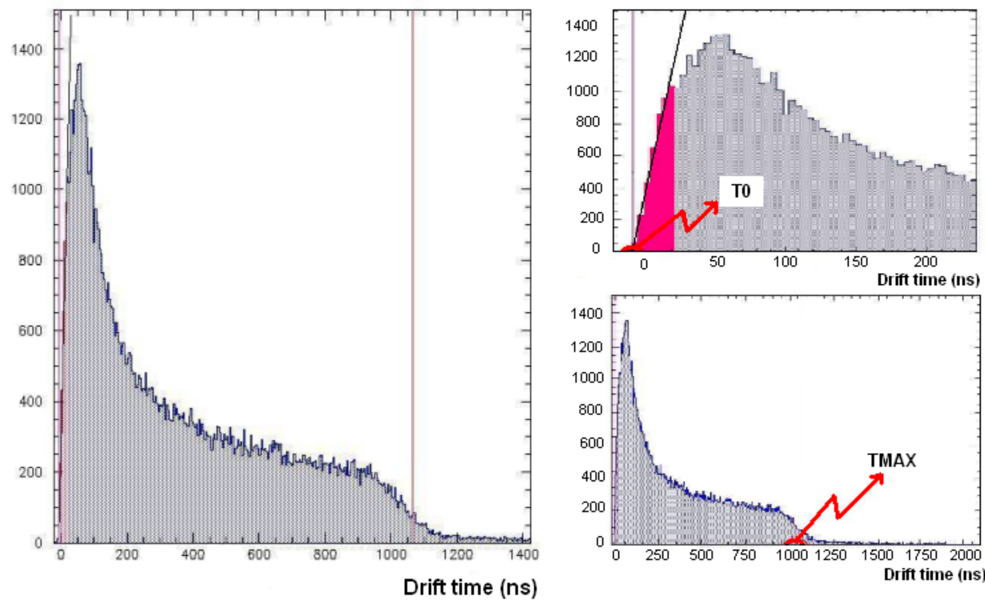


Figure 4.11: (left) Drift time distribution for region 3. (top right) Determination of $T_0$. (bottom right) Determination of $T_{max}$.

The final step of the calibration consists of the fine-tuning of the calibration parameters obtained from the above procedure. This is achieved by fitting the residuals vs drift time distribution. The way of understanding the resolution provided by tracking and so the quality of the DC calibration is through the distribution of residuals as a function of the run number. Figure 4.13 shows the final residuals obtained for superlayer 2 (all sectors) for

[11]The drift velocity function is defined as the ratio between the CALCDOCA of a particle track to the drift time.

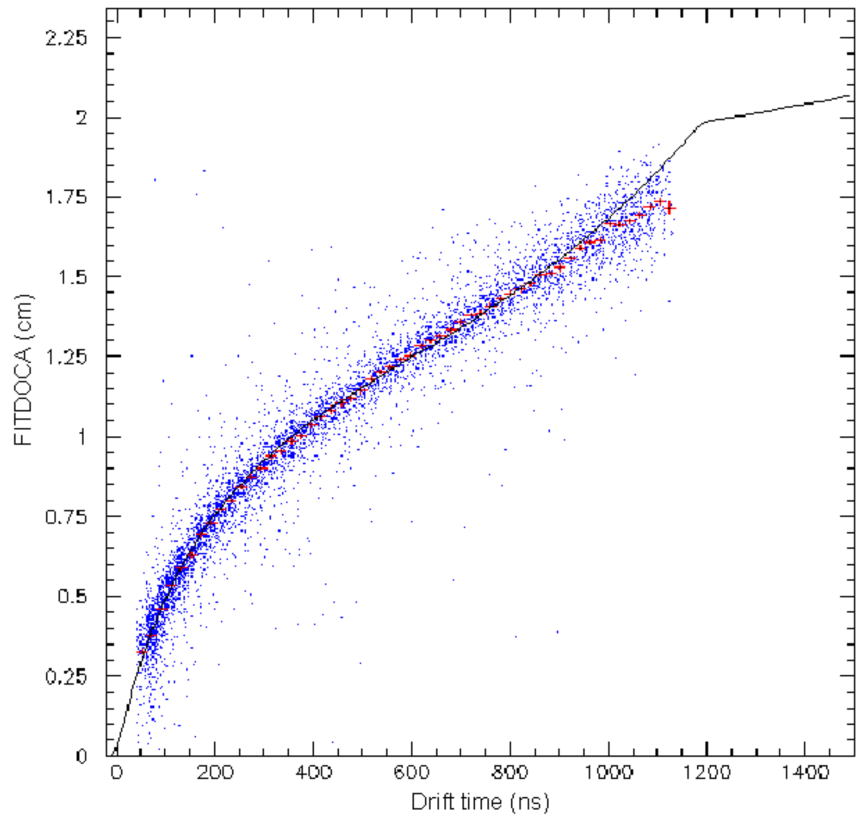


Figure 4.12: An example of the relation between FITDOCA and the drift time. Blue points represent the FITDOCA vs drift time distribution produced from CLAS data. The black solid line is the fit to the red crosses which represent a profile histogram of the blue points.

the whole g13b run period. Worthy of mention is the fact that all the residuals in g13 after the DC calibration were left to be roughly below 100 $\mu$m which is equivalent to 0.01 cm.

### 4.5.3 Start Counter

The start counter (ST) is the first subsystem triggered by a hadronic event produced in the target. Based on a coincidence with the tagger, the start counter is used to determine (at the level of data processing) which photon bunch was responsible for generating a hadronic reaction in the target[12]. Given that the photon bunches have the same 2 ns time structure as the electron bunches, the tagger-ST coincidence must be determined within less than $\pm 2$ ns.

[12]At the level of data analysis, the determination of which photon, within a specific bunch, was the most likely for having produced the reaction is explained in section 5.9.

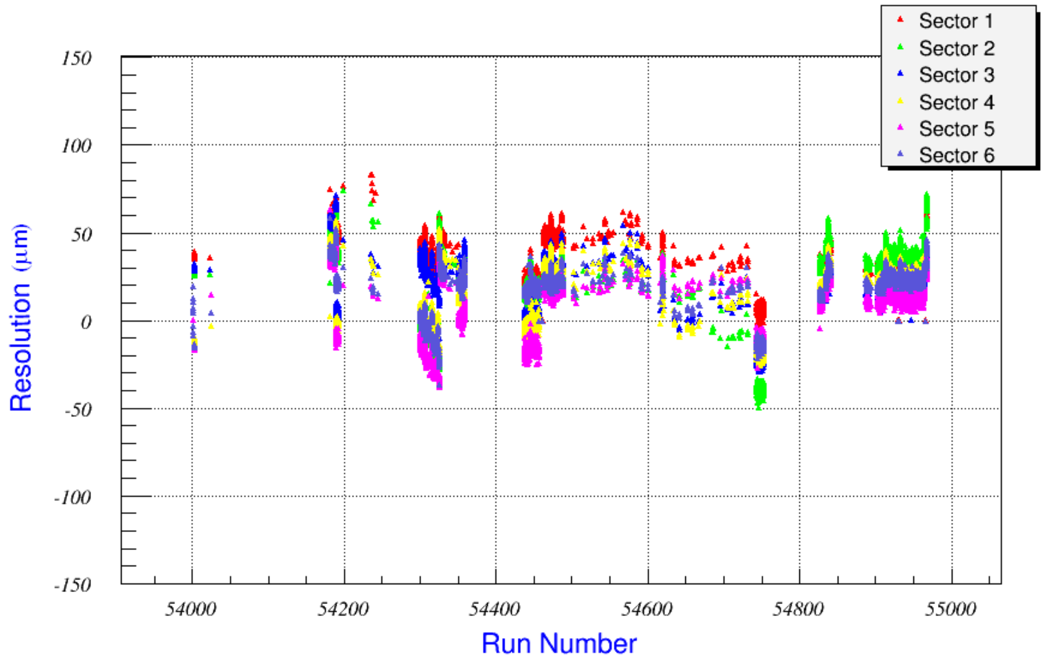


Figure 4.13: Residuals (superlayer 2, all sectors) as a function of the run number for the g13b period. Notice the residuals are roughly below 100 $\mu$m.

A basic layout of the start counter is shown in Figure 4.14. The start counter, centered about 10 cm around the target cell, consists of 24 scintillator paddles equally distributed into six identical sectors and coupled to an acrylic light guide. Each scintillator, 29 mm wide and 2.15 mm thick, constitutes a two-piece structure: a leg and a nose. The leg is the straight section of the paddle 502 mm in length; the nose is the semi-triangular section increasing the forward-angle coverage. The length of the nose paddles in each sector varies azimuthally. The two outer paddles are 30 mm long while the middle paddles are 93 mm long: 52 mm for the rectangular section and 41 mm for the truncated triangular section [66].

The efficiency of the start counter paddles for detection of charged particles is close to 100%. The time resolution varies between 292±1 ps (for leg paddles) and 324±2 ps (for nose paddles). These resolutions are sufficient to differentiate in time between neighboring photon bunches [66].

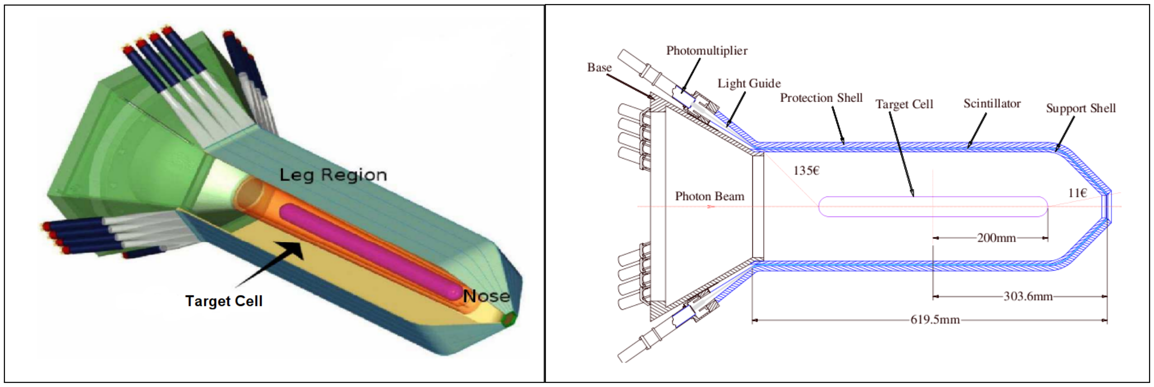


(a) (b)

Figure 4.14: Start counter: (a) Schematic view of the start counter showing the leg and nose regions. (b) Cross-sectional view.

### 4.5.4 Time-of-Flight System

The time-of-flight system (TOF) is used to determine the time it takes a charged particle to traverse CLAS (from the interaction vertex in the target to the TOF counters). Combining this timing information with tracking information allows one to determine the velocity of final-state particles inside the CLAS detector and, consequently, to reconstruct the mass of the particles [67].

The TOF system is a six-sector arrangement with double-ended scintillators located between the Cherenkov counters and the electromagnetic calorimeter; it covers the CLAS detector in the entire operational azimuthal region with a $\theta$ range between 8° and 142°. A diagram of a TOF sector is shown in Figure 4.15. Each TOF sector consists of 57 scintillator paddles distributed over 4 panels[13]. The scintillators all have the same thickness, roughly 5.1 cm, but with a width and length that vary according to the polar-angle location: forward paddles ($\theta < 45°$) are 15 cm wide and 32-376 cm long, while large-angle paddles ($45° < \theta < 142°$) are 22 cm wide and 371-445 cm long. The time resolution of the TOF counters varies between 60-160 ps for the forward counters and between 100-160 ps for the large-angle counters [66].

[13]Due to space limitations, sectors 3, 5, and 6 have apportioned only 56 scintillator paddles.

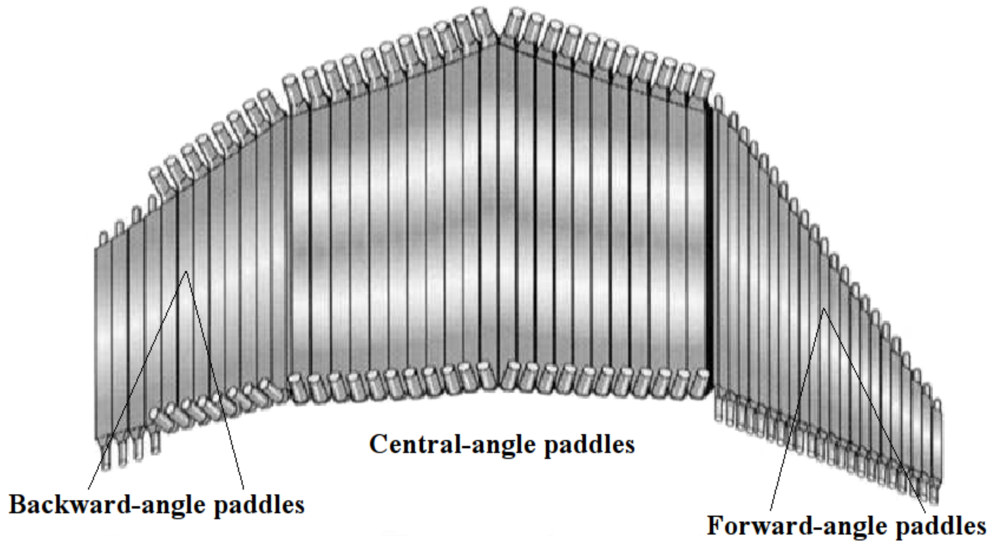


Figure 4.15: Time-of-flight system for a particular sector showing 56 paddles distributed into backward angles (12 paddles), central angles (22 paddles), and forward angles (22 paddles).

### 4.5.5 Cherenkov Counters

The Cherenkov counters (CC) are used in electroproduction experiments to separate electrons from pions and to trigger on electrons. This system is usually not used in photoproduction experiments since no lepton-meson separation is required.

The Cherenkov counters are positioned in the forward direction right after the outer DC region and consist of six sectors covering polar angles $\theta$ up to 45°. Each region is divided into 18 $\theta$-segments, with each segment separated into two symmetric modules containing a Cherenkov radiator gas, perfluorobutane ($C_4F_{10}$). This makes a total of 36 modules per sector [67]. In a module, the Cherenkov radiation is transported using shaped-mirrors, and gathered in Winston light collectors located behind the torus magnet coils. This collector location accounts for the maximum angular coverage of 45°. The gas filling the modules has an index of refraction of 1.00153, which results in a high photon yield and a high momentum radiation threshold which prevents pions from emitting Cherenkov light in the module. The electron efficiency detection within the fiducial acceptance is very close to 100% [68].

### 4.5.6 Electromagnetic Calorimeter

The forward Electromagnetic Calorimeter (EC) has three main purposes in CLAS: detection and triggering of electrons at energies above 0.5 GeV, detection of photons at energies above 0.2 GeV (for Deeply Virtual Compton Scattering (DVCS) or reconstruction of neutral mesons like the $\pi^0$ and the $\eta$), and detection of neutrons. For the work presented in this thesis, the calorimeter plays a key role since the complete identification of the reaction channel of interest requires the detection of a neutron in the final state.

At the typical energies handled in CLAS, the detection of neutral particles (photons and neutrons) is carried out using thick samples of high-$Z$ materials which enhance the probability of interaction. The interaction of these high-energy neutral particles with the high-$Z$ material results in the production of showers of particles (either electromagnetic or hadronic). The detection of those showers permits the reconstruction of the original photon or neutron that generated them. Therefore, the detection of high-energy neutrals must include the presence of both high-$Z$ materials (to produce the showers) and scintillators (to measure position, energy, and timing of the showers). This is the main idea behind the design and functioning of a sampling calorimeter. The CLAS electromagnetic sampling calorimeter [69] consists of six sectors distributed azimuthally according to the CLAS geometry and covering only the forward-angle region ($8 < \theta < 45°$). Each sector contains a triangular EC module, $\sim 47.5$ cm thick, formed by 39 alternating layers of lead ($Z = 82$) and scintillator sheets. Each layer has a lead sheet 2 mm thick and a plastic scintillator 10 mm thick. For readout purposes, each scintillator is divided into 36 strips parallel to one side of the triangle, each approximately 100 mm wide with lengths varying between 0.15 and 4.2 m. The strips are rotated 120° in each successive layer such that three succesive layers form a group of U, V, and W "views" (Figure 4.16, panel (a)) for a total of 13 of these groups. To improve hadron identification, the groups are separated into inner and outer stacks, containing 5 and 8 groups, respectively.

The reconstruction of a hit requires energy deposition in all three views (U, V, W) of the inner and/or outer stacks of an EC module. Groups of fired scintillator strips are identified in each view. The groups from each view (120° out of phase) intersect, and the corresponding

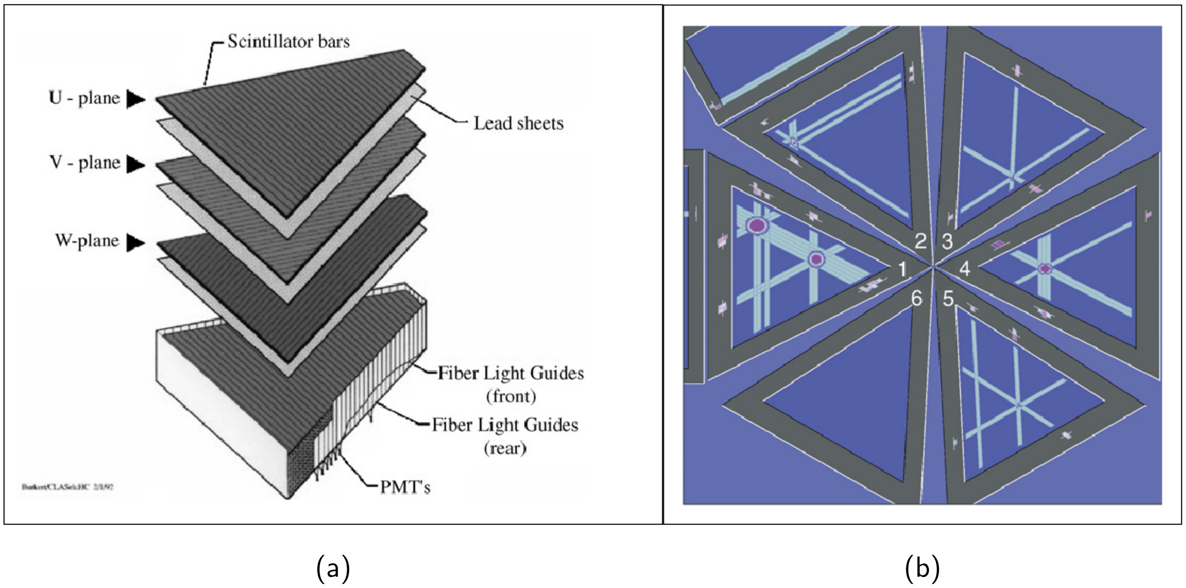


Figure 4.16: Forward Electromagnetic Calorimeter: (a) One of the six CLAS EC modules showing the U, V, W views. (b) Example of an event reconstruction in EC where five sectors are hit.

crossing points represent the "hit" (Figure 4.16, panel (b)). This procedure allows the hit position to be found in the plane containing the views ($x$-$y$ plane) with a resolution not greater than 3 cm, but does not give much information about the hit coordinate along the axis perpendicular to that plane ($z$-axis). For calibration purposes, the $z$-value is usually taken as the average length of the calorimeter. For analysis purposes, this $z$-value has to be corrected, as shown later in Section 5.6.2.1. The path length from the hit position to the readout edge is used to determine the energy and the time of the hit. For neutrons, in particular, the detection efficiency rises linearly from 5% at 0.6 GeV/c to 50% at 1.8 GeV/c, and levels off toward a plateau value of ∼55% for neutrons with momenta above 2.0 GeV/c. The discrimination between photons and neutrons for momenta up to 2.5 GeV/c is made by means of time-of-flight measurements. In this case, the time-of-flight resolution associated with the EC is about 1 ns [67].

### 4.5.7 Large Angle Calorimeter

The Large Angle Calorimeter (LAC) is a complement to the CLAS forward Electromagnetic Calorimeter mentioned above. The LAC covers only the first two CLAS sectors (-30° $<\phi<$90°) in a $\theta$ range between 45° and 75°. The LAC design is similar to the electromagnetic calorimeter. Each sector contains a module, ∼56 cm thick, with 33 rectangular layers of lead and plastic scintillator split into inner (17 layers) and outer (16 layers) stacks with individual light readouts; each layer is composed of a lead foil 0.2 cm thick and a scintillator bar 1.5 cm thick. At momenta higher than 0.5 GeV/c$^2$, neutron detection efficiencies greater than 30% can be obtained with a time resolution as low as 260 ps [67, 70].

## 4.6 Target Cell

Unpolarized targets used for photoproduction experiments in CLAS consist of cylindrical cells made of kapton with thin aluminum windows. They are designed to hold mainly liquid hydrogen or deuterium which is maintained by means of a cryogenic system.

Most of the g13 period was run using a liquid deuterium $LD_2$ target[14] positioned with its center 20 cm upstream of the nominal CLAS center to maximize acceptance. The target was 40 cm in length with a maximum diameter of 4 cm and a density of 0.1625 g/cm$^3$ [48]. A schematic view of the target utilized for the g13 run period is shown in Figure 4.17.

Figure 4.17: g13 target: a 40-cm-long liquid deuterium target.

[14] For purposes of testing and detector alignment, about 1 billion triggers were taken with a $LH_2$ target.

## 4.7 Data Acquisition Rate and Trigger

Physics events were recorded in g13 at a rate of about 10 kHz (a very high rate compared to earlier run periods), with a dead time around 15%. Approximately 50 billion events were collected during the g13 run period, 20 billion in g13a and 30 billion in g13b, resulting in a 130 TB set of raw data [57].

In g13a, the trigger was set to record charged-track events with a coincidence between ST and TOF systems in two of the six CLAS sectors. In g13b, the coincidence between the ST and TOF was required in at least one of the sectors. These trigger requirements were chosen to minimize the background from accidental detector hits, while maximizing the data acquisition rate for the desired physics events [57]. The photon trigger was not part of the g13 trigger.

## 4.8 Summary of g13 Running Conditions

As mentioned above, the g13 CLAS run period consisted of two parts: g13a and g13b. The former used circularly polarized photons; the latter used linearly polarized photons. The running conditions of each period are summarized in Table 4.1.

Table 4.1: Table summarizing the g13 running conditions.

| Running conditions | g13a | g13b |
|---|---|---|
| Electron beam current | $33 - 45$ nA | $5 - 12$ nA |
| Electron beam energy | 1.99 GeV and 2.65 GeV | $3.30 - 5.16$ GeV |
| Radiator | Gold foil ($10^{-4}$ r.l.) | Diamond ($3{\cdot}10^{-4}$ r.l.) |
| Tagged photon energy range | $0.3 - 2.5$ GeV | $1.1 - 2.3$ GeV |
| Photon polarization | Circular | Linear |
| Photon beam collimator width | 6.4 mm | 2 mm |
| Target | $LD_2$ | $LD_2$ |
| Target length | 40 cm | 40 cm |
| Target max. diameter | 4 cm | 4 cm |
| Target position | $-20$ cm | $-20$ cm |
| Main torus current | $-1500$ A | $-1500$ A |
| Trigger setting | Two-sector, no tagger | One-sector, no tagger |
| DAQ rate | $\sim 10$ kHz | $\sim 10$ kHz |
| Physics events | $\sim 20$ billion | $\sim 30$ billion |

# Chapter 5: Particle Reconstruction and Analysis

## 5.1 Overview

After the detector calibration stage, data were processed ("cooked") using the CLAS reconstruction and analysis package RECSIS [71]. Processing the data involves taking the original files, in BOS format [72], produced during the experiment by the various detector subsystems and creating new BOS files containing higher-level information (such as four-vectors) suitable for physics analysis[1].

The processed data were analyzed using the ROOTBEER (ROOT Bank Event Extraction Routine) package developed by Ken Livingston [73]. This package consists of a set of routines that allows one to convert CLAS BOS data to the more compact DST format and analyze them within a ROOT framework [74].

This chapter is aimed at describing in detail the analysis performed on the processed data to identify, in an exclusive manner, the quasi-free reaction associated with the channel

$$\gamma d \to K^+ \boxed{\Sigma^-}(p) \to K^+ \boxed{\pi^- n}(p),$$

where the box represents the decaying particle ($\Sigma^-$) and the corresponding decay products of it ($\pi^-$ and $n$), and $(p)$ is a spectator proton. The data utilized for this analysis correspond to the second part of the g13 run period (g13b), which made use of a liquid-deuterium target, a linearly polarized photon beam, and had a negative polarity for the torus magnet (*i.e.*, a field in which negative particles were outbending). The running conditions for g13b were described in detail in Chapter 4. The data were taken with six different photon energy settings: 1.1-1.3, 1.3-1.5, 1.5-1.7, 1.7-1.9, 1.9-2.1, and 2.1-2.3 GeV. These settings were produced using unpolarized electron beams with energies ranging between 3.3 GeV (for the lower photon energy settings) and 5.2 GeV (for the higher photon energy settings). The strategy and cuts applied to each photon energy setting were similar; therefore, only the analysis of one particular bin (2.1-2.3 GeV) is described in the following sections.

[1] The information is organized into BOS Banks (EVNT, TAGR, MVRT, ECPB, among others). These banks will be mentioned throughout this chapter.

## 5.2 Event Reconstruction

The $\Sigma^-$ produced in the reaction $\gamma d \to K^+\Sigma^-(p)$ decays into $n\pi^-$ with a branching ratio of 99.8% [75]. In order to carry out an exclusive analysis of this reaction, it is necessary to detect all particles but one. In the case of a quasi-free reaction on the neutron, the spectator proton is a low-momentum particle, making it hard to detect since CLAS was designed to track charged particles with momenta above 200 MeV/c [76]. One thus needs to detect the $\Sigma^-$ decay products ($\pi^-$ and $n$) and the $K^+$. For the spectator proton ($p$) and the $\Sigma^-$, the missing mass MM($K^+n\pi^-$) and the invariant mass M($n\pi^-$) are reconstructed.

## 5.3 Data Exclusion

To reduce the systematic uncertainty, some parts of the data[2] set were removed from the analysis. The selection criteria were based on the overall stability of the systems and the quality of the calibration of the CLAS subsystems. Some runs taken for diagnostic purposes rather than for physics analysis purposes also had different running conditions and were therefore excluded from the analysis.

### 5.3.1 Excluded Runs

A list of good runs for g13b data analysis was defined based on a combination of information from the logbook comments recorded during the data taking, the run list compiled using the database, and the runlist obtained from the analysis of the EPIC bank information using a single pion channel ($\gamma n \to p\pi^-$). In the list, which can be found in Ref. [77], the criteria for labeling runs as "bad" included unstable beam conditions, runs taken for normalization purposes, runs with unknown radiator or unknown polarization plane, wrong position of the coherent edge and trigger problems.

[2] The CLAS data are usually structured in terms of runs. In the case of g13b, each corresponded to about two hours of data taking.

### 5.3.2 Excluded Files

Files to be excluded from the analysis were selected based on the quality of the DC calibration. In g13b, each run consists of 40 files on average. Within particular runs, it was found that there were files showing very large residuals (residuals are discussed in Section 4.5.2) compared to those for the rest of the files comprising the run. This was observed mostly with files taken either at the beginning or at the end of those particular runs. Given that the DC calibration constants are handled on a run-by-run basis, recovering those problematic files (by recalibration of DC) for a particular run would result in calibration constants unsuitable for the other files of the run. Therefore, instead of losing a complete run, the files with relatively large residuals (within a run) were discarded from the analysis. The study was done run by run and the list of 58 excluded files in g13b is shown in Table 5.1.

Table 5.1: List of runs that have some files with very large residuals. Such bad files were excluded from the analysis.

| Run No. | Bad files No. | Run No. | Bad files No. | Run No. | Bad files No. |
|---|---|---|---|---|---|
| 54072 | A15 | 54453 | A32 | 54734 | A45 |
| 54091 | A20 | 54463 | A38 | 54747 | A41 |
| 54101 | A04, A05 | 54507 | A42 | 54764 | A48 |
| 54102 | A02, A09, A12 | 54513 | A21 | 54798 | A44 |
| 54127 | A20 | 54525 | A33, A34, A35 | 54811 | A38 |
| 54182 | A43 | 54538 | A23 | 54818 | A44 |
| 54198 | A43 | 54564 | A29 | 54915 | A01 |
| 54221 | A42 | 54596 | A22 | 54941 | A42 |
| 54222 | A42 | 54607 | A40 | 54972 | A44 |
| 54287 | A31 | 54617 | A03 | 54973 | A42 |
| 54291 | A26 | 54629 | A13 | 55047 | A41 |
| 54295 | A39 | 54636 | A55 | 55054 | A30 |
| 54296 | A15 | 54638 | A53 | 55068 | A40 |
| 54313 | A42 | 54645 | A16 | 55073 | A47 |
| 54334 | A03 | 54652 | A45 | 55107 | A45 |
| 54360 | A43 | 54690 | A44 | 55115 | A50 |
| 54399 | A17 | 54703 | A14 | 55137 | A42 |
| 54452 | A54 | 54720 | A45 | | |

### 5.3.3 Excluded Events

During the g13 experiment, there were some periods in which the beam delivered by the accelerator showed unstable conditions. Given the short duration of these periods (normally no more than a few minutes), the data acquisition system was not interrupted and the bad-quality-beam events were being recorded. In order to ensure a proper determination of the photon beam asymmetry, which could be affected by the collimation of an unstable beam, the events taken during such periods were cut out from the analysis using the standard *sync* utility package [78]. In this routine, the intervals containing beam trips are determined by taking the first interval between scaler events injected into the data stream of each file as the reference by assuming it to contain no beam trips. Intervals in a data file with a number of events different from that of the reference interval are associated with unstable-beam events and are therefore removed from the analysis[3]. In this analysis, about 18% of the total number of events were rejected by the beam-trip cut.

## 5.4 Data Reduction

The huge amount of events collected during the g13 run period makes it convenient to filter (skim) the data as an intermediate step. The two filters used in this analysis are discussed in the next subsections. The first one was produced at the level of "cooking". The other one was utilized as part of the analysis.

### 5.4.1 The First-Level Skim

During the processing ("cooking") stage, various filters were created in parallel according to three event topologies: at least $1pos1neg1neu$, at least $2pos1neg$, and at least $2pos2neg$. The first-level filter used for this analysis only included events with at least one positively charged track, one negatively charged track, and one neutral track ($1pos1neg1neu$). This reduced the data to roughly 6% of its original size. Using these filtered data files significantly reduced the CPU and disk space requirements for the analysis.

[3]In case the first scaler interval contained a beam trip, this routine failed to correctly determine the bad scaler intervals. This issue was corrected by Paul Mattione with the "tripfixer" routine [79].

### 5.4.2 The Second-Level Skim

From the general $1pos1neg1neu$ skim (after exclusion of bad runs, bad files, and beam trips), only events with at least three good entries in the EVNT bank (at least one positive, one negative, and one neutral) and at least one good entry in the TAGR bank were accepted. Good entries were selected based on the charge $q$ and the quality flags in the EVNT bank. For charged tracks, the conditions $|q|$ >0, DCstat>0, SCstat>0, and Status>0 were imposed. For neutrals, defined as clusters in the calorimeter that do not match a charged track in the drift chambers, the flags $q$=0, DCstat=0, ECstat>0, and Status>0 were required.

The strategy in the analysis was to initially accept as many candidate events as possible by assuming during skimming all good positives to be kaons ($K^+$), all good negatives to be pions ($\pi^-$), and all good neutrals to be neutrons ($n$). This means that the 4-momentum vector for each particle was calculated using the momentum measured by the drift chambers and the PDG mass [75], not the mass obtained from the time-of-flight that is found in the EVNT bank. In this scheme, all possible track combinations for the $\gamma d \to K^+\Sigma^-(p)$ reaction (including all photons in the TAGR bank) were taken into account. The number of combinations was constrained by applying loose cuts on the vertex time of each track, the MM($K^+n\pi^-$), and M($n\pi^-$) in the following way:

- Track vertex times $T_{K^+}$ and $T_{\pi^-}$ were determined (see procedure in Section 5.9) for all $K^+$and $\pi^-$ candidates.
- Photon vertex times $T_\gamma$ were determined (see procedure in Section 5.9) for each good photon in the TAGR bank[4].
- All $\gamma, K^+$ combinations with $\Delta T_{\gamma,K^+} = |T_\gamma - T_{K^+}| > 3.0$ ns were rejected.
- All $K^+, \pi^-$ combinations with $|T_{K^+} - T_{\pi^-}| > 6.0$ ns were rejected.
- Remaining photons, kaons, and pions were combined with all the neutrons into sets[5] with missing mass MM($K^+n\pi^-$) and invariant mass M($n\pi^-$).

[4]Good photons in the TAGR bank correspond to hits with status = 7 or 15. Status 7 means that one unambiguous hit was reconstructed in the tagger; status 15 means more than one unambiguous hit was reconstructed.

[5]Here, the momenta of kaons and pions were processed through the momentum and energy-loss correction procedures described in Section 5.7.

- A $5\sigma$ cut on the MM($K^+ n\pi^-$) was applied (0.7< $MM$ <1.4 GeV/c$^2$).

- A $5\sigma$ cut on the M($n\pi^-$) was applied (1.160< $M$ <1.234 GeV/c$^2$).

The effect of these cuts on the invariant mass, plotted for the sum of all combinations, is shown in Figure 5.1. The surviving events were saved into a new skim file which reduced the 333 MB first-level file to about 15 MB. The analysis steps described below are applied to this second-level skim file. As a reference, all the analysis cuts along with the events remaining after each cut are summarized in Table 5.3 at the end of this chapter.

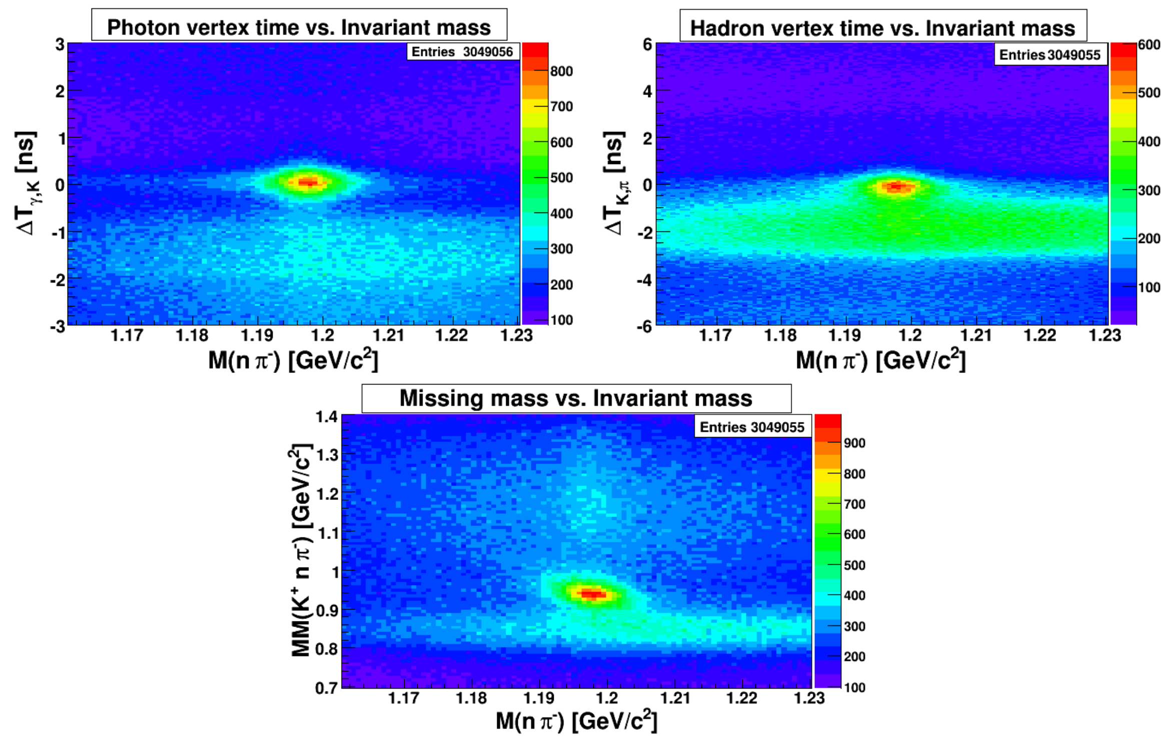


Figure 5.1: Effect of $\Delta T_{\gamma,K^+}$ (top left), $\Delta T_{K^+,\pi^-}$ (top right), and $MM(K^+n\pi^-)$ (bottom) cuts on the invariant mass $M(n\pi^-)$ in the initial skim. As can be seen, the cuts applied are conservative enough to avoid loss of good events.

## 5.5 Charged Particle Identification

The identification of a charged track in CLAS is based upon four fundamental quantities: momentum $p$, charge $q$, path length $l$, and time $T$. The momentum is determined from the radius of curvature of the reconstructed track when passing through the toroidal magnetic field, implemented in the tracking in the form of a field map. The sign of the charge is deduced from the track deflection in the field. The path is found by intersecting the track recorded by the drift chambers (DC) with a series of planes related to the beam line and to the other subsystems (ST, TOF, EC, LAC), thus defining various path lengths $l_{ST}$, $l_{TOF}$, $l_{EC}$, and $l_{LAC}$. The times for each subsystem ($T_{Tagger}$, $T_{ST}$, $T_{TOF}$, $T_{EC}$, and $T_{LAC}$) are all relative quantities measured with respect to an arbitrary reference time without physical meaning. From the above information, derived quantities such as the particle's velocity and mass can be determined.

### 5.5.1 Velocity

The velocity $c\beta_{meas}$ is calculated from a combination of tracking ($l$) and timing ($T$) information according to the relation [6]

$$c\beta_{meas} = \frac{l}{T - T_{ev}} \tag{5.1}$$

where $c$ is the speed of light and $T_{ev}$ is the time of the particle at the event vertex, which is related to the event start time[7] by an arbitrary offset. Figure 5.2 shows the (EVNT) $\beta$ distribution (from Equation 5.1) as a function of momentum for negative and positive particles at an early stage of the analysis. Dashed lines correspond to $\beta_{calc}$ calculated from the momentum and PDG mass [75]. On the left plot, the upper dashed line corresponds to $\pi^-$ and the lower one to $K^-$. On the right plot, the upper line is for $\pi^+$, the middle for $K^+$, and the lower for protons. The crossing bands seen in both plots arise from out-of-time particles from different beam buckets.

### 5.5.2 Mass

A particle's rest mass $M_{meas}$ in the EVNT bank is computed from its reconstructed momentum $p$ and reconstructed velocity $c\beta_{meas}$ following the expression:

[6] In the scheme of the EVNT bank, $\beta_{meas}$ is determined from the path length and time measured by the TOF subsystem.

[7] $T_{ev}$ is determined by the SEB (Simple Event Builder of RECSIS).

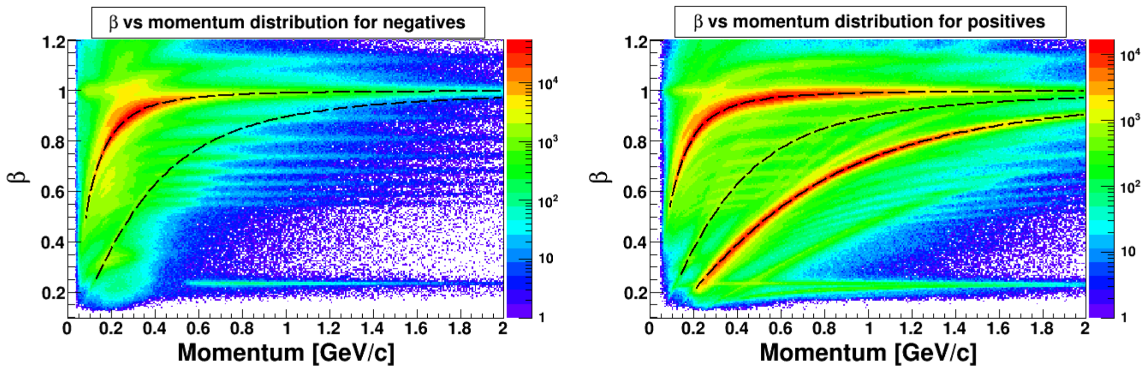


Figure 5.2: Measured $\beta_{meas}$ as a function of momentum for negatives (a) and positives (b). These plots were taken from an early stage of the analysis and show events containing at least one positive, one negative, and one neutral particle in the EVNT bank. Explanation in the text.

$$M^2_{meas} = \left(\frac{1}{\beta^2_{meas}} - 1\right) p^2 \tag{5.2}$$

Figure 5.3 shows the mass-squared distribution from Equation 5.2 for negatively and positively charged particles produced at a very early stage of the analysis. The main peak in the left plot corresponds to the $\pi^-$; the small peak observed in the right plot at about 0.25 (GeV/c$^2$)$^2$ represents $K^+$candidates. Since the yields for pions are much higher than for kaons, the $K^-$ contamination to the $\pi^-$ peak is small, as can be seen in Figure 5.3(a) near 0.24 (GeV/c$^2$)$^2$. In contrast, $K^+$identification is more complicated, since both the $\pi^+$ and proton distributions extend under the kaon peak (as seen in Figure 5.3(b)), which could lead to a significant amount of pions being misidentified as kaons. This is, in particular, an issue at higher momenta (>1.5 GeV/c), where $\beta$ approaches unity and the TOF resolution is no longer sufficient for $\pi/K$ discrimination.

### 5.5.3 $\pi^-$ Identification

The $\pi^-$ was identified from momentum-dependent $\Delta\beta$ cuts. In this case, $\Delta\beta$ was determined according to the relation:

$$\Delta\beta = \beta_{meas} - \beta_{calc} = \beta_{meas} - \frac{p}{\sqrt{p^2 + m^2}} \tag{5.3}$$

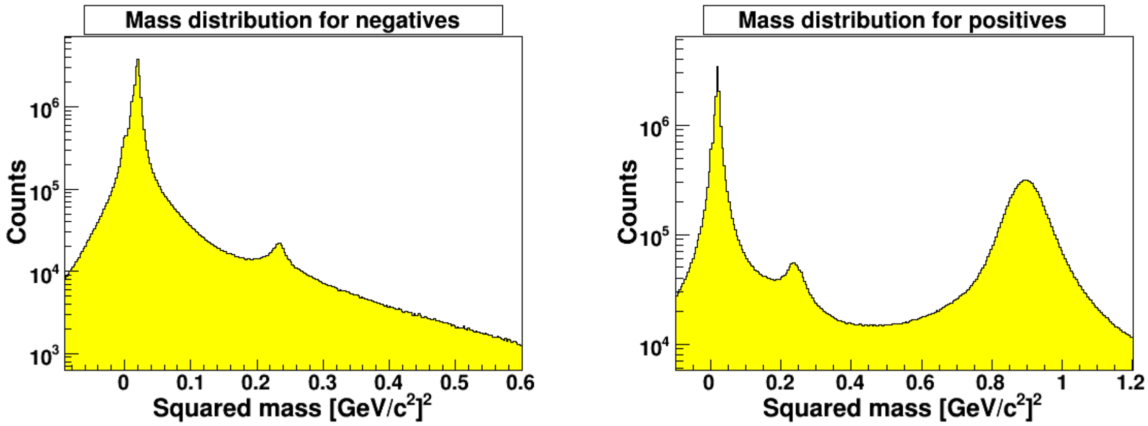


Figure 5.3: Mass-squared distribution for negatives (left) and positives (right). The plots show events containing at least one positive, one negative, and one neutral with good flags in the EVNT bank. Note the logarithmic scale on the vertical axis on both plots and the different mass ranges on the horizontal axis.

where $\beta_{meas}$ is the particle's velocity reconstructed in the EVNT bank (Equation 5.1) and $\beta_{calc}$ is the particle's velocity calculated from the measured momentum $p$ and the PDG mass $m$ for a charged pion [75].

The cuts on $\Delta\beta$ were determined by slicing the $\Delta\beta$ vs. $p$ distribution into 20 MeV/c bins along the momentum axis. Each slice was fitted with a Gaussian function. The fitting parameters (mean and sigma) associated with each slice were then used to construct $\pm 3\sigma$ functions around the $\Delta\beta$ mean value. An eighth-order polynomial fit (for $\pi^-$ momentum below 1.2 GeV/c) and a zeroth-order polynomial fit (for $\pi^-$ momentum greater than 1.2 GeV/c) performed on each of the $\pm 3\sigma$ functions defines the functional momentum-dependent form of the $\Delta\beta$ cuts used for $\pi^-$ identification. The $\Delta\beta$ vs. $p$ distribution, along with the corresponding mean and sigma values, is shown in Figure 5.4. Since, neglecting non-gaussian tails, the $\pm 3\sigma$ cut contains 99.7% of the events expected to be negative pions, the events beyond this limit were neglected as they had small impact on the overall statistics. The stability of these $\Delta\beta$ cuts throughout the analysis can be observed in Figure 5.5 where the $\Delta\beta$ vs. $p$ distribution is plotted at an initial stage of the analysis with just the initial skimming cut applied, and at a final stage after applying all of the cuts except the $\Delta\beta_{\pi^-}$ cut. As can be seen, the fit parameter (sigma) does not vary significantly between the two stages of the analysis. Similarly, the effectiveness of such cuts can be appreciated in Figure 5.6 where the correlation of the invariant mass, the missing mass, and the missing momentum with $\Delta\beta$ is presented. The $\Delta\beta$ cuts lie between -0.050 and 0.050, and clearly improve the selection of $K^+\Sigma^-$ events.

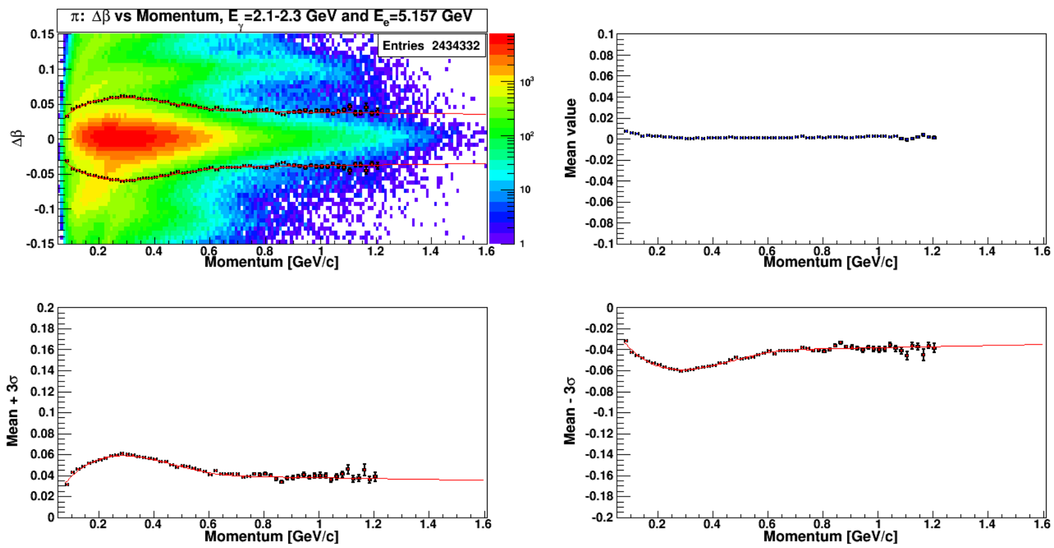


Figure 5.4: (Top left) $\Delta\beta$ distribution as a function of $\pi^-$ momentum. The red lines define the $\pm3\sigma$ momentum-dependent functions used to select $\pi^-$ candidates. (Top right) Mean value associated with the momentum-dependent functions. (Bottom left and right) $+3\sigma$ and $-3\sigma$ momentum-dependent functions. Explanation given in the text.

The final distribution for mass, momentum, polar angle, and azimuthal angle for the $\pi^-$ are presented in Figure 5.7. All the cuts, including background subtraction, are applied in this plot.

### 5.5.4 $K^+$ Identification

As discussed in Section 5.5.2, the selection of $K^+$ is more complicated than for $\pi^-$ due to:

- events related to out-of-time particles leaking into the $K^+$ signal, and
- the large amount of in-time pions and protons contaminating the $K^+$ signal.

The former source is significantly reduced by the $\Delta\beta$ cuts applied to negative particles (see Section 5.5.3), and slightly improved through the use of cuts on the $|T_{K^+} - T_{\pi^-}|$ time

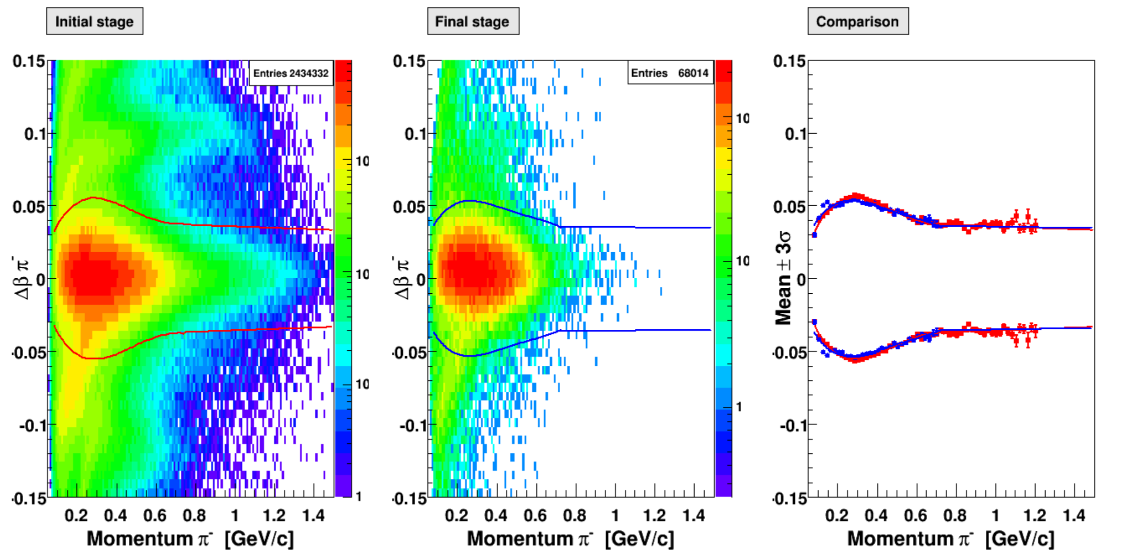


Figure 5.5: $\Delta\beta$ distribution as a function of $\pi^-$ momentum taken at two different stages of the analysis. On the left, the resulting distribution after applying only the cuts from the initial skimming is shown. In the middle, the distribution is shown (before background subtraction) after applying all the analysis cuts except the $\Delta\beta_{\pi^-}$ cut. The plot on the right compares the $\pm 3\sigma$ values obtained in both stages. The red and blue lines define the $\pm 3\sigma$ momentum-dependent functions.

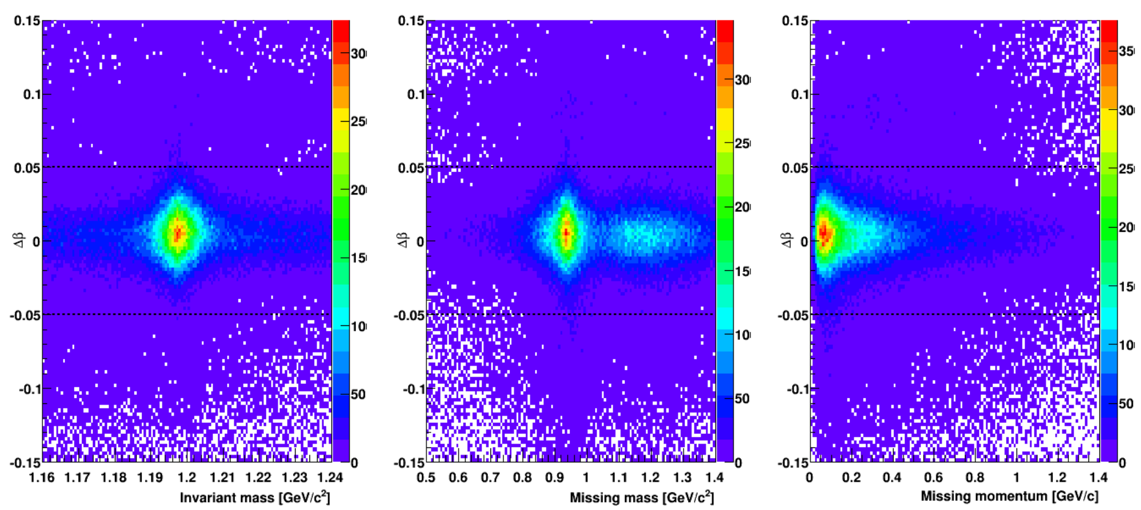


Figure 5.6: Correlation between $\Delta\beta_{\pi^-}$ and the distributions of the invariant mass $M(n\pi^-)$, the missing mass $MM(K^+n\pi^-)$, and the missing momentum. The $\Delta\beta$ cuts, which lie on average between $\pm 0.050$ (black dashed lines), help in cutting out background events without throwing out good events. The histograms were filled at a final stage of the analysis.

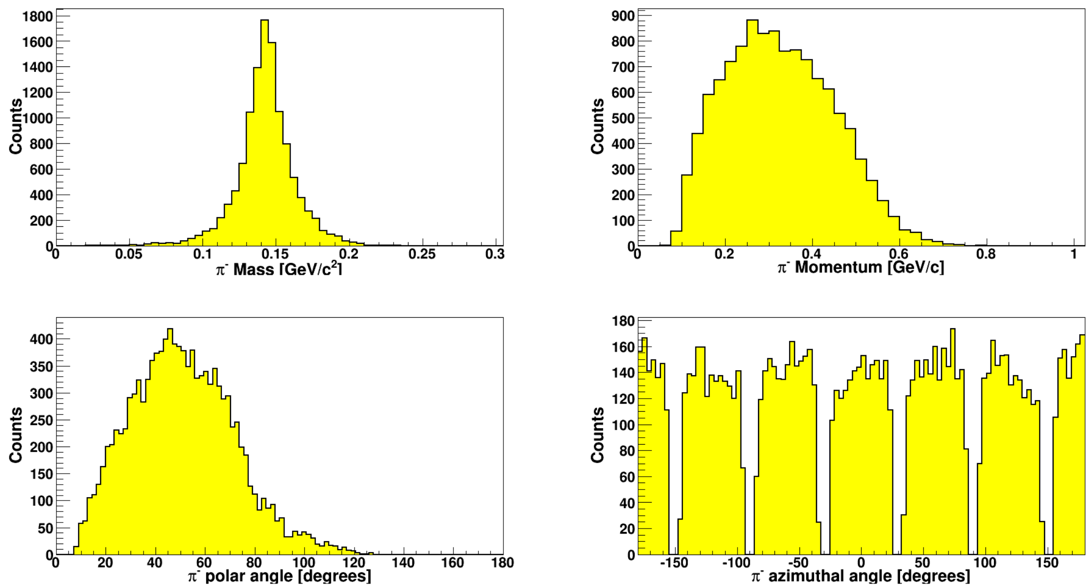


Figure 5.7: Mass, momentum, $\theta$, and $\phi$ distributions for the final $\pi^-$ sample after all the cuts are applied.

difference. The latter source is primarily suppressed by means of momentum-dependent cuts applied on the $\Delta\beta$ vs. $p$ distribution for positive particles. As a consequence of the TOF resolution, however, this cut fails at high-momentum values ($p >\sim 1.5$ GeV/c) when discriminating kaons from pions. This leaking of pions misidentified as kaons is dealt with in this analysis by defining a contour region within which the $K^+$sample is selected. Figure 5.8 shows (before applying any PID cut) the scenario for the $K^+$identification. The horizontal red lines represent the average region where the kaons lie; the two most prominent bands of out-of-time particles are delineated by polygons and the leaking of pions is delineated by an oval. The procedures for the $K^+$identification are explained in the following subsections.

#### 5.5.4.1 $|T_{K^+} - T_{\pi^-}|$ cuts

The out-of-time particles are predominantly pions coming from beam buckets that are different from the one that produced the event of interest. These appear as bands crossing through the $K^+$signal at momentum values below $\sim$1.2 GeV/c (see Figure 5.8). Although this contamination is greatly reduced after applying a $\Delta\beta$ cut on the $\pi^-$, there are still some events remaining. In order to have a cleaner $K^+$sample, one can study the events allocated

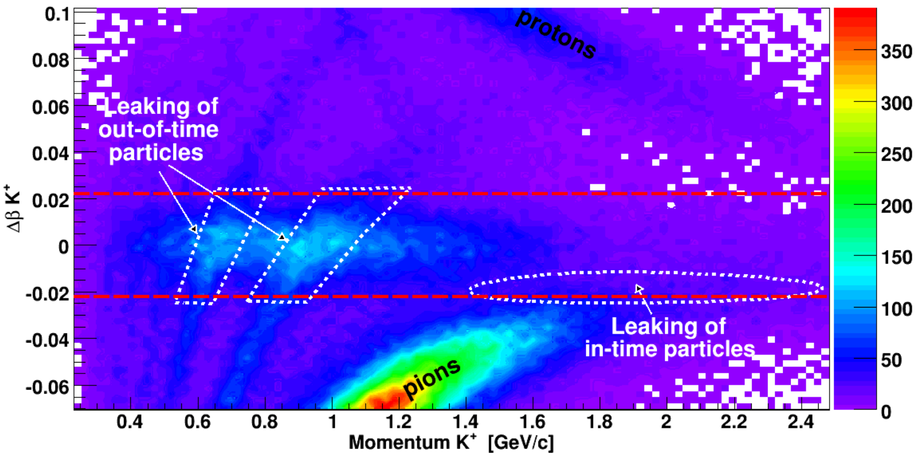


Figure 5.8: The scenario for $K^+$identification before applying any PID cut. Kaons are found, on average, in the region $\pm 0.025$ along the $\Delta\beta$ axis. Explanation given in the text.

within each one of the white dashed-line polygons defined in Figure 5.8. The top panel of Figure 5.9 corresponds to the leftmost polygon; the bottom panel, to the other one.

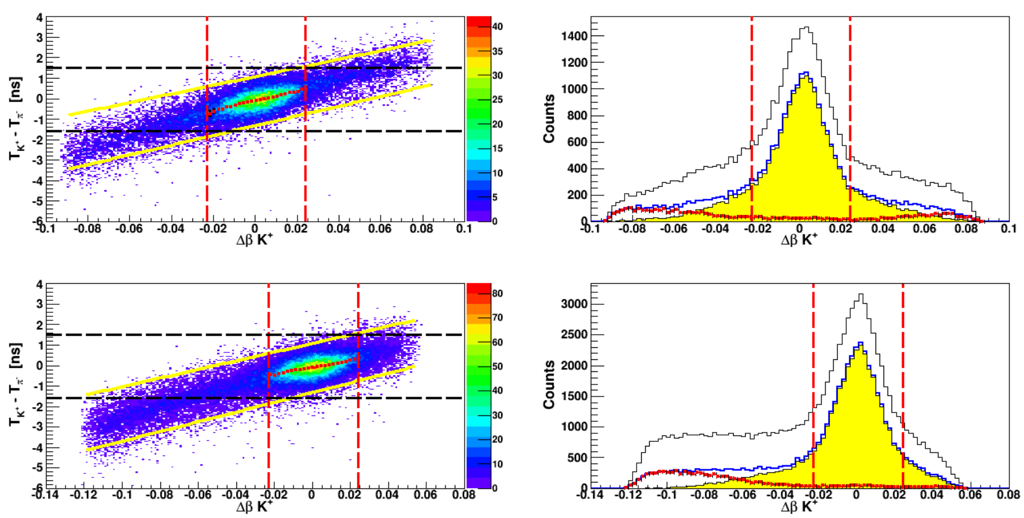


Figure 5.9: (left side) $|T_{K^+} - T_{\pi^-}|$ vs. $\Delta\beta$ distribution for out-of-time particles. (right side) $\Delta\beta$ distribution for out-of-time particles. The top panel corresponds to the leftmost polygon of out-of-time particles observed in Figure 5.8. The bottom panel coincides with the other polygon. Explanation is given in the text.

The plots on the left side show the track vertex time difference $|T_{K^+} - T_{\pi^-}|$ vs. $\Delta\beta_{K^+}$ distribution for the events remaining in each polygon after applying the $\Delta\beta_{\pi^-}$ cut. Events within the high-density region are mainly kaons while the rest are related to out-of-time pions. The distribution for each polygon was sliced along $\Delta\beta_{K^+}$ into equal-width bins and each slice was fitted with a gaussian function. In each case, a $\pm 3\sigma$ function (diagonal yellow lines) was defined using a first-order polynomial. Since both functions do not differ significantly from one another, we used a global cut on $|T_{K^+} - T_{\pi^-}|$ between -1.6 and +1.5 ns such that the amount of discarded kaons (those within the red vertical lines) is negligible. The local effect of this timing cut on the events in each polygon can be appreciated in the right-side plots of Figure 5.9. White, blue, and yellow histograms represent the $\Delta\beta_{K^+}$ distribution before any PID cut, after the $\Delta\beta_{\pi^-}$ cut, and after the $\Delta\beta_{\pi^-}$ plus the timing cut, respectively. The events rejected by the timing cut are represented by the red points; such events correspond mainly to out-of-time pions. The global impact of this timing cut on the general $K^+$ sample (the whole $p$ and $\Delta\beta_{K^+}$ range) is shown in Figure 5.10. Left and middle panels show the $\Delta\beta_{K^+}$ vs. $p$ distribution after applying the $\Delta\beta_{\pi^-}$ cut, and the $\Delta\beta_{\pi^-}$ plus the $|T_{K^+} - T_{\pi^-}|$ cuts respectively; the panel on the right shows the corresponding $\Delta\beta_{K^+}$ projections, in blue and yellow color, respectively. As can be noticed from Figures 5.9 and 5.10, this timing cut does not considerably affect the selection of $K^+$ within the region where most of them fall. What this cut does is to improve the shape of the $K^+$ sample such that subsequent distributions will be easier to fit, allowing a better set of variable-dependent cuts to be obtained. Therefore, the $|T_{K^+} - T_{\pi^-}|$ cut is to be understood in this analysis as a complement to the $\Delta\beta_{\pi^-}$ cut.

#### 5.5.4.2 $\Delta\beta_{K^+}$ cut and $K^+$ contour

The initial strategy to get rid of the pion and proton contamination (after the $\Delta\beta_{\pi^-}$ and $|T_{K^+} - T_{\pi^-}|$ cuts) was to follow a similar procedure as the one used for the $\pi^-$: momentum-dependent $\Delta\beta$ cuts. The bin size chosen for the projections was the same as that for pions (20 MeV/c). A single Gaussian function was used to fit the projections. The momentum-dependence of $\Delta\beta$ was obtained from a zeroth-order polynomial. The $\Delta\beta$ vs. $p$ distribution along with the corresponding mean and sigma distributions and polynomial functions used in the cuts are presented in Figure 5.11. Only events within $\pm 3\sigma$ were accepted. The procedure was tested at two different stages of the analysis in order to check if any correlation between

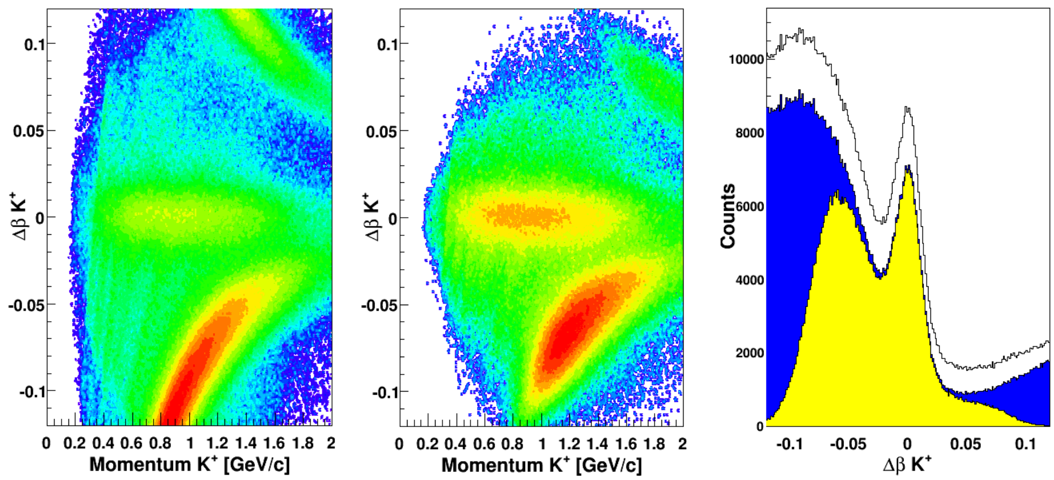


Figure 5.10: Global effect of the $|T_{K^+} - T_{\pi^-}|$ cut on the $K^+$sample. Explanation is given in the text.

the $\Delta\beta$ and the other cuts applied in the analysis were observed. Figure 5.12 shows that there is no a significant difference in the $3\sigma$ values extracted when the projections are fitted either right after applying only the initial skimming cut, or after applying all the cuts including background subtraction. The slight difference observed is due to the reduction (in the final stage) of out-of-time particles contaminating the $K^+$signal.

Any attempt to fit the $\Delta\beta_{K^+}$ vs. $p$ distribution leads to momentum-dependent functions (within $\pm 3\sigma$) that are not very successful in separating kaons from pions above momentum values of $\sim$1.2 GeV/c, since a non-negligible leaking of pions into the kaon sample is inherent to these functions. On the other hand, tighter functions (defined within $\pm 2\sigma$ or $\pm\sigma$) have the effect of throwing out too many good kaons. In order to improve the $K^+$selection for momentum values above $\sim$1.2 GeV/c, we defined a contour region greatly reducing the pion leakage. This contour is obtained from the correlation plot between the mass of positive particles and the time difference $|T_{K^+} - T_{\pi^-}|$. Figure 5.13 shows this correlation taken at two different stages of the analysis: after applying $\Delta\beta_{\pi^-}$ cuts (left panel) and after applying all the analysis cuts except the $\Delta\beta_{K^+}$ (middle panel). A time-dependent function was defined in each case by slicing the $T_{K^+} - T_{\pi^-}$ axis into equal-width bins and fitting them with a gaussian function. The resulting functions are linear and compared for each stage in the right side panel where it can be seen there is no a significant difference in both functions.

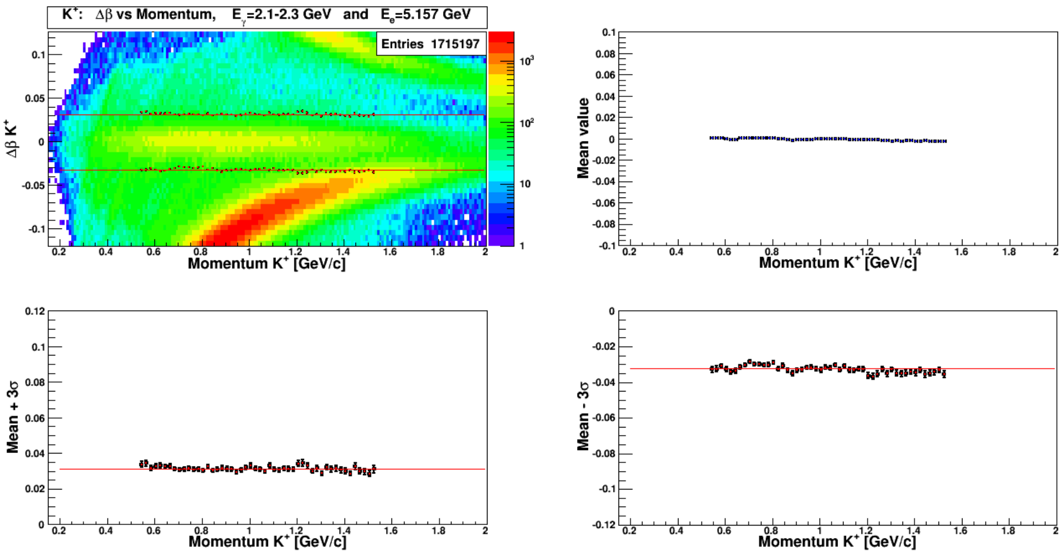


Figure 5.11: $\Delta\beta$ distribution split into 20-MeV bins of $K^+$momentum. The red lines define the $\pm 3\sigma$ momentum-dependent functions used to select $K^+$candidates. (Top right) Mean value and $\pm 3\sigma$ (Bottom left and right) momentum-dependent functions.

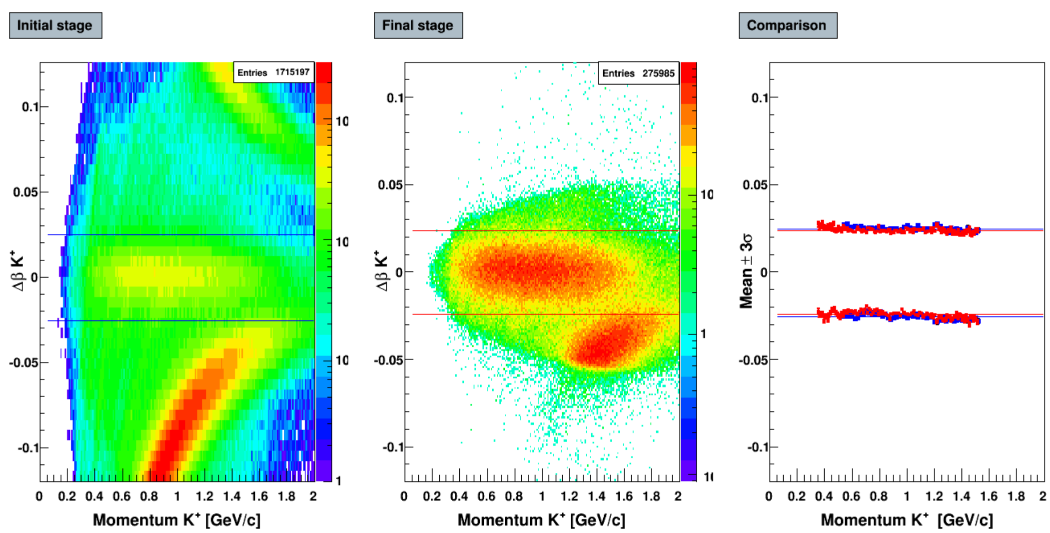


Figure 5.12: $\Delta\beta$ distribution as a function of $K^+$momentum taken at two different stages of the analysis. On the left, the resulting distribution after applying only the cuts from the initial skimming is shown. In the middle, the distribution is shown before background subtraction but after applying all the analysis cuts except the $\Delta\beta_{K^+}$ cut. The plot on the right compares the $\pm 3\sigma$ values obtained in both stages. The blue and red lines define the $\pm 3\sigma$ momentum-dependent functions.

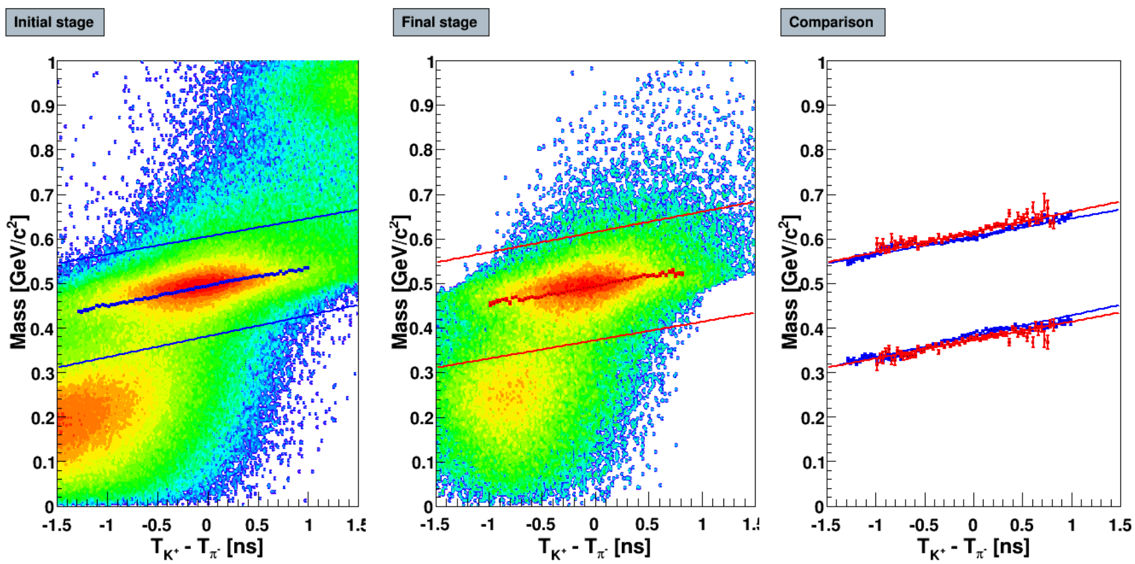


Figure 5.13: Mass for $K^+$vs. $|T_{K^+} - T_{\pi^-}|$ distribution at two different stages: (left plot) after applying the $\Delta\beta_{\pi^-}$ cut, and (middle plot) after applying all the cuts except the $\Delta\beta_{K^+}$ cut. (right plot) Comparison of the $\pm 3\sigma$ functions obtained in both stages and used for the contour selection.

The impact of the contour selection on the $\Delta\beta_{K^+}$ vs. $p$ distribution is presented in Figure 5.14 before applying the $\Delta\beta_{K^+}$ cut. The distribution with $\Delta\beta_{\pi^-}$ and $|T_{K^+} - T_{\pi^-}|$ cuts imposed is shown in the left side. The middle and right side plots show the resulting distribution for accepted and rejected events, respectively, after applying, in addition, the contour cut. Figure 5.15 shows the $\Delta\beta$, momentum $p$, and mass $m$ distributions for $K^+$obtained after the contour cut are shown, with the accepted and rejected events being represented by light yellow and light blue histograms, respectively. Based on these plots, it seems the leaking of pions into the $K^+$signal is greatly reduced but accounting for the efectiveness of this contour cut in terms of the number of $K^+$events thrown out is something that will be done in a precise way for the publication. The final selection of $K^+$in this analysis corresponds to a combination of the $\Delta\beta_{K^+}$ vs. $p$ cut plus the contour cut.

The final mass, momentum, polar angle, and azimuthal angle distributions for $K^+$after applying all the analysis cuts are shown in Figure 5.16.

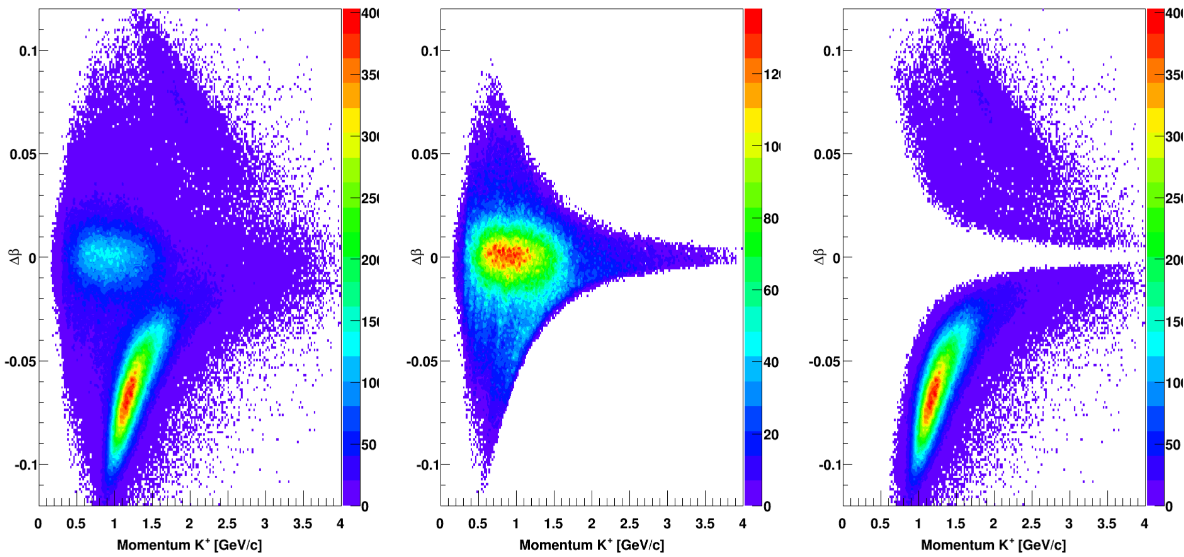


Figure 5.14: Impact of the contour cut on the selection of $K^+$. The point to notice is that the contour cut rejects a significant portion of misidentified pions. Explanation is given in the text.

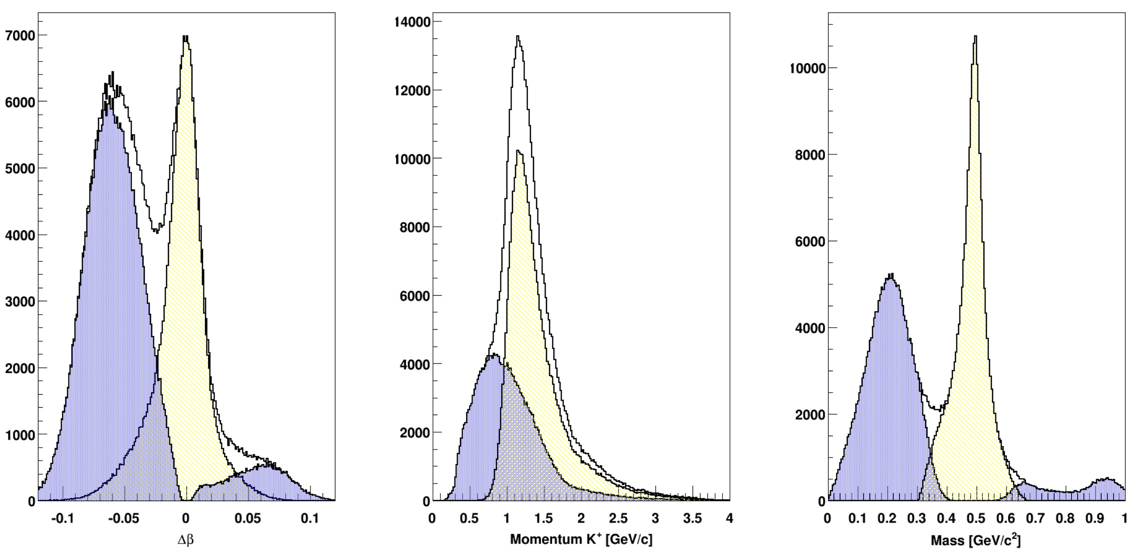


Figure 5.15: $\Delta\beta$, $p$, and $m$ distributions after applying the contour cut. Accepted and rejected events are represented by light yellow and light blue histograms, respectively. Explanation is given in the text.

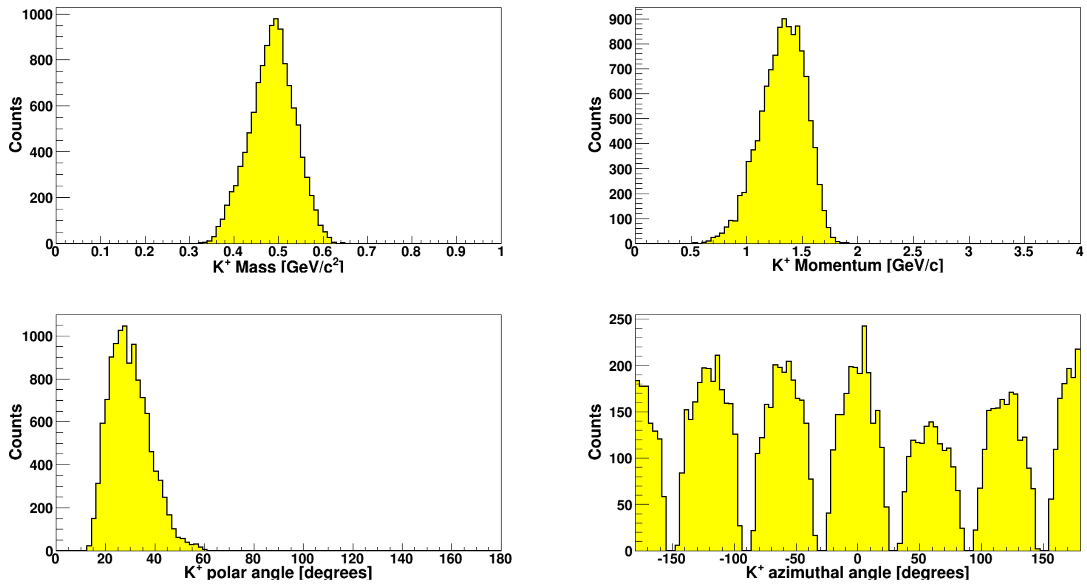


Figure 5.16: Mass, momentum, $\theta$, and $\phi$ distributions for the final $K^+$sample after all the cuts are applied. Note that kaons are mostly forward-peaked.

### 5.5.5 Vertex Cuts

The way the vertex of a single track is found in the standard CLAS software is by looking for intersections of the track, reconstructed inside the target, with the beam stop planes − planes which go through the beam line and cut perpendicularly the mid-plane of each sector. The intersection coordinates are used as the vertex coordinates for the track. In this analysis, the vertex position for each charged particle was instead determined by calculating the coordinates of the closest point along the track path to an idealized beam line defined by $(0, 0, z)$. The closest point is determined by finding the line segment that is perpendicular to both the track path and the idealized beam line.

In the $\gamma d \to K^+\Sigma^-(p)$ reaction, of the two charged particles detected, the $K^+$is the only one coming directly from the primary reaction vertex. The $\pi^-$, on the other hand, comes from a secondary vertex, that is, the decay vertex of the $\Sigma^-$after it has moved away from the reaction vertex. As will be shown below in Appendix D, the probability of a $\Sigma^-$decaying outside the target is not negligible. More importantly, the extrapolation of the $\pi^-$ track to the beamline may not coincide with the true vertex. This means that for the purpose of analyzing the $K^+\Sigma^-$channel, one should avoid rejecting pions for which the vertex position along the beamline ($z$-vertex) is outside the target boundaries since they might be related to good $K^+\Sigma^-$events. Thus, in this analysis, $z$-vertex cuts were applied only to kaons. These cuts (-39.0< $z_{K+}$ <-1.0 cm) were defined in such a way as to exclude interactions in the target windows. The resulting vertex distributions for $\pi^-$ and for $K^+$, after applying all the analysis cuts except the $z_{K+}$-vertex cut, are depicted in Figures 5.17 and 5.18, respectively. One can notice how the beam stop planes are clearly visible in the form of black, crossing strips. For the case of $\pi^-$, it is clear that a significant number of events originate outside the target walls, which is related to the fact that the $\pi^-$ comes from the decay of the $\Sigma^-$. For $K^+$the small amount of events outside the target is simply a resolution issue.

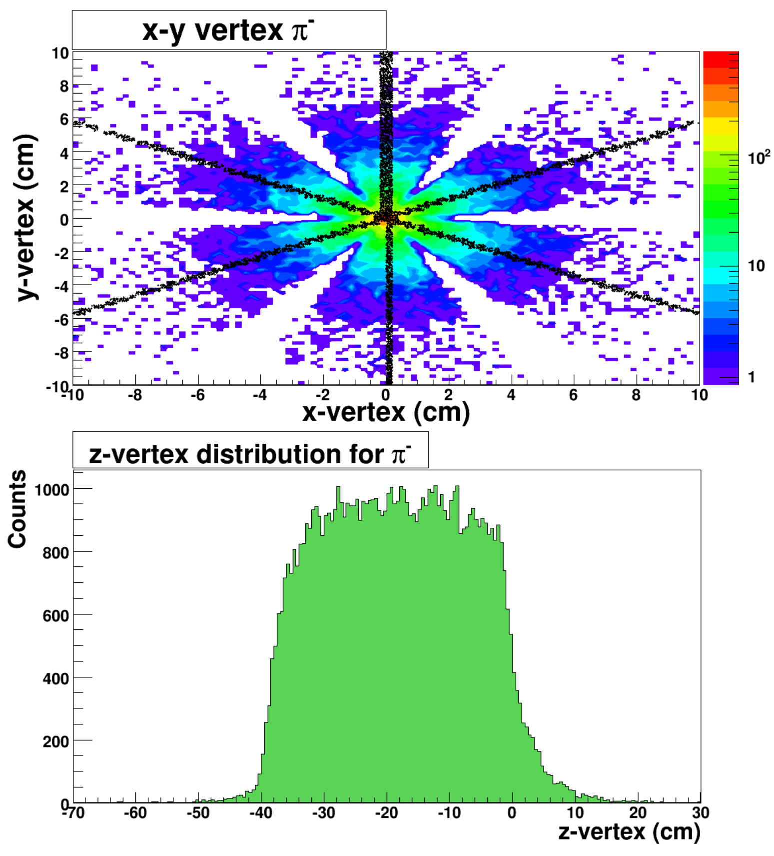


Figure 5.17: (top) $x$ vs. $y$ vertex distribution for $\pi^-$. The distribution in color represents the vertex distribution calculated in this analysis. The black crossing strips represent the $x$ vs. $y$ vertex distribution as obtained from the EVNT bank. (bottom) $z$-vertex distribution for $\pi^-$. The significant amount of events outside the target length boundaries (-40.0 and 0.0 cm) is a consequence of that the $\pi^-$ comes from the decay vertex of the $\Sigma^-$.

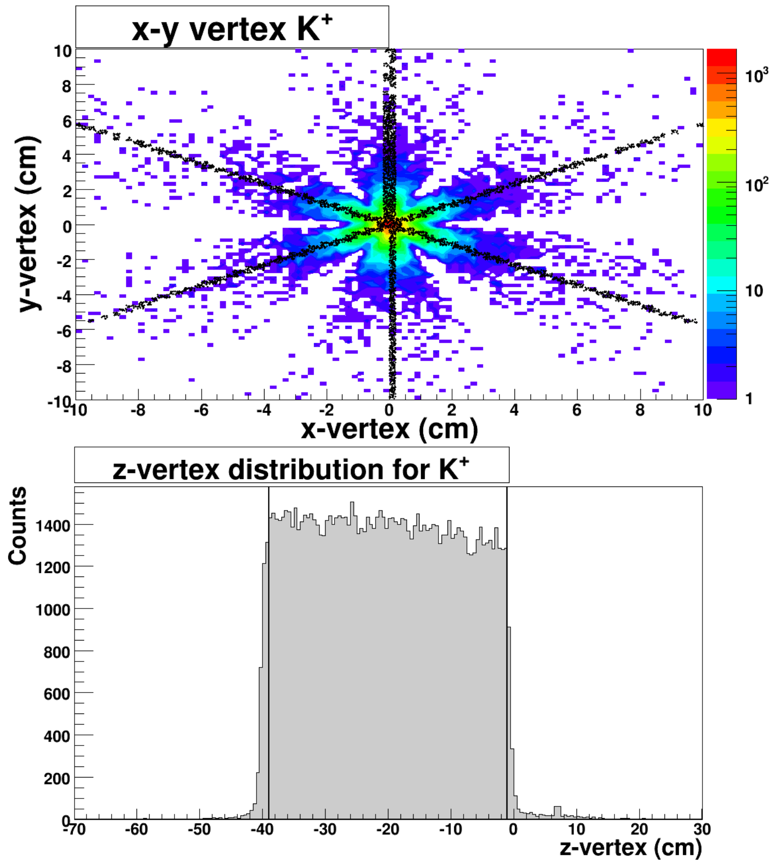


Figure 5.18: (top) $x$ vs. $y$ vertex distribution for $K^+$. The distribution in color represents the vertex distribution calculated in this analysis. The black crossing strips represent the $x$ vs. $y$ vertex distribution as obtained from the EVNT bank. (bottom) $z$-vertex distribution for $K^+$. The black vertical lines represent the $K^+$ $z$-vertex cut between -39.0 cm and -1.0 cm.

## 5.6 Neutral Particle Identification

The identification of neutral tracks in CLAS is based upon the velocity $c\beta_n$ determined according to the expression:

$$c\beta_n = \frac{l_{_{EC}}}{T_{_{EC}} - T_\gamma} \tag{5.4}$$

with $l_{_{EC}}$ and $T_{_{EC}}$ being the path length and timing information from the electromagnetic calorimeter, and $T_\gamma$ the vertex time of the incident photon (see Section 5.9).

In CLAS, neutrals are tagged as neutrons or photons depending on their $\beta_n$. In the EVNT scheme, if $\beta_n < 0.95$ then the neutral is labeled as a neutron and its momentum is calculated from the relation $p = m_n\beta_n/\sqrt{1-\beta_n^2}$. Otherwise the neutral is considered to be a photon with momentum $p = E_{tot}/0.272$, where $E_{tot}$ is the total energy deposited in the calorimeter by the particle, and 0.272 corresponds to the sampling fraction, *i.e.*, the energy fraction deposited in the active part of the calorimeter obtained from simulation studies [69]. The $\beta_n$ distribution for neutrals at a very early stage of the analysis is shown in Figure 5.19.

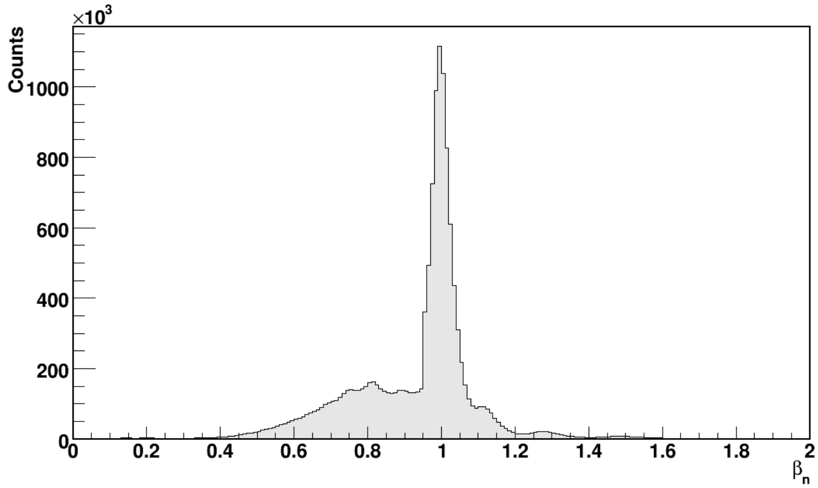


Figure 5.19: $\beta$ distribution for neutrals obtained after requesting good flags on events with at least one positive, one negative, and one neutral. The broad peak around 0.8 is associated with neutrons, while the large peak centered at 1.0 corresponds to photons. The fact that $\beta$ is greater than 1.0 is related to the resolution of the detector and with problems on the reconstruction of the path for neutrals.

### 5.6.1 Neutron Identification

The strategy followed in this analysis allowed us to relax the standard $\beta$ cut used to distinguish between neutrons and photons. In general, the idea was to assume all neutrals to be neutrons and use them throughout the analysis code without cutting on their velocity. Figure 5.20 displays the $\beta_n$ distribution for all the neutral hits at two different stages of the analysis. In the left plot, only the cuts included in the initial skimming are applied. On the right, all analysis cuts (except background subtraction) are included. After the initial skimming, the number of photons is reduced significantly, clearly showing the distribution of neutrons. After applying fiducial, PID, and timing cuts, the photons are virtually eliminated and the distribution of fast neutrals is observed to die off naturally around $\beta$=0.97. This demonstrates the effectiveness of the procedure used to reject background from final states that are not $K^+\pi^-n$ (see Section 5.4.2). Figure 5.21 shows the final $\beta$, $p$, $\theta$, and $\phi$ distributions for neutrons after all cuts and all corrections are applied.

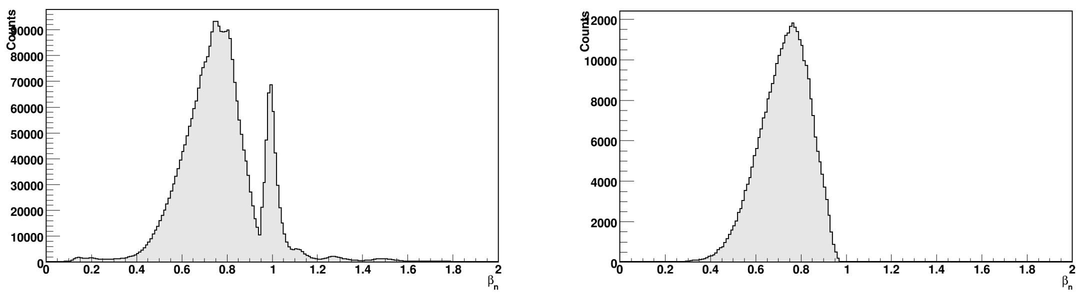


Figure 5.20: $\beta$ distribution for detected neutrals. (left) after initial skimming cuts. (right) after fiducial, PID, and timing cuts. The $\beta$ distribution dies off around 0.97 and no photon contamination is observed.

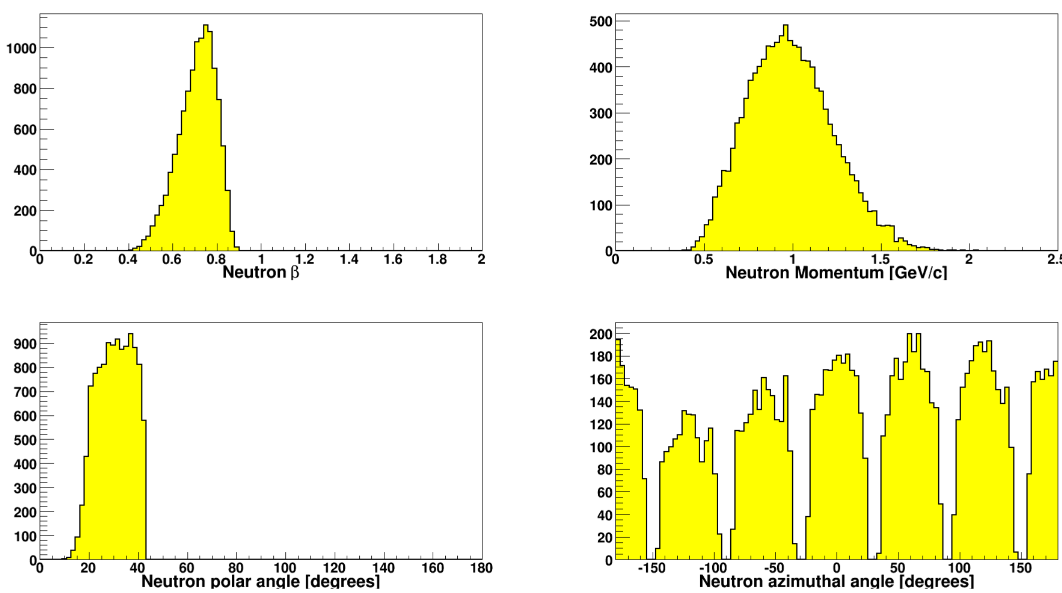


Figure 5.21: $\beta$, momentum, $\theta$, and $\phi$ for the final neutron sample after all cuts (including background) are applied. All the neutron corrections have been applied in these plots.

### 5.6.2 Path Corrections

The calculation of $\beta$ (and also $p$, $\theta$, and $\phi$) is sensitive to the determination of the path length for neutrals $|\vec{l}_{EC}|$ relative to the reaction vertex. This path, as depicted in Figure 5.22, is calculated from the vectorial sum:

$$\vec{l}_{EC} = \vec{R}_{EC} + (-\vec{V}_n) \tag{5.5}$$

where $|\vec{R}_{EC}|$ is the interaction vertex in the calorimeter and $|\vec{V}_n|$ represents the vertex position in the target. Both are given relative to the center of CLAS. These two quantities are determined by the CLAS software in a very general way, which does not always represent the best choice. Therefore, in order to obtain the most accurate value for $\beta$ (as well as $p$, $\theta$, and $\phi$), one needs to apply corrections on the values for both $|\vec{R}_{EC}|$ and $|\vec{V}_n|$. Such corrections are described in the next subsections.

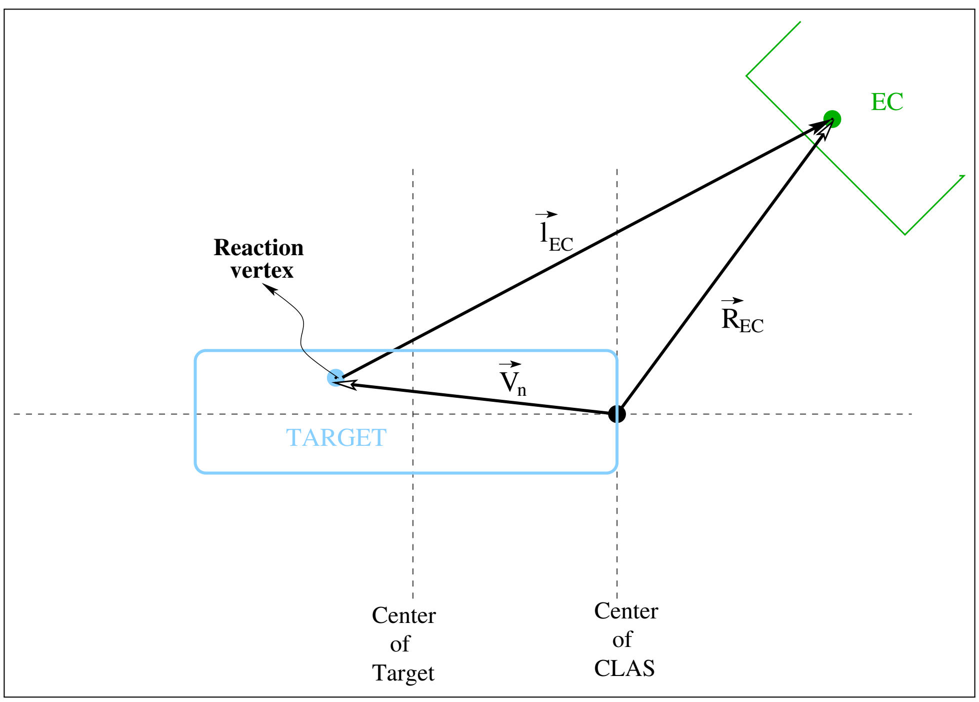


Figure 5.22: The neutral path is reconstructed in CLAS based on the vertex coordinates $\vec{V}_n$, associated with the fastest particle in the event, and the EC hit coordinates $\vec{R}_{EC}$.

#### 5.6.2.1 Correction to the Interaction Vertex in the EC

Due to their large interaction length, neutrons can interact anywhere inside the calorimeter, making it difficult to precisely determine the EC hit coordinates along the neutron momentum vector. However, any systematic shift in the reconstruction of $\vec{R}_{EC}$ can be corrected from the analysis of $\gamma d \rightarrow \pi^+\pi^- p\ n$ events. This channel has the advantage of having all the four particles generated at a common primary reaction vertex[8], eliminating the necessity of "guessing" a vertex position for the neutron in the target. The $\pi^+\pi^- p\ n$ analysis consisted of comparing the missing momentum, after applying cuts on the missing mass $MM(\pi^+\pi^- p)$, to the momentum of the neutron detected in CLAS. The correction obtained was applied as a global factor with a different value for each EC layer. A detailed description of the procedure followed to define this correction is presented in Appendix C.

#### 5.6.2.2 Correction to the Vertex Position in the Target

During the data processing stage ("cooking"), a vertex position $\vec{V}_n$ is assigned to neutrals according to the vertex of the fastest particle in the event (in most of the cases, a charged pion). For channels with neutrons coming directly from the reaction vertex, this is a good choice. However, when the neutron comes from a secondary vertex, as in the case of the $\Sigma^-$, it is less obvious where the neutron was produced, causing an uncertainty in the neutron path length. Therefore, taking into account that the $K^+$ is the only detected particle originating from the vertex of the $K^+\Sigma^-$ reaction, we assumed, as a starting point, the neutron to come from the same vertex as the kaon. This is a reasonable approximation for $\vec{V}_n$ as in many cases the $\Sigma^-$ decays right after being created. Nevertheless, the non-negligible mean decay path of the $\Sigma^-$ requires an algorithm to correct for the decay vertex location. Such an algorithm is explained in Appendix D.

### 5.6.3 Deposited Neutron Energy

When interacting in the calorimeter, the deposited energy $E_{dep}$ cannot exceed the kinetic energy $E_{kin}$ of the neutron. Therefore, the condition $E_{kin} - E_{dep} \geq 0$ was always required.

[8]The common primary vertex is extracted from the MVRT bank.

The deposited energy was extracted from the ECPB bank, while the kinetic energy was calculated as

$$E_{kin} = \sqrt{P_n^2 + M_n^2} - M_n \tag{5.6}$$

where $P_n$ is the reconstructed neutron momentum after applying path corrections, and $M_n$ is the PDG neutron mass [75]. The $E_{kin} - E_{dep}$ distribution can be seen in Figure 5.23, where the black line corresponds to the applied cut. Although the rejected events fall within the experimental resolution, they can be ignored when determining the photon beam asymmetry without a significant loss of statistics.

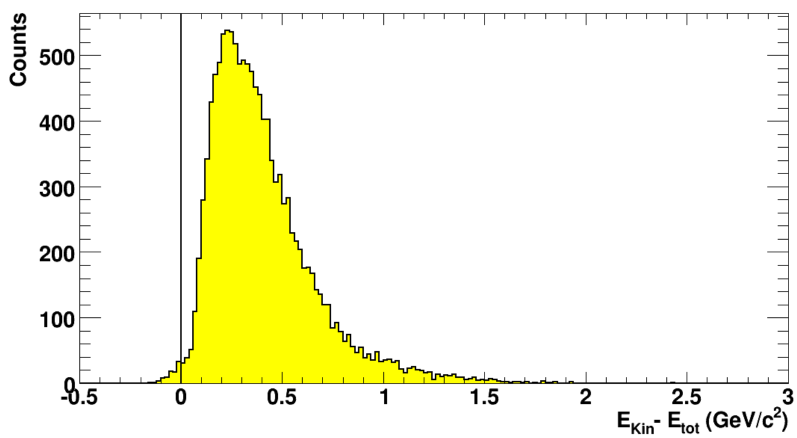


Figure 5.23: Difference between the neutron kinetic energy and the deposited energy in the calorimeter. Only events with a positive difference are accepted (above the vertical black line). The histogram is taken after applying fiducial and PID cuts.

## 5.7 Momentum and Energy Corrections

Uncertainties in the magnetic field map, misalignment of the drift chambers, and energy lost when moving through different regions of CLAS make it necessary to apply empirical corrections to the reconstructed momenta of charged particles.

### 5.7.1 Momentum Corrections

Due to the fact that the momentum reconstruction in CLAS is based on the magnetic field, an incomplete knowledge of the torus field map, as well as any geometric misalignment of the drift chambers, can lead to inaccuracies in the reconstructed momentum. The momentum thus has to be corrected to take into account such inaccuracies. The correction was determined by studying sector-by-sector the reaction $\gamma d \to pp\pi^-$ [80] under three possible scenarios: $\gamma d \to pp(\pi^-)$, $\gamma d \to p(p)\pi^-$, and $\gamma d \to (p)p\pi^-$, where $(X)$ is the reconstructed particle. In each case, the average difference between the reconstructed momentum of this particle and the momentum obtained from a kinematic fit [81, 82] defined the correction function for positively and negatively charged particles (the corrections only depend on charge and are independent of mass). Figure 5.24 shows the corrections on the momentum distributions of pions and kaons. In neither case does the correction exceed 2%.

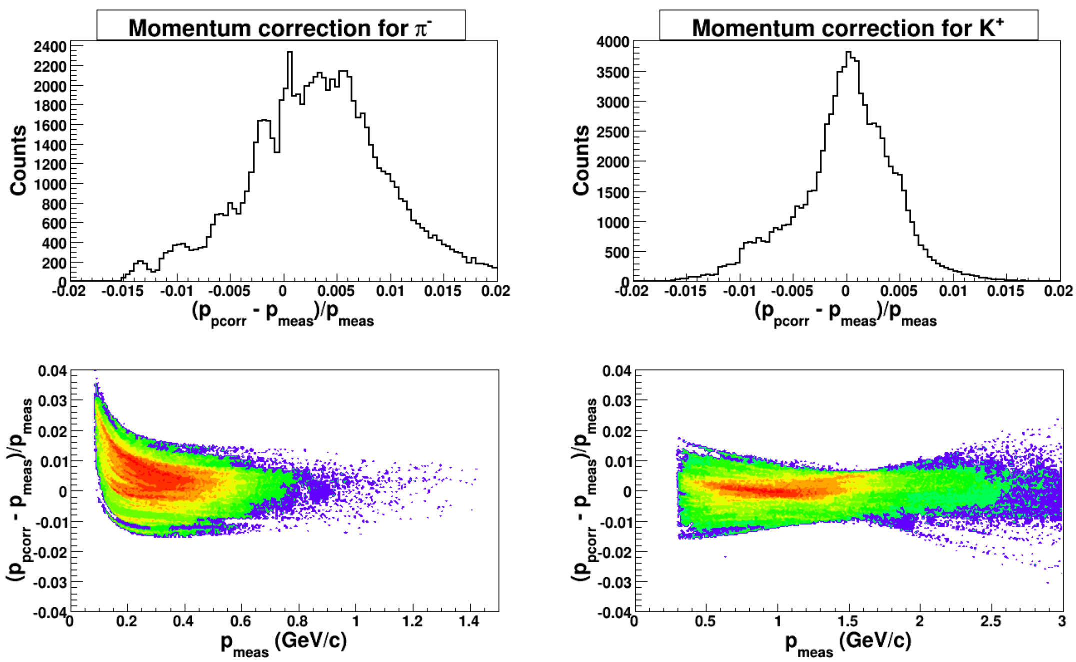


Figure 5.24: Momentum correction where $p_{corr}$ is the corrected momentum and $p_{meas}$, the measured momentum. (top left) ratio and (bottom left) ratio as a function of momentum for $\pi^-$. (top right) ratio and (bottom right) ratio as a function of momentum for $K^+$. Plots taken after applying fiducial, PID, and timing cuts.

### 5.7.2 Energy-Loss Corrections

Before their momentum is determined in the drift chambers, charged particles lose energy as they pass through the target material, the target cell walls, the beam pipe, the start counter, and the air gap between the start counter and the first region of the drift chambers. To obtain the particle momentum at the interaction vertex rather than in the drift chambers, corrections for these energy losses were applied using the *eloss* package [83]. Figure 5.25 displays the energy-loss correction on the momentum distributions of $\pi^-$ and $K^+$.

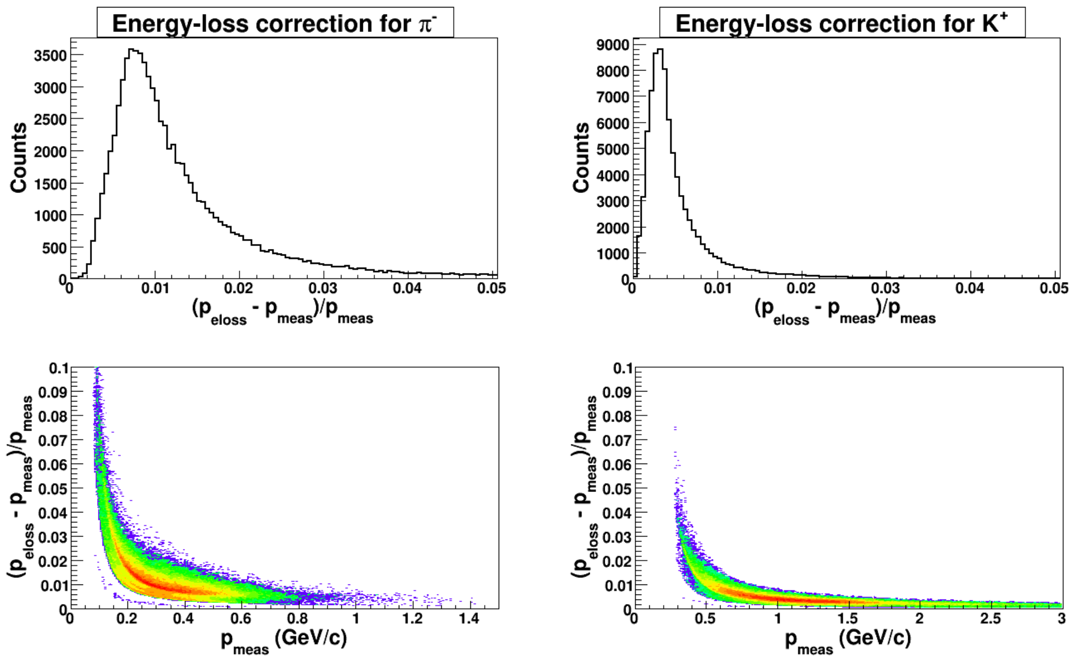


Figure 5.25: Eloss correction where $p_{eloss}$ is the eloss-corrected momentum and $p_{meas}$, the measured momentum. (top left) ratio and (bottom left) ratio as a function of momentum for $\pi^-$. (top right) ratio and (bottom right) ratio as a function of momentum for $K^+$. Plots taken after applying fiducial, PID, and timing cuts.

## 5.8 Fiducial Cuts

Fiducial cuts are implemented with the main goal of removing regions of the detector that are not well reproduced by Monte Carlo simulations. This is of particular importance for cross-section measurements, but might also be relevant to optimize the $\phi$-binning used in the determination of the beam asymmetry. In this analysis, two types of fiducial cuts are implemented: angular cuts, and bad TOF paddle cuts. The first type eliminates particles passing near the edges of the drift chambers (for charged particles) and particles passing near the edges of the calorimeter (for neutral particles) in each sector. The second type (used only for charged particles) rejects particles that hit either malfunctioning or inefficient TOF paddles.

### 5.8.1 Angular Cuts for charged particles

The toroidal magnetic field near the coil regions (edges of the drift chambers) varies non-uniformly with the position. Due to imperfections in the field maps used, any charged particle passing close to those regions will have a larger uncertainty in the measured momentum. Particles interacting with either the magnet coils or the cryostats may also end up not being detected in the outer subsystems, causing the reconstruction to fail. Consequently, these regions are difficult to model and should be removed from the analysis. The removal (fiducial cuts) in this analysis consisted of a cut of $\pm 5^\circ$ on the azimuthal angle at the edge of each sector chosen to remove the region around the coil. Figure 5.26 shows the azimuthal vs. polar angle distribution for negatively and positively charged particles. The angular cuts are represented by red vertical lines. About 5% of the events passing the initial skimming are rejected by these angular cuts.

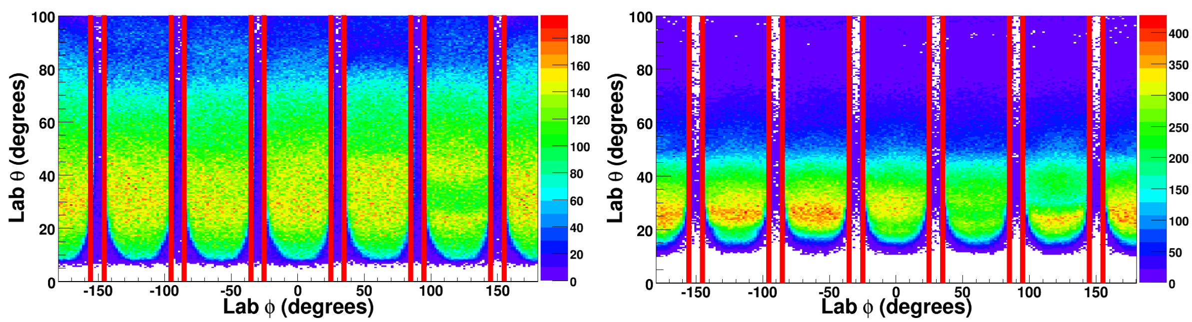


Figure 5.26: $\phi$ vs. $\theta$ distribution for negative (left) and positive (right) particles. The red vertical lines show the angular cuts. The histograms were filled right after the initial skimming and before any PID cuts.

### 5.8.2 Angular Cuts for neutral particles

For neutrals, a $\pm 5^\circ$ cut around the edges of each sector was also used. In addition, keeping in mind that neutrals are only detected with the electromagnetic calorimeter, reconstructed neutrons were required to be within the fiducial EC volume. This volume is defined as $10° < \theta_n < 43°$, where $\theta_n$ is the neutron polar angle. Figure 5.27 shows the angular cuts applied to candidate neutrons. The poor reconstruction in sector 5 (between -150° and -100°) is a consequence of the fact that the EC pedestals were never updated after the replacement of an ADC board for sector 5 at the beginning of g13b.

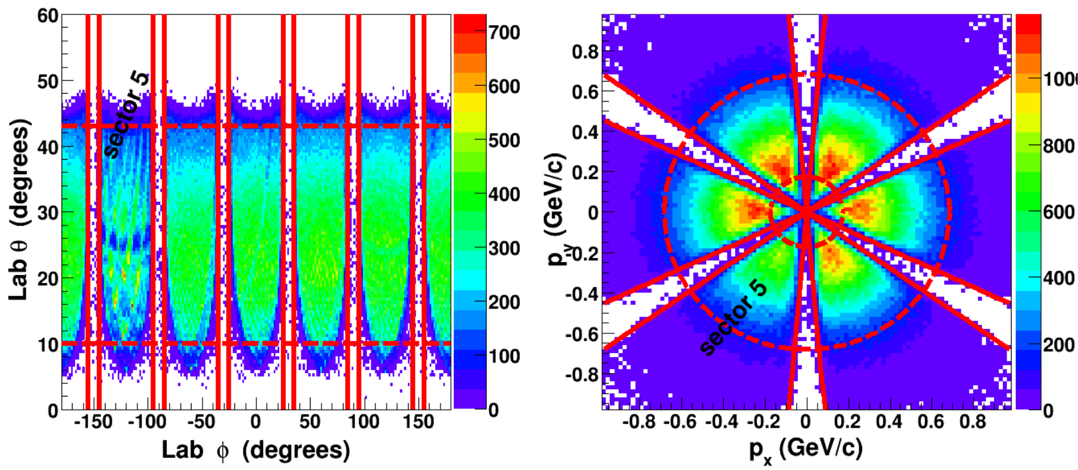


Figure 5.27: $\phi$ vs. $\theta$ distribution for neutral particles. The red lines show the angular cuts. Only initial skimming and charged particle angular cuts were applied here. The low statistics observed in sector 5 are explained in the text.

### 5.8.3 Bad Time-Of-Flight Scintillator Paddles

Inefficient paddles in the TOF subsystem were rejected from the analysis according to studies performed during calibration. Since paddles above N$^o$40 are coupled pairwise, it is very hard to make them both work at the same time. Therefore, those paddles were removed from all sectors. The list of bad paddles in each CLAS sector is shown in Table 5.2. The resulting $\phi$, $\theta$, and momentum distributions of negatively and positively charged particles after cutting out bad SC paddles are shown in Figure 5.28.

Table 5.2: List of scintillator paddles removed from the analysis.

| Sector | Paddle N$^o$ | Problem | Sector | Paddle N$^o$ | Problem |
|---|---|---|---|---|---|
| 1 | 6, 10 | Dead | 6 | 10 | Dead |
| 2 | 8, 42 | Dead | All | > 40 | Pairwise |
| 3 | 11 | Dead | | | |

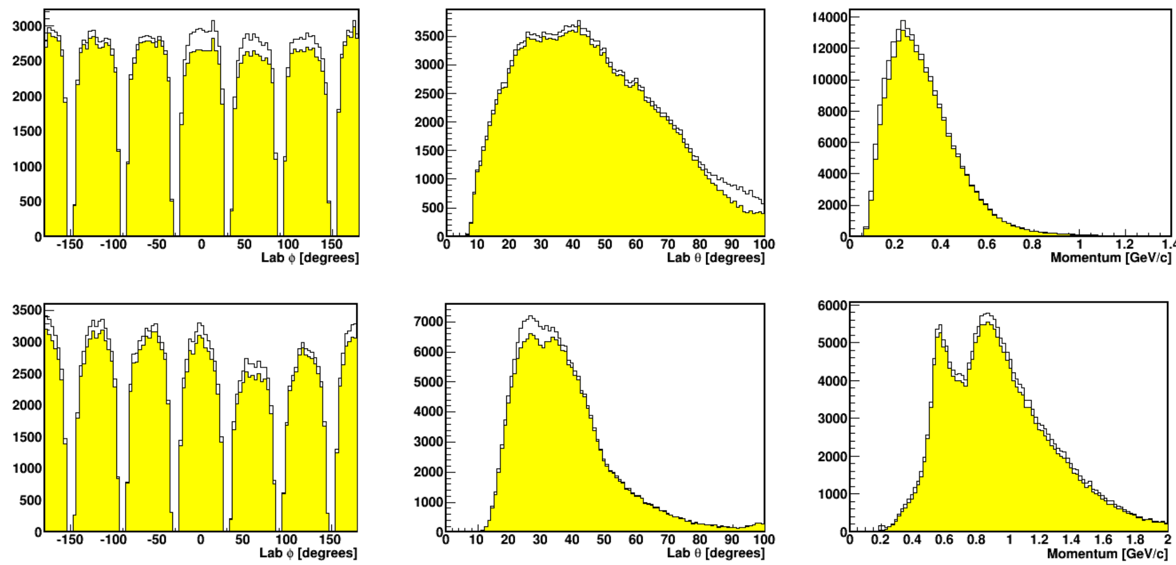


Figure 5.28: $\phi$, $\theta$, and momentum distributions for negative (top panel) and positive (bottom panel) particles. White and yellow histograms correspond to events before and after removing bad SC paddles, respectively. All plots include angular cuts.

## 5.9 Incident Photon Identification

In contrast to electron scattering experiments, where the electron causing the interaction and the produced hadrons form a coincidence inside the CLAS detector, photoproduction experiments require the photon tagger to tag all electrons that radiated a photon. Among these, the correct photon (the one that initiated the reaction) has to be identified by matching its vertex time ($T_\gamma$) to the vertex times of the hadrons ($T_h$) in CLAS. The time of arrival at the reaction vertex for each "good" photon in the TAGR bank is calculated from the relation:

$$T_\gamma = T_{Tagger} + \frac{z_h - z_{\mathrm{Off}}}{c} \tag{5.7}$$

where $T_{Tagger}$ is the time of photon arrival (after RF correction) at the center of the target, $z_h$ is the $z$-vertex coordinate for the hadron, measured with respect to the center of CLAS, and $z_{\text{Off}}$ is the offset along the beam axis between the center of the target and the center of CLAS (in g13, the target was moved 20 cm upstream from the center of CLAS).

The vertex time for a hadron can be determined based on either the start counter (ST) or the time-of-flight (TOF) subsystems. The timing information for a charged particle provided by either subsystem can be traced back to the instant at which the event took place. The calculation is as follows:

$$T_h = T_{Sub} - \frac{l_{Sub}}{c\beta_{calc}} \tag{5.8}$$

where $T_{sub}$ and $l_{Sub}$ are the particle time and the path length, and $\beta_{calc}$ is the particle's velocity calculated from the momentum as measured in the DC (not corrected for energy loss before the drift chambers) and the nominal PDG mass [75]. The high luminosity of the g13 run period increases the chance of having events with multiple hits in the same sector of the start counter which can be incorrectly associated with a particle track. The TOF not only has a higher segmentation but also a better time resolution when compared to the ST. Therefore, only the information from the TOF subsystem ($T_{TOF}$ and $l_{TOF}$) was used to determine the hadron vertex time.

In this analysis, the matching hadron corresponds to the $K^+$(see Section 5.6). The distribution $\Delta T = T_{K^+} - T_\gamma$ vs. $K^+$momentum and its projection along the $\Delta T$-axis for all good photons are shown in Figure 5.29. The correct photon was selected by applying a momentum-dependent $\Delta T$ cut. The cut was set by slicing the $\Delta T$ vs. $K^+$momentum axis into 20 MeV/c bins along the momentum axis and fitting each slice with a gaussian function. The $\pm 3\sigma$ momentum-dependent functions are defined by a combination of a third-order polynomial and a zeroth-order polynomial. These functions can be seen in the right panel of Figure 5.29. Of the total number of events that passed the fiducial, bad SC, and PID cuts, it was found that in approximately 3% of the cases, more than one good photon survived the $\Delta T$ cut (Figure 5.30). Due to the ambiguity presented by such events, those multi-photon events were rejected from the analysis. Since this thesis determines an asymmetry and not an absolute cross section, no correction is needed to account for these rejected events.

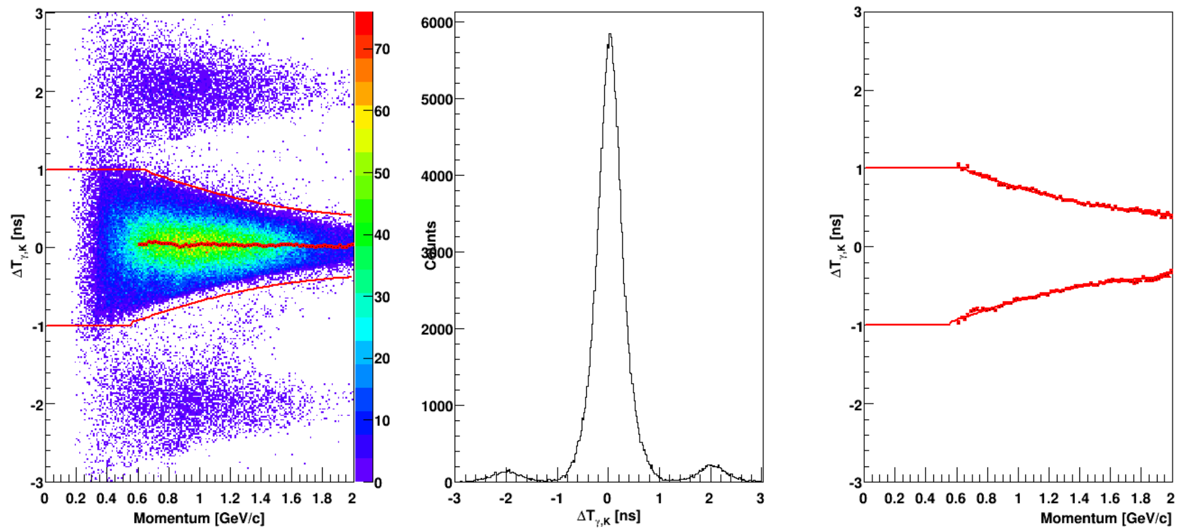


Figure 5.29: (left) Vertex time difference $\Delta T = T_{K^+} - T_\gamma$ between all the good photons in the TAGR bank and the kaon as a function of $K^+$momentum. (middle) $\Delta T$ distribution. (right) Momentum-dependent cuts applied on $\Delta T$. Red lines represent the functional form applied in the analysis. These histograms were filled after fiducial, bad SC and PID cuts.

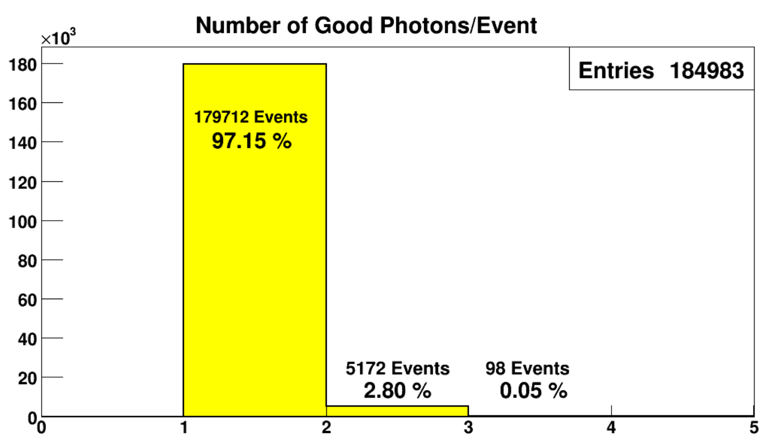


Figure 5.30: Number of good photons per event passing the $\Delta T$ cut. The histogram was filled based on the total number of events that survived the fiducial+bad SC paddles+PID set of cuts. Approximately 2.80% of that total have two good photons while 0.05% registered three good photons. These multi-photon events were discarded from the analysis.

## 5.10 The Quasi-free Reaction: $\gamma n \to K^+\Sigma^-$

After PID and photon selection, the following step in the analysis is to do the event selection for the quasi-free reaction of interest: $\gamma n \to K^+\Sigma^-$. However, the reaction studied experimentally corresponds to $\gamma d \to K^+\Sigma^-(p)$ rather than to $\gamma n \to K^+\Sigma^-$. As a consequence, there are two contributions related to the kinematics of the proton $(p)$. One contribution corresponds to the case when the proton $(p)$ does not participate in the interaction and the other, when it does. The former is the quasi-free reaction where the momentum distribution of $(p)$ is mainly dominated by Fermi motion; the latter represents rescattering in which $(p)$ is hit either by the $K^+$ or the $\Sigma^-$ and so, gains momentum.

The selection of quasi-free events in this analysis was made by restricting the momentum of the missing particle $(p)$ to low values. The cut value was defined as 0.15 GeV/c. This cut can be justified by looking at the top right panel of Figure 5.31 where the missing mass is plotted as a function of the missing momentum. This momentum cut represents a physical cut that allows one to understand better the reaction by separating rescattering events. In addition, it has implications on the background since it helps to eliminate a significant amount of non-$K^+\Sigma^-$ events observed beyond missing-mass values of $\sim$1.1 GeV/$c^2$. The bottom panels of Figure 5.31 show the missing momentum distribution and the correlation of the $\cos\theta_p^{\text{lab}}$ with the missing momentum distribution. These plots show the missing momentum cut and make evident the tendency of the missing momentum to be distributed isotropically in the lab frame at low-momentum values, as expected when Fermi motion dominates. The distribution of events is seen to be basically flat below 0.15 GeV/c, but above roughly 0.2 GeV/c, the distribution tends to peak in the forward direction which can be interpreted as a sign of the final-state interactions being the dominant process.

## 5.11 Background Subtraction

After applying the missing momentum cut, the remaining background is studied from the invariant and missing mass distributions shown in Figure 5.32. Based on the top panel of Figure 5.32 one can infer that the background is comprised of mainly two sources:

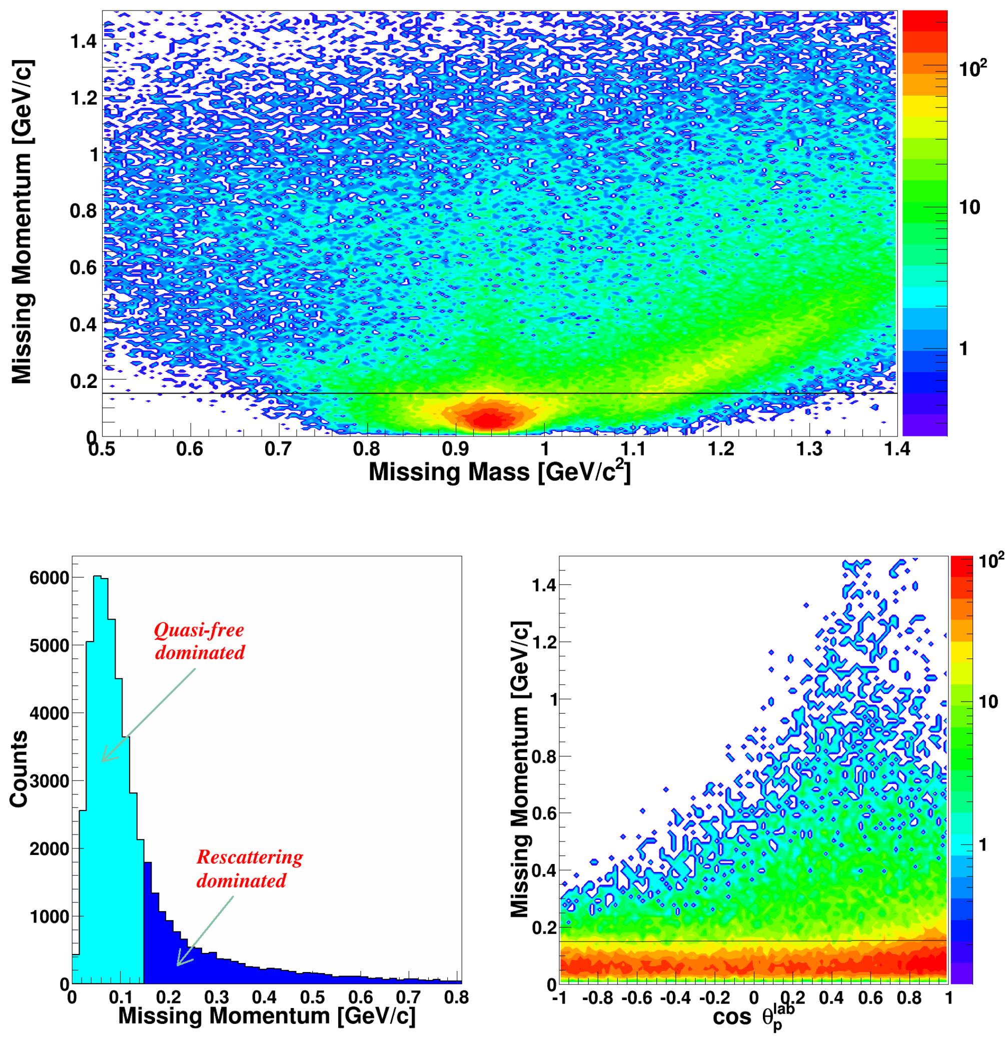


Figure 5.31: (top) Missing mass vs. missing momentum. (bottom left) Missing momentum distribution for low- (cyan) and high-momentum protons (blue). (bottom right) $\cos\theta_p^{\rm lab}$ vs. momentum distribution of the missing proton. The horizontal line at 0.15 GeV/c represents the momentum cut applied. Events below this cut define the quasi-free $\gamma n \to K^+\Sigma^-$ reaction.

- background correlated with the $\Sigma^-$, and
- background uncorrelated with the $\Sigma^-$

Both sources of background can be recognized in the bottom left and bottom right panels of Figure 5.32 where the missing and invariant mass distributions are shown, respectively. The correlated background appears as a bump peaking around 1.1 GeV/c$^2$ on the missing mass distribution. This background comes from the reactions $\gamma d \to K^{+\star}\Sigma^{-}(p)$ and $\gamma d \to K^{+}\Sigma^{-\star}(p)$ with $K^{+\star}$ and $\Sigma^{-\star}$ decaying into $K^{+}\pi^{0}$ and $\Sigma^{-}\pi^{0}$, respectively. Each of these reactions therefore contribute to $\gamma d \to K^{+}\Sigma^{-}(p)$ with an extra $\pi^{0}$ and so, they also contribute with the $\Sigma^{-}$ peak; consequently, the correlated background cannot be easily identified in the invariant mass distribution. On the other hand, the uncorrelated background, barely noticeable as a shoulder below 0.85 GeV/c$^2$ in the missing mass distribution, can be clearly appreciated as a flat distribution sitting underneath the $\Sigma^{-}$ peak in the invariant mass distribution. This background is related to particle misidentification in the analysis and the predominant reactions, uniformly distributed (phase space), are $\gamma d \to \pi^{+}\pi^{-}n(p)$ and $\gamma d \to \pi^{+}\pi^{-}n(p)\pi^{0}$ where the $\pi^{+}$ is the misidentified particle.

The strategy followed in this analysis to subtract the background from the $\Sigma^{-}$ mass distribution consists on "cutting" the correlated background and then "fitting" the uncorrelated background.

### 5.11.1 Correlated Background

Events passing the spectator momentum cut are seen in the invariant mass distribution ($\Sigma^{-}$) to come from the $K^{+}\Sigma^{-}$ and $K^{+}\Sigma^{-}\pi^{0}$ final states, with the former ($K^{+}\Sigma^{-}$) contributing the most and the latter ($K^{+}\Sigma^{-}\pi^{0}$) representing the correlated background. One can reduce such a background without significantly throwing out good $K^{+}\Sigma^{-}$ events by using the correlation between the missing mass of the $\pi^{-}n$ system (which should correspond to the mass of the $K^{+}(p)$ system) and the momentum of the $K^{+}$; the correlation shows a clear separation of the $K^{+}\Sigma^{-}$ from the $K^{+}\Sigma^{-}\pi^{0}$ final state (see Figure 5.33). The right panel shows an alternative view where the correlation is clockwise rotated in order to make the separation more clear.

The projection along the vertical axis of the rotated correlation is observed in Figure 5.34 (top panel). Because of the rotation, this projection contains information about both the $MM(\pi^{-}n)$ and the $K^{+}$ momentum and therefore, a cut on it can be thought as a two-dimensional cut. The cut applied to subtract the correlated background was chosen based on the fit of the projection with two gaussian functions: a double gaussian (blue) representing mainly the $K^{+}\Sigma^{-}$ final state and a single gaussian (red) representing the $K^{+}\Sigma^{-}\pi^{0}$ final

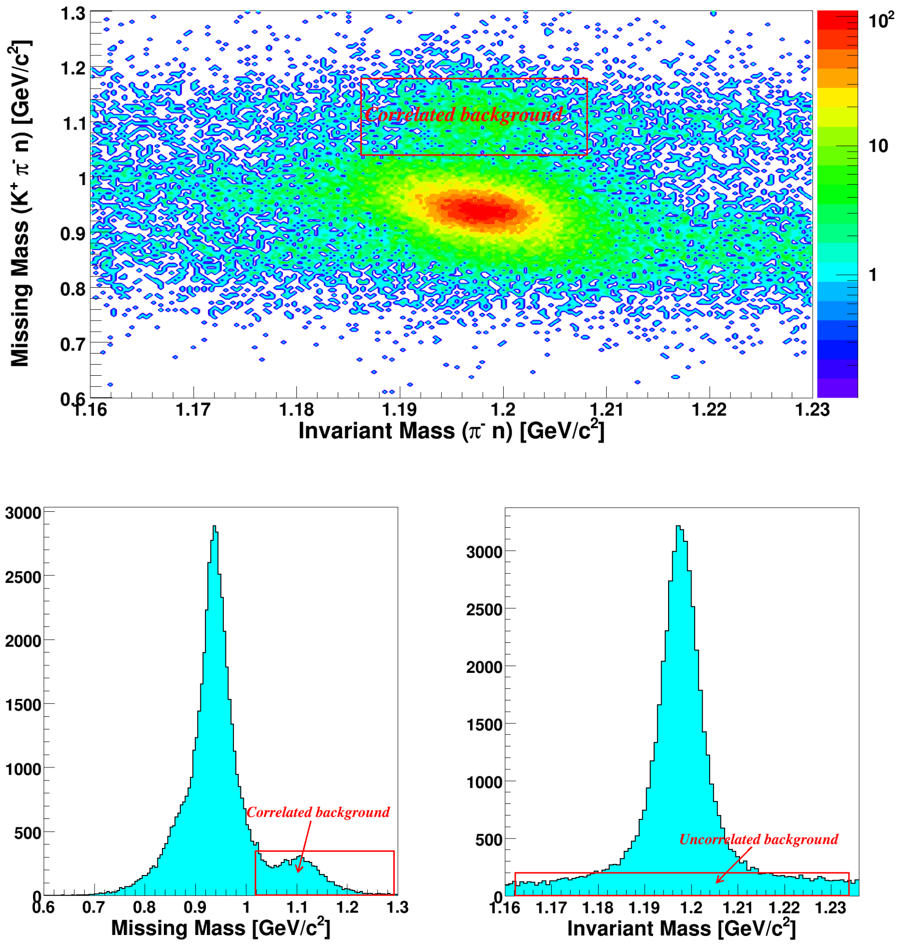


Figure 5.32: (top) Correlation between the invariant mass ($\pi^- n$) and the missing mass ($K^+\pi^- n$) distributions. (bottom left) Missing mass distribution showing a bump peaking about 1.1 GeV/c$^2$. (bottom right) Invariant mass distribution showing a flat background underneath the $\Sigma^-$ peak. Squared boxes are just an indication of the average regions where the background sources are supposed to lie. All the three histograms were taken right after applying the missing momentum cut.

states. The numerical value of the cut imposed is a trade-off between rejecting the majority of the $K^+\Sigma^-\pi^0$ events while simultaneously keeping the majority of good $K^+\Sigma^-$ events located below the missing mass peak. Integrating the single-gaussian function (red color), one can determine that the cut eliminates about 91% of the total of $K^+\Sigma^-\pi^0$ events lying within the $\Sigma^-$ signal. The bottom panel of Figure 5.34 shows the corresponding distributions for the missing and invariant mass events passing the cut (yellow histograms) as well as those being rejected by the cut (red histograms).

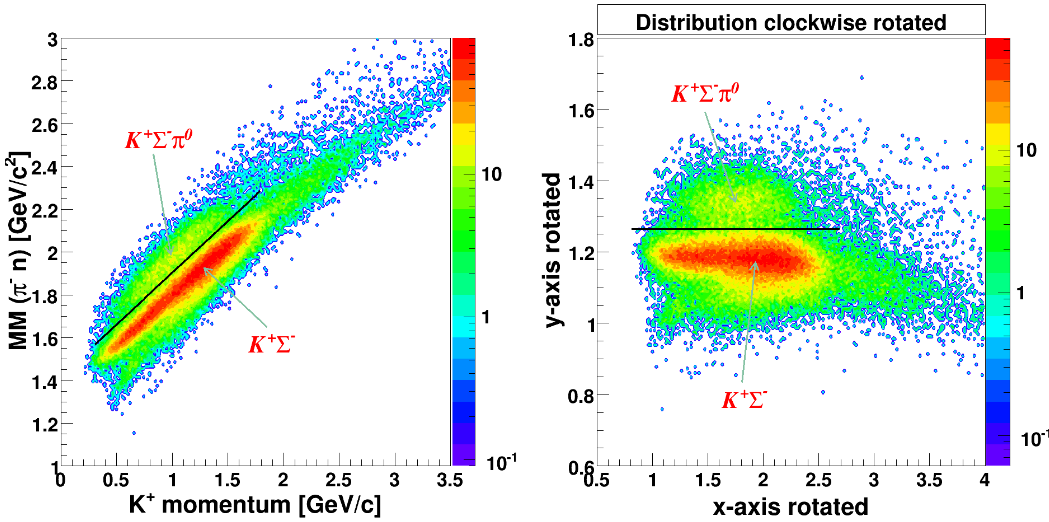


Figure 5.33: (left) Distribution of $MM(\pi^- n)$ vs. $K^+$ momentum. (right) Distribution of $MM(\pi^- n)$ vs. $K^+$ momentum clockwise rotated. Events below the black line corresponds mainly to $K^+\Sigma^-$events while those above the black line are related to $K^+\Sigma^-\pi^0$ events.

### 5.11.2 Photon Energy Cut

There is an extra background cut that plays a very important role in the determination of the beam asymmetry. This cut, referred to as the $E_\gamma$ cut and described in detail in Section 6.2, helps reduce potential polarized background events that might affect in a significant way the values obtained for the photon beam asymmetry. The $E_\gamma$ cut is applied in this analysis right after applying the correlated background cut and before subtracting the uncorrelated background. As a cross check, this cut was also applied before the correlated background cut and no significant difference between the two scenarios was noticed.

### 5.11.3 Signal-Background Subtraction

The remaining background in the invariant mass is related to contamination of $\pi^+$ misidentified as $K^+$. Since this background is not correlated with the invariant mass and is barely distinguishable in the missing mass, we dealt with it by fitting the invariant mass. The fit function prototype consists of a Voigtian function (V) plus a first-order polynomial ($L$). A Voigtian function is used in this case because it seems to describe well the non-gaussian

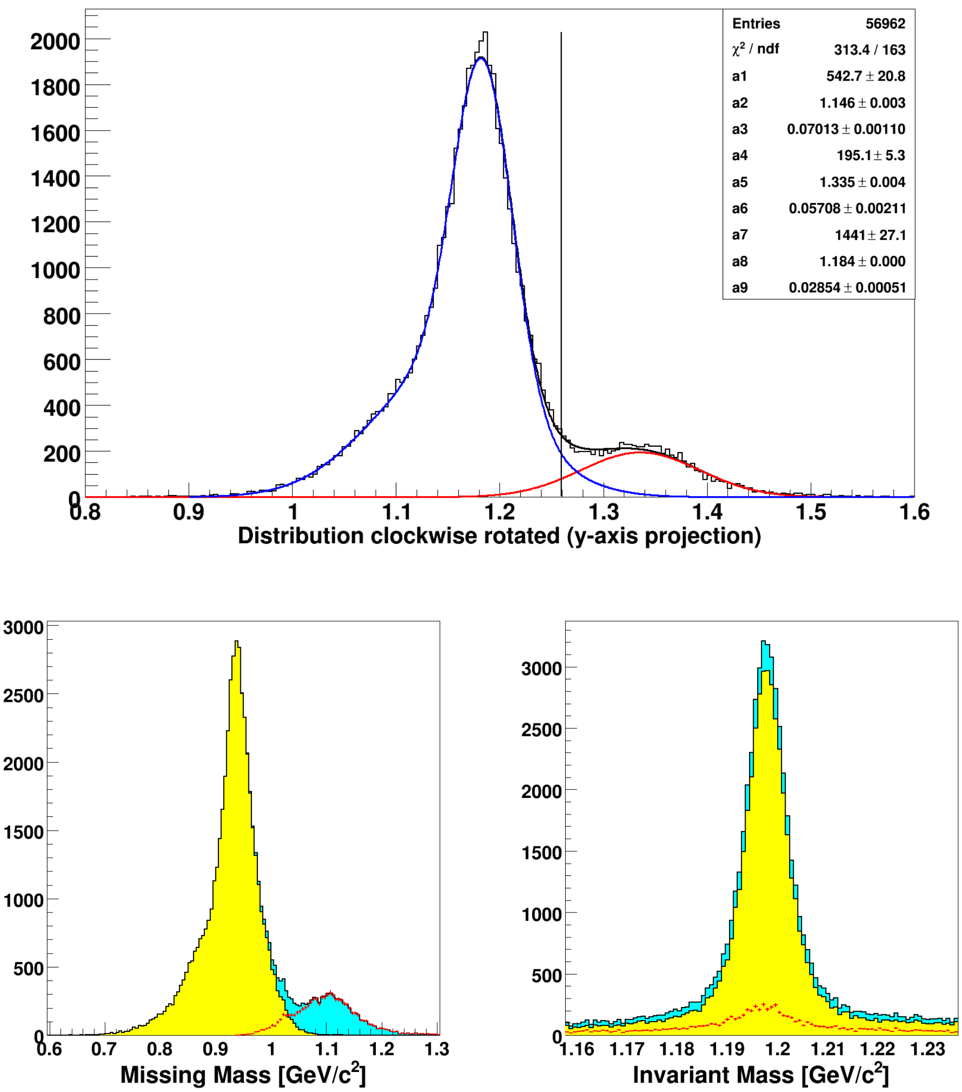


Figure 5.34: (top) Projection along the vertical axis of the right panel of Figure 5.33. The total function (black) is composed of a double-gaussian function (blue) and a single-gaussian function (red) representing $K^+\Sigma^-\pi^0$ events. Such events (correlated background) are eliminated by the black vertical line. Missing mass (left bottom panel) and invariant mass (right bottom panel) distributions before (cyan) and after (yellow and red) applying the correlated background cut. Yellow (red) histograms represent the remaining (thrown) events after applying the cut.

tails observed in the invariant mass distribution. This fact might be justified by considering the fact that the $\Sigma^-$, being reconstructed from a neutron and a negative pion, involves an experimental resolution which is a combination of the resolution of different detectors: the electromagnetic calorimeter for neutral particles and the time-of-flight and drift-chamber subsystems for charged particles.

The procedure employed to study this background is the $Q$-factors method described in reference [84]. Such a method allows one to separate (event by event) the signal from the background on a probabilistic basis. The main reason for using this procedure instead of the traditional side-band subtraction method has to do with the multiple decays and independent decay angles involved in the $\gamma n \to K^+ \Sigma^-$ reaction, each of these angles being associated with a different phase space region. The background will depend on each phase space region and so, a method where one basically attempts to estimate the background under the signal by examining the side-band regions where there is presumably no signal and only background (the side-band method) is not a very suitable choice for the type of reaction studied in this analysis since only a specific phase-space region is studied. The $Q$-factors method, on the contrary, represents a technique where the relevant decay phase space regions can be incorporated in a simultaneous way.

#### 5.11.3.1 $Q$-factors method

The $Q$-factors method is defined [84] as a probabilistic event-weighting method aimed at separating signal from background on an event-by-event basis. The main idea of the method is to choose a representative distribution $\xi$ (in this analysis, the $\Sigma^-$ mass distribution) and define, for each event, a group of closest neighbors to it. The neighbors are determined calculating the closest "distance" between the event (or rather, the $\xi_i$ value associated with the event) and the other events in the distribution. For this reaction, the nearest distance $d_{ij}$ between the $i$ and $j$ events is calculated based on the angular variables $\cos\theta^\star_{K^+}$ and $\phi_{K^+}$ according to the expression

$$d_{ij} = \sum_k \left[ \frac{(x_k)_i - (x_k)_j}{r_{ij}} \right]^2 \tag{5.9}$$

where the sum runs over $k$, the number of variables used, $(x_k)_i$ represents the value of $\cos\theta^\star_{K^+}$ and $\phi_{K^+}$ for the $i$-th event, and $r_{ij}$ is the maximum difference between any pair of events for each of the variables (in this case, it can be either 2 or $2\pi$). Usually a group of 100, 200, 500, or 1000 closest neighbors are used. Each group of closest neighbors (which includes the event itself) is fitted by means of a signal $S(\xi)$ + background $B(\xi)$ function previously defined by the user. Based on the resulting fit parameters, the pre-defined signal and background functions are evaluated at the $\xi_i$ value of the event and the probability $Q_i$ that the $i$-th event corresponds to the signal is calculated as $S(\xi_i)/(S(\xi_i) + B(\xi_i))$. Signal and background can thus be separated for any distribution (*e.g.*, $\Sigma^-$, $\cos\theta^{\star}_{K^+}$, $\phi_{K^+}$) by weighting it with either $Q_i$ (signal) or $1-Q_i$ (background). Figure 5.35 shows the signal and background separation of the invariant mass distribution using four different numbers of neighbors: 100, 200, 500, and 1000. The left panel of Figure 5.36 compares the number of total and signal events in each case. The right panel shows the signal-to-background ratio evaluated between 1.18 and 1.215 GeV/c$^2$. As can be seen, there is roughly 5% of background sitting beneath the $\Sigma^-$ peak and the values obtained in the different neighbors scenarios differ by no more than 0.5%. Based on such a small difference, $N$=200 was chosen as the reference for further systematic studies since it provides enough events to get reliable fits and also requires low-computational time compared to $N$=500 or 1000.

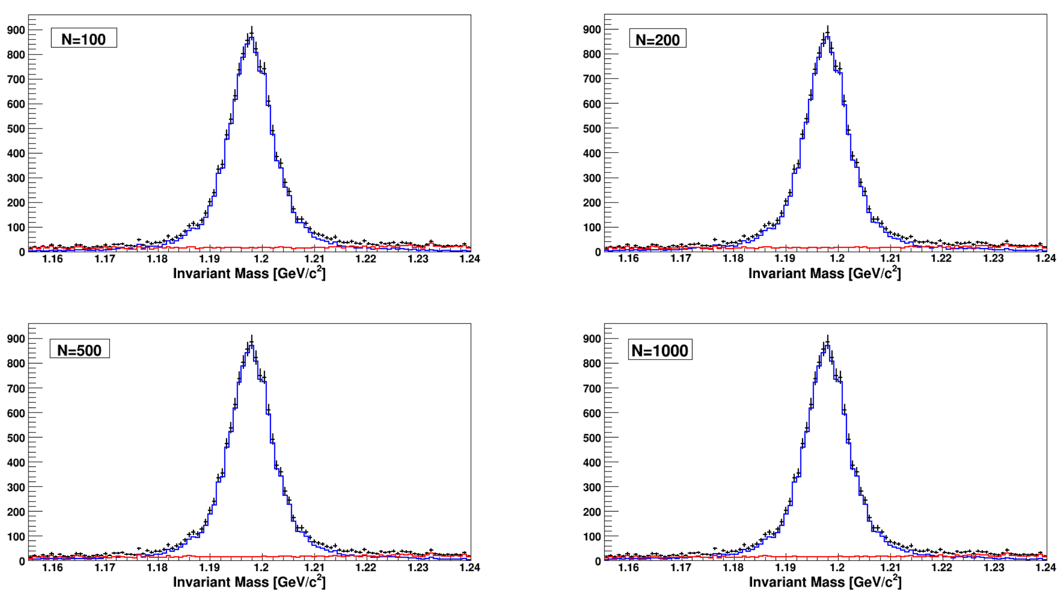


Figure 5.35: $Q$-factors method using four different number of neighbors. The invariant mass distribution (black crosses) is separated into signal (blue histogram) and background (red histogram) using a Voigtian + $1^{st}$ order polynomial function.

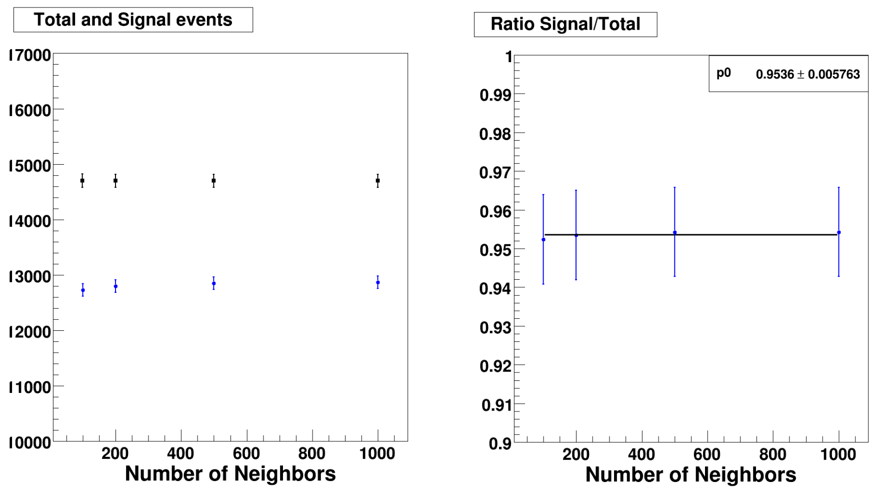


Figure 5.36: (left) Comparison between total (black) and signal (blue) number of events obtained in each neighbor scenario. (right) Signal-to-background ratio defined within a 3Γ region with Γ being the Voigtian width of about 6 MeV. The estimated background accounts for about 5% of the total number of events.

#### 5.11.3.2 Error estimation on the background subtraction

Following Reference [84], the fit error ($\sigma_{Q_i}$) of a given $Q_i$ weighting factor can be computed using the functional forms for the signal $S$ and background $B$ defined as

$$\begin{aligned} S(\xi_i) &= N\,V(\xi_i) \\ B(\xi_i) &= a_0 + a_1\xi_i \\ f_i(\xi_i,\eta) &= \frac{S(\xi_i)}{S(\xi_i)+B(\xi_i)}, \end{aligned} \tag{5.10}$$

and the inverse of the covariance matrix of the fit parameters $C_\eta$ where $\vec{\eta}$ represents the adjustable parameters $N$, $a_0$, and $a_1$. The error in $Q_i$ is thus written as

$$\sigma^2_{Q_i} = \sum_{j,k} \frac{\partial f_i}{\partial \eta_j} (C_\eta)^{-1}_{jk} \frac{\partial f_i}{\partial \eta_k} \tag{5.11}$$

Since the algorithm used to obtain the values of $Q_i$ leads to highly correlated results between each event, the resulting error on extracting the number of signal events in a specific bin is calculated assuming 100% correlation (overestimation):

$$\sigma^2_Q = \left(\sum_i \sigma_{Q_i}\right)^2 \tag{5.12}$$

with the index $i$ running over the number of events in the bin. For any distribution (*i.e.*, the $\Sigma^-$ distribution), the total error per bin $\sigma_T$ is obtained by adding in quadrature the statistical error on the number of events in the bin $\sqrt{N_{\text{signal}}}$ to Equation (5.12):

$$\sigma_T^2 = N_{\text{signal}} + \sigma_Q^2 = \sum_i Q_i + \left(\sum_i \sigma_{Q_i}\right)^2 \tag{5.13}$$

## 5.12 Summary of Cuts

All the cumulative cuts applied in the analysis are shown in Table 5.3. The remaining events are referred to the percentage of events left (respect to the initial number of events) after applying each cut.

Table 5.3: List of all cuts used in the exclusive analysis of the reaction $\gamma d \to K^+\Sigma^-(p)$.

| Section | Subsection | Cut applied | Surviving events | Remaining events (%) |
|---|---|---|---|---|
| | | Initial number of events | 28562731 | 100.00% |
| Initial skim | 5.4.2 | Beam trips | 23260668 | 81.44% |
| | 5.4.2 | 1pos&1neg&1neu in EVNT | 22766733 | 79.70% |
| | 5.4.2 | $\lvert T_{K^+} - T_\gamma \rvert < 3.0$ ns | 16489815 | 57.73% |
| | 5.4.2 | $\lvert T_{K^+} - T_{\pi^-} \rvert < 6.0$ ns | 9786136 | 34.26% |
| | 5.4.2 | Missing mass ($5\sigma$) | 4483394 | 15.70% |
| | 5.4.2 | Invariant mass ($5\sigma$) | 3049055 | 10.67% |
| Fiducial cuts | 5.8.1 | Angular cuts | 2572970 | 9.00% |
| | 5.8.3 | Bad SC paddles | 2434332 | 8.52% |
| Depos. energy | 5.6.3 | $E_{kin} - E_{tot} \geq 0$ | 2408665 | 8.43% |
| Charge PID | 5.5.3 | $\pi^-$ identification | 1717872 | 6.01% |
| | 5.5.4 | $K^+$ identification | 202630 | 0.71% |
| Vertex cut | 5.5.5 | $z$-vertex $K^+$ | 191205 | 0.67% |
| Photon select. | 5.9 | $\lvert T_{K^+} - T_\gamma \rvert < 3\sigma$ ns | 184983 | 0.65% |
| | 5.9 | $N_\gamma = 1$ | 174540 | 0.61% |
| Event select. | 5.10 | $P_{missing} < 0.150$ GeV/c | 56962 | 0.20% |
| Background | 5.11.1 | Correlated background | 49237 | 0.17% |
| Background | 5.11.2 | Photon Energy Cut | 14398 | 0.05% |

# Chapter 6: Beam Asymmetry

This chapter outlines the steps followed in this analysis to determine the photon beam asymmetry $\Sigma$ for the quasi-free reaction $\gamma\, d \to K^+\Sigma^-(p)$.

## 6.1 General definitions

The kinematics of reactions with a two-body final-state can be completely described by two parameters. Typical choices are the Mandelstam variables $s$ and $t$, or the photon energy $E_\gamma$ and the polar angle $\theta$. In this analysis, the photon beam asymmetry was determined as a function of $E_\gamma$ (lab frame) and $\cos\theta^\star_{K^+}$ (c.m. frame). Figure B.1 depicts the kinematics of the $\gamma\, n \to K^+\Sigma^-$ reaction.

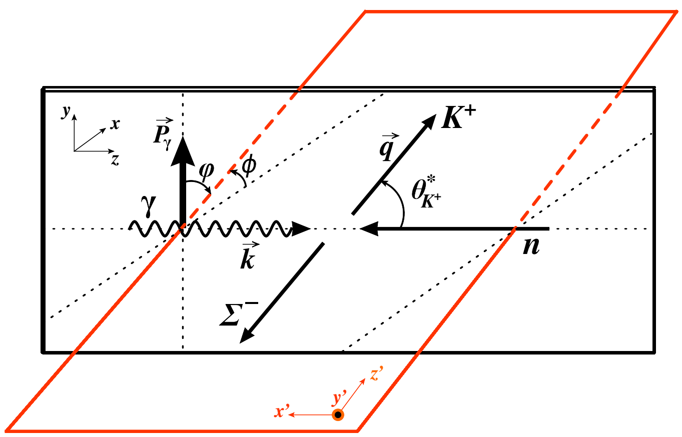


Figure 6.1: Kinematic variables for the reaction $\gamma n \to K^+\Sigma^-$ in the center-of-mass frame. The reaction plane (red rectangle) is defined by the normalized vector $\vec{k}\times\vec{q}$, where $\vec{k}$ is the momentum of the incoming photon (along the $z$-axis) and $\vec{q}$ is the momentum of the outgoing kaon. $\theta^*_{K+}$ is the scattering angle, $\varphi$ is the angle between the photon polarization vector $\vec{P}_\gamma$ (along the $y$-axis) and the reaction plane, and $\phi$ is the azimuthal angle between the $x$-axis and the reaction plane. The $x'$ and $y'$ axes are parallel and perpendicular to the reaction plane, respectively.

In g13b, two types of radiators were used: amorphous carbon and diamond. Unpolarized data taken with the carbon radiator are labeled as AMOrphous (a). For the diamond, the linearly polarized data are labeled as either PARAllel ($\|$) or PERPendicular ($\perp$), depending on whether the electric field vector $\vec{E}$ was parallel or perpendicular to the Hall B floor.

For the AMO data, the events produced on the target are uniformly distributed over the azimuthal angle $\phi$[1] (defined in Figure B.1). The only $\phi$-dependence in the recorded sample thus comes from the detector acceptance. In contrast, for the polarized data sets (PARA or PERP) the distribution is intrinsically non-uniform over $\phi$. The functional form of these distributions can be expressed as [85, 86]:

$$N(\phi)_a \sim A(\phi)F_a \tag{6.1}$$

$$N(\phi)_{\parallel} \sim A(\phi)F_{\parallel}(1 - P_{\parallel}\Sigma\cos 2(\phi + \phi_0)) \tag{6.2}$$

$$N(\phi)_{\perp} \sim A(\phi)F_{\perp}(1 + P_{\perp}\Sigma\cos 2(\phi + \phi_0)) \tag{6.3}$$

where $A(\phi)$ is the acceptance function, $F_a$, $F_{\parallel}$, and $F_{\perp}$ represent the photon fluxes for each data set, $P_{\parallel}$ and $P_{\perp}$ are the parallel and perpendicular photon beam polarizations, and $\phi_0$ gives information about how closely the spatial orientation of the photon polarization vector coincides with the nominal orientation with respect to the floor (PARA or PERP).

Due to the difficulties in accurately determining $A(\phi)$, it is more effective to extract the beam asymmetry from the ratio between distributions of events from the different data sets rather than directly from one particular distribution. If the flux ratio is known, taking such ratios also has the advantage of canceling out the effects of the acceptance. Using the ratio of polarized to unpolarized distributions ($N(\phi)_{\perp}/N(\phi)_a$ or $N(\phi)_{\parallel}/N(\phi)_a$), however, does not provide an optimal method to extract $\Sigma$ as the lower statistics taken for amorphous data ($\sim$10% of the total g13b data) significantly increases the statistical uncertainties. A better choice is to determine $\Sigma$ by calculating the asymmetry of the number of polarized events in each $\phi$-bin $\Big(N(\phi)_{\parallel} - N(\phi)_{\perp}\Big) / \Big(N(\phi)_{\parallel} + N(\phi)_{\perp}\Big)$.

## 6.2 Binning

As mentioned above, the photon beam asymmetry is extracted for different bins of photon energy $E_\gamma$ and cosine of the polar angle $\theta^\star_{K^+}$. One can think of two extreme strategies for binning, either equal statistics or equal spacing of the bin centers. The former leads to

[1] The angle $\phi$ is the same in the lab and the center-of-mass frames since the difference is only a boost along the photon direction ($z$-axis).

asymmetric bins (large and small intervals), and loss of information when integrating over the large intervals. In the latter case, one faces the problem of low statistics and large error bars in some bins. Therefore, it can sometimes be advantageous to select a binning that produces a compromise between small errors and small intervals.

For $E_\gamma$, the chosen bin size was 200 MeV, corresponding to the spacing between the experimental settings. The reason for this binning is that the figure of merit (FOM) goes as $NP^2$ where $N$ is the number of photons at a certain photon energy and $P = P(E_\gamma)$ is the polarization of that photon. Therefore, although a wider photon energy bin improves statistics it does not have a significant impact on the FOM since the polarization decreases when moving away from the coherent edge position[2] ($E'_\gamma$). At the same time, having a wider energy bin will increase the background (some of it may even be polarized), and increase the systematic uncertainty in the polarization. The $E_\gamma$ binning was implemented by selecting a 200-MeV region below the coherent edge in the photon energy distribution for the polarized data. As shown in Figure 6.2, the upper limit of the region was defined to be 50 MeV away from $E'_\gamma$ to avoid issues with the stability of the coherent peak.

For $\cos\theta^\star_{K^+}$ a total of 11 asymmetric bins (per $E_\gamma$ bin) were used. Figure 6.3 shows the $\cos\theta^\star_{K^+}$ distributions for polarized data in the center-of-mass frame for the photon energy setting 2.1-2.3 GeV. The poor statistics at very forward angles is a consequence of the reversed torus field, optimized for low-momentum $\pi^-$ from hyperon decay, which bends the $K^+$ towards the beam pipe. Those angles, however, have been measured before (see Chapter 3) and are not as important for $N^\star$ physics since they are usually dominated by $t$-channel and not $s$-channel where the $N^\star$ resonances live. On the other hand, this field setting in g13 made it possible to collect significant statistics over a wide angular range, and in particular at backward angles. The percentage of events per $\cos\theta^\star_{K^+}$ bin is presented in Table 6.1.

[2]The coherent edge is defined as the part of the slope of the photon energy peak with the most negative gradient. Usually the midpoint of the slope is taken as the value for the coherent edge position.

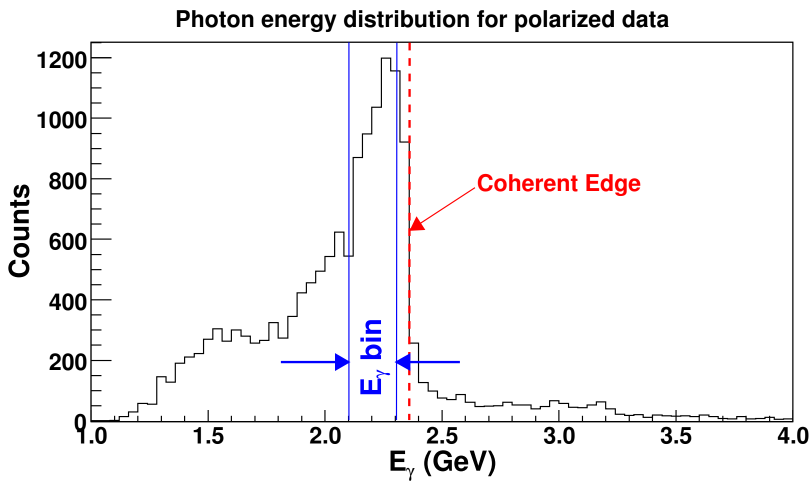


Figure 6.2: Photon energy distribution for the 2.1-2.3 GeV photon energy setting. The main coherent peak located at around 2.3 GeV corresponds to the highest degree of linear polarization obtained for the energy setting. The red dashed line represents the coherent edge position ($E'_\gamma$) and the blue vertical lines, the photon energy range selected (between approximately $E'_\gamma - 0.2$ GeV and $E'_\gamma$) to determine the photon beam asymmetry $\Sigma$.

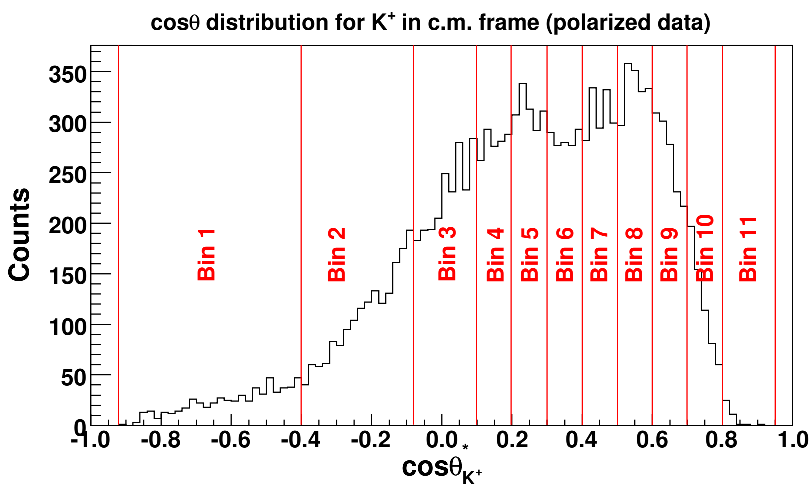


Figure 6.3: $K^+$ $\cos\theta$ distributions (C.M. frame) for the 2.1-2.3 GeV energy setting. The red vertical lines represent the binning used for the determination of the photon beam asymmetry $\Sigma$. Notice the significant statistics at backward angles. The histogram was filled after applying all the analysis cuts discussed in the previous chapter.

## 6.3 Parameters for $\Sigma$ extraction

The photon beam asymmetry extraction depends strongly on three parameters: the photon polarization, the $\phi_0$ offset, and the photon flux ratio. All of these are independent of

Table 6.1: Binning in $\cos\theta^*_{K+}$ used to determine the photon beam asymmetry for the 2.1-2.3 GeV energy setting. The binning is the same for PARA and PERP data sets. The percentage of the total number of events in each bin is shown in the rightmost column. Due to the very low statistics, the very forward angle bin (0.8-0.95) was discarded from the analysis.

| Bin No. | Angular range | Events (%) |
|---|---|---|
| 1 | $-0.92 \leq \cos\theta^*_{K+} < -0.40$ | 2.6 |
| 2 | $-0.40 \leq \cos\theta^*_{K+} < -0.08$ | 4.0 |
| 3 | $-0.08 \leq \cos\theta^*_{K+} < 0.10$ | 12.5 |
| 4 | $0.10 \leq \cos\theta^*_{K+} < 0.20$ | 12.9 |
| 5 | $0.20 \leq \cos\theta^*_{K+} < 0.30$ | 12.4 |
| 6 | $0.30 \leq \cos\theta^*_{K+} < 0.40$ | 12.4 |
| 7 | $0.40 \leq \cos\theta^*_{K+} < 0.50$ | 12.6 |
| 8 | $0.50 \leq \cos\theta^*_{K+} < 0.60$ | 13.5 |
| 9 | $0.60 \leq \cos\theta^*_{K+} < 0.70$ | 11.5 |
| 10 | $0.70 \leq \cos\theta^*_{K+} < 0.80$ | 5.0 |
| 11 | $0.80 \leq \cos\theta^*_{K+} \leq 0.95$ | 0.3 |

kinematic and final-state parameters, so they do not necessarily have to be obtained from the reaction of interest. The first one can be determined from Bremsstrahlung calculations, and the other two from high-statistics channels (single-$\pi$ channels) where one is limited by systematics and not by statistics. The way they are determined in this analysis is shown below.

### 6.3.1 Photon polarization

As explained in Section 4.3.2, the position of the coherent peak $E'_\gamma$ depends on the orientation of the diamond with respect to the incident electron beam, and the degree of photon linear polarization depends on the electron beam energy $E_e$ and on the ratio $(E'_\gamma/E_e)$. Therefore one can obtain the same coherent peak with different $E_e$. However, the degree of linear polarization will be different in each case.

For a fixed value of $E'_\gamma$ and $E_e$, the photon polarization is determined based on the ANalytic Bremsstrahlung calculation code (ANB)[3] [87]. This code implements realistic

[3]The ANB code is an analytical calculation of bremsstrahlung spectra with an approximate treatment of

theoretical functions for both the enhancement (defined as the ratio between polarized and unpolarized spectra) and the beam polarization through the incorporation of smearing due to beam collimation and beam divergence, coherent bremsstrahlung contributions from different reciprocal lattice vectors of the crystal, and incoherent contributions from the crystal. Such features are included in the theoretical functions in the form of five adjustable parameters. The main idea of the procedure employed to calculate the photon beam polarization is based on the determination of these five parameters. The best set of values is obtained by fitting the experimental enhancement with the corresponding theoretical function defined in the ANB code. The five extracted fitting parameters are then input in the theoretical expression for the polarization, producing as a final output the polarization for each crystal plane (PARA or PERP) as a function of the photon energy (see Figure 6.4). As a result, a look-up polarization table is produced for each photon energy (or each 9 MeV wide E-counter) and for each coherent-edge position (in steps of 1 MeV).

Due to instabilities in the position of the electron beam, the coherent-edge position can drift significantly during a run, leading to have not one single coherent edge position but a distribution of them. This requires several polarization tables for a specific photon-energy setting, and so what is determined for each photon-energy setting is actually a photon polarization averaged over all the look-up polarization tables. Two different methods can be used to determine the average polarization: an analysis-independent method and an analysis-related method. The former takes all the coherent edges and weights the polarization in each E-counter $P_i(E_j)$ according to the number of events $N_i$ in the corresponding coherent edge distribution. For a total of $M$ coherent edges, the weighted polarization $P_w(E_j)$ for the $j$-th E-counter can be expressed as:

$$P_w(E_j) = \frac{\displaystyle\sum_{i=1}^{M} P_i(E_j)\, N_i}{\displaystyle\sum_{i=1}^{M} N_i} \tag{6.4}$$

where the index $i$ runs over the coherent edge distribution and index $j$ over the E-counters. This reduces the polarization tables to only one table per plane per photon energy setting per electron energy beam in which each E-counter has an average polarization given

beam divergence, multiple scattering, and finite beam spot size.

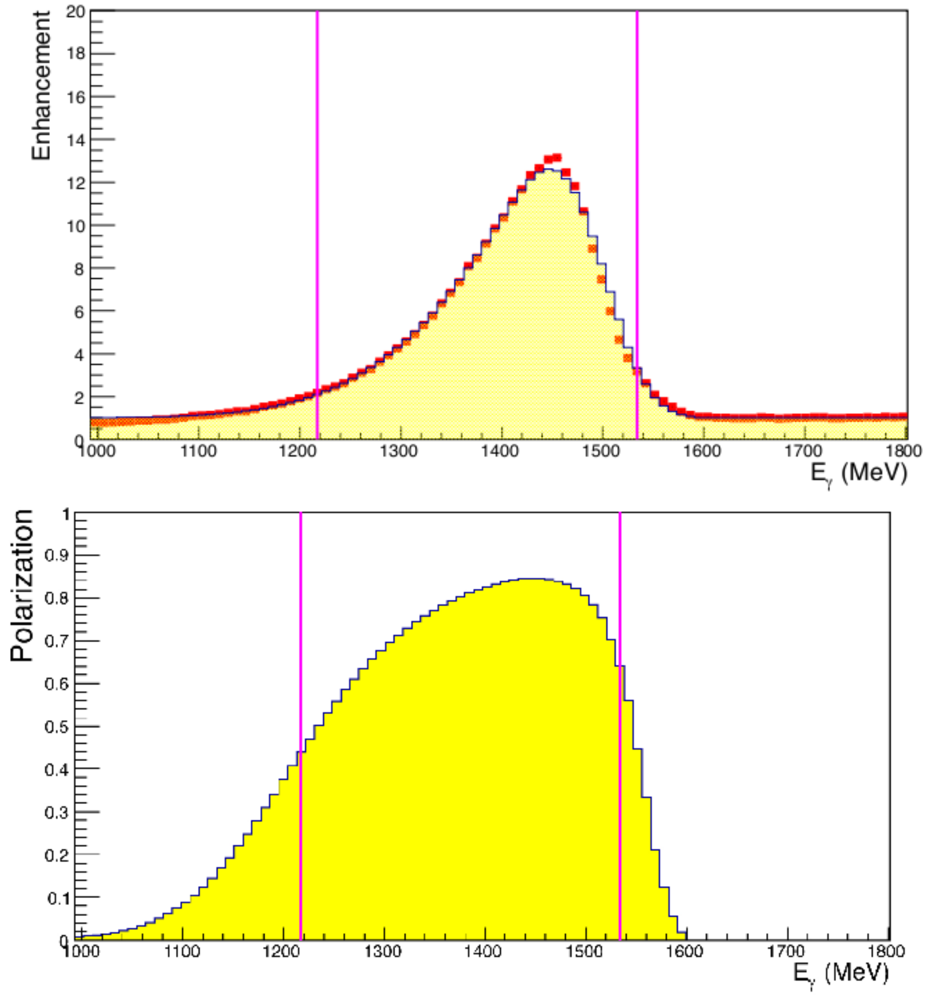


Figure 6.4: Enhancement (top panel) for Para event-by-event data (red squares) with the coherent-edge positioned at about 1.501 GeV. Degree of photon polarization (bottom panel) determined from the corresponding enhancement fit. The blue line in the upper panel corresponds to the fitted enhancement function implemented in the ANB code. The magenta lines represent just a visualization guide to compare the enhancement and the photon polarization plots. Figure taken from [88].

by (6.4). A single mean polarization number $\bar{P}$ for each plane can be obtained by weighting the polarization in each E-counter $P_w(E_k)$ with the number of photons $N(E_k)$ in the corresponding E-counter:

$$\bar{P} = \frac{\sum_k P_w(E_k)\, N(E_k)}{\sum_k N(E_k)} \tag{6.5}$$

with $k$ running over the E-counters. This method is completely general in the sense that no relation to a specific analysis reaction is needed.

An alternative method calculates the average polarization directly from the events of interest (the yields) of the reaction under study. For each event passing all the selection criteria, the polarization of the associated photon is retrieved from the look-up tables depending on the event's coherent-edge position and on the photon energy. An accumulated polarization (for each plane) is obtained by adding up the polarization of each good event. When this sum is divided by the total number of good events, an average photon polarization over the corresponding photon-energy setting is obtained. The simplicity and analysis-dependent character of this method makes it more reliable, which is the reason for which it was chosen in this analysis to determine the average photon beam polarization. Table 6.2 shows the polarization values obtained.

Table 6.2: Mean polarization values for g13b data determined in this analysis.

| Coherent peak [GeV] | Electron energy beam [GeV] | Mean polarization $\bar{P}$ PARA (%) | PERP (%) |
|---|---|---|---|
| 2.1 | 5.057 | 76 | 76 |
| 2.3 | 5.157 | 72 | 72 |

### 6.3.2 $\phi_0$ offset

Being a mechanical parameter, $\phi_0$ can be assumed to have remained fixed at least between realignments of the diamond radiator. This parameter was determined from an independent analysis [89] using a channel with high statistics ($\gamma n \to p\pi^-$) for the photon energy setting 1.1-1.3 GeV, integrating over all $\cos\theta$ bins with a positive beam asymmetry. As displayed in Figure 6.5, the corresponding $\phi$ distributions were fitted based on the asymmetry of (not normalized) polarized events $(N_\parallel - N_\perp)/(N_\parallel + N_\perp)$. The $\phi_0$ value obtained from this analysis was $0.125° \pm 0.172°$. This is the value used for the extraction of the $\Sigma^-$ beam asymmetry.

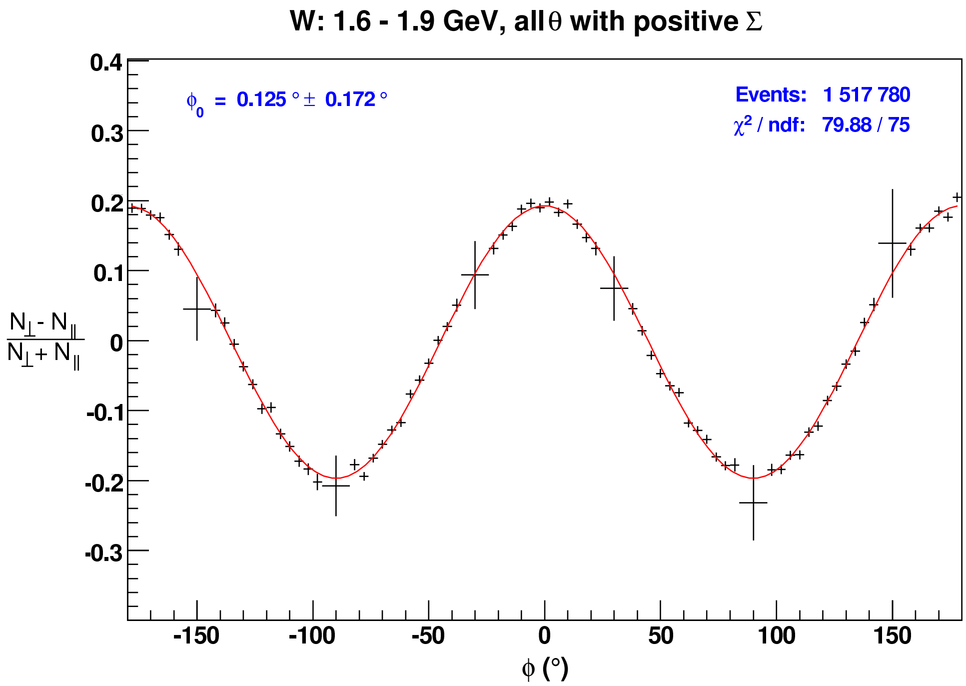


Figure 6.5: Asymmetry distribution of polarized events for the $\gamma n \to p\pi^-$ reaction for the photon energy setting 1.1-1.3 GeV. Only $\cos\theta$ bins with a positive beam asymmetry (-0.7< $\cos\theta^\star$ <-0.1, and 0.6< $\cos\theta^\star$ <0.8) were taken into account in the fit of the distribution. The plot was taken from reference [89].

### 6.3.3 Photon flux ratio $F_R$

The photon flux ratio should ideally be determined from a reaction offering good statistics and systematics. Since the $\gamma n \to K^+\Sigma^-$ is a low-statistics channel, the final values of the flux ratio used in this work were taken from the analysis of the high-statistical channel $\gamma d \to pn$ studied with the g13b data [88]. Table 6.3 shows such average flux ratios. The main idea behind the procedure followed to obtain the average flux ratio values consists of fixing the polarization ratio and the $\phi_0$ parameters, and extract the flux ratio from the fit of $(N_{\parallel} - N_{\perp})/(N_{\parallel} + N_{\perp})$ by integrating over all the polar angle. In this way, the sensitivity of the fits to any statistical fluctuations is greatly reduced.

Table 6.3: Average photon-flux ratios $F_R$ obtained from a high-statistical channel [88].

| Coherent peak [GeV] | $F_R$ | $\Delta F_R$ |
|---|---|---|
| 2.1 | 1.233 | 0.038 |
| 2.3 | 0.944 | 0.039 |

## 6.4 Photon beam asymmetry extraction

In this analysis the photon beam asymmetry was extracted using two different approaches: the $\phi$-bin method and method of moments. These methods, along with the corresponding asymmetries, are presented in the following subsections.

### 6.4.1 The $\phi$-bin method

In this approach, for each $E_\gamma$ and $\cos\theta^*_{K^+}$ bin, the photon beam asymmetry is extracted by fitting the corresponding azimuthal distribution. The functional form of the fit function can be derived by taking the asymmetry of the distribution of polarized events $N(\phi)_{\parallel}$ and $N(\phi)_{\perp}$ (Equations 6.2 and 6.3, respectively) as follows:

$$\frac{N(\phi)_{\perp} - N(\phi)_{\parallel}}{N(\phi)_{\perp} + N(\phi)_{\parallel}} = \frac{F_{\perp}(1 + P_{\perp}\Sigma\cos 2(\phi+\phi_0)) - F_{\parallel}(1 - P_{\parallel}\Sigma\cos 2(\phi+\phi_0))}{F_{\perp}(1 + P_{\perp}\Sigma\cos 2(\phi+\phi_0)) + F_{\parallel}(1 - P_{\parallel}\Sigma\cos 2(\phi+\phi_0))} \tag{6.6}$$

which can be written in a more suitable fitting form as:

$$\boxed{\frac{N(\phi)_{\perp} - N(\phi)_{\parallel}}{N(\phi)_{\perp} + N(\phi)_{\parallel}} = \frac{(1-A) + \left(\dfrac{1+A\,B}{1+B}\right) 2C\cos[2(\phi+D))]}{(1+A) + \left(\dfrac{1-A\,B}{1+B}\right) 2C\cos 2[(\phi+D))]}} \tag{6.7}$$

where $A = F_R$ is the flux ratio $F_{\parallel}/F_{\perp}$, $B = P_R$ is the polarization ratio $\bar{P}_{\parallel}/\bar{P}_{\perp}$, $C = \bar{P}\Sigma$ with $\bar{P}$ corresponding to the average polarization $(\bar{P}_{\parallel} + \bar{P}_{\perp})/2$, and $D = \phi_0$. Hence, by obtaining $C$ from the fit and knowing $\bar{P}$, it is possible to extract the beam asymmetry $\Sigma$.

Since this method requires binning in the azimuthal angle, and $K^+\Sigma^-$ is a relatively low-statistics channel, one runs into the problem of finding the best $\phi$ binning. On one hand, having many bins means that one is not integrating out any of the dependence on $\phi$; on the other hand, the systematic uncertainty in the signal extraction gets worse for bins with low statistics. Thus, the ideal scenario would be to be in a plateau between these two extremes where there is sufficient statistics but the integration over $\phi$ does not produce a significant loss of information.

Different binning of constant width for $\phi$ ($\Delta\phi$ =12.5, 16.67, and 25°) was tried in order to choose the one where as much of the angular information per bin is retained without picking up too much systematic uncertainty. The $\Delta\phi$ bin sizes were selected following the angular fiducial cuts (Section 5.8.1) in which 5° are removed from the edge of each sector. Except at very forward angles, this cuts out the coil regions, reducing the azimuthal coverage of each sector from 60° to 50°. Therefore, $\Delta\phi$=12.5°, for instance, means dividing the 50° region of each sector into four equal parts. In addition, the lower and upper limits of $\phi$ were set between -35° and +325° in order to avoid the usual separation of sector 4 when the limits are set between -180 and +180°. These two conditions prevent data from migrating towards the coil regions. Figures 6.6 and 6.7 show an example of the azimuthal angular distribution for $\Delta\phi$ =12.5, and 25°, respectively, for the 2.1-2.3 GeV photon energy setting and for all $\cos\theta^{\star}_{K^+}$ bins. The bad fit observed in the very forward angular bin is caused by its very low statistics. For this reason, that bin was not taken into account in the determination of the beam asymmetry.

Each fit is performed by fixing the $F_R$, $P_R$, and $\phi_0$ parameters with the values defined above (Section 6.3). This leaves Equation (6.7) as a function of a single parameter, $C$, from which the beam asymmetry can be extracted. The fit to each ($E_\gamma$, $\cos\theta^{\star}_{K^+}$) bin therefore produces a unique beam asymmetry point. Figure 6.8 shows the photon beam asymmetries as a function of $\cos\theta_{K^+}$ in the center-of-mass frame for the 2.1-2.3 GeV photon energy bin and for different $\Delta\phi$ widths. The systematic uncertainty due to the choice of binning is significant compared with the statistical uncertainty in each bin, but there is no obvious trend. This fact makes it difficult to select the optimal $\Delta\phi$ bin.

A study concerned with the sensitivity of the beam asymmetry $\Sigma$ on different parameters

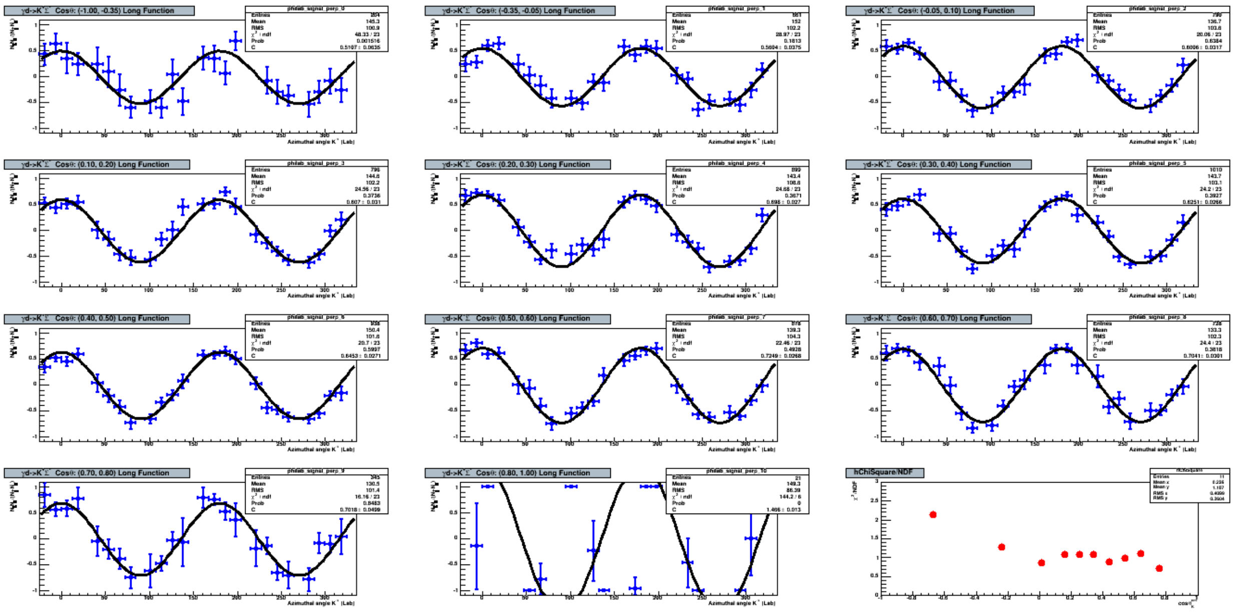

Figure 6.6: Asymmetry distribution for the photon energy setting 2.1-2.3 GeV and $\Delta\phi$=12.5°. The bottom right corner plot shows the corresponding $\chi^2$ of each fit.

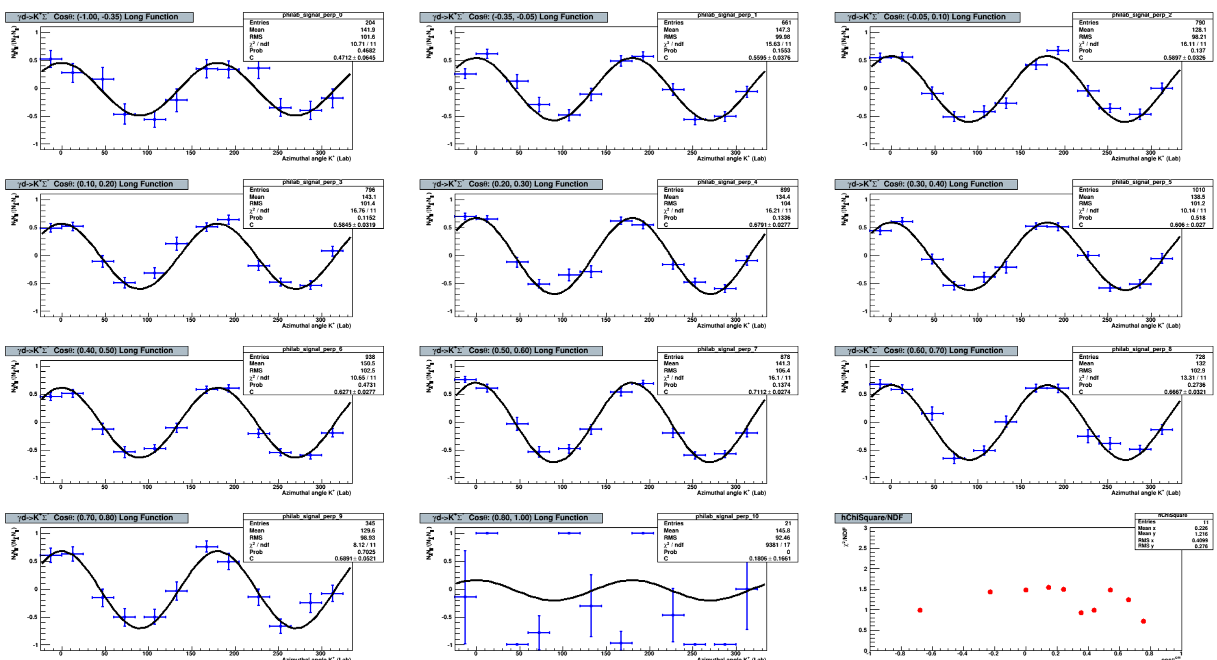

Figure 6.7: Asymmetry distribution for the photon energy setting 2.1-2.3 GeV and $\Delta\phi$=25°. The bottom right corner plot shows the $\chi^2$ associated with each fit.

has been carried out recently by Zachariou and Ilieva [90]. From these studies, the authors developed a correction factor related to the sensitivity of $\Sigma$ on the $\phi$-bin width. In the

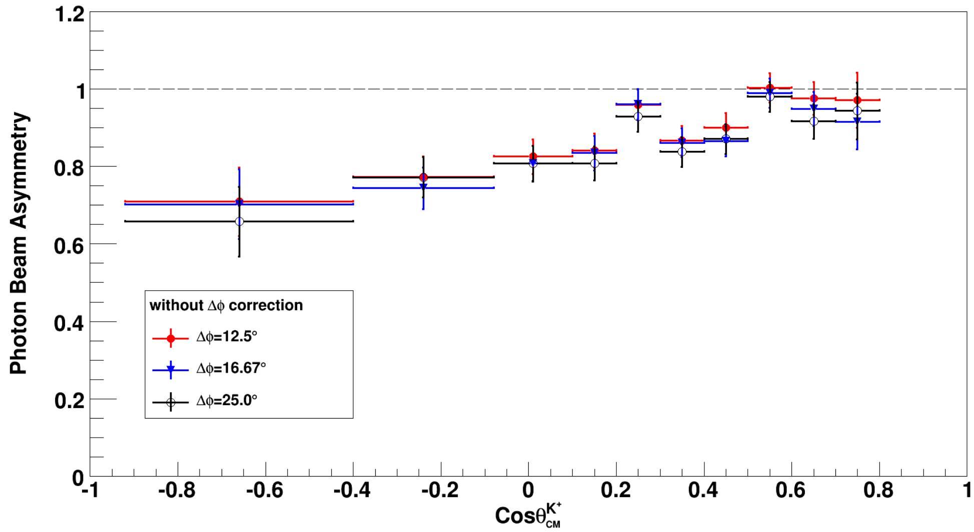


Figure 6.8: Photon beam asymmetry as a function of $\cos\theta^{\star}_{K^+}$ extracted using the $\phi$-bin method through Equation (6.7) for different $\Delta\phi$ widths: 12.5, 16.67, and 25° for the 2.1-2.3 GeV photon energy setting. The asymmetry $\Sigma$ is obtained from the fit parameter $C = \bar{P}\Sigma$. Only statistical uncertainties are shown.

general case of a $\phi$-bin width of size $\Delta\phi$, Equation (6.7) would actually determine the parameter $C = \bar{P}\Sigma\dfrac{\sin[\Delta\phi]}{\Delta\phi}$ rather than $C = \bar{P}\Sigma$. The term $\sin[\Delta\phi]/\Delta\phi$ represents a correction factor which in the limit of infinitely small bin width $\left(\lim\limits_{\Delta\phi\to 0}(\sin[\Delta\phi]/\Delta\phi) = 1\right)$ reproduces $C = \bar{P}\Sigma$. The photon beam asymmetries resulting after applying the correction factor are shown in Figure 6.9. It can be seen that the systematic uncertainties on the asymmetries due to the $\phi$ binning choice seem to be reduced. The effect of the $\Delta\phi$ correction can be observed more clearly in Figure 6.10 where the differences between the asymmetries obtained with $\Delta\phi$=25° and those obtained with the other two $\Delta\phi$=12.5, and 16.67° are calculated. As can be seen, the correction factor makes the differences approach more closely to zero, indicating the validity of the correction. The differences, however, tend to be significantly larger in the case of small $\Delta\phi$ widths. Without the correction, the highest difference obtained $[\Sigma(25°) - \Sigma(12.5°)]$ accounts, on average, for about 2.9%; with the correction in place, such a difference does not scale, on average, over about 0.82%. For the case of $[\Sigma(25°) - \Sigma(16.67°)]$, the correction reduces the difference from roughly 1.2% to 0.3% while for $[\Sigma(25°) - \Sigma(16.67°)]$, the difference is reduced from about 1.7% to 1.2%.

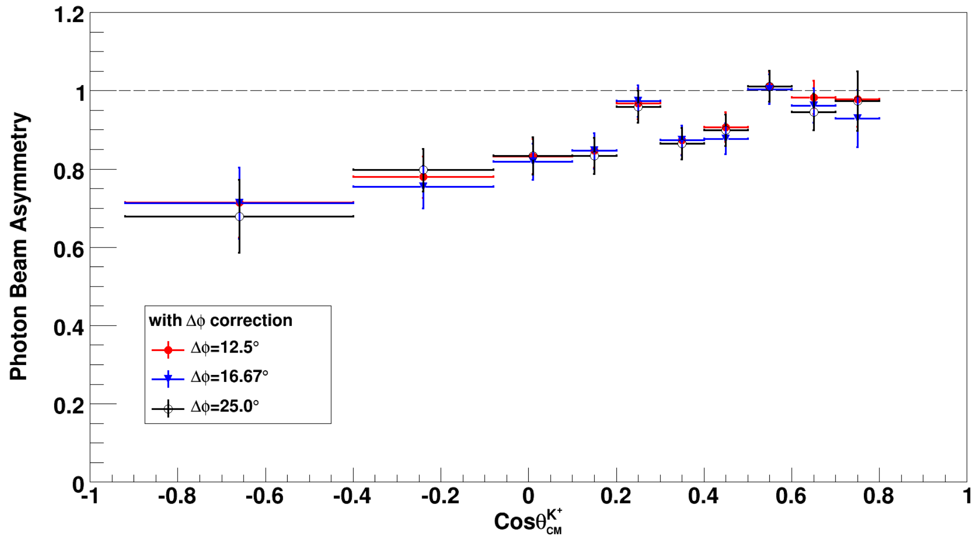


Figure 6.9: Photon beam asymmetry as a function of $\cos\theta^{\star}_{K^+}$ extracted using the $\phi$-bin method through Equation (6.7) for different $\Delta\phi$ widths: 12.5, 16.67, and 25° for the 2.1-2.3 GeV photon energy setting. The asymmetry $\Sigma$ is obtained from the fit parameter $C = \bar{P}\Sigma(\sin[\Delta\phi]/\Delta\phi)$. Only statistical uncertainties are shown.

#### 6.4.1.1 Uncertainty in the $\phi$-bin method

The statistical uncertainty $\sigma_R$ of the ratio $R = \dfrac{N(\phi)_{\perp} - N(\phi)_{\parallel}}{N(\phi)_{\perp} + N(\phi)_{\parallel}}$ is calculated by propagating the uncertainties related to $N_{\perp}$ and $N_{\parallel}$ [91]. $\sigma_R$ is then given by

$$\sigma_R = \frac{2\sqrt{N(\phi)_{\perp} N(\phi)_{\parallel}}}{(N(\phi)_{\perp} + N(\phi)_{\parallel})^{3/2}} \tag{6.8}$$

By assuming that $F_{\perp} = F_{\parallel}$, $P_{\perp} = P_{\parallel} = P$, and by neglecting the uncertainty in $P$, an estimate of the statistical error associated with the determination of the beam asymmetry via the $\phi$-bin method is obtained according to:

$$\sigma_{\Sigma} = \frac{\sigma_R}{P} = \frac{2\sqrt{N(\phi)_{\perp} N(\phi)_{\parallel}}}{P[N(\phi)_{\perp} + N(\phi)_{\parallel}]^{3/2}} \tag{6.9}$$

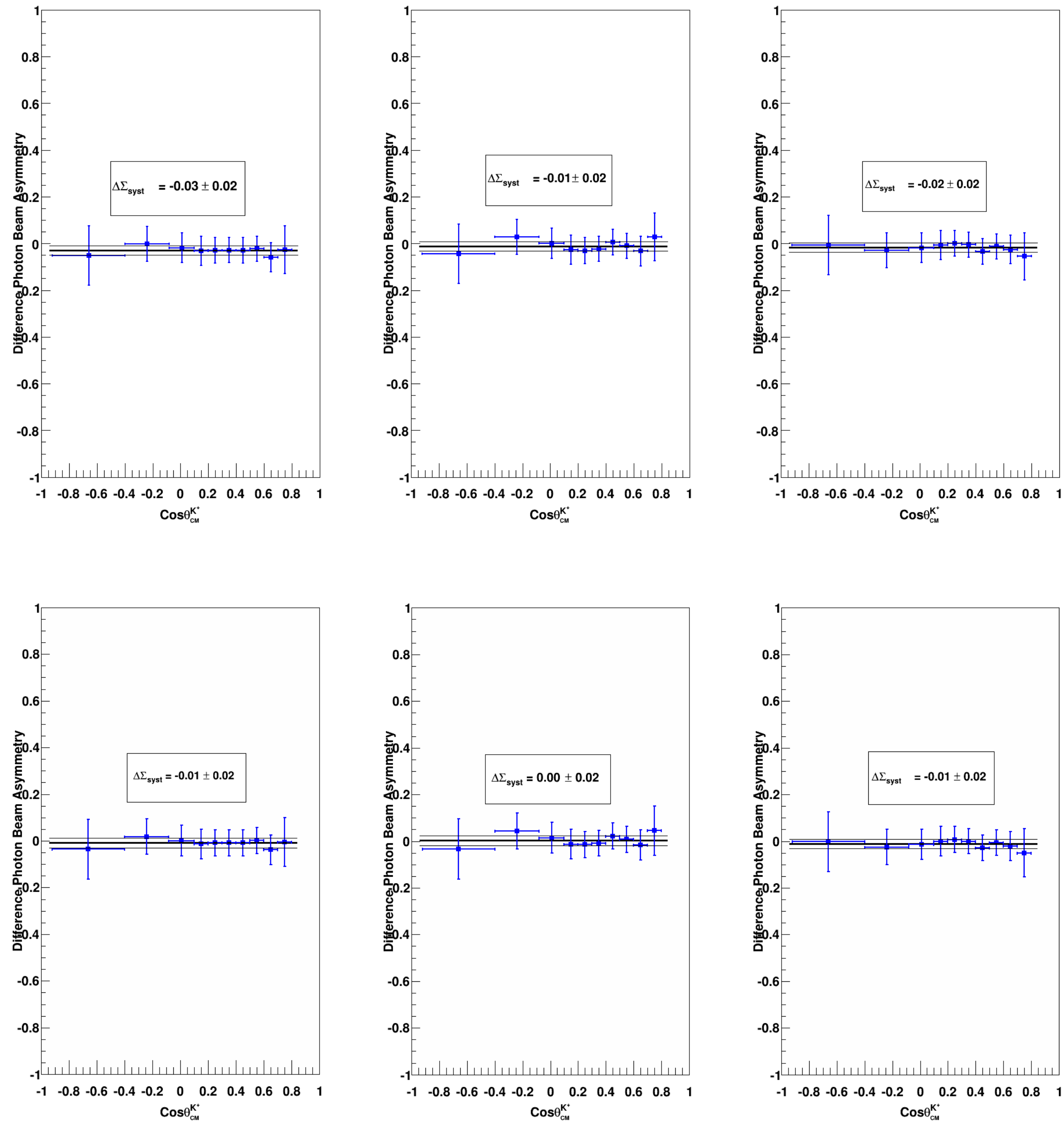


Figure 6.10: Difference between the photon beam asymmetries as a function of $\cos\theta^{\star}_{K+}$ determined by using different $\Delta\phi$ widths for the 2.1-2.3 GeV photon energy setting. (left) $\Sigma(25°)$-$\Sigma(12.5°)$, (middle) $\Sigma(25°)$-$\Sigma(16.67°)$, and (right) $\Sigma(16.67°)$-$\Sigma(12.5°)$. Top panels show the asymmetries without the $\Delta\phi$ correction factor. Bottom panels include the correction factor.

### 6.4.2 Method of moments

Another approach to extract the photon beam asymmetry is the method of moments, which is based on a Fourier moment extraction algorithm. This is the first time this approach is applied to a low-statistics channel in CLAS. The method of moments, derived in Ref. [92], consists of constructing moment-$n$ histograms for a relevant distribution (in this case, the $\Sigma^-$ invariant mass distribution). The moments (either for $\parallel$ or $\perp$) are calculated as:

$$Y_0 = \sum_{i=1}^{N} 1 \times Q_i$$
$$Y_m = \sum_{i=1}^{N} \cos[m(\phi_i + \phi_0)] \times Q_i$$

where $m$ can be any positive integer, $\phi_i$ is the azimuthal angle corresponding to the $i$th-event, $\phi_0$ is the azimuthal offset (Section 6.3.2), $N$ the total number of $\Sigma^-$ events, and $Q_i$ is the corresponding Q-factor value. Examples of some of those moments histograms are shown in Figure 6.11.

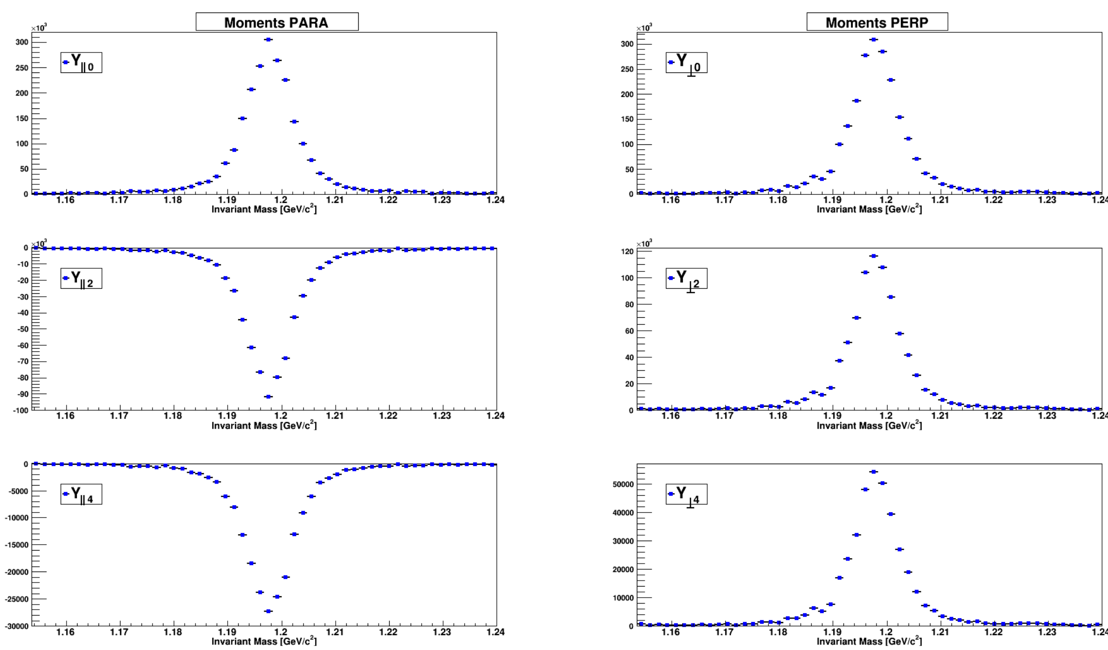


Figure 6.11: 0, 2, and 4th moments histograms for the invariant mass distribution: on the left, para data; on the right, perp data. In the method of moments, the photon beam asymmetry is calculated based on these histograms.

The histograms for different moments are combined to calculate the beam asymmetry $\Sigma$ according to the relation:

$$\boxed{\Sigma = \frac{2\left(F_R Y_{\perp 2} - Y_{\parallel 2}\right)}{F_R \bar{P}_{\parallel}(Y_{\perp 0} + Y_{\perp 4}) + \bar{P}_{\perp}(Y_{\parallel 0} + Y_{\parallel 4})}} \tag{6.10}$$

where $F_R$ is the photon flux ratio, $\bar{P}_{\parallel}$ and $\bar{P}_{\perp}$ are the mean polarizations, and $Y_{\parallel,\perp 0}$, $Y_{\parallel,\perp 2}$, and $Y_{\parallel,\perp 4}$ are the 0, 2, and 4th moments for both polarization orientations. The values used for $F_R$, and $\bar{P}_{\parallel}$ and $\bar{P}_{\perp}$ are the same used in the $\phi$-bin method. An example of the numerator and denominator of Equation (6.10) is shown in Figure 6.12 for the 0.6$<\cos\theta^{\star}_{K^+}<$0.7 bin and the 2.1-2.3 GeV photon-energy setting.

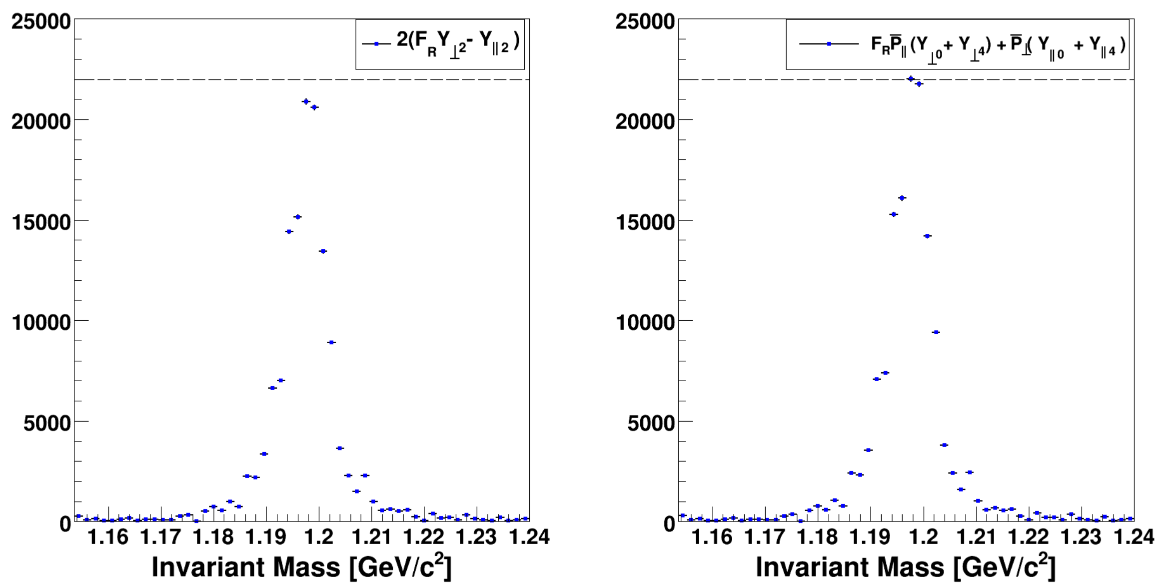


Figure 6.12: Histograms for the numerator and denominator of Equation (6.10) projected on the invariant mass distribution for the 0.6$<\cos\theta^{\star}_{K^+}<$0.7 bin. The distribution correspond to the 2.1-2.3 GeV photon-energy setting.

The advantage of the method of moments is that instead of partitioning the data for a given $E_\gamma$ and $\cos\theta^{\star}_{K^+}$ into various $\phi$ bins, all the data are used simultaneously to determine the beam asymmetry $\Sigma$. This avoids losing information when integrating over the bin in the azimuthal angle as is the case for the $\phi$-bin method. It has been argued that this should make the method of moments more reliable for bins with low statistics. Figure 6.13

shows the photon beam asymmetries obtained with the method of moments for the 2.1-2.3 photon-energy bin.

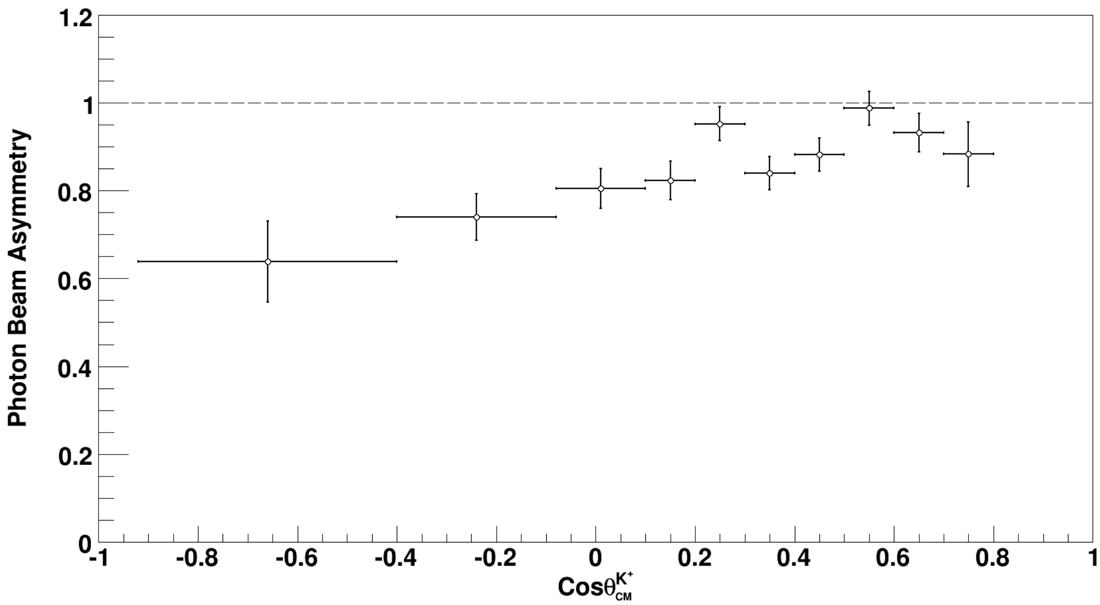


Figure 6.13: Photon beam asymmetry as a function of $\cos\theta^{\star}_{K^+}$ extracted using the method of moments through Equation (6.10) for the 2.1-2.3 GeV photon energy setting. Only statistical uncertainties are shown.

#### 6.4.2.1 Uncertainties in the method of moments

According to Ref. [92], the variance $\sigma^2_\Sigma$ associated with the method of moments is calculated from the relation:

$$\sigma^2_\Sigma = \Sigma^2 \left( \frac{\sigma^2_{num}}{num^2} + \frac{\sigma^2_{den}}{den^2} - \frac{2Cov(num, den)}{num \times den} \right) \tag{6.11}$$

with

$$\sigma^2_{num} = \frac{1}{2}\left( F^2_R (Y_{\perp 0} + Y_{\perp 4}) + (Y_{\parallel 0} + Y_{\parallel 4}) \right),$$

$$\sigma^2_{den} = \frac{1}{8}\left( F^2_R \bar{P}^2_\parallel (3Y_{\perp 0} + 4Y_{\perp 4} + Y_{\perp 8}) + \bar{P}^2_\perp (3Y_{\parallel 0} + 4Y_{\parallel 4} + Y_{\parallel 8}) \right),$$

and

$$Cov(num, den) = \frac{1}{4}\left( F^2_R \bar{P}^2_\parallel (3Y_{\perp 2} + Y_{\perp 6}) - \bar{P}^2_\perp (3Y_{\parallel 2} + Y_{\parallel 6}) \right)$$

where $num$, $den$, and $Cov(num, den)$ represent the numerator, denominator, and covariance of the Equation 6.10, respectively. The statistical error associated with the determination of the beam asymmetry via the method of moments corresponds then to the square root of the variance $\sqrt{\sigma_{\Sigma}^2}$.

In summary, the photon beam asymmetries for the quasi-free reaction $\gamma n \rightarrow K^+\Sigma^-$ were determined from an exclusive analysis using two different methods: the $\phi$-bin method and the method of moments. A detailed study of the systematic uncertainties related to the determination of the beam asymmetry using these two methods as well as to kinematical cuts and parameters involved in the determination of $\Sigma$ is carried out in the next Chapter.

# Chapter 7: Systematics on the Beam Asymmetry Determination

The estimation of systematic errors associated with the determination of the photon beam asymmetry is performed based on three main factors:

- the method employed to determine the photon beam asymmetry,
- the kinematical cuts used to extract the $\Sigma^-$ yields, and
- the sensitivity of the asymmetry with the parameters $\bar{P}_{\parallel}$, $\bar{P}_{\perp}$, $\phi_0$, and $F_R$.

## 7.1 Systematics Related to the Extraction Method

In the previous Chapter the photon beam asymmetry was determined by using two different methods: the $\phi$-bin method and the method of moments. Since the fitting uncertainties will be large once the data are sliced up into $\phi$ bins, the method of moments is expected to produce more reliable results in low statistics bins. Based on this, the method of moments is chosen as the reference method from which all the systematics are calculated. This section investigates the systematic errors on the beam asymmetry associated with the use of both methods.

Given that the method of moments [Equation (6.10)] requires the perpendicular and parallel yields to be balanced, it is more convenient for comparison purposes to require a similar balancing act for the $\phi$-bin method. Equation (6.7) can then be rewritten in the short form

$$\frac{F_R P_R N_{\perp} - P_R N_{\parallel}}{F_R P_R N_{\perp} + N_{\parallel}} = D \cos 2(\phi + \phi_0) \tag{7.1}$$

such that the fit is restricted to depend only on one free parameter: $D = P_{\parallel} \Sigma(\sin[\Delta\phi]/\Delta\phi)$. This should more tightly constrain the fit to be more comparable to the method of moments. Figure 7.1 shows the photon beam asymmetry obtained with each method. As can be noticed, the systematic errors are more significant at backward and forward angles where the statistics is limited compared to the central bins.

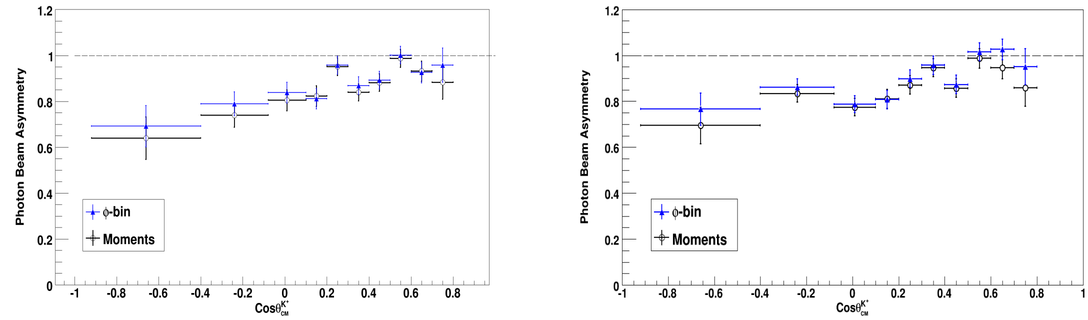


Figure 7.1: Photon beam asymmetry as a function of $\cos\theta^{\star}_{K+}$ determined using the $\phi$-bin method (solid blue triangles) and the method of moments (open black circles) for the 2.1-2.3 GeV (left) and 1.9-2.1 GeV (right) photon energy settings.

The difference of such asymmetries as a function of $\cos\theta^{\star}_{K+}$ is presented in Figure 7.2. Since there is not an obvious dependence of the difference with $\cos\theta^{\star}_{K+}$, the points were fitted using a $0^{th}$-order polynomial to determine the mean value. The mean values $\Delta\Sigma$, along with their uncertainties, are indicated by horizontal lines. On average, these differences correspond to about -0.02 $\pm$ 0.02 (2.1-2.3 GeV set) and -0.03 $\pm$ 0.02 (1.9-2.1 GeV set) of the photon beam asymmetry $\Sigma$.

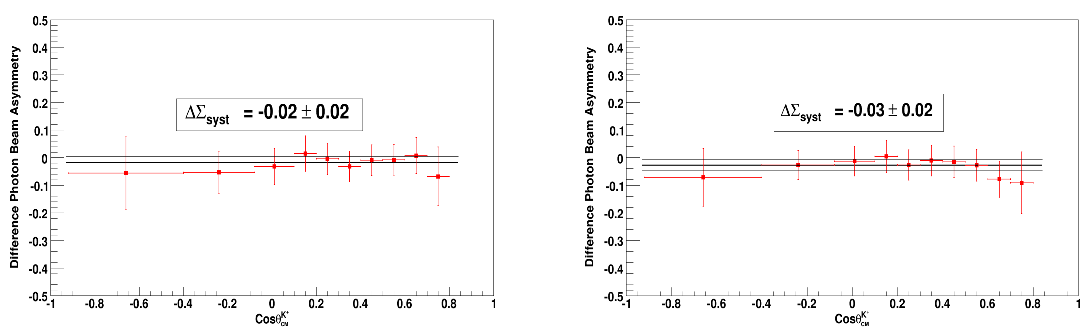


Figure 7.2: Difference between the photon beam asymmetry determined from the method of moments and from the $\phi$-bin method as a function of $\cos\theta^{\star}_{K+}$ for the 2.1-2.3 GeV (left) and 1.9-2.1 GeV (right) photon energy settings.

## 7.2 Systematics Related to the $\Sigma^{-}$ Yields

The estimation of systematic errors related to the $\Sigma^{-}$ yield extraction are evaluated by exploring the quality of the numerical values used to define the standard cuts. The variation of the standard cuts (one by one) can show the impact of each one on the final results for the beam asymmetry. Among all the kinematical cuts utilized for the extraction of the $\Sigma^{-}$ yields, a set of five cuts were chosen which might have an impact on the event selection. This set of cuts comprises: $\Delta\beta_{\pi^-}$ cut, contour cut, $\Delta\beta_{K^+}$ cut, $\Delta T_\gamma$ cut, and correlated background cut.

When evaluating the effect of each cut, it is assumed that there is no correlation between the cuts; this eliminates the need for optimizing the other cuts when one of them is varied. Given that the background underneath the invariant mass is small (less than 5%), the selected cuts are explored only by loosening them in order to investigate if their numerical values are good enough or, on the contrary, are throwing out too many good events. The effect of each cut on the asymmetry extraction is then determined by taking the difference between the asymmetry obtained with a loose cut ($4\sigma$ value) and that obtained with the standard cut ($3\sigma$ value). Since this clearly assumes the 4-$\sigma$ and 3-$\sigma$ data are independent, one really ends up inferring from these studies an upper limit on the estimated systematic uncertainties using the mean and RMS values of the difference between the corresponding beam asymmetries.

### 7.2.1 $\Delta\beta_{\pi^-}$ cut

The sensitivity of the beam asymmetry with the $\Delta\beta_{\pi^-}$ cut is studied by varying the cut from $3\sigma$ to $4\sigma$. The asymmetries obtained after applying a $3\sigma$ and a $4\sigma$ cut on $\Delta\beta_{\pi^-}$ are shown in Figure 7.3 for the 2.1-2.3 GeV and 1.9-2.1 GeV photon energy settings. Figure 7.4 shows the corresponding difference between both asymmetries as a function of $\cos\theta^{\star}_{K^+}$. Since there is not a clear angular dependence, the mean difference, determined by fitting the difference with a $0^{th}$-order polynomial, is used as a means to estimate the systematic uncertainty of the $\Delta\beta_{\pi^-}$ cut. The values obtained are consistent with zero: 0.00$\pm$ 0.02 (for the 2.1-2.3 GeV set) and 0.00 $\pm$ 0.02 (for 1.9-2.1 GeV set).

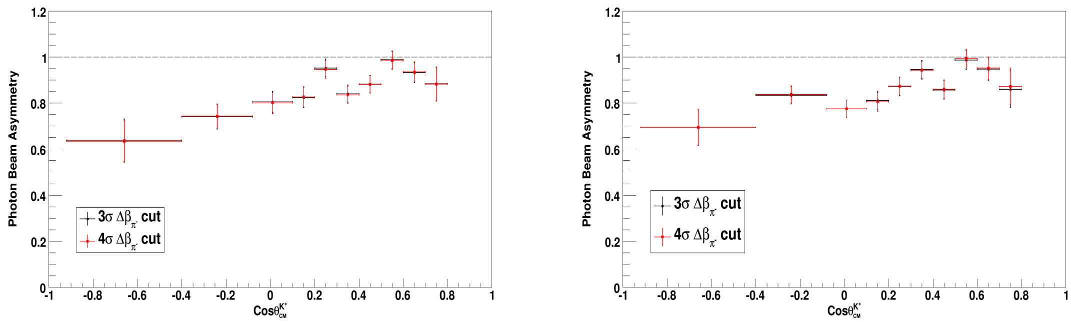


Figure 7.3: Photon beam asymmetry as a function of $\cos\theta^{\star}_{K+}$ determined using a $3\sigma$ (black points) and a $4\sigma$ (red points) cut on $\Delta\beta_{\pi^-}$ for the 2.1-2.3 GeV (left) and 1.9-2.1 GeV (right) photon energy settings.

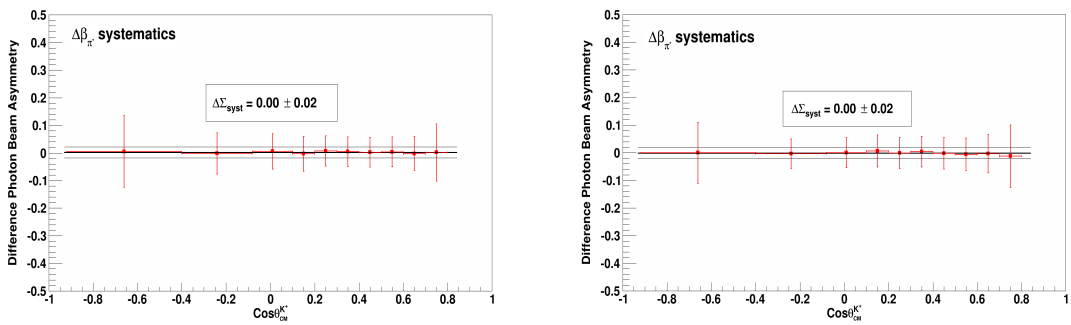


Figure 7.4: Difference between the photon beam asymmetry as a function of $\cos\theta^{\star}_{K+}$ determined using a $3\sigma$ and a $4\sigma$ cut on $\Delta\beta_{\pi^-}$ for the 2.1-2.3 GeV (left) and 1.9-2.1 GeV (right) photon energy settings.

### 7.2.2 Contour Cut

The systematic uncertainty on $\Sigma$ associated with the contour cut is determined by loosening this cut from $3\sigma$ to $4\sigma$. The corresponding photon beam asymmetries as a function of $\cos\theta^{\star}_{K+}$ for the 2.1-2.3 GeV and 1.9-2.1 GeV photon energy settings are shown in Figure 7.5. The difference between both asymmetries as a function of $\cos\theta^{\star}_{K+}$ are shown in Figure 7.6. Given that there is not an evident dependence with the polar angle, the mean difference (taken as an estimate of the systematic uncertainty of the contour cut) is calculated from a fit with a constant function. On average, it is found $0.01 \pm 0.02$ (for the 2.1-2.3 GeV photon energy bin) and $0.00 \pm 0.02$ (for the 1.9-2.1 GeV photon energy bin) of systematic uncertainty on $\Sigma$ due to the contour cut.

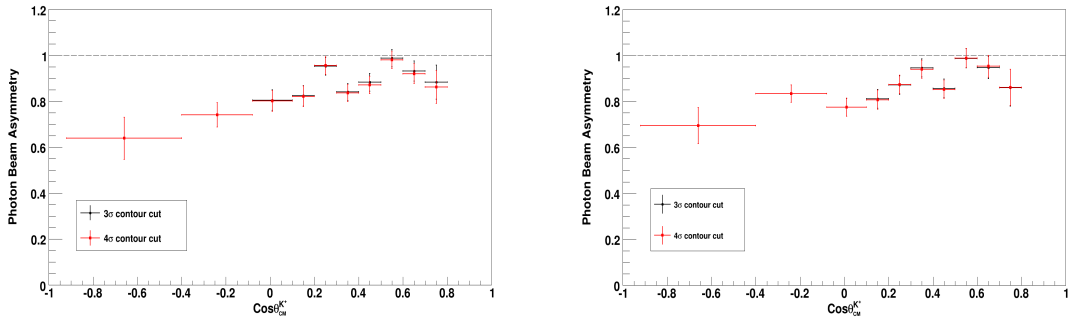


Figure 7.5: Photon beam asymmetry as a function of $\cos\theta^{\star}_{K+}$ determined by applying a $3\sigma$ (black points) and a $4\sigma$ (red points) contour cut for the 2.1-2.3 GeV (left) and 1.9-2.1 GeV (right) photon energy settings.

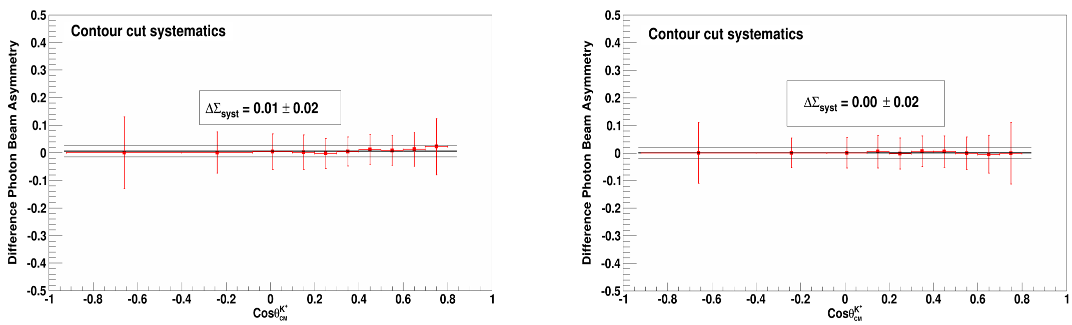


Figure 7.6: Difference between the photon beam asymmetry as a function of $\cos\theta^{\star}_{K+}$ determined by applying a $3\sigma$ and a $4\sigma$ contour cut for the 2.1-2.3 GeV (left) and 1.9-2.1 GeV (right) photon energy settings.

### 7.2.3 $\Delta\beta_{K+}$ cut

The effect of the $\Delta\beta_{K+}$ cut on the photon beam asymmetry is determined by comparing the results obtained with the standard $3\sigma$ cut and with a $4\sigma$ cut. Figure 7.7 shows the corresponding photon beam asymmetries for the 2.1-2.3 GeV and 1.9-2.1 GeV photon energy settings. The difference between both asymmetries is shown as a function of $\cos\theta^{\star}_{K+}$ in Figure 7.8. The systematic uncertainty on $\Sigma$ related to the $\Delta\beta_{K+}$ cut is estimated from the corresponding mean difference since there is not an obvious trend with $\cos\theta^{\star}_{K+}$. This difference is seen to be about $0.00 \pm 0.02$ (for the 2.1-2.3 GeV photon energy bin) and 0.00 $\pm$ 0.02 (for the 1.9-2.1 GeV photon energy bin).

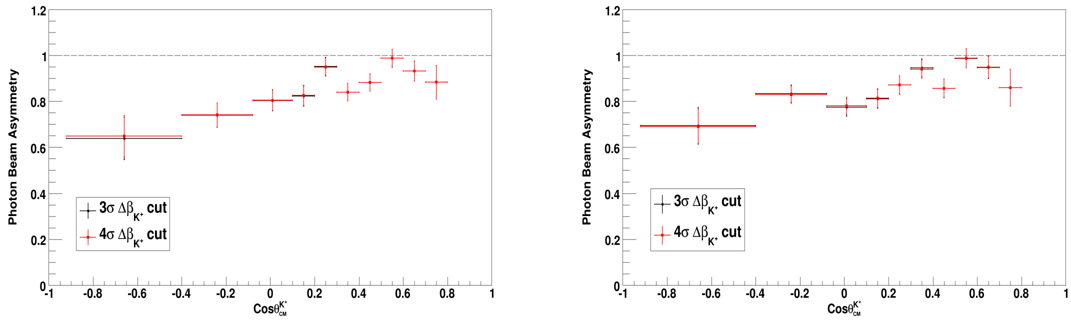


Figure 7.7: Photon beam asymmetry as a function of $\cos\theta^{\star}_{K+}$ determined using a $3\sigma$ (black points) and a $4\sigma$ (red points) cut on $\Delta\beta_{K+}$ for the 2.1-2.3 GeV (left) and 1.9-2.1 GeV (right) photon energy settings.

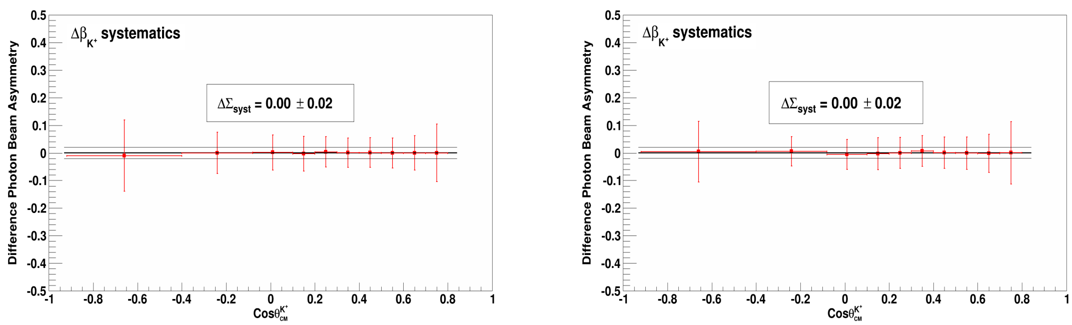


Figure 7.8: Difference between the photon beam asymmetry as a function of $\cos\theta^{\star}_{K+}$ determined using a $3\sigma$ and a $4\sigma$ cut on $\Delta\beta_{K+}$ for the 2.1-2.3 GeV (left) and 1.9-2.1 GeV (right) photon energy settings.

### 7.2.4 $\Delta T_\gamma$ cut

The photon beam asymmetries determined with a $3\sigma$ and a $4\sigma$ $\Delta T_\gamma$ cut are superimposed in Figure 7.9 as a function of $\cos\theta^{\star}_{K+}$ for the 2.1-2.3 GeV and 1.9-2.1 GeV photon energy settings. The difference $\Delta\Sigma$ between the asymmetries can be seen in Figure 7.10. Since there is not an evident dependence of $\Delta\Sigma$ with $\cos\theta^{\star}_{K+}$, the systematic uncertainty on the asymmetry associated with the $\Delta T_\gamma$ cut is estimated based on the mean difference. Such a mean value along with its uncertainty, determined with a $0^{th}$-order polynomial, are obtained to be about $0.00 \pm 0.02$ (for the 2.1-2.3 GeV set) and $0.00 \pm 0.02$ (for the 1.9-2.1 GeV set).

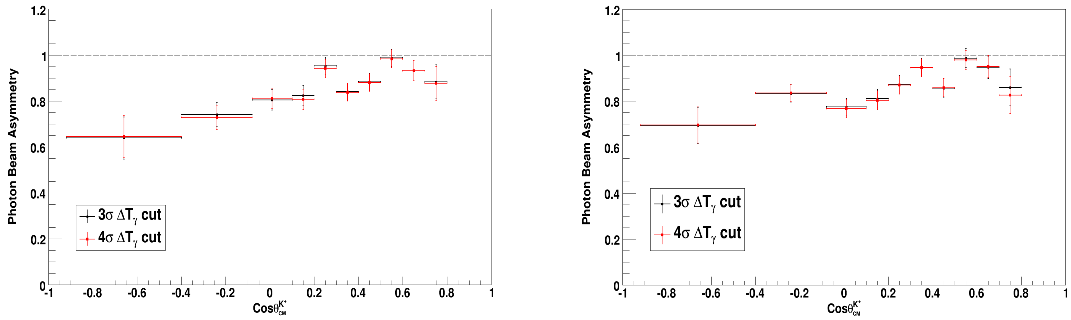


Figure 7.9: Photon beam asymmetry as a function of $\cos\theta^{\star}_{K+}$ determined using a $3\sigma$ (black points) and a $4\sigma$ (red points) cut on $\Delta T_\gamma$ for the 2.1-2.3 GeV (left) and 1.9-2.1 GeV (right) photon energy settings.

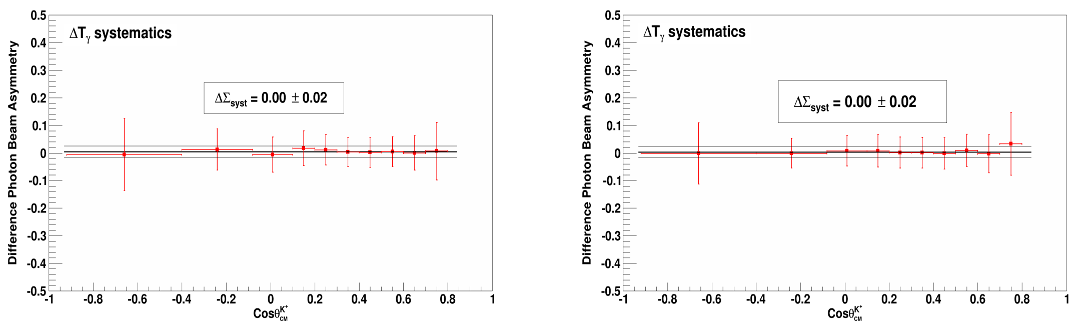


Figure 7.10: Difference between the photon beam asymmetry as a function of $\cos\theta^{\star}_{K+}$ determined using a $3\sigma$ and a $4\sigma$ cut on $\Delta T_\gamma$ for the 2.1-2.3 GeV (left) and 1.9-2.1 GeV (right) photon energy settings.

### 7.2.5 Correlated background cut

The sensitivity of $\Sigma$ with the correlated background cut is studied by comparing the photon beam asymmetries determined with $3\sigma$ and $4\sigma$ cuts. Figures 7.11 and 7.12 show the photon beam asymmetries and the corresponding difference $\Delta\Sigma$, respectively, as a function of $\cos\theta^{\star}_{K+}$ for the 2.1-2.3 GeV and 1.9-2.1 GeV photon energy settings. Since there is not a clear $\cos\theta^{\star}_{K+}$ dependence observed in $\Delta\Sigma$, the mean difference is calculated using a polynomial of order zero. The systematic uncertainty on $\Sigma$ associated with the correlated background cut is therefore estimated to be, on average, $0.00 \pm 0.02$ (for the 2.1-2.3 GeV photon energy bin) and $0.00 \pm 0.02$ (for the 1.9-2.1 GeV photon energy bin), with the very backward angular bin showing the maximum effect.

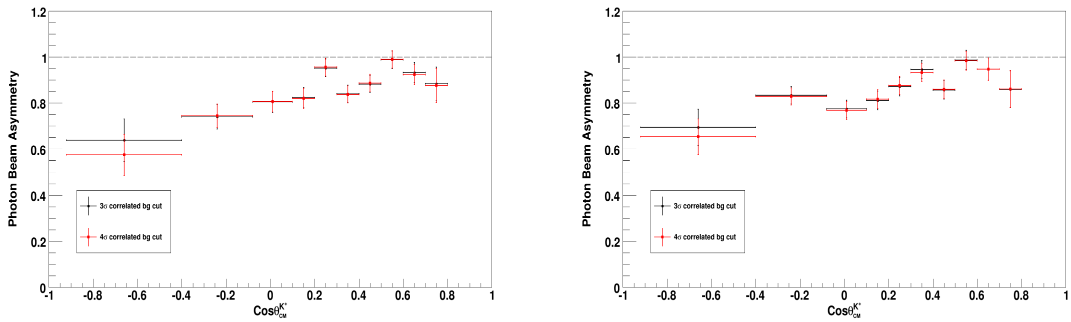


Figure 7.11: Photon beam asymmetry as a function of $\cos\theta^{\star}_{K+}$ using a $3\sigma$ (black points) and a $4\sigma$ (red points) correlated background cut for the 2.1-2.3 GeV (left) and 1.9-2.1 GeV (right) photon energy settings.

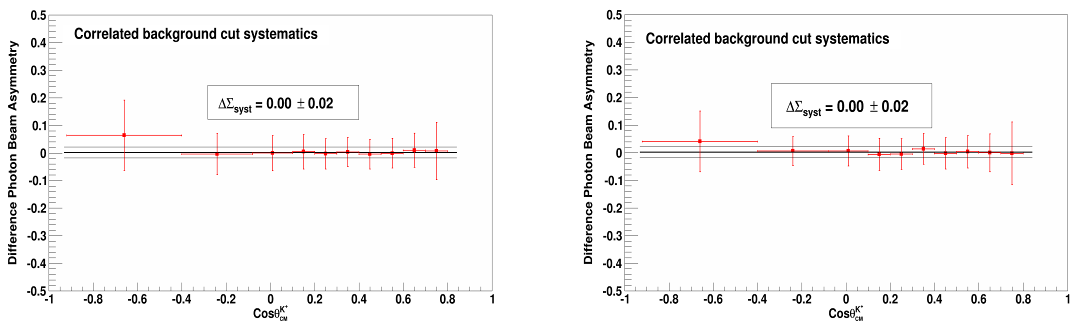


Figure 7.12: Difference between the photon beam asymmetry as a function of $\cos\theta^{\star}_{K+}$ determined using a $3\sigma$ and a $4\sigma$ correlated background cut for the 2.1-2.3 GeV (left) and 1.9-2.1 GeV (right) photon energy settings.

## 7.3 Systematics Related to the Parameters $\bar{P}_{\parallel}$, $\bar{P}_{\perp}$, $\phi_0$, and $F_R$

The dependency of the photon beam asymmetry with the parameters $\bar{P}_{\parallel}$, $\bar{P}_{\perp}$, $\phi_0$, and $F_R$ is given by Equation (6.10). The systematic uncertainties on $\Sigma$ related to these parameters can be estimated (as an upper limit) by varying the parameters between their minimum and maximum value and comparing the corresponding photon beam asymmetries.

### 7.3.1 $\bar{P}_{\parallel}$ and $\bar{P}_{\perp}$ parameters

According to studies of a high-statistical channel ($\gamma p \to p\pi^0$) using g8 data [93], the determination of the photon beam polarization in CLAS has associated a 7% uncertainty. Although neither polarization ratios $P_R$ nor mean polarizations $\bar{P}$ are involved in the method of moments, the propagation of errors of Equation (6.10) shows the upper limit in the uncertainty on $\Sigma$ due to the photon beam polarization can be estimated (for all the photon energy bins) in about 5%.

### 7.3.2 $\phi_0$ parameter

The uncertainty due to the $\phi_0$ parameter is studied by determining the difference in the photon beam asymmetry when the minimum and maximum values of $\phi_0$ are used in the determination of the moments and so, in Equation (6.10). These values are calculated as:

$$\begin{aligned} \phi_0^{min} &= \phi_0 - \Delta\phi_0 \\ \phi_0^{max} &= \phi_0 + \Delta\phi_0 \end{aligned} \tag{7.2}$$

The photon beam asymmetries $\Sigma$ obtained in both cases are shown in Figure 7.13 as a function of $\cos\theta^{\star}_{K+}$ for the 2.1-2.3 GeV and 1.9-2.1 GeV photon energy settings. The corresponding difference $\Delta\Sigma$ is illustrated in Figure 7.14. As can be noticed, the systematic uncertainty of the $\phi_0$ parameter on the photon beam asymmetry is consistent with zero for both the 2.1-2.3 GeV set and the 1.9-2.1 GeV set. In both cases, there is not a clear signal of a significant difference in the very backward and forward angular bins.

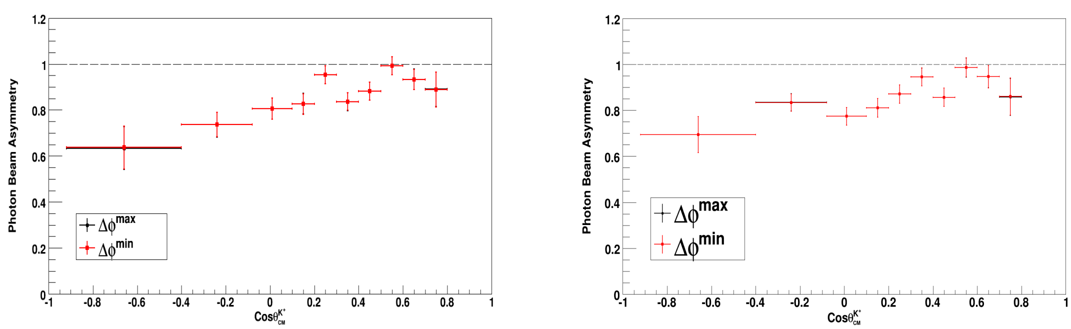


Figure 7.13: Photon beam asymmetry as a function of $\cos\theta^{\star}_{K+}$ using the minimum (red points) and maximum (black points) values of $\phi_0$ for the 2.1-2.3 GeV (left) and 1.9-2.1 GeV (right) photon energy settings.

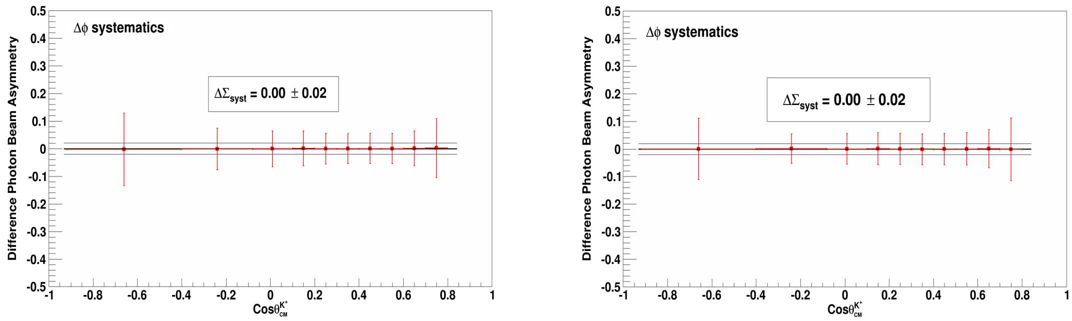


Figure 7.14: Difference between the photon beam asymmetry as a function of $\cos\theta^{\star}_{K^+}$ determined using the minimum and maximum values of $\phi_0$ for the 2.1-2.3 GeV (left) and 1.9-2.1 GeV (right) photon energy settings.

### 7.3.3 $F_R$ parameter

The effect the $F_R$ parameter has on the beam asymmetry is evaluated following the same procedure as for $\phi_0$. The minimum and maximum values of $F_R$ are calculated according to the uncertainties determined in Reference [88]:

$$F_R^{min} = F_R - \Delta F_R \tag{7.3}$$
$$F_R^{max} = F_R + \Delta F_R$$

Figures 7.15 and 7.16 show the photon beam asymmetries associated with $F_R^{min}$ and $F_R^{max}$ and the corresponding difference, respectively, as a function of $\cos\theta^{\star}_{K^+}$. Without an evident dependence of the difference with the polar angle, the systematic uncertainty on $\Sigma$ due to the variation of $F_R$ is estimated based on the mean value of the difference. The difference and its uncertainty are obtained to be about 0.00 ± 0.02 for the 2.1-2.3 GeV photon energy bin, and 0.00 ± 0.02 for the 1.9-2.1 GeV photon energy bin.

In summary, the systematic uncertainties on the photon beam asymmetry due to the methods, kinematical cuts and parameters used in its determination were evaluated. The highest impact is related to the photon beam polarization uncertainty ($\sim 5\%$) and with the method employed in the determination of the beam asymmetry ($2-3\%$). These studies were carried out after subtracting the background through the $Q$-factors technique and with the method of moments as the reference extraction method. Assuming there is no correlation between the different sources of uncertainties, the total systematic uncertainty was obtained

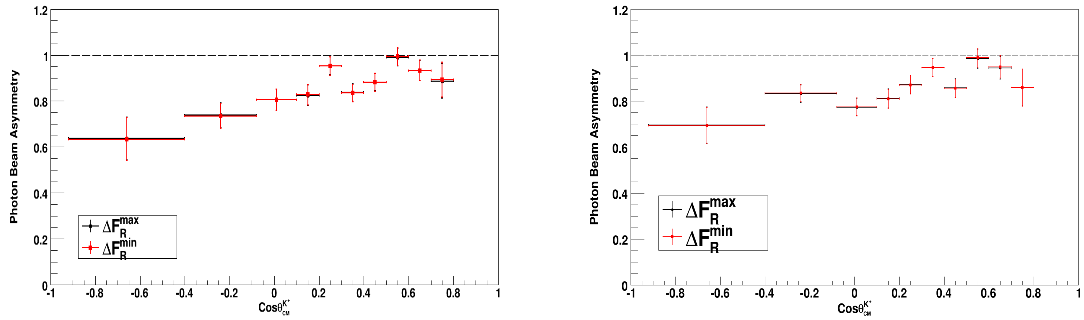

Figure 7.15: Photon beam asymmetry as a function of $\cos\theta^{\star}_{K+}$ using the minimum (red points) and maximum (black points) values of $F_R$ for the 2.1-2.3 GeV (left) and 1.9-2.1 GeV (right) photon energy settings.

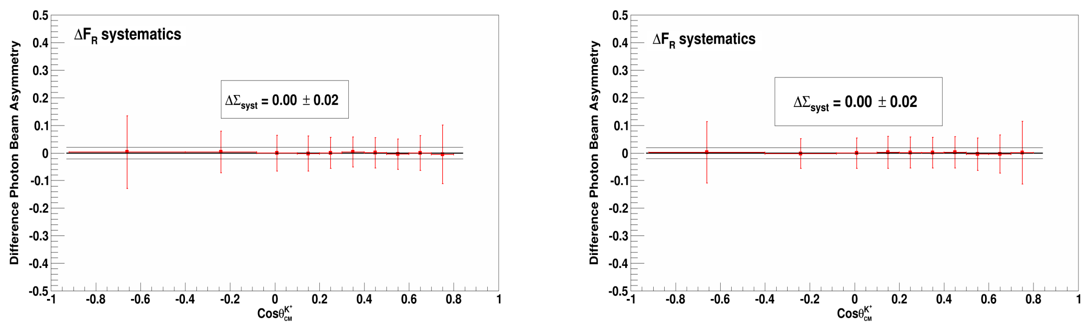

Figure 7.16: Difference between the photon beam asymmetry as a function of $\cos\theta^{\star}_{K+}$ determined using the minimum and maximum values of $F_R$ for the 2.1-2.3 GeV (left) and 1.9-2.1 GeV (right) photon energy settings.

by adding in quadrature the individual uncertainties, resulting in a total of about 5.7% for the 1.9-2.1 GeV photon energy setting and 5.4% for the 2.1-2.3 GeV photon energy setting. Tables 7.1 and 7.2 show the systematic uncertainties related to each source and each photon energy setting.

Table 7.1: Summary of the systematic uncertainties $\Delta\Sigma$ associated with the determination of the photon beam asymmetry for the quasi-free reaction $\gamma n \rightarrow K^+\Sigma^-$ for the 1.9-2.1 GeV photon-energy setting.

| Photon Energy [GeV] | Electron Energy [GeV] | Source of systematic errors | $\lvert\overline{\Delta\Sigma}\rvert$ | $\sigma_{\Delta\Sigma}$ |
|---|---|---|---|---|
| 1.9-2.1 | 5.057 | $\Sigma$ extraction method | 0.03 | 0.02 |
| | | $\Delta\beta_{\pi^-}$ cut | 0.00 | 0.02 |
| | | Contour cut | 0.00 | 0.02 |
| | | $\Delta\beta_{K^+}$ cut | 0.00 | 0.02 |
| | | $\Delta T_\gamma$ cut | 0.00 | 0.02 |
| | | Correlated bg cut | 0.00 | 0.02 |
| | | Polarization | 0.05 | $--$ |
| | | $\phi_0$ parameter | 0.00 | 0.02 |
| | | $F_R$ parameter | 0.00 | 0.02 |

Table 7.2: Summary of the systematic uncertainties $\Delta\Sigma$ associated with the determination of the photon beam asymmetry for the quasi-free reaction $\gamma n \rightarrow K^+\Sigma^-$ for the 2.1-2.3 GeV photon-energy setting.

| Photon Energy [GeV] | Electron Energy [GeV] | Source of systematic errors | $\lvert\overline{\Delta\Sigma}\rvert$ | $\sigma_{\Delta\Sigma}$ |
|---|---|---|---|---|
| 2.1-2.3 | 5.157 | $\Sigma$ extraction method | 0.02 | 0.02 |
| | | $\Delta\beta_{\pi^-}$ cut | 0.00 | 0.02 |
| | | Contour cut | 0.01 | 0.02 |
| | | $\Delta\beta_{K^+}$ cut | 0.00 | 0.02 |
| | | $\Delta T_\gamma$ cut | 0.00 | 0.02 |
| | | Correlated bg cut | 0.00 | 0.02 |
| | | Polarization | 0.05 | $--$ |
| | | $\phi_0$ parameter | 0.00 | 0.02 |
| | | $F_R$ parameter | 0.00 | 0.02 |

# Chapter 8: Final Results

The methods followed to select the $\Sigma^-$ yields and to determine the photon beam asymmetry as well as their corresponding systematic uncertainties have been discussed in the previous chapters. The goal of this chapter is to show the final results for the photon beam asymmetry determined in this work as well as their comparison with the current existing asymmetries and predictions found in the literature.

## 8.1 Comparison CLAS and LEPS Data

As mentioned in Chapter 3, the only published results currently existing on the photon beam asymmetry $\Sigma$ for the reaction $\gamma n \to K^+\Sigma^-$ come from the inclusive analysis of data from the SPring-8/LEPS facility. Figures 8.1 and 8.2 show the comparison as a function of $\cos\theta^{\star}_{K+}$ between the photon beam asymmetry determined in this work (using the method of moments) for the 1.9-2.1 GeV and 2.1-2.3 GeV photon energy settings and those determined in [21] from LEPS data. Since the two detectors complement each other, there are only two experimental points to compare with, the points centered at 0.6 and 0.7 in $\cos\theta^{\star}_{K+}$. The asymmetries obtained in this work (red points in Figures 8.1 and 8.2) were determined with a photon energy width of 200 MeV and cover an angular range from about 38° to 155° in the center of mass of the reaction; the results from LEPS correspond (black triangles for 2.05 GeV and magenta triangles for 2.15 GeV in Figures 8.1 and 8.2) were obtained with a photon energy width of 100 MeV and cover a 5° to 55° angular range in the center of mass frame. It is evident then that the results determined in this work represent a significant increment in the kinematic coverage of the data currently existing in the literature for the beam asymmetry of $K^+\Sigma^-$. The tabulated data are presented in Appendix A.

The photon beam asymmetry $\Sigma$ is seen to be positive at all angles and at both photon energy bins, showing a mild polar angle dependence and reaching a maximum value of about 0.99 at $\cos\theta^{K+}_{CM} \approx 0.55$ ($\theta^{K+}_{CM} \approx 56°$). The results from both data sets (CLAS and LEPS) agree well within the error bars at the photon energy bins studied. For CLAS data both statistical and systematics errors are shown. The statistical errors are in general smaller

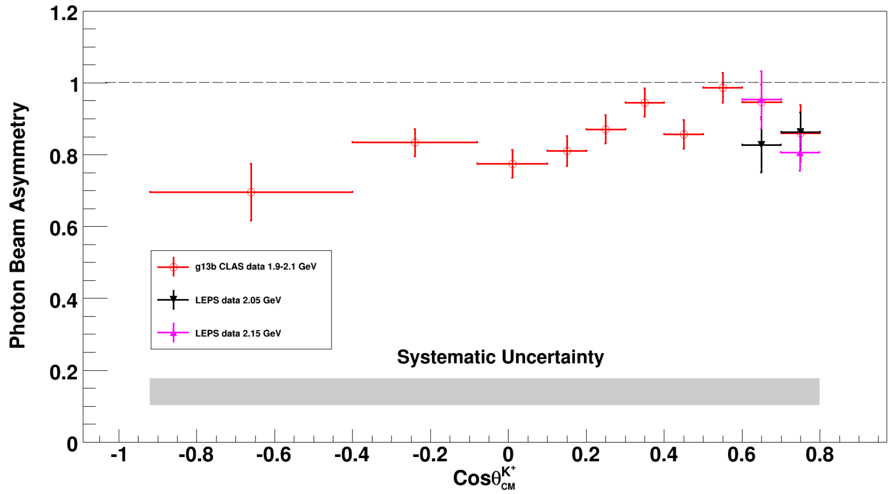


Figure 8.1: Comparison of the photon beam asymmetry as a function of $\cos\theta^{\star}_{K^+}$ determined in this work (open red circles) for the 1.9-2.1 GeV photon energy setting. LEPS results are shown for the 2.05 GeV (black triangles) and the 2.15 GeV (magenta triangles) photon-energy bins. Both statistical (red points) and systematics (gray band) uncertainties for the asymmetries determined in this work are shown.

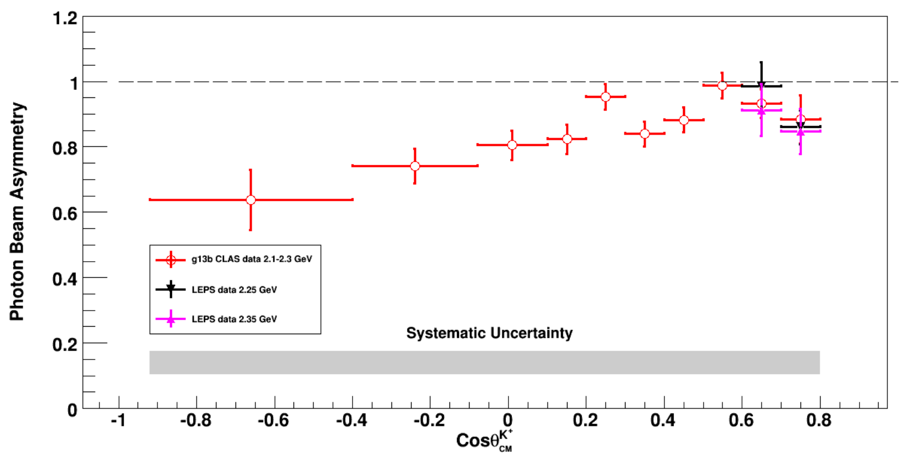


Figure 8.2: Comparison of the photon beam asymmetry as a function of $\cos\theta^{\star}_{K^+}$ determined in this work (open red circles) for the 2.1-2.3 GeV photon energy setting. LEPS results are shown for the 2.25 GeV (black triangles) and the 2.35 GeV (magenta triangles) photon-energy bins. Both statistical (red points) and systematics (gray band) uncertainties for the asymmetries determined in this work are shown.

than the systematic errors except at the very backward and the very forward angles where the statistics is low and the systematic error bars are smaller by about 10%. For LEPS data only the statistical errors are shown. When comparing both data sets, the statistical error bars are of the same magnitude.

## 8.2 Comparison CLAS Data and Kaon-MAID Predictions

Kaon photoproduction is usually described theoretically from the scheme of hadron exchanges. In the $s$-channel, $N$, $N^\star$ and $\Delta^\star$ are the exchanged particles; ground-state and excited hyperons are exchanged in the $u$-channel while $K$ and $K^\star$ mesons are the ones contributing in the $t$-channel, being this last meson-exchange contribution expected to be dominant at forward angles. At this point, the photon beam asymmetry $\Sigma$ plays a key role to identify the type of meson exchanged since at small values of $|t|$ and at high energies, $\Sigma$ tends to reach the value $+1$ or $-1$ depending on whether it is the $K^\star$ or the $K$ the meson being exchanged [21]. As discussed in Chapter 3, the Kaon-MAID model assumes the dominance of the $K$ meson in the $t$-channel leading then to predictions of negative beam asymmetries for the $K^+\Sigma^-$ channel. On the contrary, the data obtained in this analysis show that the beam asymmetries have positive values indicating the $t$-channel should be dominated by the exchange of the $K^\star$ meson. Figure 8.3 shows the comparison between the Kaon-MAID predictions and the CLAS results determined in this work for the photon beam asymmetry of $K^+\Sigma^-$ at the 2.1 GeV photon energy bin. Predictions from Kaon-MAID at higher photon energies ($>$ 2.1 GeV) are not available. These experimental results indicate therefore the need for an improvement in the current Kaon-MAID-like phenomenological models.

## 8.3 Conclusions

In this work, the azimuthal photon beam asymmetry $\Sigma$ has been determined for the quasi-free reaction $\gamma n \to K^+\Sigma^-$ for two different photon energy bins: $E_\gamma$=1.9-2.1 GeV with $E_e$=5.057 GeV, and $E_\gamma$=2.1-2.3 GeV with $E_e$=5.157 GeV using CLAS data from the g13b run period. The determination of $\Sigma$ was carried out by doing an exclusive analysis of the reaction $\gamma d \to K^+\Sigma^- K^+ (p)$ where the $K^+$ as well as the decay products of the $\Sigma^-$, $\pi^-$ and $n$, were detected. The quasi-free reaction $\gamma n \to K^+\Sigma^-$ was defined by imposing the condition for the momentum of the proton ($p$) to be less than 150 MeV. The results obtained in this

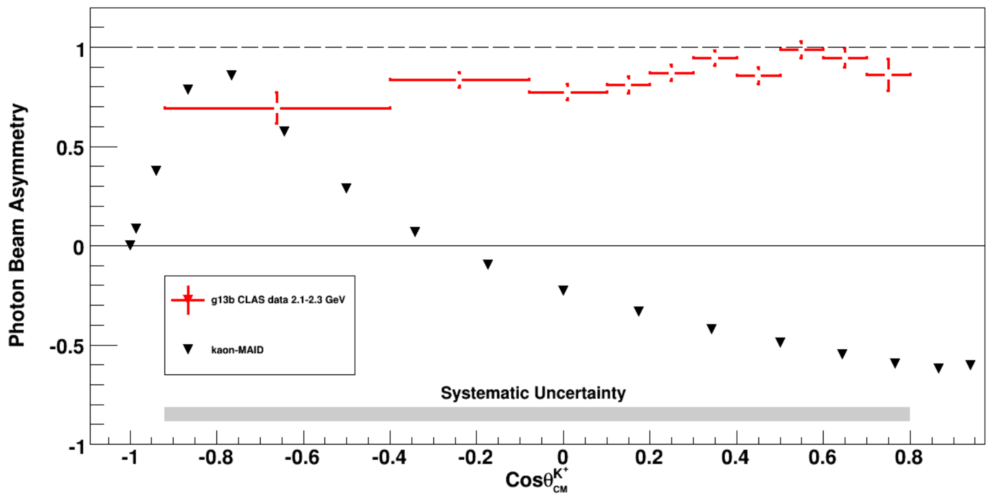


Figure 8.3: Comparison of the photon beam asymmetry as a function of $\cos\theta^{\star}_{K^+}$ determined in this work (open red circles) for the 1.9-2.1 GeV photon energy setting with the Kaon-MAID predictions (black triangles) at 2.1 GeV. Both statistical (red points) and systematics (gray band) uncertainties for the asymmetries determined in this work are shown.

work provide the only data of $\Sigma$ available for the reaction $\gamma n \rightarrow K^+\Sigma^-$ covering the range between 55° and 155° in the kaon azimuthal center-of-mass angle in the 1.9-2.3 GeV energy range. The clear discrepancy with the predictions of the Kaon-MAID model illustrate that these data provide important constraints in the search for missing N$^\star$ states, and will be a valuable input for theoretical efforts, for instance at the new Physics Analysis Center at JLab.

# Bibliography


[1] The original papers are collected in M. Gell-Mann and Y. Ne'eman, *The Eightfold Way*, New York Benjamin, 1964.

[2] V. E. Barnes *et al.*, Phys. Rev. Lett. **12**, 204 (1964).

[3] An extensive bibliography on the quark model is given by 0. W. Greenberg, *Am.J. Phys.* **50**, 1074 (1982). Many of the classic papers (including the original unpublished one by G. Zweig) are reprinted in D. B. Lichtenberg and S. P. Rosen, eds., *Developments in the Quark Theory of Hadrons*, Hadronic Press, 1980.

[4] A. Bettini, *Introduction to Elementary Particle Physics* (Cambridge University Press, 2008).

[5] F. Halzen and A. D. Martin, *Quarks and Leptons: An Introductory Course in Modern Particle Physics* (John Wiley & and sons, 1984).

[6] D. J. Gross and F. Wilczek, Phys. Rev. Lett. **30**, 1343 (1973).

[7] D. Politzer, Phys. Rev. Lett. **30**, 1346 (1973).

[8] S. Bethke, Prog. Part. Nucl. Phys. **58**, 351 (2007).

[9] http://www.particleadventure.org/quark_confinement.html.

[10] B. Povh, K. Rith, C. Scholz, and F. Zetsche, *Particles and Nuclei: An Introduction to the Physical Concepts* (Springer, 2008).

[11] S. D. Bass, Rev. Mod. Phys. **77**, 1257 (2005).

[12] O. Gayou *et al.*, Phys. Rev. Lett. **88**, 092301 (2002).

[13] V. Punjabi *et al.*, Phys. Rev. **C 71**, 055202 (2005).

[14] A. J. R. Puckett *et al.*, Phys. Rev. Lett. **104**, 242301 (2010).

[15] P. A. M. Guichon and M. Vanderhaeghen, Phys. Rev. Lett. **91**, 142303 (2003).

[16] P. Hägler *et al.*, Phys. Rev. **D 68**, 034505 (2003).

[17] S. Capstick and W. Roberts, Phys. Rev. **D 58**, 074011 (1998).

[18] V. A. Nikonov *et al.*, nucl-th:0008024 (2000).

[19] V. A. Nikonov *et al.*, arXiv:0707.3600v1 (2007).

[20] R. Bradford *et al.*, Phys. Rev. **C 75**, 035205 (2007).

[21] H. Kohri *et al.*, Phys. Rev. Lett. **97**, 082003 (2006).

[22] T. Mart *et al.*, *http://www.kph.uni-mainz.de/MAID/kaon/kaonmaid.html* (, 2000).

[23] A. W. Thomas and W. Weise, *The Structure of the Nucleon* (Wiley-VCH, 2001).

[24] A. de Rjula, H. Georgi, and S. L. Glashow, Phys. Rev. **D 12**, 147 (1975).

[25] N. Isgur and G. Karl, Phys. Rev. **D 18**, 4187 (1978).

[26] N. Isgur and G. Karl, Phys. Rev. **D 19**, 2653 (1979).

[27] S. Godfrey and N. Isgur, Phys. Rev. **D 32**, 189 (1985).

[28] S. Capstick and W. Roberts, Prog. Part. Nucl. Phys. **45**, S241 (2000).

[29] M. Lüscher, Annales Henri Poincare **4**, S197 (2003).

[30] A. Ukawa and C.-P. . J. collaboration, Nucl. Phys. **B (Proc. Suppl.) 106**, 195 (2002).

[31] A. M. Green, *Hadronic Physics from Lattice QCD* (World cientific Publishing Co, 2004).

[32] N. Suzuki, T. Sato, and T.-S. Lee, Phys. Rev. **C 79**, 025205 (2009).

[33] R. Shankar, *Principles of Quantum Mechanics* (Second edition. Springer, 1994).

[34] I. Barker, A. Donnachie, and J. Storrow, Nucl. Phys. **B 95(2)**, 347 (1975).

[35] R. A. Arndt, R. L. Workman, Z. Li, and L. D. Roper, Phys. Rev. **C 42**, 1853 (1990).

[36] M. Jacob and G. C. Wick, Annals of Physics **7**, 404 (1959).

[37] J. Napolitano, *Prepared for 13th Annual HUGS at CEBAF (HUGS 98), Newport News, Virginia, 26 May - 2 June 1998.*

[38] W.-T. Chiang and F. Tabakin, Phys. Rev. **C 55**, 2054 (1997).

[39] E. Hourany, Romanian Reports in Physics **59**, 457 (2007).

[40] http://gwdac.phys.gwu.edu.

[41] D. Drechsel *et al.*, Nucl. Phys. **A 645**, 145 (1999).

[42] I. Blomqvist and J. M. Laget, Nucl. Phys. **A 280**, 405 (1977).

[43] R. L. Anderson, F. Turkot, and W. M. Woodward, Phys. Rev. **123**, 3 (1961).

[44] http://www.jlab.org/exp_prog/proposals/89/PR89-045.pdf.

[45] http://www.jlab.org/exp_prog/proposals/03/PR03-113.pdf.

[46] S. A. Pereira *et al.*, Phys. Lett. B **688**, 289 (2010).

[47] http://hepdata.cedar.ac.uk/View/6514308.

[48] P. Nadel-Turoński *et al.*, *Kaon Production on the Deuteron Using Polarized Photons* (JLab Experiment: E-06-103, 2006).

[49] D. Douglas *et al.*, Proceedings of the 1989 Particle Accelerator Conference , 557 (1989).

[50] Y. Chao *et al.*, Proceedings of EPAC 2004 , 1509 (2004).

[51] S. A. Bogacz and V. A. Lebedev, Proceedings of the 1999 Particle Accelerator Conference , 2897 (1999).

[52] A. Krycuk, J. Fugitt, A. Johnson, R. Kazimi, and L. Turlington, Proceedings of the 1993 Particle Accelerator Conference (1993).

[53] C. Hovater *et al.*, Linac proceedings (1996).

[54] R. Milburn, Phys. Rev. Lett. **10**, 3 (1963).

[55] T. Nakano *et al.*, Nucl. Phys. **A 684**, 71c (2001).

[56] H. Olsen and L. C. Maximon, Phys. Rev. **114**, 3 (1959).

[57] P. Nadel-Turoński *et al.*, Few Body Syst. **43**, 227 (2008).

[58] H. Überall, Phys. Rev. **103**, 4 (1956).

[59] U. Timm, Forschritte der Physic **17**, 765 (1965).

[60] D. Lohmann *et al.*, Nucl. Instr. and Meth. A **343**, 494 (1994).

[61] F. Rambo *et al.*, Phys. Rev. **C 58**, 1 (1998).

[62] N. Hassall, *Spin Observables in Kaon Photoproduction from the bound Neutron in a Deuterium target with CLAS*, PhD thesis, University of Glasgow, 2010.

[63] W. J. Briscoe *et al.*, NSF Major Research Instrumentation, NSF award 9724489 .

[64] D. I. Sober *et al.*, Nucl. Instr. and Meth. B **440**, 263 (2000).

[65] D. Lawrence and M. Mestayer, CLAS-Note (2002).

[66] Y. G. Sharabian *et al.*, Nucl. Instr. and Meth. A **556**, 246 (2006).

[67] B. Mecking *et al.*, Nucl. Instr. and Meth. A **503**, 513 (2003).

[68] G. Adams *et al.*, Nucl. Instr. and Meth. A **465**, 414 (2001).

[69] M. Amarian *et al.*, Nucl. Instr. and Meth. A **460**, 239 (2001).

[70] V. Sapunenko *et al.*, Nucl. Instr. and Meth. A , to be submitted.

[71] A. Freyberg, Recsis: http://www.jlab.org/~freyberg/recsis.html.

[72] V. Blobel, *The BOS system for CLAS detector. Dynamic memory management* (Third updated printing. Institut für Experimental physik, Universität Hamburg, 1995).

[73] K. Livingston, Rootbeer: http://nuclear.gla.ac.uk/~kl/rootbeer/manual/html/rootbeer.php.

[74] Root: http://root.cern.ch/drupal/.

[75] R. M. Barnett *et al.*, Phys. Rev. **D 54**, 1 (1996).

[76] M. D. Mestayer *et al.*, Nucl. Instr. and Meth. A **449**, 81 (2000).

[77] N. Zachariou, g13b run list: https://clasweb.jlab.org/rungroups/g13/wiki_secure/index.php/G13b_Run_List.

[78] J. Ball and E. Pasyuk, CLAS-Note **2005**, 002 (2005).

[79] P. Mattione, Tripfixer: http://clasweb.jlab.org/rungroups/g13/wiki/index.php/TripFixer.

[80] P. Mattione, Momentum corrections: http://clasweb.jlab.org/rungroups/g13/MomentumCorrections.

[81] S. Brandt, *Statistical and Compuattional Methods in Data Analysis* (North Holland Publishing Company, 1970).

[82] M. Williams and C. A. Meyer, CLAS-Note **17** (2003).

[83] E. Pasyuk, Eloss package, clas cvs, clas/packages/utilities/eloss.

[84] M. Williams, M. Bellis, and C. A. Meyer, CLAS-Note **13** (2007).

[85] G. Knöchlein, D. Dreschsel, and L. T. L., Phys. A **352**, 327 (1995).

[86] R. A. Adelseck and B. Saghai, Phys. Rev. **C 42**, 108 (1990).

[87] F. A. Natter, P. Grabmayr, T. Hehl, R. O. Owens, and S. Wunderlich, Nuclear Instruments and Methods in Physics Research Section B: Beam Interactions with Materials and Atoms **211**, 465 (2003).

[88] N. Zachariou, *Determination of the Azimuthal Asymmetry of Deuteron Photodisintegration in the Energy Region $E_gamma$ = 1.1 2.3 GeV*, PhD thesis, The George Washington University, 2012.

[89] D. Sokhan, *Beam Asymmetry Measurement from Pion Photoproduction on the Neutron*, PhD thesis, University of Edinburgh, 2009.

[90] N. Zachariou and Y. Ilieva, CLAS-Note **11** (2012).

[91] W. R. Leo, *Techniques for Nuclear and Particle Physics Experiments* (Springer, 1992).

[92] M. Dugger, B. G. Ritchie, P. Collins, and E. A. Pasyuk, CLAS-Note **35** (2008).

[93] M. Dugger and B. G. Ritchie, CLAS-Note **02** (2012).

[94] P. Mattione, Kinematic fitting of detached vertices, Master's thesis, Rice University, 2007.

# Appendix A: Tabulated Results

This appendix presents the results determined in this work for the photon beam asymmetry associated with the quasi-free reaction $\gamma n \rightarrow K^+\Sigma^-$ for the 1.9 - 2.1 GeV and 2.1 - 2.3 GeV photon energy bins.

Table A.1: Photon beam asymmetry for $E_\gamma$=1.9-2.1 GeV.

| $\cos\theta_{CM}^{K^+}$ | $\Sigma$ | $\Delta\Sigma^{stat}$ | $\Delta\Sigma^{syst}$ |
|---|---|---|---|
| -0.66 | 0.694 | 0.079 | 0.057 |
| -0.24 | 0.834 | 0.038 | 0.057 |
| 0.01 | 0.774 | 0.039 | 0.057 |
| 0.15 | 0.811 | 0.041 | 0.057 |
| 0.25 | 0.871 | 0.040 | 0.057 |
| 0.35 | 0.945 | 0.039 | 0.057 |
| 0.45 | 0.857 | 0.040 | 0.057 |
| 0.55 | 0.986 | 0.042 | 0.057 |
| 0.65 | 0.947 | 0.049 | 0.057 |
| 0.75 | 0.860 | 0.080 | 0.057 |

Table A.2: Photon beam asymmetry for $E_\gamma$=2.1-2.3 GeV.

| $\cos\theta_{CM}^{K^+}$ | $\Sigma$ | $\Delta\Sigma^{stat}$ | $\Delta\Sigma^{syst}$ |
|---|---|---|---|
| -0.66 | 0.638 | 0.092 | 0.054 |
| -0.24 | 0.740 | 0.053 | 0.054 |
| 0.01 | 0.805 | 0.045 | 0.054 |
| 0.15 | 0.823 | 0.044 | 0.054 |
| 0.25 | 0.953 | 0.039 | 0.054 |
| 0.35 | 0.840 | 0.037 | 0.054 |
| 0.45 | 0.882 | 0.038 | 0.054 |
| 0.55 | 0.987 | 0.038 | 0.054 |
| 0.65 | 0.932 | 0.044 | 0.054 |
| 0.75 | 0.883 | 0.073 | 0.054 |

# Appendix B: CLAS Coordinate Systems

Two coordinate systems are used in CLAS: the laboratory coordinate system and the sector coordinate system. Both systems are shown in Figure B.1. In the lab coordinate system, $z_{lab}$ is collinear with the beam line, $y_{lab}$ points in the opposite direction to gravity, and $x_{lab}$ goes from the center of CLAS to the middle of sector 1 (parallel to the floor). The polar angle $\theta$ is the angle measured between the beam line and the track path, and the azimuthal angle $\phi$ is the angle measured between the $x_{lab}$ axis and the projection of the track path on the $x_{lab}$–$y_{lab}$ plane.

The separation of CLAS into six independent sectors makes it convenient to also use a coordinate system for each sector (six sector coordinate systems). For a given sector, $x_{sec}$ coincides with $z_{lab}$, $y_{sec}$ goes from the center of CLAS to the middle of the sector, and $z_{sec}$ is perpendicular to the $x_{sec}$–$y_{sec}$ plane forming a right-hand system. The transformation from lab coordinates to sector coordinates is given by:

$$\begin{pmatrix} x_{sec} \\ y_{sec} \\ z_{sec} \end{pmatrix} = \begin{pmatrix} z_{lab} \\ x_{lab}\cos\alpha + y_{lab}\sin\alpha \\ -x_{lab}\sin\alpha + y_{lab}\cos\alpha \end{pmatrix}$$

where $\alpha = \frac{\pi}{3}(m_{sector} - 1)$ and $m_{sector}$ is the sector number (1, 2, 3, 4, 5, or 6).

Tracks are reconstructed in CLAS based on the sector coordinate systems. The reconstruction, as seen in Figure B.1, defines a set of five tracking parameters: $q/p$, $\lambda$, $\phi_{sec}$, $D_0$, and $Z_0$. The first parameter, $q/p$, is the ratio between the charge $q$ of the particle and its momentum $p$ measured in CLAS; $\lambda$ is the angle between the track and the sector's $x_{sec}$–$y_{sec}$ plane; $\phi_{sec}$ corresponds to the projection of the angle between the track and the beam line in the sector's $x_{sec}$–$y_{sec}$ plane (in sector 1, $\phi_{sec}$ coincides with $\phi$); $D_0$ is defined as the distance of closest approach from the track to the beam line, and $Z_0$ is the $z_{sec}$ coordinate of the track in the sector's $x_{sec}$–$z_{sec}$ plane [94]. Based on the cartesian components of $p$ ($p_x$, $p_y$, and $p_z$) in the laboratory system, the track reconstruction parameters are determined

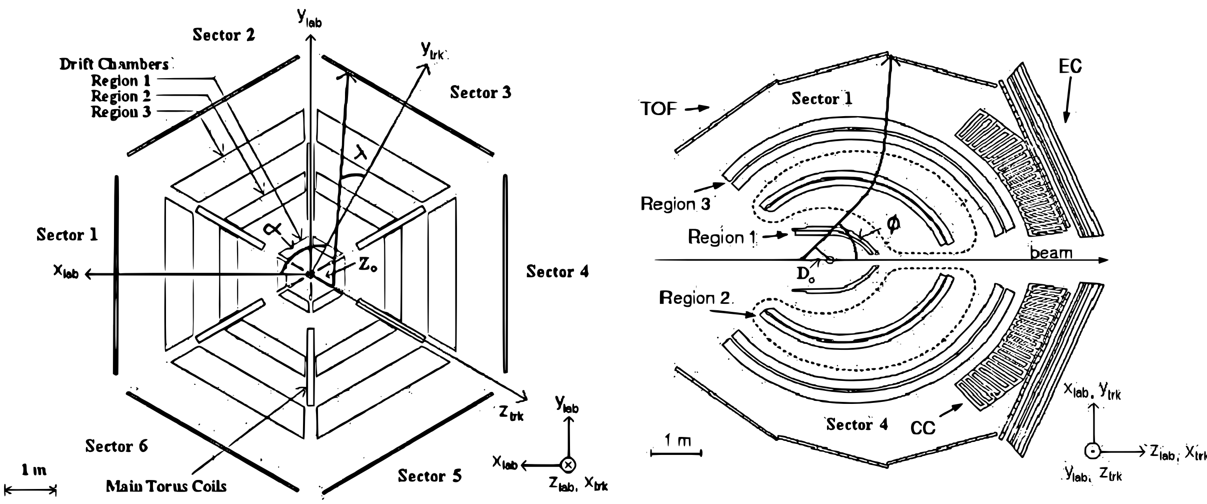


(a) (b)

Figure B.1: Laboratory and sector coordinate systems used in the CLAS detector. (a) A cut through the CLAS perpendicular to the beam line. (b) Top view of the CLAS detector cut along the beam line. Figure taken from [94].

according to:

$$\begin{pmatrix} \lambda \\ \phi_{sec} \\ D_0 \\ Z_0 \end{pmatrix} = \begin{pmatrix} \sin^{-1}((p_y \cos\alpha - p_x \sin\alpha)/p) \\ \tan^{-1}((p_x \cos\alpha + p_y \sin\alpha)/p_z) \\ \cos\phi_{sec}(x_{lab}\cos\alpha + y_{lab}\sin\alpha) - z_{lab}\sin\alpha \\ y_{lab}\cos\alpha - x_{lab}\sin\alpha - (x_{lab}\cos\alpha + y_{lab}\sin\alpha)\tan\lambda/\sin\phi_{sec} \end{pmatrix}$$

The reconstruction of the $\Sigma^-$ decay vertex is carried out using some of these tracking parameters.

# Appendix C: Analysis of $\gamma d \to \pi^+\pi^- np$ for corrections in the EC interaction vertex

A global correction factor to the interaction vertex in the electromagnetic calorimeter is required to improve the neutron identification. The correction factor was obtained in this work by analyzing the reaction $\pi^+\pi^- p\ n$. The analysis began by selecting events with exactly two positives, one negative, and one neutral. Pions and protons were identified from tight cuts on the mass from time-of-flight: 0.005< $M_\pi^2$ <0.04 GeV/c$^2$ and 0.81< $M_p^2$ <0.97 GeV/c$^2$, respectively. A condition on the vertex time difference between the various charged tracks was set to be less than 2.0 ns, and the incident photon was selected from $|T_\gamma - T_{\pi^-}|$ <1.0 ns. In addition, bad SC paddles were removed, and fiducial cuts as well as momentum and energy loss corrections were applied (using similar routines as those described for kaons and pions).

The procedure to obtain the correction consists of comparing the missing particle ($X$) in the reaction $\gamma d \to \pi^+\pi^- p(X)$, identified from a 3-$\sigma$ cut around MM($\pi^-\pi^+ p$), to the neutron detected in CLAS ($\beta_n < 0.95$ was used) in the reaction $\gamma d \to \pi^+\pi^- pn$. In order to ensure that the neutron was really detected in the expected EC region, the angle $\alpha$ between the missing 3-momentum $\vec{P}_{miss}$ and the detected 3-momentum $\vec{P}_n$ was required to fulfill the condition $\cos\alpha > 0.995$. With all the above conditions in place, the difference between the calculated missing path ($l_{miss} = c\beta_{miss}(T_n - T_\gamma)$) and the reconstructed path (from Equation 5.5) was plotted and fitted with a Gaussian function, as shown in Figure C.1, for four different scenarios: with no distinction in the EC layer hit and distinguishing between hits in the inner, outer, or both EC layers. In the first scenario, the path difference distribution peaks around zero making evident the overall good quality of the data. However, the mean values obtained in the other three scenarios correspond to 15.0, 7.5, and -8.5 cm for both, inner, and outer layers, respectively. Those values were taken as average correction terms applied in an EC-layer dependent manner to improve the calculated neutron path $l_{EC}$.

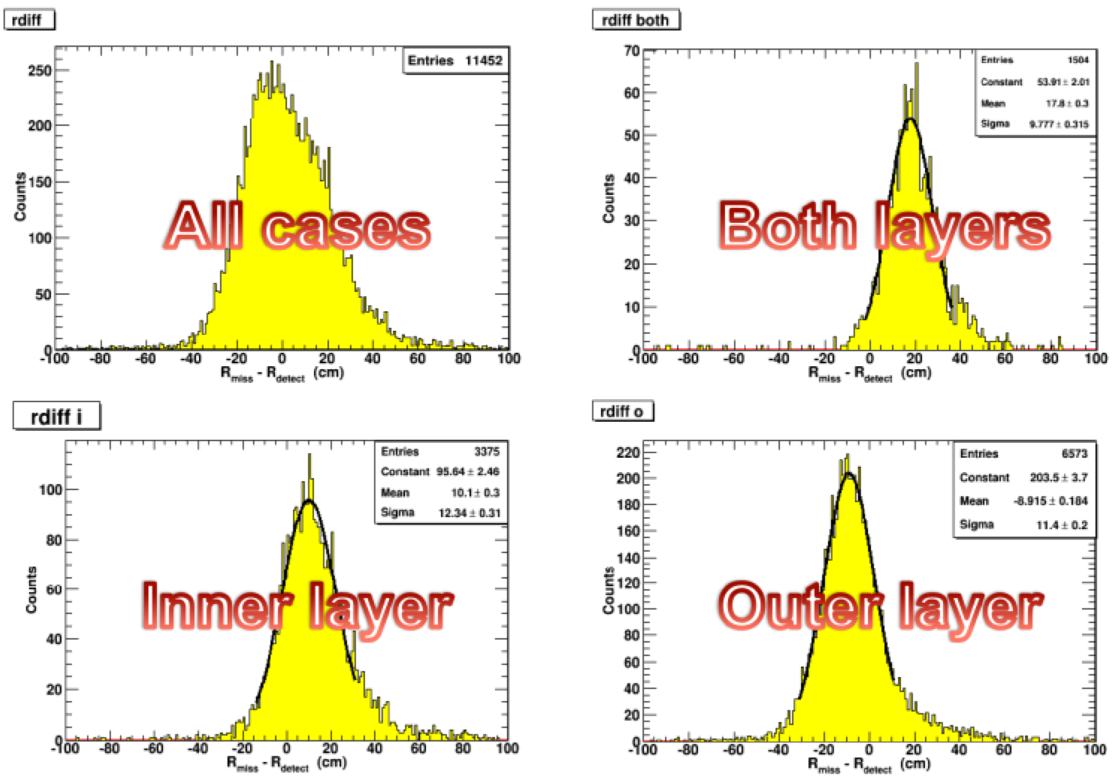


Figure C.1: Neutron path difference $l_{miss} - l_{EC}$ obtained by comparing information from a missing neutron and from a detected neutron. The plots are organized in the following way: (top left) all the EC hits are plotted, (top right) only hits that occurred on both EC layers (inner and outer) are included. (bottom left) Hits when only the inner EC layer was fired. (bottom right) Only outer layer was hit. The Gaussian fit in each case provides a global correction used to improve the neutron path length determination.

# Appendix D: Reconstruction of the $\Sigma^-$ Decay Vertex

The non-negligible mean decay path of the $\Sigma^-$ requires an algorithm to correct for the decay vertex location. The algorithm, shown schematically in Figure D.1, was developed as an iterative procedure aimed at finding the $\Sigma^-$ decay vertex. The algorithm is based on the fact the $\Sigma^-$ should have decayed somewhere along the $\pi^-$ path ($l_{\pi^-}$), even though the tracking extrapolates the $\pi^-$ path to the beamline. The search for the $\Sigma^-$ decay vertex is performed by moving along $l_{\pi^-}$ (on a "binary search" basis) in steps $s_i$. This requires the decay to occur within the straight region of the pion path, meaning that the algorithm is not valid beyond the first drift chamber region (R1). This is, however, a very large distance in comparison with the $\Sigma^-$ decay path. The lower and upper limits (the initial values for the binary search) were defined as the nominal vertex position of the $\pi^-$ and the front face of R1, respectively. The latter was calculated from a piecewise function [94] depending on whether the pion struck the flat or circular portion of R1. Using the sector coordinate system with tracking parameters $D_0, \lambda$, and $\phi$ [1], the flat portion corresponds to the condition $D_0 \geq 57.88 \cos\phi$. In that case, the upper limit $L'$ for the pion path is given by

$$L' = \frac{57.88}{\cos\lambda \sin\phi} \tag{D.1}$$

If $D_0 < 57.88 \cos\phi$, the upper limit for the circular portion is given by:

$$L' = \frac{1}{\cos\lambda}\left(\sqrt{12306 - (53\cos\phi - D_0)^2} - D_0\cos\phi - 53\sin\phi\right). \tag{D.2}$$

Taking into account that the $n$ and $\pi^-$ originate at the same vertex, one can calculate the neutron path length[2] at each step $\vec{l}_n(s_i)$ (see Equation 5.5) as well as the neutron time-of-flight to the calorimeter $T'_n(s_i)$. Based on those two quantities, the velocity and momentum are derived. The latter, $\vec{P}_n(s_i)$, is combined with the (uncorrected) measured

[1] $D_0$ is defined as the distance of closest approach from the track to the beam line; $\lambda$ is the angle between the track and the sector's $x-y$ plane; $\phi$ is the angle in the sector's $x-y$ plane between the track and the beam line. The sector coordinate system and the tracking parameters are defined in Appendix B.

[2] The calculation of the neutron path length at each step takes into account only the path correction associated with the uncertainty in the EC hit coordinates.

momentum of the pion, $\vec{P}_{\pi^-}$, to determine the direction the $\Sigma^-$would have had (green arrows in Figure D.1) if it had decayed at that particular point $s_i$. Likewise, one can define the four-momentum vector for the neutron $p_n(s_i)$ and pion $p_{\pi^-}$ to determine the invariant mass M($\pi^-$ $n(s_i)$). To find the point $s_i$ corresponding to the decay vertex, a *reference* vector from the production vertex (known from the $K^+$) to $s_i$ is drawn (black dashed arrows in Figure D.1). As a first condition, if the $\cos\theta_i$ function (where $\theta_i$ is the angle between the momentum of the $\Sigma^-$and the *reference* vector) is maximized at that point, $s_i$ is assumed to be a potential candidate for the decay vertex. A second condition requires checking if the invariant mass M($\pi^-$ $n(s_i)$) calculated at $s_i$ has improved (if it is closer to the $\Sigma^-$PDG mass of 1.197 GeV/c$^2$ [75]) compared to the invariant mass $M$ calculated before starting the algorithm. If so, then the iteration stops and $s_i$ is saved as the decay vertex. If not, the iteration stops and no correction at all is applied to the decay vertex. From preliminary studies, it was found that just 12% of the events are corrected by the algorithm. For the other 88%, no good $s_i$ point is found and therefore no correction is applied. In this situation, the interpretation is that most (88%) of the $\Sigma^-$decay close to where they were produced, and so within the experimental uncertainty, the production vertex ends up being a good choice for the decay vertex. Figures D.2 and D.3 show some results obtained only for the events corrected by the algorithm. Figure D.4 displays the effect of the correction on the invariant mass, $M(\pi^- n)$, distribution. The effect on the missing mass $MM(K^+\pi^- n)$ is negligible.

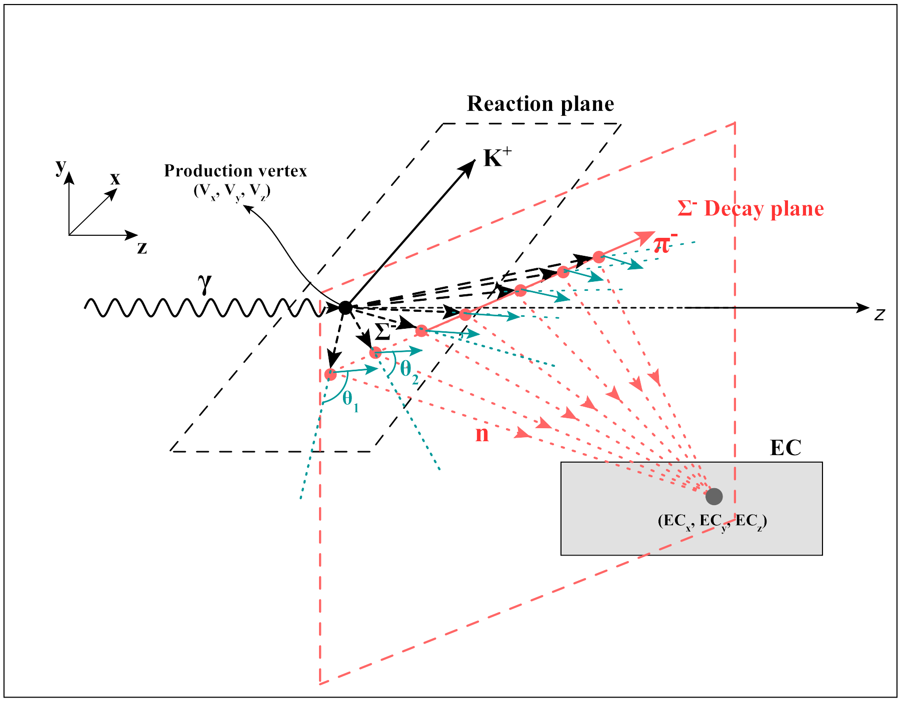


Figure D.1: Schematic view of the $\Sigma^-$decay vertex correction. The algorithm consists on moving in different steps along the $\pi^-$ path (red solid arrow) and try at each step a possible trajectory, beta and momentum for the neutron (red dashed vectors). The vector momentum for $\Sigma^-$calculated at each iteration (green arrows) is compared to a reference vector (black arrows) drawn from the production vertex to the vector position associated with each step. The iteration ends when, at certain step, the angle between the $\Sigma^-$momentum and the reference vector is found to be the closest to zero.

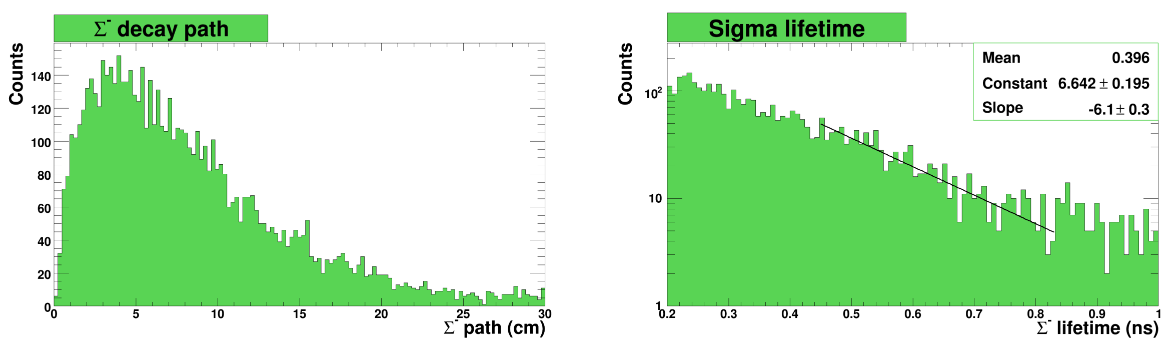


(a) (b)

Figure D.2: $\Sigma^-$path length (a) and lifetime (b) reconstructed by the algorithm. In the range 0.4-0.8 ns, the lifetime fit (0.610 ns$^{-1}$) agrees well with the PDG value (0.676 ns$^{-1}$) [75]. This indicates that the algorithm successfully reconstructs the $\Sigma^-$decay vertex. In the code, the algorithm was implemented right after applying fiducial, PID, and timing cuts. Notice the logarithmic scale on the right plot.

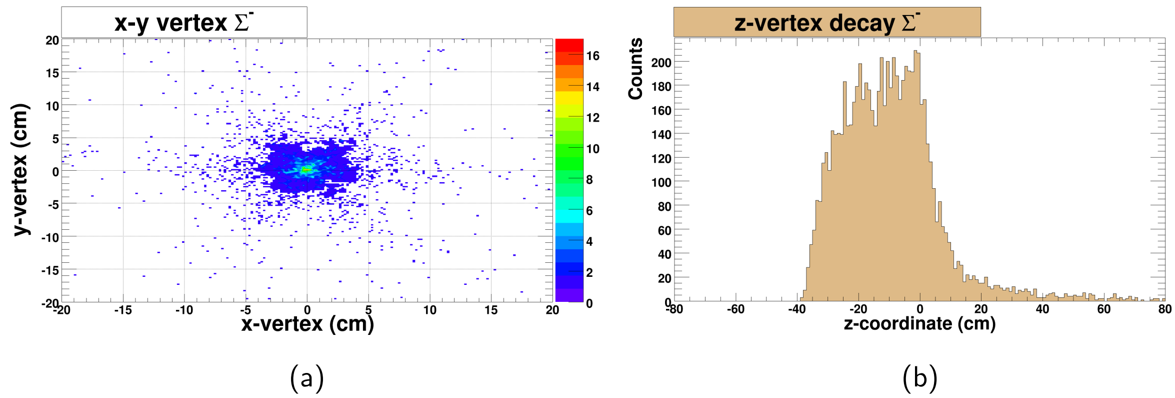


Figure D.3: (a) $x$ vs $y$ distribution for the $\Sigma^-$decay vertex reconstructed by the algorithm. (b) $z$-coordinates for the $\Sigma^-$decay vertex. Note the significant amount of $\Sigma^-$decaying beyond the target wall at $z$=0 cm. In the code, the algorithm was implemented right after applying fiducial, PID, and timing cuts. The histograms show only the events corrected by the algorithm ($\sim$ 12%).

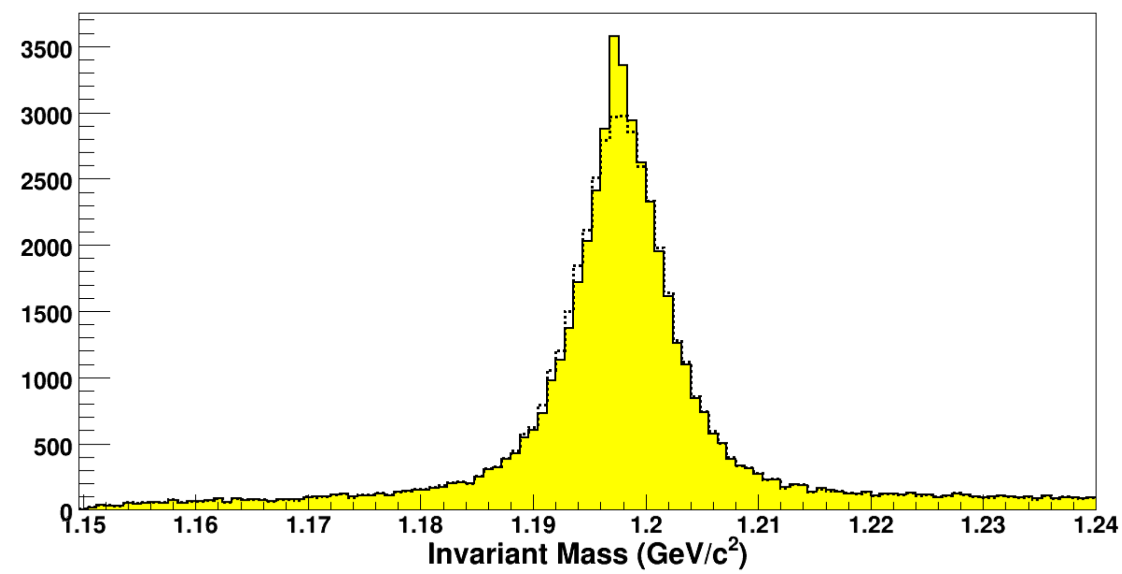


Figure D.4: Invariant-mass distribution $M(\pi^- n)$ before (dashed histogram) and after (yellow-solid histogram) applying the $\Sigma^-$decay vertex correction. Histograms were filled after fiducial, PID, and timing cuts.